

2015

Ballistic atom pumps

Tommy Byrd

College of William & Mary - Arts & Sciences

Follow this and additional works at: <https://scholarworks.wm.edu/etd>

Recommended Citation

Byrd, Tommy, "Ballistic atom pumps" (2015). *Dissertations, Theses, and Masters Projects*. Paper 1539623999.

<https://dx.doi.org/doi:10.21220/s2-xhfm-vr13>

This Dissertation is brought to you for free and open access by the Theses, Dissertations, & Master Projects at W&M ScholarWorks. It has been accepted for inclusion in Dissertations, Theses, and Masters Projects by an authorized administrator of W&M ScholarWorks. For more information, please contact scholarworks@wm.edu.

Ballistic Atom Pumps

Tommy Byrd

Bristol, Tennessee

Master of Science, College of William and Mary, 2011
Bachelor of Science, East Tennessee State University, 2008

A Dissertation presented to the Graduate Faculty
of the College of William and Mary in Candidacy for the Degree of
Doctor of Philosophy

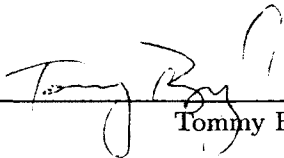
Department of Physics

The College of William and Mary
January, 2015

APPROVAL PAGE

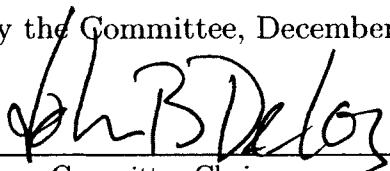
This Dissertation is submitted in partial fulfillment of
the requirements for the degree of

Doctor of Philosophy




Tommy Byrd

Approved by the Committee, December, 2014

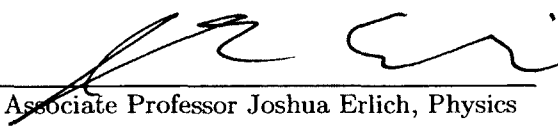


Committee Chair

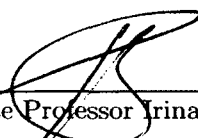
Professor John Delos, Physics
The College of William and Mary




Associate Professor Seth Aubin, Physics
The College of William and Mary



Associate Professor Joshua Erlich, Physics
The College of William and Mary



Associate Professor Irina Novikova, Physics
The College of William and Mary



Professor Nahum Zobin, Mathematics
The College of William and Mary

ABSTRACT

Researchers have long been interested in electron transport through mesojunctions containing time-dependent potential energies, a process often called “quantum pumping.” A useful model of such a system is a ballistic atom pump, which consists of two reservoirs of neutral ultracold atoms connected by a channel containing oscillating repulsive potential-energy barriers. Under certain conditions, such pumps can create net transport of atoms from one reservoir to the other, and energy can be pumped out of or into each reservoir even when there is no net particle transport. These pumps are studied from classical and quantum-mechanical perspectives, and semiclassical theory is used to explain some scattering properties which are not easily explained by quantum theory. This system is also a nice model of chaotic transport. Escape-time plots showing the time for classical trajectories to escape the barrier region display a type of fractal self-similarity. A topological theory using a discrete map of the system in the phase plane is developed, and this theory predicts and explains the features seen in escape-time plots.

TABLE OF CONTENTS

Acknowledgments	v
List of Tables	vi
List of Figures	vii
CHAPTER	
1 Introduction	2
2 Scattering from a Single Amplitude-Modulated Potential-Energy Barrier	7
2.1 Model	9
2.2 Quantum and Classical Descriptions	11
2.2.1 Quantum Description	11
2.2.2 Classical Description	15
2.3 Semiclassical Description	20
2.4 Case Studies	25
2.5 Proposed Experiment	30
2.6 Remarks	31
3 Particle Transport in Ballistic Atom Pumps	33
3.1 Model	35
3.2 Particle Diodes	39
3.2.1 An Elevator Model	39
3.2.2 Quantum Suppression of Classical Transmission	48
3.2.3 Gaussian Barriers	51
3.3 Symmetric Pumps: A General Theorem	53

3.4	Symmetric Rectangular Barriers	56
3.4.1	No space between the barriers	56
3.4.2	Separated barriers	64
3.5	Symmetric Gaussian Barriers	73
3.6	Remarks	77
4	Energy and Heat Transfer in Ballistic Atom Pumps	79
4.1	Summary of Results	80
4.2	System	80
4.3	Method	82
4.4	Results	84
4.4.1	Region I: No particle transport; left reservoir heated	84
4.4.2	Region IV: No particle transport; both reservoirs cooled	85
4.4.3	Region II: Net left-to-right particle transport	86
4.4.4	Region III: Net right-to-left particle transport	87
4.4.5	Averaging over energies	88
4.5	Remarks	88
5	Homotopic Lobe Dynamics (HLD)	90
5.1	Phase Space	92
5.2	Homoclinic Tangles	96
5.3	Homotopic Lobe Dynamics	102
5.3.1	Fundamental Segments	103
5.3.2	Neighbors	104
5.3.3	Holes	105
5.3.4	Bridges	106
5.3.5	Symbolic Dynamics	109

5.3.6	Epistrophes	111
6	HLD for a Full Scattering Problem with a Heteroclinic Tangle	114
6.1	Computation of Escape Times	116
6.2	Topological Analysis – Sketch of the Theory	119
6.3	Comparison of Topologically-Predicted and Computed Escape Segments	123
6.4	Homotopic Lobe Dynamics for a Full Scattering Problem with a Hete- roclenic Tangle	127
6.4.1	Heteroclinic Tangle	128
6.4.2	Initial Conditions	134
6.4.3	Homotopic Lobe Dynamics: Overview	137
6.4.4	Fundamental Segments	138
6.4.5	J-neighbors	138
6.4.6	Holes	139
6.4.7	Bridges	143
6.4.8	Additional Bridges	146
6.4.9	Topological Predictions	148
6.5	Case Study	150
6.6	Remarks	157
7	Conclusion	159
 APPENDIX A		
	Introduction to Semiclassical Theory	163
A.1	WKB Approximation in Configuration Space	164
A.2	WKB Approximation in Momentum Space	167
A.3	Changing Coordinates to Describe the Wave Function	173
A.3.1	Stationary Phase Method	174
A.4	Time-Dependent Semiclassical Approximation	178

APPENDIX B	
Implementation of Semiclassical Theory	179
B.1 Local Wavefunction	179
B.1.1 Maslov Index	189
B.1.2 Theorem I	193
B.1.3 Corrections Near Momentum Turning Points	194
B.1.4 Relation to Airy Function	197
B.1.5 Classically-Forbidden Regions	201
B.2 Global Wavefunction	206
B.3 Semiclassical Implications of Periodicity	208
Bibliography	213
Vita	222

ACKNOWLEDGMENTS

I owe many thanks to John Delos, Seth Aubin, Kevin Mitchell, Kunal Das, Megan Ivory, and A. J. Pyle for their role in this work.

LIST OF TABLES

5.1	Notation used to describe manifold segments.	100
6.1	Escape segments predicted by the level of initial topological information used in the example, and the number of escape segments seen in directly-computed trajectories.	127
6.2	Notation used to describe manifold segments.	131
A.1	Semiclassical Formulas.	164

LIST OF FIGURES

1.1 A ballistic atom pump.	4
2.1 Snapshots from a typical quantum-mechanical calculation	11
2.2 Quantum and classical momentum probability densities for scattering from a single barrier.	14
2.3 Final momentum vs. initial position and final momentum probabilities. . .	18
2.4 Momentum distributions for fixed velocity of incident packet but for differ- ent values of ω	19
2.5 Probability distributions of final momenta.	21
2.6 Quantities that determine the phase evolution and interference of three trajectories ending with the same final momentum.	24
2.7 Final momentum probabilities for a case of pure classical transmission. . .	25
2.8 Final momentum probabilities for a case of pure classical reflection.	28
2.9 Final momentum probabilities for a case of classical partial reflection and partial transmission.	29
2.10 Proposed experimental implementation of oscillating barrier scattering. . .	31
3.1 Types of barriers considered in this chapter.	37
3.2 Qualitative schematic of a diode with rectangular barriers.	41
3.3 Fractional transport of particles, $C_P(p_i)$, for a diode with rectangular bar- riers.	44
3.4 Semiclassical analysis of scattering from a rectangular diode.	47
3.5 Suppression of classical transmission.	50
3.6 Dynamics for Gaussian diode.	52
3.7 Geometric proof of why a symmetric pump cannot preferentially pump par- ticles if initial classical distributions are uniform.	55
3.8 Dynamics for touching, rectangular barriers.	60
3.9 Dynamics for wider touching, rectangular barriers.	62
3.10 Effect of barrier width on classical particle scattering from rectangular bar- riers that touch.	65
3.11 Dynamics for separated, rectangular barriers.	66
3.12 Semiclassical analysis of scattering from separated rectangular barriers. . .	69

3.13	Effect that separating the rectangular barriers has on classical particle scattering.	71
3.14	Dynamics for symmetric Gaussian barriers.	74
3.15	Quantum and semiclassical analysis of scattering from symmetric Gaussian barriers.	76
4.1	Energy and heat transfer in an example ballistic atom pump.	85
5.1	Continuous escape times for particles temporarily trapped between two oscillating, Gaussian-shaped barriers.	91
5.2	Phase space for two static Gaussian potentials.	93
5.3	The potential $V(x) = x - x^3 + 2e^{-(x-1)^2/2}$ and its corresponding phase space.	94
5.4	An example homoclinic tangle.	96
5.5	Development of a homoclinic tangle.	99
5.6	Escape segments of an arbitrary L_0 inside a typical homoclinic tangle.	103
5.7	Holes punctured in the phase plane for use in HLD in the context of a homoclinic tangle.	106
5.8	Escape segments of an arbitrary L_0 inside a typical homoclinic tangle, with epistrophes and strophes labeled.	113
6.1	Escape-time plot for trajectories escaping the heteroclinic tangle in the double-barrier system.	118
6.2	A homoclinic tangle (left) and a heteroclinic tangle	120
6.3	Computed escape segments as a function of position along the initial-condition line.	125
6.4	Escape segments seen at the third iterate for directly-computed trajectories.	126
6.5	Surface of section showing portions of the four stable (dotted red curves) and four unstable (solid blue curves) manifolds for two unstable points of the system,	129
6.6	Segments of stable and unstable manifolds.	132
6.7	An appropriate initial-condition line for the full scattering problem.	136
6.8	Holes and subholes.	140
6.9	\mathbb{U}^T and \mathbb{U}^B , U_0^T and U_0^B and their first $J = 3$ forward iterates (solid blue curves), and \mathbb{S}^T , S^L , and \mathbb{S}^B (dotted red curves) for a given set of parameters.	144
6.10	Qualitative graph showing an initial-condition line and manifold segments.	147

6.11	Computed manifold segments and initial-condition line.	150
6.12	J -neighbors.	152
6.13	J -neighbors and J -subneighbors.	153
6.14	Bridge classes.	156
A.1	Highly oscillatory functions, for which the stationary phase method is an appropriate method for approximating the integral of.	176
B.1	A typical Lagrangian manifold for the one-barrier system.	182
B.2	Different views of a typical Lagrangian manifold for one-barrier system. . .	184
B.3	Slice of Lagrangian manifold at an intermediate time.	185
B.4	Primitive and corrected forms of local wavefunctions.	200
B.5	Functions used for extrapolating momentum-space actions into classically-forbidden regions.	203
B.6	Functions used for extrapolating amplitudes into classically-forbidden regions.	205
B.7	“Comb” functions which are responsible for sharply-peaked final momentum probabilities.	211

BALLISTIC ATOM PUMPS

CHAPTER 1

Introduction

Scattering dynamics involving periodic time-varying potentials is of fundamental importance to quantum transport physics and related applications in mesoscopic condensed matter physics. The quantum-mechanical treatment of an oscillating barrier was first studied by Büttiker and Landauer in order to understand electron tunneling times [1], and their work built on previous work on photon-assisted tunneling in superconducting diode junctions [2]. Since then several workers have developed theoretical tools for treating time-varying barrier or well potentials, for studying photon-assisted tunneling [3, 4, 5], quantum pumping [6], and electron scattering by intense laser-driven potentials [7]. These systems can display rich quantum and classical dynamics that include chaotic scattering and chaos-assisted tunneling [8, 9, 10, 11, 12], dynamical localization [13], and quantum interference [14].

In electronic solid-state systems, the transport of electrons through mesojunctions having time-dependent potential barriers, a phenomenon often called “quantum pumping,” has been theorized for decades [15, 16, 17, 18, 19, 6, 20, 21, 22, 23, 24, 25, 26, 27, 28, 29, 30, 31]. It has been shown that such a system can pump electrons from one reservoir to

another with no bias (such as a potential difference). Despite its technological promise of generating highly controlled and reversible currents at the single electron level [20], however, quantum pumping in normal mesoscopic conductors remains elusive [32, 33] (though it has been recently observed in a hybrid superconducting system [34]). Scattering by an amplitude-modulated potential barrier is of fundamental interest on its own, and it is also a building block for the more complex time-dependent potentials used in quantum pumping [15, 16, 35].

More recently, Das and Aubin have proposed simulating such electron pumps using a system of neutral cold atoms with optical potentials as the driving forces [36, 37, 38]. Neutral atom transport is becoming increasingly important in its own right due to the ongoing development of atomtronics, which seeks to replicate properties of electronics using neutral atoms, and in the field of quantum computing [39]. Experimental systems based on ultracold atoms offer the possibility of conducting precision tests of quantum pumping theories, while avoiding the capacitive coupling and rectification effects that have plagued attempted solid state implementations. Furthermore, the use of ultracold atomic gases allows control over the momenta of the pumped particles and the coherence of the gas, permits precision imaging of the transport [40] and velocity measurements, as well as the choice between Bose-Einstein and Fermi-Dirac statistics. Analogues of batteries, diodes, transistors, and recently hysteresis [41, 42, 43] have been explored in ultracold neutral atom systems.

This dissertation examines ballistic atom pumps from a theoretical perspective. A ballistic atom pump consists of two or more reservoirs of neutral-charge ultracold atoms connected by a channel (see Fig. 1.1). Within the channel is a time-dependent potential energy, which for our purposes consists of two repulsive potential energy barriers, one or both of which oscillates. If both barriers oscillate, they oscillate at the same frequency, but with a relative phase difference. Particles move through the pump independently,

and only interact with the potential energy. The primary questions of interest are (i) can such pumps preferentially pump atoms from one reservoir to the other?, (ii) can such pumps create a net transfer of energy from one reservoir to the other?, (iii) do particles, on average, gain or lose energy while passing through the pump region? We examine the system from classical, semiclassical, and quantum-mechanical perspectives. Most previous work on similar systems has used quantum theory exclusively, but we find that much more can be learned using the classical dynamics, and we use semiclassical theory to understand the similarities and differences between classical and quantum treatments of the scattering processes.

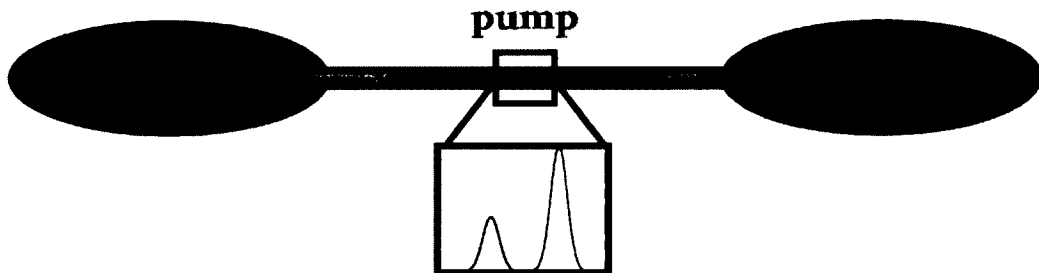


FIG. 1.1: A ballistic atom pump.

Previous studies of these pumps have generally been within the quantum regime, and largely focus on charge or spin transport associated with fermionic carriers. Here we also study the classical analogues of such pumps, and focus on the differential transfer of particles, energy, and heat. This broadens the study of quantum pumps into a new and largely unexplored regime.

These classical analogues of quantum pumps are also interesting because they provide models of chaotic transport, which occurs in a great variety of systems on scales from nuclei to galaxies [44, 45, 46, 47, 48, 49, 50, 51, 52, 53, 54]. When multiple barriers are present in the channel, classical trajectories are chaotic, and escape-time plots, which

show the relative time for trajectories to escape the barrier region as a function of initial condition, display a type of fractal structure. We generalize an existing topological theory and implement it on this system in order to understand this fractal structure.

The structure of the dissertation is as follows. In Chapter 2, we study classical, semi-classical, and quantum dynamics of one-dimensional scattering by an amplitude-modulated Gaussian barrier. Our main theoretical results are based on calculations of the scattered momentum distribution for atomic wavepackets of well-defined incident velocity, such as propagating Bose-Einstein condensates. We start with this basic study of scattering from a single barrier due to the complexity of scattering from multiple barriers. In Chapter 3, we study different types of ballistic atom pumps, which have two potential energy barriers. We study cases in which one barrier oscillates, and cases in which both barriers oscillate with a relative phase difference in their oscillations. The main focus of Chapter 3 is net particle transport in the system. In Chapter 4, we again examine a two-barrier system, but our focus is on energy and heat transfer within the system.

We then turn our attention to the chaotic-transport aspect of ballistic atom pumps, which is considered from a topological perspective, using a theory called Homotopic Lobe Dynamics (HLD). Earlier work using this method of topological analysis has primarily investigated models of chaotic transport involving escape of excited electrons from atoms in strong electric and magnetic fields, escape of light or sound from a vase-shaped enclosure, and escape of points from a region of the phase plane in an abstract two-dimensional map [55, 56, 57, 58, 59, 60, 61, 62, 63, 64, 65, 66, 67]. In all of these cases, a classical description of the system leads to a homoclinic tangle, the interior of which we call a “complex.” In these studies, trajectories typically begin on some line in the tangle, and the theory reveals details about the escape of orbits from this complex (sometimes referred to as a “half-scattering” problem). Chapter 5 introduces the mathematical concepts used in this type of analysis, and they are discussed using a system that is less complicated than a

ballistic atom pump. In Chapter 6, we use these topological tools and examine transport in a ballistic atom pump. The material from the preceding chapter is generalized and modified to account for the differences in the system. Details on modifications are given, and once the theory is developed, we implement it on a ballistic atom pump.

Finally, Appendix A introduces semiclassical theory in configuration and momentum space, and Appendix B fully describes the semiclassical description we use.

CHAPTER 2

Scattering from a Single Amplitude-Modulated Potential-Energy Barrier

Due to the complexity of scattering processes involving multiple barriers, we first study scattering from a single oscillating, Gaussian-shaped barrier. We use the results learned here as a framework for studying ballistic atom pumps, which have more complicated potential energies and scattering properties. Scattering by an amplitude-modulated potential barrier is of fundamental interest on its own, and it is also a building block for the more complex time-dependent potentials used in quantum pumping [15, 16, 35]. In this chapter, we study such systems using classical, semiclassical, and quantum theories.

When I joined this research group, classical and quantum calculations were already being performed by others in the group. My role in the work presented in this chapter consisted primarily of semiclassical analysis, and an alternative type of classical analysis. However some calculations by others are included in this chapter in order to place my

work within the proper context. All work by others is noted.

Motivated by possible experimental implementations with ultracold atoms, our main theoretical results are based on calculations of the scattered momentum distribution for atomic wavepackets of well-defined incident velocity, such as propagating Bose-Einstein condensates (BEC). By employing a semiclassical formalism, we start with the classical dynamics and selectively turn on “quantum” processes such as interference and diffraction. The main results of this chapter can be summarized as follows. (i) Quantum theory predicts that the final momentum distribution will be a set of sharp peaks, or sidebands, at energies E_n equal to the initial energy plus $n\hbar\omega$, where ω is the frequency of oscillation of the barrier. Quantum calculations display this result, but they give no insight regarding the energy-range of sidebands or their heights. (ii) Classical physics predicts a continuous distribution of final momenta, with an upper bound and a lower bound. We find that the quantum sidebands are small outside these bounds. For each cycle of the barrier there is an even number of classical paths arriving at each final momentum between the bounds. (iii) Semiclassical theory describes interference of waves travelling along these classical paths. This interference changes the classical continuous distribution of momenta to the set of sidebands seen in quantum theory, and it predicts the heights of the peak for each sideband. Specifically, the peaks are produced by inter-cycle interference, while the heights are predicted by intra-cycle interference.

The chapter is structured as follows: We present our model in Sec. 2.1, and in Sec. 2.2 display results of quantum and classical calculations for this model. Sec. 2.3 explains the algorithm used for the semiclassical calculation, and Sec. 2.4 compares and discusses the semiclassical and full quantum methods. Sec. 2.6 summarizes our main results. Appendices A and B give additional details on the semiclassical method used here and in subsequent chapters.

2.1 Model

Our model is motivated by recent proposals [37, 36] to simulate mesoscopic transport processes by studying ultracold atomic wavepackets propagating in quasi-one-dimensional waveguides that scatter from well-defined, localized potentials. A laser beam, blue-detuned from an atomic resonance, and tightly focused at the center of the wave guide, can create a potential barrier with a Gaussian profile, its width determined by the laser spot size and its amplitude by the intensity of the laser.

We choose a 1D Gaussian barrier, centered at the origin, whose amplitude is modulated sinusoidally at frequency ω , with potential energy $U(x, t)$ given by

$$U(x, t) = U_0(1 + A \sin(\omega t + \phi))e^{-x^2/(2\sigma^2)}. \quad (2.1)$$

U_0 is the average energy amplitude of the barrier, A is the relative modulation amplitude, σ is the standard deviation width of the barrier, and ϕ is the phase of the modulation. The Hamiltonian describing particle motion and scattering from this potential is

$$H = \frac{p^2}{2m} + U(x, t). \quad (2.2)$$

We use wavepackets with initial momentum $p_0 > 0$, centered at a point \bar{x} far to the left of the barrier, and whose initial position-space wavefunction is given by

$$\Psi(x, t = 0) = F(x) e^{ip_0 x}, \quad (2.3)$$

where $F(x)$ is the initial envelope of the wavepacket and is typically a Gaussian of width

β ,

$$F(x) = F_G(x) = \frac{1}{(2\pi)^{1/4}} e^{-(x-\bar{x})^2/4\beta^2}. \quad (2.4)$$

Alternatively, the initial envelope may have a Thomas-Fermi distribution of radius β , such that

$$F(x) = F_{TF}(x) = \begin{cases} \sqrt{\beta^2 - (x - \bar{x})^2} & , |x - \bar{x}| < \beta \\ 0 & , |x - \bar{x}| > \beta \end{cases} \quad (2.5)$$

The Thomas-Fermi and Gaussian envelopes are typical of BEC wavefunctions in strongly interacting and non-interacting limits, respectively. Unless otherwise noted, we use wavepackets that are much wider than the barrier width ($\beta \gg \sigma$), with packet width β sufficiently large such that $\beta \gg 2\pi|p_0|/m\omega$, ensuring that many barrier oscillations occur while the packet interacts with the barrier.

In the rest of the chapter, unless otherwise mentioned, we use $U_0 = m = \hbar = 1$, $A = 0.5$, $\sigma = 10$, and $\beta = 300$. The values of the incident momentum are in the range $p_0 \simeq 1 - 2$, the oscillation frequency $\omega \simeq 0 - 0.2$, and in most cases the phase, ϕ , is set equal to 0. In the case of a Gaussian packet, we select $\bar{x} = -1500$ to ensure separation of the initial packet from the barrier.

We also typically use a theoretical unit convention based on $\hbar = 1$ and $m = 1$, which is equivalent to selecting an arbitrary time unit t_u and a related length unit $l_u = \sqrt{\hbar t_u/m}$, with $\hbar = 1.054 \times 10^{-34}$ J·s. The corresponding energy unit is $E_u = \hbar/t_u$, while the mass unit is that of the particle, $m_u = m$, and the momentum unit is $p_u = \sqrt{\hbar m/t_u}$.

2.2 Quantum and Classical Descriptions

Here we consider both quantum-mechanical and classical descriptions of the scattering process. This dual framework allows us to distinguish the classical and quantum nature of a variety of scattering features.

2.2.1 Quantum Description

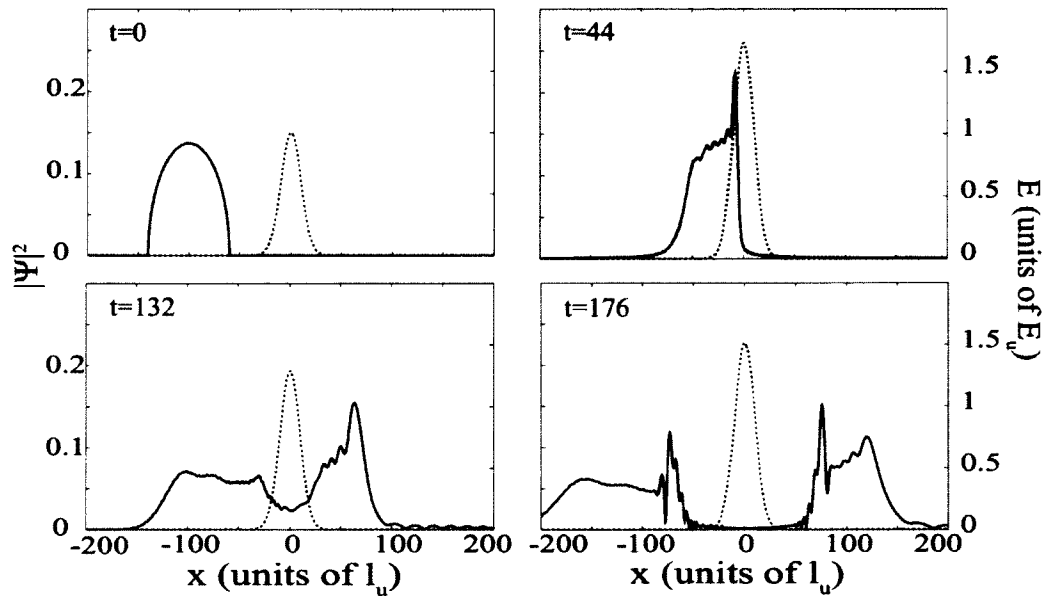


FIG. 2.1: Snapshots from a typical quantum-mechanical calculation, showing a Thomas-Fermi (Eq. (2.5)) wavepacket (left axis; solid red line) scattering off a Gaussian barrier (right axis; dotted green line). The amplitude of the barrier varies in time according to Eq. (2.2) with $U_0 = 1$, $A = 0.9$. The barrier width ($\sigma = 10$) here is typical in our simulations, but the packet width ($\beta = 40$) is much less (to show more details) than used elsewhere ($\beta = 300$) in the chapter. These calculations were done by A.J. Pyle and Kunal Das.

All quantum calculations were carried out by A.J. Pyle using methods developed together with Kunal Das. The quantum-mechanical approach is based on propagating the

wavepacket with the Schrödinger equation:

$$-\frac{\hbar^2}{2m}\partial_x^2\Psi + U(x,t)\Psi = i\hbar\partial_t\Psi \quad (2.6)$$

via a split-step operator method [68] that incorporates the time-variation of the scattering potential $U(x,t)$. The numerical calculation is done using a Fast-Fourier Transform (FFT) in a parallelized routine in FORTRAN. With periodic boundary conditions implicit in the FFT, the spatial range R (typically ~ 8000 in dimensionless units) is chosen sufficiently large to allow the entire wavepacket to interact with the barrier at $R/2$ without significant wraparound. The spatial grid density and the time step for propagation are both taken to be of the order of 0.1 in dimensionless units. The resulting momentum grid density $2\pi/R \simeq 10^{-3}$ is more than sufficient to resolve the narrowest momentum space features that we encounter.

Figure 2.1 shows a quantum calculation of a Thomas-Fermi wavepacket in position space at four separate times as it scatters from an amplitude-modulated Gaussian barrier. The packet width in (x,t) -space for this simulation is much more narrow than in those of our typical calculations, in order to show more details of the scattering process. In the figure, the initial wavepacket can be seen to partially transmit and partially reflect. The transmitted and reflected portions appear to have structure, but lack an obvious pattern aside from spatial oscillations. Studying the scattering process in momentum space, however, offers more insight into the relevant physics.

The wavefunction in momentum space is constructed at a chosen large time, $t = t_f$, after the packet has moved away from the potential barrier. It is computed via the Fourier transform of $\Psi(x, t_f)$:

$$\tilde{\Psi}(p, t_f) = \frac{1}{\sqrt{2\pi}} \int_{-\infty}^{\infty} e^{-ipx} \Psi(x, t_f) dx. \quad (2.7)$$

We also compute the corresponding quantum final-momentum probability density,

$$\tilde{P}_Q^F(p_f) = |\tilde{\Psi}(p_f, t_f)|^2. \quad (2.8)$$

Here, p_f is used to indicate momentum at the chosen final time. Also, we note that for sufficiently large times, such that the packet has moved far from the barrier, the final momentum distribution is constant in time, while the momentum-space wavefunction is not.

A time-periodic potential produces energy and momentum sidebands to the incident carrier momentum state, which can be described by Floquet theory, the temporal analog of Bloch's theorem. In our model, a wavepacket is incident on the barrier with fixed group momentum p_0 and associated kinetic energy $E_0 = p_0^2/(2m)$. Since we use spatially-broad packets, the incident packet has a very narrow momentum spread. The interaction of the incident wavepacket with the amplitude-modulated barrier produces a series of discrete momentum states separated in energy by $\hbar\omega$. According to Floquet theory, the allowed final-momentum states must obey the equation

$$p_f(n) = \pm\sqrt{2m(E_0 + n\hbar\omega)} \quad (2.9)$$

where n is any integer satisfying $n \geq -E_0/\hbar\omega$, and with (+) and (−) corresponding to transmission and reflection, respectively.

Fig. 2.2 shows the momentum-space distribution of reflected and transmitted portions of an initial wavepacket, after scattering from an amplitude-modulated barrier. The results of the full quantum calculation show discrete momentum states consistent with Eq. (2.9). Fig. 2.2 also plots the classical final momentum-space distribution resulting from an initial Gaussian distribution of particles with the same initial momentum spread as

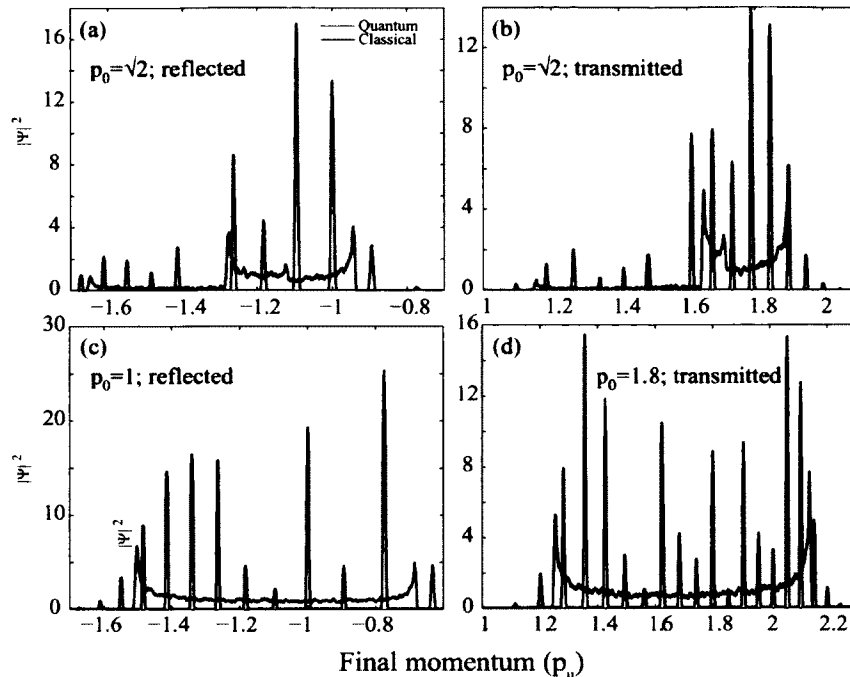


FIG. 2.2: Quantum and classical momentum probability densities for scattering from a single barrier. Quantum (sharply peaked curves, blue) and classical (green) momentum distribution for fixed $\omega = 0.1$, $U_0 = 1$, $A = 0.5$, $\sigma = 10$, $\beta = 300$, but different incident packet velocities, p_0 . The classical distributions were obtained via the histogram method, and statistics account for the fluctuations seen in the curves. (a) The reflected and (b) transmitted parts for $p_0 = 1.4142$; (c) reflected part for $p = 1.0$, when transmission is negligible; (d) transmitted part $p_0 = 1.8$, when reflection is negligible. These calculations were done by Megan Ivory and Kunal Das.

the initial quantum wavepacket (see next subsection for details). This classical calculation was performed by Megan Ivory. The classically-allowed bounds for the final momentum roughly constrain the Floquet peaks on both the reflected and transmitted portions, though we find that the peaks often extend slightly past the classically-allowed bounds and into classically-forbidden regions. However, the amplitude of the peaks do not appear to have any obvious pattern, and only loosely follow the strength of the classical final-momentum distribution.

The semiclassical approach presented in Sec. 2.3 and Appendix B will provide an alternative explanation for the positions of the Floquet peaks in terms of inter-cycle interference, and will provide an explanation for the relative amplitudes of the peaks in terms of intra-cycle interference.

2.2.2 Classical Description

The classical description of the scattering dynamics is based on propagating trajectories based on the Hamiltonian of Eq. (2.2). In the case of a static barrier, incident particles that have an energy greater than U_0 are transmitted past the barrier, and those with an energy less than U_0 reflect from the barrier. The final energy of any particle is equal to its incident energy. In the case of an amplitude-modulated barrier, however, the barrier oscillations modulate the energy of incident particles as they pass over the barrier. For a monoenergetic distribution of particles incident on the barrier that have energy less than the maximum height of the barrier, the final outcome of each particle is heavily dependent upon the phase at which it encounters the barrier. Two particles that encounter the barrier at slightly different phases can scatter differently; e.g., one may reflect, while the other is transmitted past the barrier.

Our quantum and semiclassical calculations suppress the role of the phase of the barrier oscillation, ϕ , by studying Heisenberg-limited wavepackets with a large position spread and a well-defined momentum, so that many barrier oscillations occur while the wavepacket is interacting with it. We mimic such wavepackets in our classical approach by using initial distributions of particles with initial conditions whose position and momentum distributions, $P_C^0(x)$ and $\tilde{P}_C^0(p)$, match those of the quantum distributions:

$$P_C^0(x) = |\Psi(x, t = 0)|^2 \quad (2.10a)$$

$$\tilde{P}_C^0(p) = \left| \tilde{\Psi}(p, t = 0) \right|^2. \quad (2.10b)$$

Generally, our initial momentum distributions are sufficiently narrow that classical particles can begin with a fixed initial momentum, distributed along a line segment that substantially covers the width of the initial wave packet, with statistical weights $P_C^0(x)$.

The classical distribution $\tilde{P}_C^F(p_f)$ of final momenta p_f can be obtained by numerically integrating trajectories and grouping them in bins of final momentum to plot a histogram, as shown in Fig. 2.2 and Fig. 2.3(b). This method produces a classical final momentum distribution that is somewhat “noisy;” the fluctuations in these curves can be diminished by using a larger number of particles in the simulation. Alternatively, we can compute trajectories numerically to obtain the final momentum as a function of initial position x_0 and final time t_f , $p_f = p(x_0, t_f)$, as shown in Fig. 2.3(a). We note that due to the periodicity of the barrier amplitude and our use of wavepackets that are wide in position space, p_f is a continuous periodic function of x_0 , with period $2\pi|p_0|/\omega m$. Any such periodic function has a maximum and minimum, which define the classically-allowed range of p_f , as shown in Fig. 2.3. Furthermore, this periodicity means that many initial positions $x_0^j(p_f, t_f)$ contribute to the final momentum distribution $\tilde{P}_C^F(p_f)$. Each $x_0^j(p_f, t_f)$ contributes to $\tilde{P}_C^F(p_f)$ a term proportional to $|\partial x_0^j / \partial p_f| = |\partial p(x_0, t_f) / \partial x_0|^{-1}|_{x_0=x_0^j(p_f, t_f)}$, so

$$\tilde{P}_C^F(p_f) = \sum_j P_C^0(x_0^j(p_f, t_f)) \left| \partial x_0^j / \partial p_f \right| \quad (2.11)$$

Figure 2.3 shows the final classical momentum distribution $\tilde{P}_C^F(p_f)$ computed by both the histogram method (noisy red curve; calculated by Megan Ivory) and according to Eq.

(2.11) (dashed black curve). The final quantum momentum distribution is also shown. The black curve, computed using Eq. (2.11), eliminates the statistical fluctuations that arise via the histogram method (red curve). The maximum and minimum of p_f define the classically-allowed region, with $\partial p_f / \partial x_0$ going to zero at these locations, and its reciprocal in Eq. (2.11) tending to infinity [69].

When we compare the quantum calculation to this classical calculation (Figs. 2.2 and 2.3(b)) we see that the boundaries of the classically-allowed region accurately define the region of momentum space in which Floquet peaks are large. Small peaks also appear outside but close to the classically-allowed region. As we show in the semiclassical treatment (Sec. 2.3), these are the result of momentum-space tunneling (or diffraction) into the classically-forbidden region.

We also find that the barrier oscillation frequency ω , an easily variable experimental parameter, can be used to control the degree of concordance of the classical and quantum calculations, with good agreement in the limits of very high and low frequencies. For a static barrier, momentum conservation in classical and quantum theories ensures agreement. As the frequency is increased, but is still small, classical and quantum calculations tend to agree well. Since Floquet peaks are separated by in energy by integer units of $\hbar\omega$, small ω values yield quantum distributions with peaks that are not well-defined (one may think of them as “blurring” together because the widths of the peaks are larger than, or comparable to, the peak separations). As the frequency is increased, keeping the initial packet unchanged, the agreement gets poorer (Figs. 2.4(b) and 2.3(b)). The classical momentum distribution broadens, and the quantum distribution acquires a “comb” structure since Floquet peaks begin to resolve as their separations become greater than their widths (which depend inversely on the width of the initial packet in position space). This is the range of particular interest in all of our studies. At very high frequencies, the incident particles cannot respond fast enough to the modulation of the barrier, and so they effectively

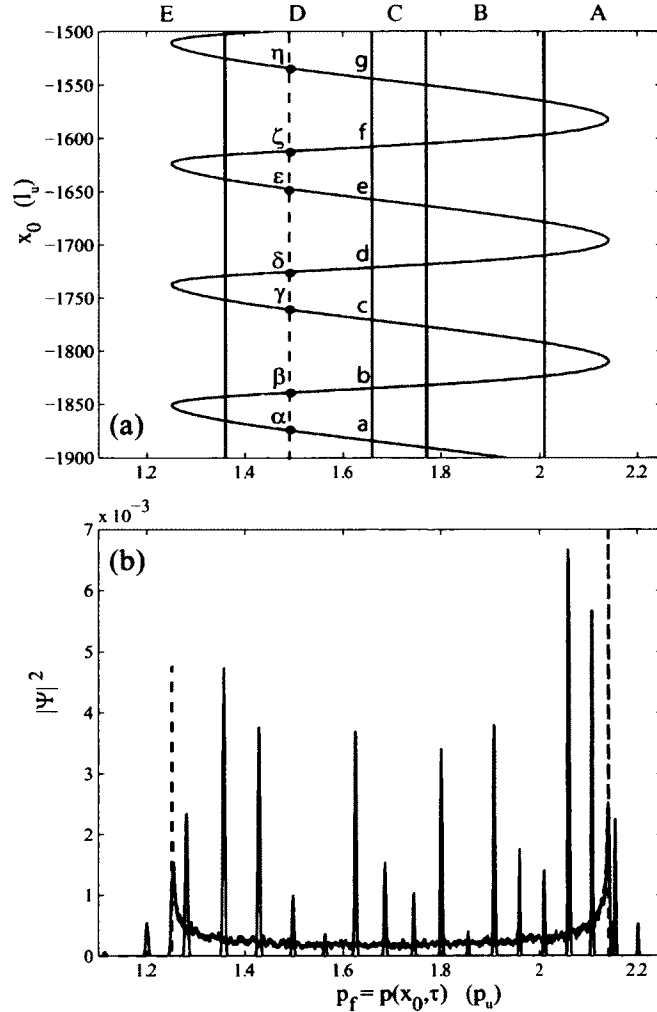


FIG. 2.3: Final momentum vs. initial position and final momentum probabilities. Final momentum vs. initial position for $A = 0.5$, $\omega = 0.1$, $p_0 = 1.8$. Capital letters correspond to different momentum regions (separated by solid vertical lines; see App. B). At a selected p_f , marked by the dashed line, paths arrive after beginning at many different x_0 ; those points are labeled by Greek letters. Each lies on a branch of the multivalued function $x_0(p_f, t_f)$, and each branch is labeled by a Roman letter. (b) Final-momentum distributions calculated quantum-mechanically and classically. The classical calculations show a histogram (solid line, red) and $P_C^F(p_f)$ from Eq. (2.11) (dashed curve, black). Fluctuations in the histogram arise for statistical reasons. The red curve was calculated by Megan Ivory, and the quantum distribution was calculated by A.J. Pyle and Kunal Das.

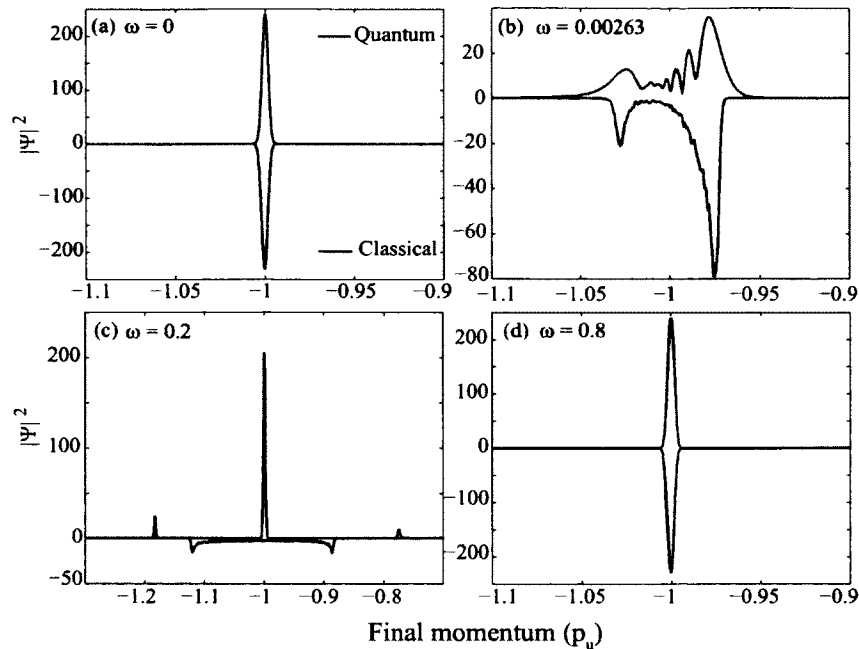


FIG. 2.4: Momentum distributions for fixed velocity of incident packet but for different values of ω . Comparison of quantum (blue and above axis) and classical (green and below axis) momentum distributions for $p_0 = 1.0$ with $\omega = 0, 0.00263, 0.2, 0.8$. Quantum and classical results are correlated for low and high values of ω , with significant differences appearing at intermediate values. These calculations were done by Megan Ivory, A.J. Pyle, and Kunal Das.

interact with the time-average of the potential. The classically-allowed region narrows, while in the Floquet picture, the spacing between the Floquet peaks increases (Fig. 2.4(c)) as ω increases. When there is only one non-negligible Floquet peak remaining, it coincides with the classically-allowed region, resulting again in good agreement between the two methods (Fig. 2.4(d)). As ω is increased further, the two approaches continue to agree well for that reason.

To summarize, we see that classical calculations describe the range of momenta over which Floquet peaks are large, and they agree with quantum calculations at very high and very low frequencies. However the heights of the Floquet peaks in the quantum calculations

remain mysterious. They will be explained using a semiclassical method described in the next section.

2.3 Semiclassical Description

It is a general principle of quantum mechanics [70] that when in classical mechanics we add probabilities associated with different paths leading to the same final state as in Eq. (2.11), in quantum mechanics we add amplitudes. In the semiclassical approach, each amplitude is the square root of the classical density combined with a phase. In the present case, Eq. (2.11) is replaced by

$$\tilde{P}_{SC}^F(p_f) = \left| \tilde{\Psi}_{SC}(p_f, t_f) \right|^2, \text{ with} \quad (2.12)$$

$$\begin{aligned} \tilde{\Psi}_{SC}(p_f, t_f) &= \sum_j F(x_0^j(p_f, t_f)) \left| \tilde{\mathcal{J}}_j(p_f, t_f) \right|^{-1/2} \\ &\times \exp\left(i \left[\tilde{\mathcal{S}}_j(p_f, t_f) / \hbar - \tilde{\mu}_j \pi / 2 \right]\right) \end{aligned} \quad (2.13)$$

where we are again using $p_f = p(x_0, t_f)$. $F(x_0)$ is the envelope of the initial wave packet, either $F_G(x_0)$ in Eq. (2.4) or $F_{TF}(x_0)$ in Eq. (2.5), and $x_0^j(p_f, t_f)$ has the same meaning as in the paragraph above Eq. (2.11): trajectories that arrive at any one p_f began from a large number of discrete $x_0^j(p_f, t_f)$.

Re-examining Fig. 2.3(a), and thinking about $x_0(p_f, t_f)$ as a smooth but multivalued function of p_f , we divide the points $x_0^j(p_f, t_f)$ into intracycle and intercycle groups, where a cycle is one period of $p_f(x_0)$, which corresponds to one cycle of the barrier. In Fig. 2.3(a), we may say that the pair of points (α, β) belongs to one cycle, the pair (γ, δ) to another cycle, etc. Alternatively, we may say that the pair (β, γ) belongs to one cycle, (δ, ϵ) to the next, etc. Summing over all the points $x_0^j(p_f, t_f)$ then means summing over points on distinct branches of $x_0(p_f, t_f)$ within a cycle, and then summing over cycles. Thus the

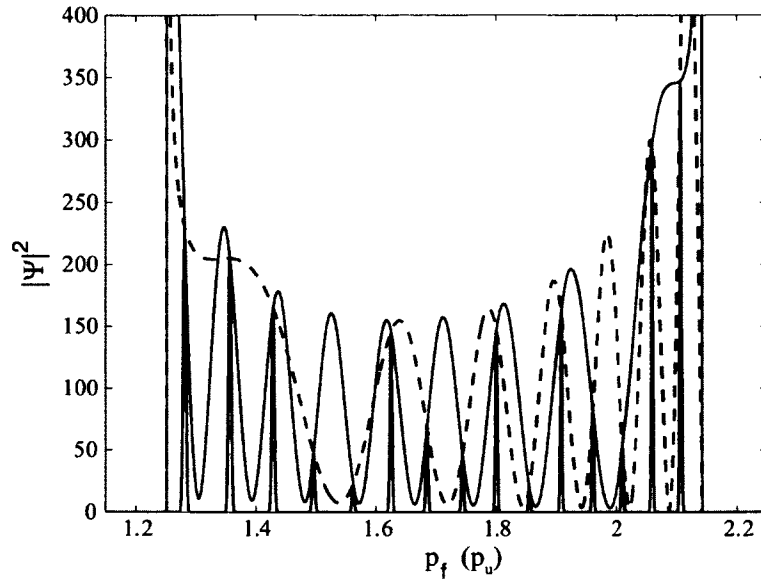


FIG. 2.5: Probability distributions of final momenta. The sharp peaks (blue) are obtained by summing over all branches of all cycles. Their heights are all multiplied by the same constant so that they are comparable to the other two curves. The oscillating curves are obtained by combining two branches of a single cycle, but with different definitions of the cycle. The solid curve (red) corresponds to a cycle spanning branches (b, c) in Fig. 2.3(a), and the dashed curve (black) is for a cycle spanning branches (c, d) . Where those two curves intersect, the different cycles add in phase with each other, producing the sharp peaks.

index j may become composite index, $j = (b, c)$, where b is an integer labeling a branch within a cycle, and c is an integer labeling the cycle.

$\tilde{\mathcal{J}}(p_f, t_f)$ is a Jacobian, which in the present case is the same derivative defined in Eq. (2.11),

$$\tilde{\mathcal{J}}_j(p_f, t_f) = \left| \frac{\partial p_f(x_0, t_f)}{\partial x_0} \right|_{x_0=x_0^j(p_f, t_f)} \quad (2.14)$$

Since p_f is a periodic function of x_0 , the values of this derivative depend on the branches within a cycle, but do not depend on which cycle is examined: $\tilde{\mathcal{J}}_{(b,c)}(p_f, t_f)$ depends on the branch b but is independent of the cycle c . In Fig 2.3(a), $\tilde{\mathcal{J}}_\alpha(p_f, t_f) =$

$\tilde{\mathcal{J}}_\gamma(p_f, t_f) = \tilde{\mathcal{J}}_\epsilon(p_f, t_f) = \dots$, while $\tilde{\mathcal{J}}_\beta(p_f, t_f) = \tilde{\mathcal{J}}_\delta(p_f, t_f) = \tilde{\mathcal{J}}_\zeta(p_f, t_f) = \dots$

$\tilde{\mathcal{S}}_j(p_f, t_f)$ is a classical momentum-space action integrated along the path from $x_0^j(p_f, t_f)$ to the final point. This integral is

$$\begin{aligned}\tilde{\mathcal{S}}_j(p_f, t_f) &= - \int x dp - \int E dt \\ &= - \int_0^{t_f} x(x_0, t) \frac{dp(x_0, t)}{dt} dt \\ &\quad - \int_0^{t_f} E(t) dt\end{aligned}\tag{2.15}$$

There is a simple relationship between the values of $\tilde{\mathcal{S}}_{(b,c)}(p_f, t_f)$ for different cycles at fixed p_f . Let label c increase with decreasing $x_0^{(b,c)}$; i.e., it increases by 1 with each successive cycle of the oscillating barrier. Then

$$\tilde{\mathcal{S}}_{(b,c+N)}(p_f, t_f) = \tilde{\mathcal{S}}_{(b,c)}(p_f, t_f) + N\Delta ET,\tag{2.16}$$

where T is the period of one oscillation, N is the number of periods separating the cycles, and ΔE is the change of energy of the particle

$$\Delta E = (p_f^2 - p_0^2) / 2m.\tag{2.17}$$

Finally, we introduce the Maslov index μ_j associated with each branch of $x_0(p_f, t_f)$. The rule for determining it is given in Appendix B. Here let it suffice to say that in Fig. 2.3(a), $\tilde{\mu}_j$ can be taken to equal one on branches a, c, e, g, \dots and equal to zero on branches b, d, f, \dots

In our calculations, we compute the final momentum as a function of initial position $p_f(x_0, t_f) = p(x_0, t_f)$, then for each p_f we identify initial points $x_0^{(b,c)}(p_f, t_f)$ for all branches b within a *single* cycle c . For each of them we find $\tilde{\mathcal{J}}_b(p_f, t_f)$, $\tilde{\mu}_b$, and $\tilde{\mathcal{S}}_{(b,c)}(p_f, t_f)$

for that particular cycle. We then calculate $\tilde{S}_{(b,c)}(p_f, t_f)$ for other cycles using Eq. (2.16), and then compute the sum Eq. (2.13) numerically. Steps are also taken to correct the semiclassical approximation near divergent points, and the calculation is extended into the classically-forbidden regions; this procedure incorporates diffraction, or momentum space tunneling, into the semiclassical dynamics. These steps consist of using an alternative description of the wave function near divergent points and in classically-forbidden regions, and matching coefficients of the two forms to smoothly go from one form to the other (similar to WKB approximation in configuration space). These details are fully described in Appendix B.

Terms in the sum over cycles add with incommensurate phases, and tend to cancel unless $\Delta ET/\hbar = 2\pi K$ where K is any integer. This condition explains the Floquet picture introduced earlier: *the momentum distribution becomes a “comb” function, with the “teeth” occurring at momenta that satisfy the commensurate phase condition,*

$$\frac{p_f^2}{2m} = \frac{p_0^2}{2m} + \frac{2\pi K \hbar}{T}. \quad (2.18)$$

In Fig. 2.5 we show the absolute squares of two single-cycle wavefunctions, one using branches (b, c) (solid curve, red) in Fig. 2.3(a), the other using branches (c, d) (dashed curve, black). When $F(x_0)$ is constant, these single-cycle probabilities intersect exactly at momenta satisfying Eqs. (2.9) and (2.18) (for non-constant $F(x_0)$, the intersections occur at approximately the locations of the Floquet peaks). The relative amplitudes of these intersections are determined by both the classical densities and the differences in momentum-space action, Eq. (2.15), among the paths contributing to the wavefunction at each p_f .

Fig. 2.6 shows quantities that determine the phase differences and interference for three trajectories ending with the same final momentum. Figs. 2.6(a) and 2.6(b) show the

position and momentum, respectively, versus time. Both plots show that particles see a decrease in velocity (and momentum) as they approach the potential barrier. Figs. 2.6(c) and 2.6(d) illustrate the differences in the momentum-space action, Eq. (2.15). The differences in areas under the curves determine the phase differences between pairs of trajectories. Interference associated with phase differences related to $E(t)$ for different cycles (Fig. 2.6(d)) produces Floquet peaks. Phase differences between pairs of trajectories in the same cycle (Figs. 2.6(c) and 2.6(d)) give the interference that determines relative heights of Floquet peaks.

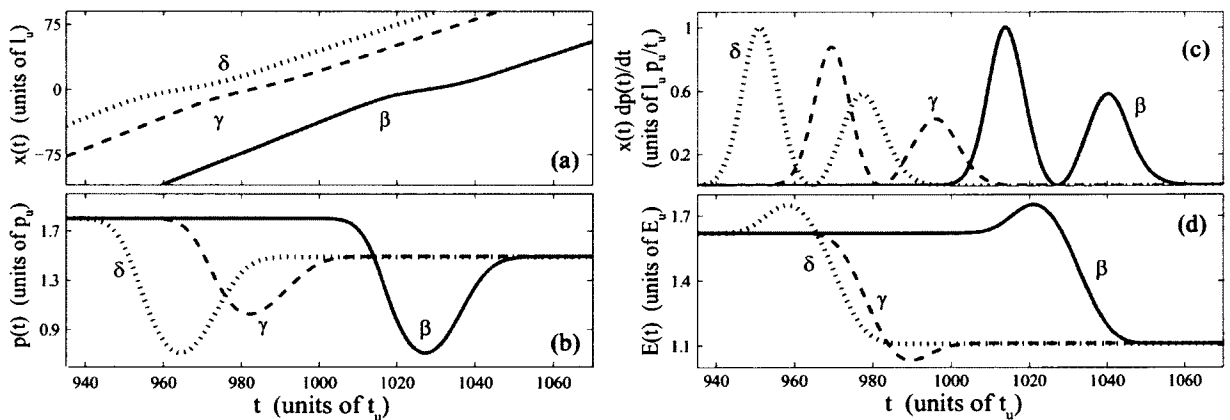


FIG. 2.6: Quantities that determine the phase evolution and interference of three trajectories ending with the same final momentum. The solid (blue), dashed (red), and dotted curves (black) correspond to the trajectories associated with $(p_f, x_0) = \beta, \gamma,$ and δ in Fig. 2.3(a), respectively. One may think of the (β, γ) trajectories as being from a single cycle, with the δ trajectory one cycle ahead of the β trajectory. (a) Position versus time. Each trajectory shows a decrease in velocity as the barrier is initially encountered near $x = 0$. (b) Momentum versus time. (c) $x(t)dp(t)/dt$ term in the momentum-space action (Eq. 2.15) versus time. (d) Energy term, $E(t)$, in the momentum-space action (Eq. (2.15)) versus time.

When we sum over cycles, the resulting probability is sharply peaked at the locations where the single-cycle probabilities intersect (Fig. 2.5), and *the heights of the peaks correspond to the relative magnitude of the single-cycle probability at these locations.* Finally,

we have an explanation for the relative heights of the Floquet peaks.

2.4 Case Studies

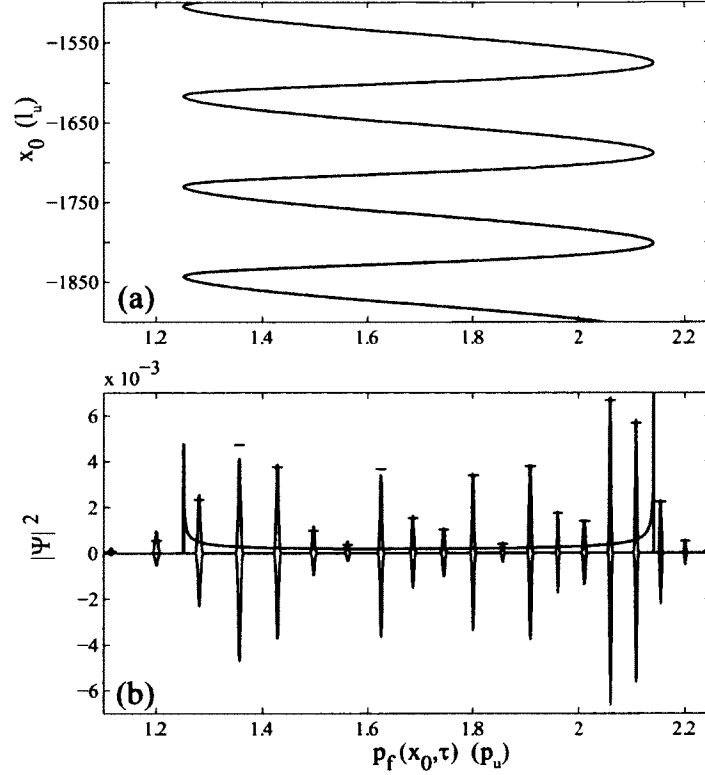


FIG. 2.7: Final momentum probabilities for a case of pure classical transmission. (a) Final momentum vs initial position for the $\omega = 0.1$, $p_0 = 1.8$ case. (b) Comparison of classical (plotted upwards, black), semiclassical (plotted upwards, blue) and quantum-mechanical (plotted downwards, red) momentum distributions. The horizontal lines in the upper portion of the graph correspond to the heights of the quantum-mechanical peaks. The quantum calculation was performed by A.J. Pyle and Kunal Das.

In this section, we study three separate scattering cases for identical barrier parameters, but different incident momenta that result in (i) pure transmission, (ii) pure reflection, and (iii) partial transmission and partial reflection. We also compare the full quantum re-

sults with the predictions of the semiclassical approach and find relatively good agreement. While there is a large range of possible scattering behaviors that can be studied by adjusting the five input parameters of our model, these three cases capture most of the essential physics.

Pure Transmission

The initial Gaussian wave packet is centered at $\bar{x} = -1500$, with $\beta = 300$, with initial momentum $p_0 = 1.8$, and with barrier parameters $A = 0.5$ and $\omega = 0.1$. This is the same case that was shown earlier in Figs. 2.2(d), 2.3, 2.5. This initial momentum corresponds to an energy higher than the maximum amplitude of the barrier. It takes more than fifteen barrier oscillations for the packet to pass over the barrier. There are two branches per cycle, as shown in Fig. 2.7(a). The classically-allowed momentum values range from $p_f \approx 1.2506$ to 2.1411 .

A comparison of $\tilde{P}_{SC}^F(p_f)$ (plotted upwards, blue), $\tilde{P}_Q^F(p_f)$ (plotted downwards, red) and $P_C^F(p_f)$ (plotted upwards, black), is shown in Fig. 2.7(b). The semiclassical and quantum-mechanical results can be seen to agree well. The final probability has fifteen peaks within the classical envelope. Both the classical density and interference contribute to the relative heights of peaks. At least two non-negligible classically-forbidden peaks can be seen for momentum values on either side of the classical envelope. The semiclassical calculation has corrected divergent peaks near momentum turning points by using Airy forms of local wavefunctions (see Appendix B).

Pure Reflection

We employ the same barrier parameters as in the previous case, but use an incident momentum of $p_0 = 1.0$, which corresponds to an energy equal to the minimum amplitude of the barrier. The barrier undergoes more than twenty-eight oscillations during the time the

wave packet is interacting with it. There are two branches per cycle, shown in Fig. 2.8(a), with the classical envelope ranging from $p_f \approx -1.5043$ to -0.6825 .

A comparison of $\tilde{P}_{SC}^F(p_f)$ (plotted upwards, blue), $\tilde{P}_Q^F(p_f)$ (plotted downwards, red) and $P_C^F(p_f)$ (plotted upwards, black), is shown in Fig. 2.8(b), again with good agreement between the semiclassical and quantum-mechanical results. The final-momentum probability has nine peaks within the classical envelope. We see at least three non-negligible peaks for classically-forbidden momentum values less than the minimum of the classical envelope, but only one non-negligible peak for forbidden momentum values greater than the maximum value of the classical envelope. This is because peaks are more closely spaced for large absolute momenta than for small absolute momenta, because they are equally spaced in energy. The exponential decay of the wavefunction again makes the peaks negligible outside the region shown.

Mixed Reflection and Transmission

We implement the same barrier parameters as in the previous cases, but use an incident momentum of $p_0 = 1.4142$, which corresponds to an energy between the minimum and maximum of the barrier amplitude range. In this case, the wavepacket is partially reflected and partially transmitted. The periodic relationship between final momentum and initial position is more complicated in this case. The left and right columns of Fig. 2.9 show the reflected and transmitted portions of the trajectory ensemble, respectively. Some classically-allowed final momenta have as many as six interfering trajectories within each cycle. The classical envelope ranges from $p_f \approx -1.6730$ to 1.8987 .

Comparisons of the reflected and transmitted portions of $\tilde{P}_{SC}^F(p_f)$ (plotted upwards, blue), $\tilde{P}_Q^F(p_f)$ (plotted downwards, red) and $P_C^F(p_f)$ (plotted upwards, black) are shown in the left and right columns of Fig. 2.9, respectively. Every extremum in the $p_f(x_0, t_f)$ graph gives a “turning point” or caustic, at which $P_C(p_f)$ diverges. The classical ampli-

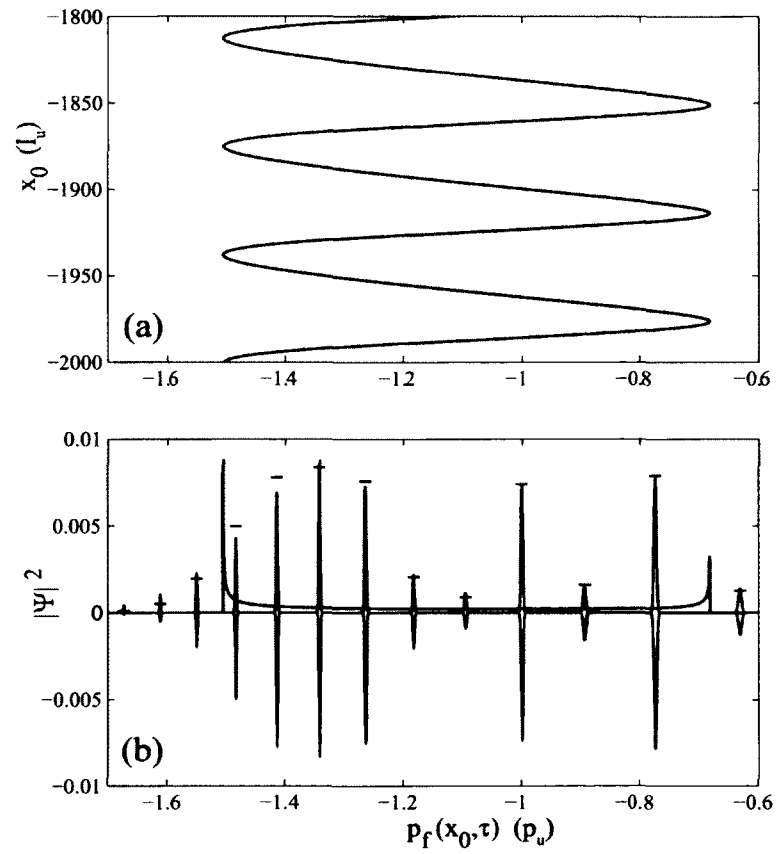


FIG. 2.8: Final momentum probabilities for a case of pure classical reflection. All curves are as described in Fig. 2.7. The quantum calculation was performed by A.J. Pyle and Kunal Das.

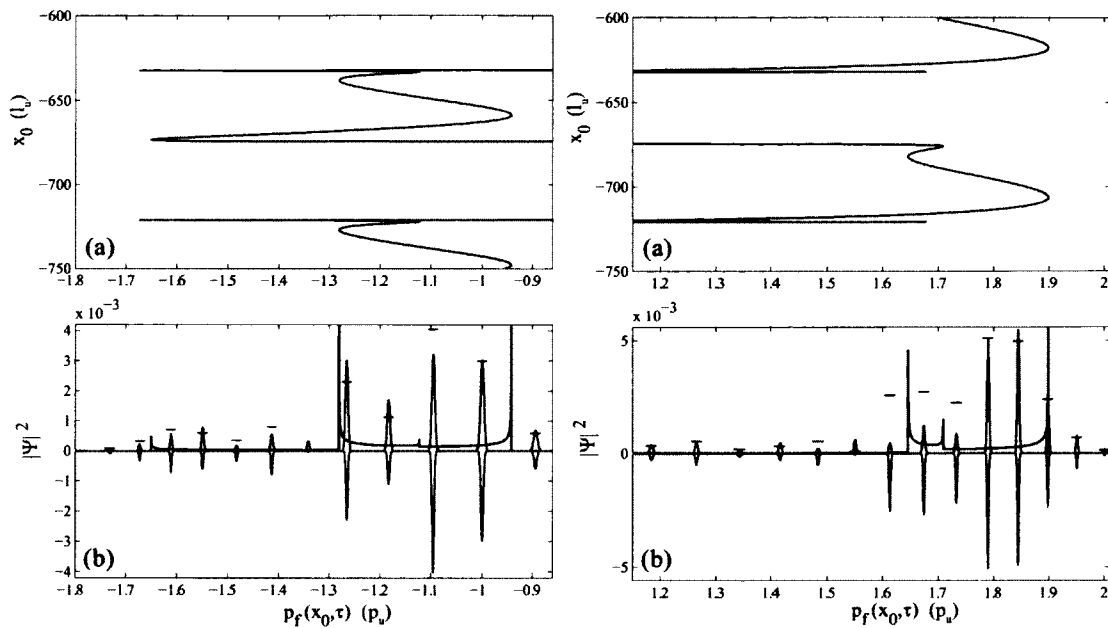


FIG. 2.9: Final momentum probabilities for a case of classical partial reflection and partial transmission. Left column: (a) Reflected portion of final momentum vs. initial position for the $\omega = 0.1$, $p_0 = 1.4142$ case. (b) Semiclassical (plotted upwards, blue), quantum-mechanical (plotted downwards, red), and classical (plotted upwards, black) final-momentum probabilities for the reflected portion of the wavepacket. Right column: (a) Transmitted portion of final momentum vs. initial position for the $\omega = 0.1$, $p_0 = 1.4142$ case. (b) Semiclassical (plotted upwards, blue), quantum-mechanical (plotted downwards, red), and classical (plotted upwards, black) final-momentum probabilities for the transmitted portion of the wavepacket. The quantum calculation was performed by A.J. Pyle and Kunal Das.

tude is markedly higher for larger momentum values in both the reflected and transmitted portions of the wave packet; consequently, the semiclassical and quantum-mechanical final-momentum distributions have their largest peaks in these regions. Agreement between semiclassical and quantum methods is less precise in this case, particularly where turning points are close together. (Turning points that are close together are the most significant cause of disagreement between semiclassical and quantum-mechanical calculations. Agreement can sometimes be improved by refinements of the semiclassical theory).

2.5 Proposed Experiment

A proposed experimental implementation uses a BEC of ^{39}K atoms in the $|F = 1, m_F = +1\rangle$ hyperfine ground state, which has a vanishing s-wave scattering length at 350 G [71]. A red-detuned optical dipole trap can trap a BEC with a Gaussian-shaped density profile. A blue-detuned Gaussian-shaped repulsive barrier can be created with a 532 nm laser focused to a radius of $\sigma = 10 = 2.5\mu\text{m}$ with a barrier amplitude of $U_0 = 1 = 197$ nK. Selecting this length scale, along with the mass of ^{39}K , and using the equations given at the end of Section 2.1, a theoretical incident momentum of $p_0 = 2$ corresponds to a velocity of 12.9 mm/s. For this incident velocity, modulating the barrier at a frequency $\omega = 2\pi \times 1.4$ kHz (which corresponds to $\omega = 0.35$ in theoretical units) with a modulation strength of $A = 1$ yields pure transmission of the incident wavepacket, and its predicted final momentum probability is shown in Fig. 2.10.

The parameters used in the remainder of the paper are in the general regime discussed in the previous paragraph. Our selection of parameters was generally dictated by interesting dynamics within these experimentally-accessible parameter regimes. All theoretical parameter choices in the remainder of the dissertation can be converted to SI units via the paragraph at the end of Section 2.1.

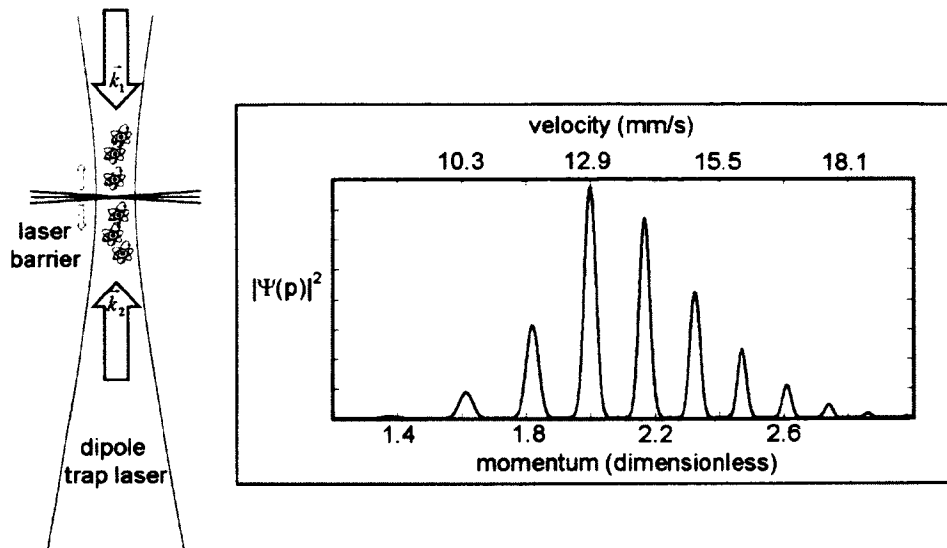


FIG. 2.10: Proposed experimental implementation of oscillating barrier scattering. Atoms are confined in the optical dipole trap, and the barrier is produced via a laser. The momentum distribution pictured is predicted for a BEC of ^{39}K atoms (see the text).

2.6 Remarks

In summary, we have studied scattering from an amplitude-modulated Gaussian barrier, and determined the final momentum-space probability distributions using classical, semiclassical, and quantum formalisms. We find that classical and quantum treatments of scattering agree reasonably well in the limits of very high and low barrier oscillation frequencies, but sharply differ in the intermediate frequency regime. We also find that classical mechanics defines the boundaries of a classically-allowed region of final momenta. Quantum calculations show: (i) the probability that particles end with momentum outside the classically-allowed region is small; (ii) the momentum distribution is peaked at momenta consistent with Floquet's theorem (see Eq. (2.9)); (iii) the heights of the Floquet peaks vary widely and seemingly erratically. Semiclassical calculations show that (a) for any final momentum inside the classically-allowed region, many classical paths arrive;

(b) interference of waves propagating along these paths produces peaks consistent with Floquet theory, and determines their heights. Specifically, inter-cycle interference leads to discrete final momentum states, while intra-cycle interference determines the peak heights. Finally, momentum-space tunneling leads to diffractive population of momenta beyond the classically-allowed bounds.

The semiclassical and full quantum propagation formalisms employed in this chapter are well suited for studying scattering from a turnstile pumping potential formed from two separated barriers, amplitude-modulated out of phase from each other. While no choice of system parameters for the single-barrier system leads to classical chaos, the addition of a second barrier introduces classically-chaotic trajectories, with quantum dynamics well suited to the type of semiclassical treatment developed in this chapter. Such a treatment is essential for understanding the quantum and classical aspects of particle pumping in a turnstile pump, since interference and tunneling can be selectively included. Moreover, the scattering theories developed in this work can also be extended to examine spatial tunneling [73] through narrower barriers, and scattering from a potential well.

In the next chapter, we use the framework developed here on ballistic atom pumps, which contain multiple barriers.

CHAPTER 3

Particle Transport in Ballistic Atom Pumps

The pumps we consider in this chapter have two reservoirs and a pump which is effectively one-dimensional, so the Hamiltonian is

$$H(p, x) = p^2/2m + V(x, t). \quad (3.1)$$

We choose $V(x, t)$ to consist of two repulsive barriers oscillating with the same frequency ω , but not necessarily with the same amplitude or phase. We study rectangular barriers (easiest theoretically) and Gaussian barriers (easiest experimentally using optical forces). The questions we address are: Can such systems pump atoms preferentially from one side to the other without an external bias, such as a difference in chemical potentials in the reservoirs? In particular, can we make an atom “diode” that will allow atoms to pass through the pump in only one direction? In order to understand the quantum features of such a pump, it is necessary to develop a clear understanding of classical scattering by a pair of oscillating potential barriers.

We begin with a precise specification of the models we study. Then we consider simple asymmetric pumps that rectify net particle transport, which we call “particle diodes” because they allow transport in only one direction for certain ranges of initial particle energy. These diodes have one barrier fixed and one oscillating barrier. Then we consider pumps that are symmetric in the sense that the two barriers are identical, but their oscillations are not in phase with each other. We prove a symmetry theorem which shows that such pumps can give no net particle pumping if the behavior of the particles is classical and the initial phase-space distribution is uniform in both reservoirs. However, if the phase-space distribution is not uniform, then such pumps can produce net particle transport in either direction. We also show that if the two potential barriers are separated by a modest distance, atoms can get stuck in a “complex” or ‘resonance zone” between them, and the system is a nice model of chaotic transport [55, 56, 74, 75, 76, 77, 78, 79, 80, 81, 82, 83, 84, 85, 86, 87, 88, 89, 90, 91, 92, 93, 94, 95, 96, 97, 98, 99, 100, 101, 102, 103, 104, 105, 106, 107]. (The details of chaotic transport are analyzed separately in Chapters 5 and 6).

The relationships among classical, semiclassical, and quantum descriptions for transport past a single oscillating Gaussian barrier were discussed in detail in Chapter 2. To make this chapter self-contained, we repeat the summary of results here. Consider the case that atoms enter the pump from one side with fixed momentum p_i and kinetic energy E_i . In the quantum description, because the barriers are oscillating with a fixed frequency, Floquet theory tells us that after passing through the pump, the spectrum of transmitted energies is a set of narrow peaks at energies $E_n = E_i + n\hbar\omega$, where n is an integer. The heights of these peaks can be computed numerically by solving the Schroedinger equation, but in general no patterns are visible in those heights.

In the classical description (again assuming that particles enter with a fixed initial momentum p_i but a range of positions x_i), then the final momentum p_f is a bounded periodic function of the initial position x_i , $p_f = \mathcal{P}_f(x_i)$. The upper and lower bounds of

the range of this function define the classically allowed region. Inside this classically allowed region, provided that $\mathcal{P}_f(x_i)$ is continuous, there must be an even number of trajectories leading to each final momentum. The distribution of final momenta is a smooth function except at extrema of $\mathcal{P}_f(x_i)$, where the distribution has an integrable singularity. One finds that the Floquet peaks obtained in the quantum description are large primarily in the classically allowed region, with small spillover past the boundaries (momentum-space tunneling). Still the heights of peaks are incomprehensible.

Finally, in semiclassical theory, for each final momentum one sums over the initial positions that give trajectories leading to that final momentum, and incorporates phases for each such orbit (momentum-space action plus Maslov indices). Summing over one cycle of $\mathcal{P}_f(x_i)$ produces a smooth function, and the relative heights of the Floquet peaks are discrete values of it. Summing over many cycles of $\mathcal{P}_f(x_i)$ causes the peaks seen in the quantum description to emerge, with good agreement between the two methods (see Figs. 3.6 and 3.15).

We show a few representative calculations of each type in this chapter, but we concentrate on the classical description, with the understanding that semiclassical calculations can be carried out when desired, and that the semiclassical description agrees well with the quantum description.

3.1 Model

Our atom pump consists of two repulsive potential barriers with amplitude oscillations that have the same frequency, but are not in phase with one another:

$$V(x, t) = U_L(x, t) + U_R(x, t). \quad (3.2)$$

In this chapter we examine both rectangular and Gaussian potentials. The rectangular barrier potentials are given by:

$$U_L(x, t) = \begin{cases} \hat{U}_L(1 + \alpha_L \cos(\omega t)) & , b_{L-} < x < b_{L+} \\ 0 & , \text{elsewhere} \end{cases} \quad (3.3a)$$

$$U_R(x, t) = \begin{cases} \hat{U}_R(1 + \alpha_R \cos(\omega t + \phi)) & , b_{R-} < x < b_{R+} \\ 0 & , \text{elsewhere} \end{cases} , \quad (3.3b)$$

where $b_{L-} = -\hat{x} - \sigma_L$, $b_{L+} = -\hat{x} + \sigma_L$, $b_{R-} = \hat{x} - \sigma_R$, $b_{R+} = \hat{x} + \sigma_R$, $\hat{U}_{L,R}$ is the average height of each barrier, $\alpha_{L,R}$ is the amplitude of oscillation of each, $\omega = 2\pi/T$ is the common frequency and T is the period, ϕ is an additional phase term, and $2\sigma_{L,R}$ is width of each barrier. The left and right barriers are centered at $x = -\hat{x}$ and $x = \hat{x}$, respectively, and always have a center-to-center distance of $\Delta x = 2\hat{x}$. When the barriers touch, i.e., have no separation, $\sigma_{L,R} = \hat{x}$. If only the left-hand barrier is oscillating then $\alpha_R = 0$.

The Gaussian potential barriers are given by

$$U_L(x, t) = \hat{U}_L(1 + \alpha_L \cos(\omega t)) \exp\left(\frac{-(x + \hat{x})^2}{2\sigma_L^2}\right) \quad (3.4a)$$

$$U_R(x, t) = \hat{U}_R(1 + \alpha_R \cos(\omega t + \phi)) \exp\left(\frac{-(x - \hat{x})^2}{2\sigma_R^2}\right), \quad (3.4b)$$

where $\sigma_{L,R}$ is the standard deviation of the Gaussian. Fig. 3.1 shows the parameters for the barriers.

Without loss of generality, we can choose units of mass, energy and time such that $m = 1$, $\hat{U}_L = \hat{U}_R = 1$, and $\omega = 1$. The remaining parameters are the barrier widths σ_L and σ_R , the barrier oscillation amplitudes α_L and α_R , and the phase difference between the barriers, ϕ . In this chapter, we typically choose $\sigma_L = \sigma_R$. In quantum and semiclassical mechanics one additional parameter arises, the value of \hbar , which we set as $\hbar = 1$. The

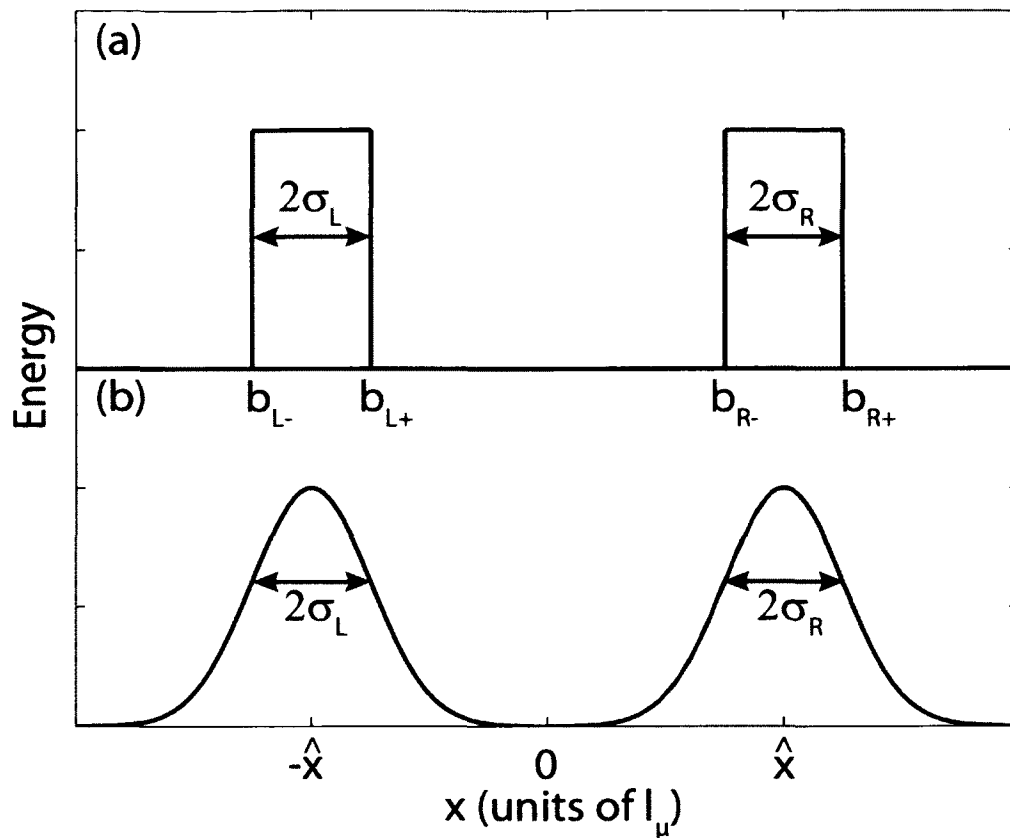


FIG. 3.1: Types of barriers considered in this chapter. (a) Rectangular barriers, which are centered at $\pm\hat{x}$ and have width $2\sigma_{L,R}$. If $\sigma_{L,R} = \hat{x}$, the barriers touch. (b) Gaussian barriers centered at $\pm\hat{x}$ which have standard deviation $\sigma_{L,R}$.

general way to apply such scaling principles is given in [108].

The units used in this chapter are theoretical, and are the same as those used in Chapter 2. Namely, the choice of a theoretical unit convention based on $\hbar = 1$ and $m = 1$ is equivalent to selecting an arbitrary time unit t_u and a related length unit $l_u = \sqrt{\hbar t_u / m}$, with $\hbar = 1.054 \times 10^{-34}$ J-s. The corresponding energy unit is $E_u = \hbar / t_u$, while the mass unit is that of the particle, $m_u = m$. The parameters we use in this chapter are in the same regime as those in Chapter 2 and are experimentally-accessible.

We start with a distribution of particles far to the left of the barriers, far to the right, or both. For our classical calculations, the distribution has a single momentum (i.e. it is a delta-function in momentum space centered at p_i). The distribution in position space is uniform over a length $L = vT$ where v is the initial velocity of the particles (i.e. uniform over a length corresponding to the distance the incident particles travel in one cycle of the barriers). In semiclassical and quantum calculations, we begin with a wave packet that is narrow in momentum space, centered at p_i , and correspondingly wide in position space, $\Delta x_i \gg L$. Thus its magnitude is nearly uniform over the length L corresponding to a cycle. The wave function in position space at the initial time is given by

$$\Psi(x_i, t_i = 0) = F(x_i)e^{ip_ix_i}. \quad (3.5)$$

where $F(x_i)$ is

$$F(x_i) = (1/2\pi)^{1/4} e^{-(x_i+x_c)^2/4\beta^2}. \quad (3.6)$$

The initial probability density is thus $|\Psi(x_i, t_i = 0)|^2 = F^2(x_i)$, which is a Gaussian centered at $-x_c$ with standard deviation β . Our quantum calculations are performed in the same fashion as in Chapter 2, and are based on propagating the wave packet with the time-dependent Schrödinger equation via a split-step operator method [68]. Again, all quantum calculations were performed by A.J. Pyle.

We determine the net particle transport in these systems by the following process:

- 1) For each initial momentum, launch particles toward the barriers from the left, and compute and record the fraction transmitted and reflected. Also record the final momenta of transmitted and reflected particles.
- 2) Launch particles with the same initial energy toward the barriers from the right, and compute the fraction transmitted and reflected, and their final momenta.
- 3) Sum the results of each of these to obtain the net fraction

of particles transmitted left to right (which may be negative if more are transmitted from right to left). 4) If appropriate, average over initial momenta.

We define the fractional transport of particles through the pump as

$$C_P(|p_i|) = \frac{R(|p_i|) - L(|p_i|)}{R(|p_i|) + L(|p_i|)}, \quad (3.7)$$

where $R(|p_i|)$ is the number of particles per cycle scattered to the right for each $|p_i|$, and $L(|p_i|)$ is the number of particles per cycle scattered to the left. The sum $R(|p_i|) + L(|p_i|)$ represents all particles for a given $|p_i|$. $C_P(|p_i|)$ is positive when more particles are scattered to the right for a given $|p_i|$, and negative when more particles are scattered to the left. When equal numbers of particles scatter to the right and left, e.g. when all particles are reflected or transmitted, $C_P(|p_i|) = 0$.

3.2 Particle Diodes

3.2.1 An Elevator Model

A double-barrier particle pump can make a kind of diode, in which net particle pumping can only be in one direction at certain initial energies. This type of diode consists of one static barrier which is high enough to prevent transmission of particles incident from one direction, and one oscillating barrier which can lift particles approaching from the other direction over the static barrier. This is analogous to photon-assisted tunneling [2, 3, 4, 5]. When the incident energy of particles is greater than the height of the static barrier, net particle transport is only possible in the opposite direction. It is simplest if the two barriers are touching each other. Let us simplify the description of the potentials

to

$$\begin{aligned} U_R(x, t) &= \hat{U} \quad , \quad 0 < x < b \\ U_L(x, t) &= Q(t) \quad , \quad -b < x < 0, \end{aligned} \tag{3.8}$$

where $Q(t)$ is a periodic function of t with period $T = 2\pi$, and \hat{U} is a constant. Suppose

$$Q(t) = \begin{cases} 0 & , \quad 0 \leq t \pmod{2\pi} < \pi \\ \hat{U} & , \quad \pi \leq t \pmod{2\pi} < 2\pi. \end{cases} \tag{3.9}$$

Then particles incident from the right with kinetic energy $K_i < \hat{U}$ cannot pass over the right barrier. From the left, (see Fig. 3.2(a)) a stream of particles having fixed kinetic energy $K_i < \hat{U}$ and density independent of position all file into the elevator when it is on the ground floor (Fig. 3.2(b)), and then at $t = \pi$ they are lifted abruptly to the penthouse level on the roof, where the back door of the elevator opens (Fig. 3.2(c)). The particles keep their kinetic energy in this process, and politely file out in line onto the roof (Fig. 3.2(d)). At $t = 2\pi$ they are all lined up on top of the right-hand barrier, and one-by-one they slide down the edge of that barrier and escape to the right with kinetic energy $K_f = K_i + \hat{U}$ (Fig. 3.2(e)). Meanwhile the door of the elevator has slammed again and it abruptly returns to ground level.

For this system, if the barrier width is $b = |p_i|\pi/\omega$ and if the first particle arrives at the left edge of the left barrier at $t = 0$, half of the particles incident on the elevator from the left – the ones that arrive for $0 \leq t \pmod{2\pi} < \pi$ – go over the barrier, and the other half – arriving for $\pi \leq t \pmod{2\pi} < 2\pi$ – are reflected by the left-hand barrier, so the transmitted fraction is half of the incident fraction.

Is this the theoretical maximum for transport? We cannot think of any other function $Q(t)$ that would improve the performance. However, we can get a larger fraction trans-

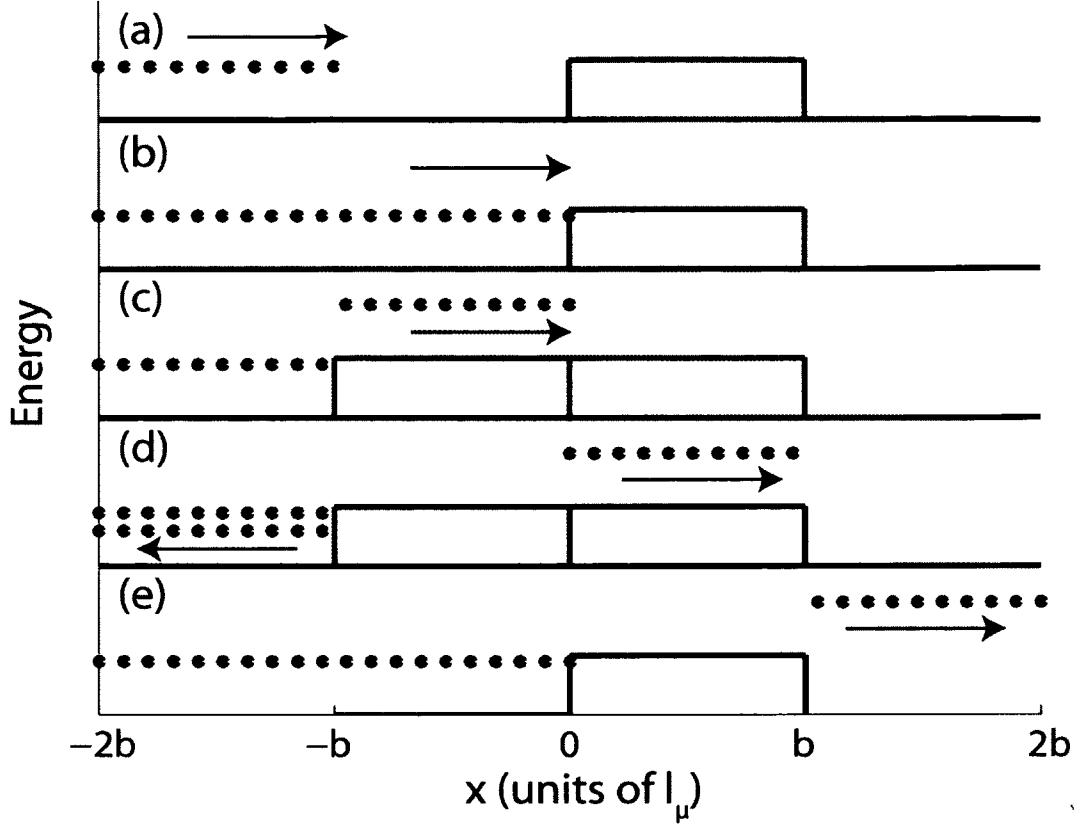


FIG. 3.2: Qualitative schematic of a diode with rectangular barriers. Particles approach from the left in (a) and (b). In (c), the left barrier abruptly rises to $E = \hat{U}$, and particles on top of it gain enough energy to transmit past the right barrier, as seen in (d) and (e).

mitted if on the elevator for $\pi \leq t(\text{mod}2\pi) < 2\pi$ a pusher shoves the passengers to the right so they exit the elevator more quickly.

Clearly, when the energy of incident particles is less than the amplitude of the static barrier, the only possible direction of fractional particle transport is left-to-right. This is because all particles approaching from the right are reflected, while some particles incident from the left may hop onto the oscillating barrier and gain enough energy from it to transmit over the static barrier. On the other hand, suppose the energy of incident particles is

higher than the peak of the static barrier, and suppose that an equal number of particles approaches from the left and from the right. Then the only possible direction of net transport is the opposite direction, from right-to-left. In this regime, all particles approaching from the right transmit over both barriers. However, presuming smooth oscillations of the left-hand barrier, particles incident from the left may lose energy while riding that barrier down, and can then be reflected from the static barrier.

The pumping mechanism of a diode is easily pictured by thinking about rectangular barriers, but it also applies to smooth barriers with smooth time dependence. To keep the analysis simple, let us consider rectangular elevators with some smooth dependence on t . Again particles approach from the left with fixed kinetic energy K_i , and uniform spatial density. Let t_{-b} be the time that a particle arrives at the point $x = -b$. It is reflected if $K_i < Q(t_{-b})$; otherwise it jumps onto the elevator and moves across it with constant kinetic energy

$$K_L = K_i - Q(t_{-b}). \quad (3.10)$$

It reaches $x = 0$ at time

$$t_0 = t_{-b} + \frac{b}{\sqrt{2K_L}} = t_{-b} + \frac{b}{\sqrt{2(K_i - Q(t_{-b}))}} \quad (3.11)$$

when its total energy is

$$E_0 = K_i + Q(t_0) - Q(t_{-b}). \quad (3.12)$$

(Here the index 0 does not mean “initial,” but rather “when the particle arrives at $x = 0$.”) If $E_0 < \hat{U}$, the particle is reflected by the right-hand barrier. Otherwise it is transmitted, with kinetic energy

$$K_R = E_0 - \hat{U}. \quad (3.13)$$

At $x = b$, its potential energy is converted to kinetic energy, and it escapes to the right

with kinetic energy $K_f = E_0$. Summarizing, for $0 < t_{-b} < 2\pi$ and initial kinetic energy K_i , we get transmission with final kinetic energy $K_f = K_i + Q(t_0) - Q(t_{-b})$ provided that i.) $K_i > Q(t_{-b})$, and ii.) $K_i + Q(t_0) - Q(t_{-b}) > \hat{U}$, where t_0 is given by Eq. (3.11).

Each particle trajectory beginning at x_{i_k} and ending near momentum $p_f = (2mK_f)^{1/2}$ contributes a term to the classical probability density $P^C(p_f)$, given by

$$\begin{aligned} P^C(p_f) &= \sum_k |\Psi(x_i(p_f), t_i = 0)|^2 \left| \frac{\partial p_f}{\partial x_i} \right|_{x_i=x_{i_k}(p_f)}^{-1} \\ &= \sum_k |\Psi(x_i(p_f), t_i = 0)|^2 |\tilde{J}_k(p_f)|^{-1}, \end{aligned} \quad (3.14)$$

where $\tilde{J}_k(p_f)$ is the Jacobian for the k^{th} trajectory ending near p_f . Summing over all trajectories gives a smooth result which diverges at extrema of $\mathcal{P}_f(x_i)$.

The ‘‘primitive’’ semiclassical wave function in momentum space is obtained via the same method as in [109], and is similar to the methods in [110, 111, 112, 113, 114, 115, 116, 117, 118, 119, 120]. For each p_f at the final time t_f , we sum semiclassical terms

$$\begin{aligned} \tilde{\Psi}_k^{SC}(p_f, t_f) &= F(x_i(p_f, t_f)) |\tilde{J}_k(p_f, t_f)|^{-1/2} \\ &\quad \times \exp\left(i\tilde{\mathcal{S}}_k(p_f, t_f)/\hbar\right) \exp(-i\tilde{\mu}_k\pi/2), \end{aligned} \quad (3.15)$$

where $\tilde{\mu}_k$ is the Maslov index for the k^{th} branch of the function $p_f(x_f)_{t=t_f}$, and

$$\tilde{\mathcal{S}}_k(p_f, t_f) = - \int \left[x(t) \frac{dp(t)}{dt} \right] dt - \int E(t) dt \quad (3.16)$$

is integrated over the classical path from initial to final time (see Appendix B for discussion of the Maslov index). The primitive semiclassical approximation in Eq. (3.15) applies only in classically-allowed regions, and it diverges at the boundaries of these regions. However, the divergences can be repaired and the function can be extended into classically-forbidden

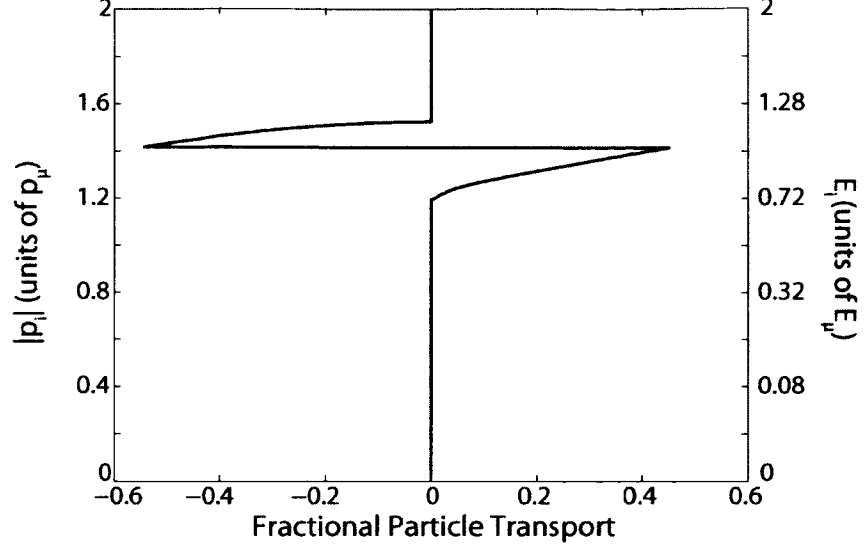


FIG. 3.3: Fractional transport of particles, $C_P(|p_i|)$, for a diode with rectangular barriers. The diode is described by Eq. (3.20) with $\alpha = 0.9$, $\omega = 0.07$, $b = 5$, and $\hat{U} = 1$. The incident energy E_i corresponding to each $|p_i|$ is shown on the right-hand axis. The fractional transport abruptly switches direction at $E_i = \hat{U}$.

regions via the method in Appendix B.

For rectangular barriers, particle momentum changes only at the barrier edges (i.e., $x = 0$ and $x = \pm b$), so for particles which transmit past both barriers,

$$\begin{aligned} \tilde{S}_k(p_f) = & -[b\Delta p_b - b\Delta p_{-b}] - K_i t_{-b} \\ & - \int_{t_{-b}}^{t_0} [K_L + Q(t)] dt - E_0(t_f - t_0) \end{aligned} \quad (3.17)$$

where

$$\Delta p_{-b} = \sqrt{2mK_L} - \sqrt{2mK_i} \quad (3.18)$$

$$\Delta p_b = \sqrt{2mK_f} - \sqrt{2mK_R}. \quad (3.19)$$

We now examine a diode described by

$$\begin{aligned} U_L(x, t) &= 0.5 [1 + \alpha \sin(\omega t)] \quad , \quad -b < x < 0 \\ U_R(x, t) &= \hat{U} \quad , \quad 0 < x < b, \end{aligned} \quad (3.20)$$

with $\alpha = 0.9$, $\omega = 0.07$, $b = 5$, $\hat{U} = 1$. The left barrier oscillates between a minimum value of $U_L = 0.05$ and a maximum value of $U_L = 0.95$, while the right barrier is static with a height of $\hat{U} = 1$.

Fig. 3.3 shows fractional transport $C_P(|p_i|)$ for this diode. In this example, when incoming particles have $E_i = K_i < \hat{U}$, $C_P(|p_i|) = 0$ below the energy at which particles incident from the left begin to gain enough energy from the oscillating barrier to transmit past the static barrier. When particles incident from the left begin to transmit, particles incident from the right are all reflected, $C_P(|p_i|) > 0$, and there is left-to-right fractional transport. As the incident particle energy increases, fractional transport monotonically increases until $E_i > \hat{U}$, which is the threshold energy for particles approaching from the right to transmit past both barriers. At this point, fractional transport abruptly reverses direction to right-to-left ($C_P(|p_i|) < 0$). As E_i increases, $C_P(|p_i|) \rightarrow 0$ as particles incident from both sides transmit past both barriers.

We now analyze the behavior of particles with an initial energy of $E_i = 0.99$ (initial momentum $p_i = \pm\sqrt{2E_i}$). Particles incident from the right do not have enough energy to transmit past the right barrier, and are reflected with final energy $E_f = 0.99$ (final momentum $p_f = \sqrt{2E_f}$). The initial wave packet approaching from the left has an envelope shape given by Eq. (3.6) centered at $-x_c = -1500$ with $\beta = 300$. Particles incident from the left all have enough energy to hop onto the left barrier; approximately 43.4% gain enough energy while traversing the left barrier to transmit past the right barrier, while the others are reflected from the right barrier.

Fig. 3.4 shows classical and semiclassical results for particles approaching from the left. Fig 3.4(a) shows initial position as a function of final momentum, $x_i(p_f)$. Only a small portion of initial positions are shown. Since the wave packet is wide in position space ($\Delta x_i \gg L$), there is a periodic relationship between final momentum and initial position. Because the potential is not smooth, $x_i(p_f)$ is discontinuous between transmitted and reflected portions. Each branch of the function $x_i(p_f)$ contributes a term $\tilde{\Psi}_n^{SC}(p_f)$ to the primitive semiclassical wave function, given by Eq. (3.15). The complete primitive wave function $\Psi_f^{SC}(p_f)$ is obtained by summing Eq. (3.15) over all branches of $x_i(p_f)$. Fig. 3.4(b) shows $P_f^{SC}(p_f) = |\Psi_f^{SC}(p_f)|^2$, the final primitive semiclassical probability density. Fig 3.4(a) shows that many trajectories end with any given p_f inside the classically-allowed regions. The sharp peaks in $P_f^{SC}(p_f)$ arise from interference among all trajectories ending with any given p_f . This calculation has not been extended into the classically-forbidden regions, so all peaks lie within the classically-allowed regions for both the transmitted and reflected portions.

Since $P_f^{SC}(p_f)$ includes interference from a great number of trajectories, it is useful to differentiate between two distinct types of interference: i) interference from within a single cycle of $x_i(p_f)$ (intracycle interference), and ii) interference among all cycles (intercycle interference). To view intracycle interference, we choose an arbitrary $x_i(p_f)$ and sum the corresponding $\tilde{\Psi}_n^{SC}(p_f)$ terms from within one cycle of the chosen $x_i(p_f)$ to obtain $\Psi_s^{SC}(p_f)$.

Figures 3.4(c) and (d) show the classical probability density $P^C(p_f)$ (dashed curve). Note that the scales are different in Figs. 3.4(c) and (d). We see that whereas classical theory gives a slowly-varying probability density $P^C(p_f)$, the primitive semiclassical single-cycle probability density $P_s^{SC} = |\Psi_s^{SC}(p_f)|^2$ (thick solid curve, red) is oscillatory. The oscillations arise from interference among trajectories in the cycle that end with the same final momentum. The discontinuities seen in $P_s^{SC}(p_f)$ and $P^C(p_f)$ in Fig. 3.4(c) at $p_f \approx -1.2$ are due to the behavior of the branches in $x_i(p_f)$ in Fig. 3.4(a): for $p_f \gtrsim -1.2$

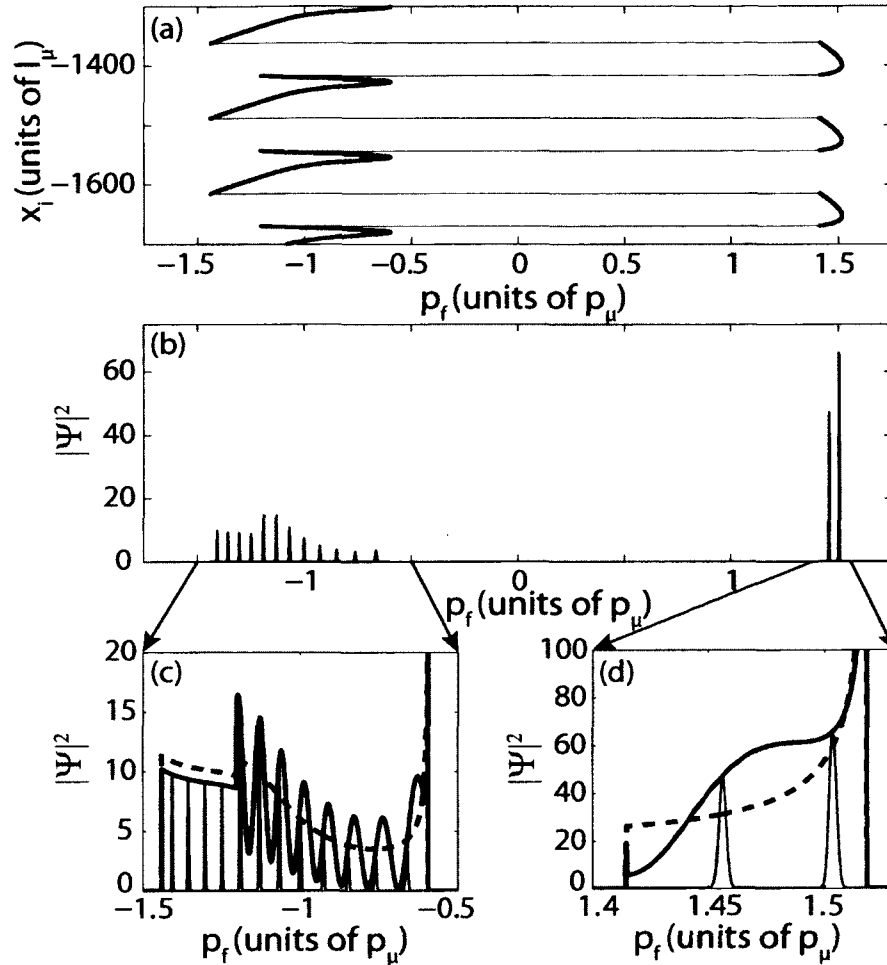


FIG. 3.4: Semiclassical analysis of scattering from a rectangular diode. (a) Initial position vs. final momentum for particles approaching the diode described by Eq. (3.20) with $\alpha = 0.9$, $\omega = 0.07$, $b = 5$, and $\dot{U} = 1$ from the left with $p_i = \sqrt{2E_i} = \sqrt{1.98}$. (b) $P_f^{SC}(p_f)$, the absolute square of the primitive semiclassical wave function, for the particles in (a). (c) and (d) Expansions of (b). The dashed curve is the classical probability density, $P^C(p_f)$, for reflection or transmission with final momentum near p_f . The smoothly-varying solid curve (red) is a single-cycle primitive semiclassical probability, $P_s^{SC}(p_f)$ [109]. The sharp peaks are the full primitive semiclassical probability summed over all cycles. These occur at momenta corresponding to Floquet energies.

within the classically-allowed final momentum region of the reflected segments, there are two interfering branches per cycle, but for $p_f \lesssim -1.2$, there is only one branch per cycle.

Summing $\Psi_s^{SC}(p_f)$ over all cycles yields the full primitive wavefunction $\Psi_f^{SC}(p_f)$, the square of which is $P_f^{SC}(p_f)$, the sharply-peaked function in Figs. 3.4(b), (c), and (d). This function has peaks at energies $E_n = K_i + n\hbar\omega$, consistent with Floquet theory. In Figs. 3.4(c) and (d), $P^C(p_f)$ and $P_s^{SC}(p_f)$ are scaled (multiplied by the same constant). When plotted in this fashion, one can see that the relative heights of the peaks in $P_f^{SC}(p_f)$ closely align with $P_s^{SC}(p_f)$, i.e., the relative heights of the Floquet peaks are governed by the single-cycle probability. This occurs for any arbitrary $x_i(p_f)$ chosen as the beginning of a cycle; while different choices yield different $P_s^{SC}(p_f)$, they all intersect at the locations of the Floquet peaks.

3.2.2 Quantum Suppression of Classical Transmission

Another interesting phenomenon arising from a similar elevator system is the quantum suppression of classical transmission. It may happen that the classical transmission probability is large, but the range of transmitted momenta is small – so small that no Floquet peaks lie in the classically-allowed range. Then quantum interference (we might better say semiclassical interference) among trajectories from different cycles prevents transmission that is classically allowed. In such a case, a narrow initial wave packet (in x_i) may allow transmission both classically and quantum-mechanically, not because it is broad in momentum space, but because it interacts with the barrier for only one (or a few) cycles.

These phenomena occur for a diode described by

$$\begin{aligned}
U_L(x, t) &= 0.92 [1 + \alpha \sin(\omega t)] \quad , \quad -b < x < 0 \\
U_R(x, t) &= \hat{U} \quad , \quad 0 < x < b,
\end{aligned}
\tag{3.21}$$

with $\alpha = 1 - (.88/.92) \approx 0.0435$, $\omega = 0.07$, $b = 5$, and $\hat{U} = 1$. In this example, the left barrier oscillates between a minimum of 0.88 and a maximum of 0.96, and particles approach the barriers from both sides with initial energy $E_i = 0.99$ (initial momentum $p_i = \pm\sqrt{2E_i}$). Particles approaching from the right do not have enough energy to hop onto the right barrier, and are reflected with final energy $E_f = 0.99$ (final momentum $p_f = \sqrt{2E_f}$). Particles approaching from the left all have enough energy to hop onto the left barrier, and classically, more than one third (approximately 37.3%) of these particles gain enough energy to transmit past the right barrier (see Fig. 3.5). These transmitted particles all end with p_f inside a very small range.

For the semiclassical calculation, we took an envelope given by Eq. (3.6) with $-x_c = -1500$ and $\beta = 300$. Fig. 3.5(b) shows the primitive semiclassical final momentum probability $P_f^{SC}(p_f)$ in the classically-allowed regions. In contrast to the classical result, we see no visible transmission. Figures 3.5(c) and (d) show the classical transmission probability and the single-cycle and final primitive semiclassical probabilities (similar to Fig. 3.4). The single-cycle primitive semiclassical calculation gives an even larger total transmission than the classical result, but the final semiclassical result is essentially zero.

The explanation is that Floquet peaks occur at energies $E_n = K_i + n\hbar\omega$, and the corresponding momenta for $n = (-1, 0, 1)$ are $p_n \approx 1.36, 1.41, \text{ and } 1.46$. None of these momenta lie inside the classically-allowed region of transmission. Therefore, when summing interference from all cycles, this interference is destructive across the entire range of transmitted momentum, and at this level of approximation, there is no transmission.

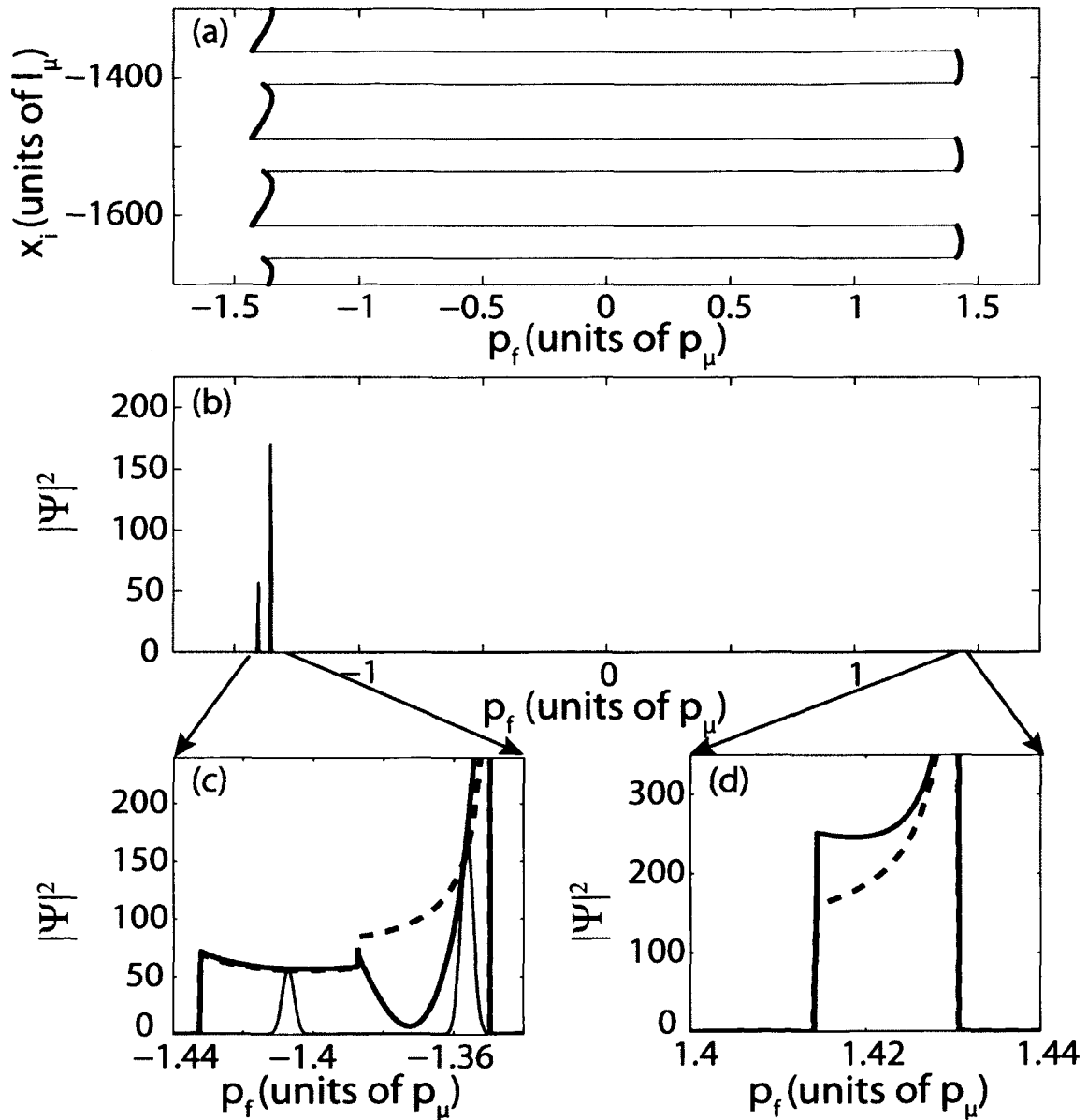


FIG. 3.5: Suppression of classical transmission. Quantum interference suppresses classical transmission for the diode described by Eq. (3.21) with $\alpha = 1 - (.88/.92) \approx 0.0435$, $\omega = 0.07$, $b = 5$, and $\hat{U} = 1$. All curves are as described in Fig. 3.4.

(A uniform semiclassical approximation would extend into classically-forbidden regions, but the decay of the wave function in these regions combined with the Floquet “comb” would yield small peaks, comparable to those seen outside the classically-allowed regions in Fig. 3.15 and in Chapter 2).

In this example, quantum interference suppresses the classical probability density for transmitted particles.

3.2.3 Gaussian Barriers

A more realistic type of diode is one which has Gaussian barriers described by Eqs. (4.2) and (3.4b) with $\alpha_R = 0$. We examine one such case with barriers described by $\hat{U}_R = \hat{U}_L = 1$, $\alpha_L = 1$, $\omega = 0.30$, $\sigma = 2.5/2\sqrt{2\ln 2}$ (full width at half maximum of 2.5), and $\hat{x} = 3.75$. The right barrier has static height $\hat{U}_R = 1$ and the left barrier oscillates between zero and twice the height of the static barrier. Fig. 3.6 shows classical, semiclassical, and quantum calculations for particles incident on this diode from both directions with $|p_i| = \pm 1.25$ ($E_i \approx .78$). Particles incident from the right with this initial energy are all classically reflected, but approximately 30.3% of particles incident from the left transmit, and there is left-to-right fractional transport of particles. Fig. 3.6(a) shows classical $x_i(p_f)$ for particles incident from the left. Classical trajectories are chaotic, as some particles are reflected from the left oscillating barrier, others directly transmit past both barriers, and others are temporarily trapped between the barriers before finally reflecting or transmitting. Fig. 3.6(a) shows three periods of the function $x_i(p_f)$, and Fig. 3.6(b) shows a zoom consisting of 10% of a period (30X magnification of (a)). Extreme dependence on initial position is apparent, and there is a large number of trajectories ending with any classically-allowed p_f .

Fig. 3.6(c) shows quantum-mechanical (plotted downward, red) and primitive semi-

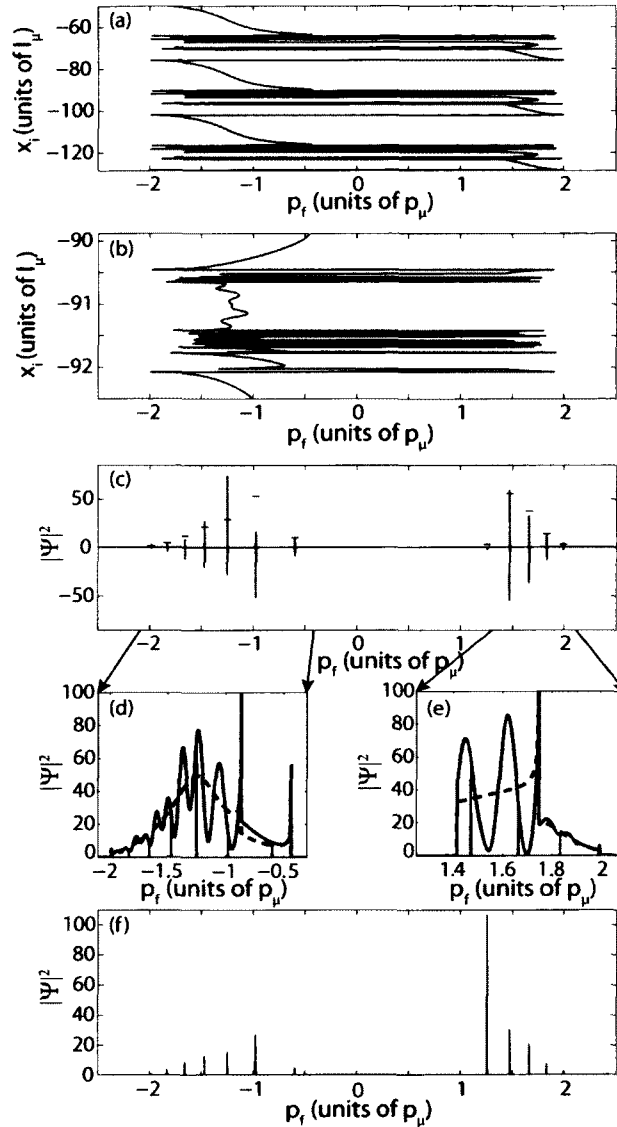


FIG. 3.6: Dynamics for Gaussian diode. (a) Three cycles of $x_i(p_f)$ for the packet approaching a Gaussian diode from the left. (b) Zoom of (a), showing the complexity of chaotic trajectories. (c) Quantum (downward, red) and primitive semiclassical (upward, blue) final momentum probabilities. The semiclassical calculation only includes the contributions of slowly-varying branches of $x_i(p_f)$. (d) and (e) $P^C(p_f)$ (dashed curve), $P_s^{SC}(p_f)$ (oscillatory curve, red), and $P_f^{SC}(p_f)$ (sharply-peaked curve, blue). (f) Quantum-mechanical final momentum probability for incoherent packets approaching the barriers from both sides.

classical (plotted upward, blue) final momentum probabilities for the packet incident from the left. The initial packet is described by Eq. (3.6) with $\beta = 300$ and $-x_c = -1250$. The primitive semiclassical probability $P_f^{SC}(p_f)$ only includes contributions from slowly-varying branches of the function $x_i(p_f)$ (i.e., regions of chaotic scattering are omitted). This rough approximation agrees reasonably well with the quantum probability $P_f^Q(p_f)$ except for peaks located at $p_f = -1.25$ and $p_f \approx -0.98$. Figs. 3.6(d) and (e) show zooms of the primitive semiclassical approximation, along with the single-cycle momentum probability $P_s^{SC}(p_f)$ (thick oscillatory curves, red) and classical momentum probability $P_f^C(p_f)$ (dashed curve). As before, the single-cycle probability governs the relative heights of the Floquet peaks seen in the full primitive semiclassical probability.

Fig. 3.6(f) shows the quantum-mechanical final momentum probability for particles approaching the barriers from both sides with $|p_i| = \pm 1.25$. The largest probability is at $p_f = 1.25$, which is primarily caused by the reflection of particles incident from the right. Particles incident from the left that are transmitted contribute only a small amount to this momentum state (see Fig. 3.6(c)); these transmitted particles have a much higher probability of ending with $p_f = \sqrt{2(E_i + n\hbar\omega)}$ with $n = 1, 2, 3$. The total probability in the quantum calculation for $p_f > 0$ is approximately 65.9%. The classical fractional transport $C_P(|p_i| = 1.25) \approx 0.303$ corresponds to approximately 65.1% of particles ending with $p_f > 0$, showing good agreement between classical and quantum theories.

3.3 Symmetric Pumps: A General Theorem

In the remainder of this chapter, we consider pumps that are “symmetric” in the sense that $\hat{U}_L = \hat{U}_R = \hat{U}$, $\alpha_L = \alpha_R = \alpha$, and $\sigma_L = \sigma_R = \sigma$, so the barriers are identical, but not in phase with each other. Intuitively one might have guessed the following behavior. Suppose that we consider the case of the classic turnstile pump for which $\phi = -\pi/2$, so

the barrier on the right oscillates a quarter-cycle behind the one on the left. Then the two barriers together imitate a rightward-moving wave, $\sin(kx - \omega t)$. We might then expect that the system would preferentially pump particles from left to right.

Nothing of the sort happens, however. Classically, if particles begin with a distribution that is uniform in *both* momentum and position (*i.e.* the distribution includes all initial energies E_i and is independent of E_i) then for every particle going from left to right, another goes from right to left – there is no net pumping at all.

This symmetry theorem can be violated if the initial distribution of particles is not uniform in phase space. For example, if the phase space distribution is constant only up to some maximum initial energy, then some net pumping is possible. More important, if particles begin from both sides with the same fixed energy, then there can be a net flow in one direction or the other. The amount and direction of this flow depends on that energy, so the apparent natural direction of the pump is an illusion.

The critical step in proving this no-pumping result is choosing a reference phase of the oscillations, and then using a surface of section at integer number of cycles from this reference phase. We choose the reference phase to be when the two oscillating barriers have equal height, and the left barrier is going up and the right barrier is going down (see Fig. 3.7(a)(inset)). If we take such a point in any cycle to be $t = 0$, then for any ϕ and all t and x we have

$$V(-x, -t) = V(x, t). \quad (3.22)$$

Let $M : (x, p) \mapsto (x', p')$ be the map that evolves a point (x, p) forward one pumping period to (x', p') , and let $R = R^{-1}$ be the operator that reflects the position through the origin: $R(x, p) = (-x, p)$. A trajectory on the left of the pump moving right sees the closest barrier going up, whereas a trajectory on the right moving left sees its closest

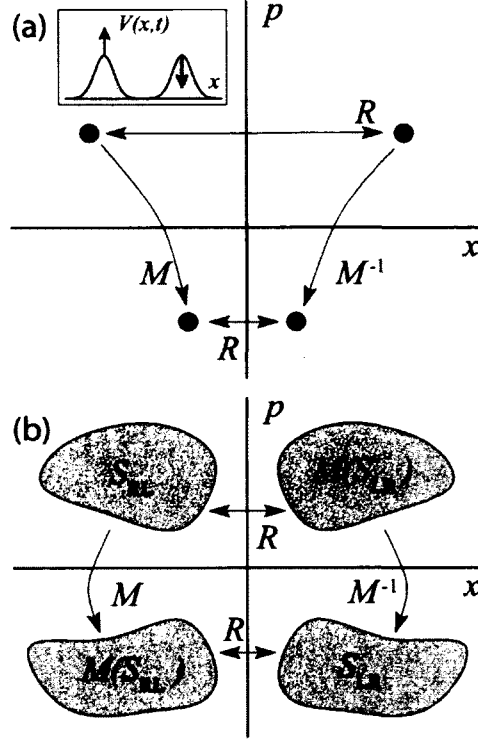


FIG. 3.7: Geometric proof of why a symmetric pump cannot preferentially pump particles if initial classical distributions are uniform. (a) An illustration of Eq. (3.23); The phase of the sampling is chosen so that both barriers have the same height with the left barrier moving up and the right moving down (inset). (b) Illustration of the sets S_{RL} and S_{LR} and the relation $S_{LR} = RM(S_{RL})$. The double arrows reflect the fact $R = R^{-1}$.

barrier going down. A mirror image thus converts the upward moving barrier to downward and vice-versa, i.e. it reverses the time-dependence of the barriers, so the particle follows the time-reversed trajectory. Consequently, $M^{-1}(-x, p)$ will be a mirror image of $M(x, p)$. More formally,

$$M^{-1} = RMR. \quad (3.23)$$

This relation is demonstrated in Fig. 3.7(a).

Now define S_{RL} to be the set of points moving to the right that are ultimately reflected, i.e.

$$S_{RL} = \{(x, p) | p > 0, p' < 0 \text{ where } (x', p') = M(x, p)\}. \quad (3.24)$$

We define S_{LR} similarly

$$S_{LR} = \{(x, p) | p < 0, p' > 0 \text{ where } (x', p') = M(x, p)\}. \quad (3.25)$$

Assuming a uniform initial distribution in phase space, the single-period net flux F of rightward to leftward moving trajectories is thus

$$F = \text{area}(S_{RL}) - \text{area}(S_{LR}). \quad (3.26)$$

We now show $S_{LR} = RM(S_{RL})$. (See Fig. 3.7b.) Let $(x, p) \in S_{RL}$ be arbitrary. We then have $p > 0$ and $p' < 0$ where $(x', p') = M(x, p)$. The point $(x'', p'') = RM(x, p)$ is then an arbitrary point of $RM(S_{RL})$; note $p'' = p'$. Now,

$$M(x'', p'') = MRM(x, p) = R(x, p) = (-x, p), \quad (3.27)$$

where the second equality follows from Eq. (3.23). Since $p'' = p' < 0$ and $p > 0$, we find $(x'', p'') \in S_{LR}$. Hence, $RM(S_{RL}) \subset S_{LR}$. The reverse inclusion follows similarly.

Since $S_{LR} = RM(S_{RL})$ and R and M both preserve phase-space area, $\text{area}(S_{RL}) = \text{area}(S_{LR})$. Hence $F = 0$, i.e. there is no net flux pumped across the barrier. All of our numerical simulations of symmetric pumps have confirmed this theorem.

3.4 Symmetric Rectangular Barriers

3.4.1 No space between the barriers

We now consider symmetric turnstile pumps in which both barriers oscillate smoothly in time, with rectangular potential barriers described by Eqs. (3.3a) and (3.3b). We first

examine the simplest pump of this type, which has no space between the barriers. In this case, any incident particle can either be reflected by the first barrier, hop onto the first barrier and be reflected from the second barrier, or transmit over both barriers. If the particle has enough energy to transmit over one or both barriers, it can gain or lose energy during the time it spends on top of the barrier(s).

As in Section 3.2.1, since the barriers are rectangular, particles only experience acceleration at the boundaries of barriers, and have constant momentum everywhere else. A particle beginning to the left of the barriers is launched with momentum $p_i > 0$ and arrives at the leftmost edge of U_L at time t_{-b} , at which time the height of the left barrier is $U_L(t_{-b})$, and the total energy of the particle is $E_i = p_i^2/2$. If $E_i \leq U_L(t_{-b})$, the particle is reflected from the first barrier with final momentum $p_f = -p_i$. Otherwise, the particle is transmitted over the first barrier with momentum

$$p_{b_1} = \sqrt{2(E_i - U_L(t_{-b}))}. \quad (3.28)$$

The time at which the particle reaches the opposite edge of the first barrier (and therefore the first edge of the second barrier) is

$$t_0 = \frac{2\sigma}{p_{b_1}} + t_{-b}. \quad (3.29)$$

The corresponding $U_L(t_0)$ and $U_R(t_0)$ are given by Eqs. (3.3a) and (3.3b), respectively, and $E(t_0) = U_L(t_0) + p_{b_1}^2/2$. If $E(t_0) \leq U_R(t_0)$, the particle is reflected from the second barrier with $p = -p_{b_1}$ and spends another time interval $2\sigma/p_{b_1}$ going back over the first barrier, after which it falls off onto the left-hand side of the pump with final momentum

$$p_f = -\sqrt{2 \left[U_L \left(t_0 + \frac{2\sigma}{p_{b1}} \right) + \frac{p_{b1}^2}{2} \right]}. \quad (3.30)$$

If $E(t_0) > U_R(t_0)$, the particle is transmitted over the second barrier with momentum

$$p_{b2} = \sqrt{2(E(t_0) - U_R(t_0))}. \quad (3.31)$$

The time at which the particle falls off the second barrier is

$$t_b = \frac{2\sigma}{p_{b2}} + t_0, \quad (3.32)$$

at which time the height of the right-hand barrier is $U_R(t_b)$, and the final momentum is

$$p_f = \sqrt{2 \left(U_R(t_b) + \frac{p_{b2}^2}{2} \right)}. \quad (3.33)$$

A similar algorithm is followed for particles beginning on the right of the pump with negative initial momentum. There is never more than one reflection of a particle. We calculate all particle trajectories using Eqs. (3.28)-(3.33) to obtain each particle's final momentum p_f .

We examine the net particle fractional transport for mirrored sets of particle packets approaching the barriers from opposite directions with $\pm p_i$. Classical computations shown in the remaining sections are done as follows. For a selected set of barrier parameters, we first choose a range of initial particle energies ΔE_i . Each E_i in this range has two corresponding momenta, $\pm p_i$. For each $|p_i|$, we construct two incoming packets of particles: one starts to the left of the barriers with $p_i = +|p_i|$, and the other starts to the right of the barriers, with $p_i = -|p_i|$. The width in x_i of each packet is $\Delta x_i = |p_i|T = |p_i|2\pi/\omega$

(recall $m = 1$). We start all trajectories at $t_i = 0$. The edge of each packet which is closest to the barriers is placed a distance $d = |p_i|2\pi/\omega$ away from the outer edge of the first barrier, which ensures that the first particle of each packet reaches the outer edge of the first barrier at $t = 2\pi/\omega$.

For these initial conditions, we define the time of arrival at the barrier as $\theta = t - 2\pi/\omega$; with this definition, the particle in each packet which starts closest to the barriers arrives at the outer edge of the first barrier at $\theta = 0$. Our choice of packet width ensures that the last particle in each packet to arrive at the outer edge of the first barrier arrives at $\theta = 2\pi/\omega$, which represents one full cycle of the barriers. Referring to Eq. (3.3a), a particle that arrives at the left-hand edge of the left barrier at $\theta = 0$ or $\theta = 2\pi/\omega$ encounters the barrier at its maximum, and one that arrives at $\theta = \pi/\omega$ encounters that barrier at its minimum.

The numerical results for barriers with $\hat{U} = 1$, $\omega = 1$, $\phi = 3\pi/2$, $\hat{x} = \sigma = 1.25$ and $\alpha = 1$ are shown in Fig. 3.8. Figure 3.8(a) represents particles approaching the barriers from the left, and 3.8(b) represents particles approaching from the right. In both plots, individual particles are represented by their initial momenta $|p_i|$ and the time θ at which they arrive at the outer edge of the first barrier. The colors in both plots correspond to the final momentum $p_f = p_f(|p_i|, \theta)$ of each particle. Blue represents particles which scatter to the left ($p_f(|p_i|, \theta) < 0$) of the barriers, and red corresponds to particles which scatter to the right of the barriers ($p_f(|p_i|, \theta) > 0$). The intensity of the color corresponds to the magnitude of the particle's final momentum, as seen in the colorbar.

The lowermost blue region in Fig. 3.8(a) represents particles approaching from the left that are initially reflected from the left barrier, and the lowermost yellow region in Fig. 3.8(b) represents particles approaching from the right that are directly reflected by the right barrier. In both cases, if there were no other barrier, then the region above this lowermost boundary would be entirely of the opposite color, as all particles not initially

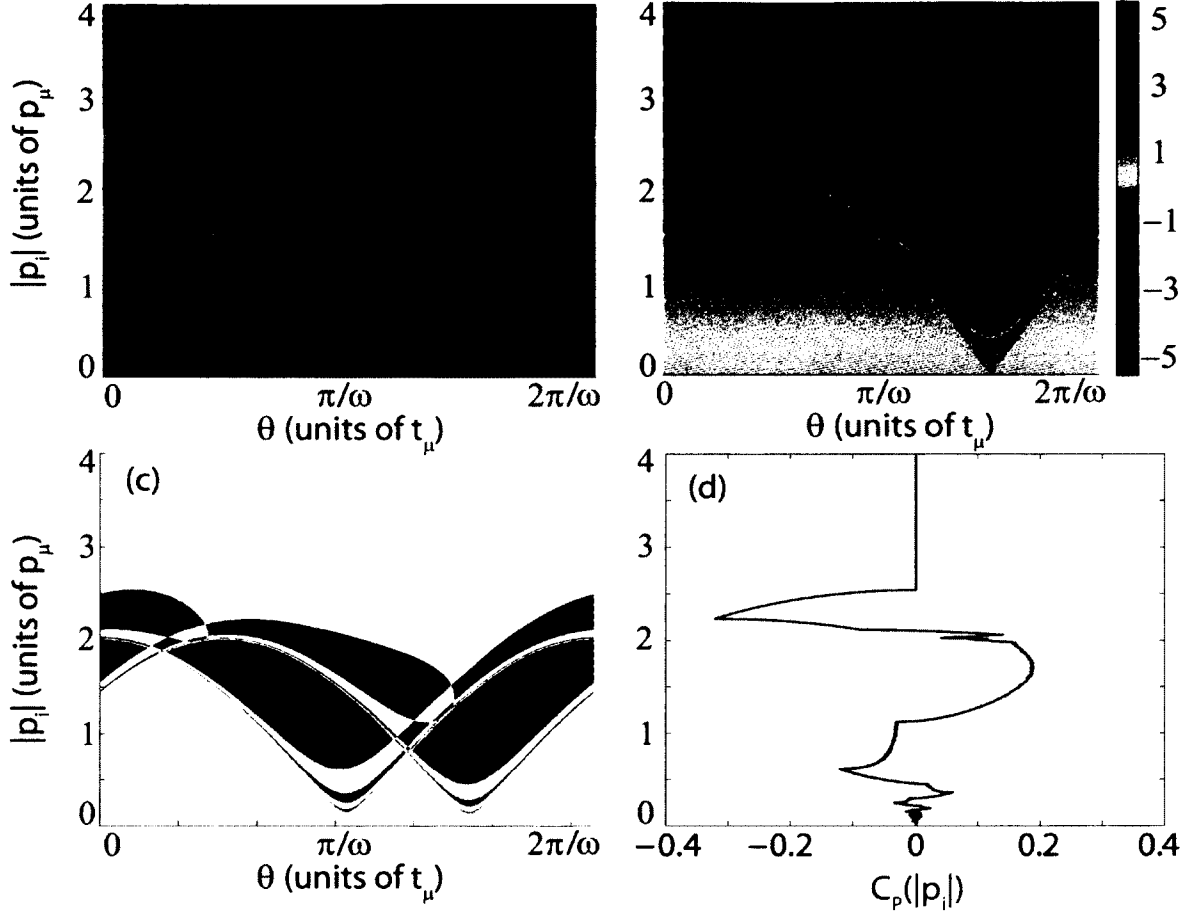


FIG. 3.8: Dynamics for touching, rectangular barriers. (a) and (b) $p_f(|p_i|, \theta)$ for particles incident on rectangular barriers described by $\hat{U} = 1$, $\omega = 1$, $\phi = 3\pi/2$, $\hat{x} = \sigma = 1.25$ and $\alpha = 1$. (a) represents particles approaching from the left, and (b) represents particles approaching from the right. (c) Sum of $p_f(|p_i|, \theta)$ for particles approaching the barriers from both directions with $p_i = \pm|p_i|$. Red indicates both particles scatter to the right, and blue indicates both particles scatter to the left. (d) Fractional transport, $C_P(|p_i|)$.

reflected would be transmitted. It follows that all of the striping effects just above this boundary are due to the presence of the second barrier. Just above this boundary, a particle has just enough energy to hop onto the first barrier it encounters. Consequently, its momentum p_{b_1} on the first barrier is small, it moves across the barrier slowly, and the barrier may oscillate many times while the particle is on it. In the limit that $p_{b_1} \rightarrow 0$, an infinite number of oscillations occurs while the particle is on the barrier. Hence, there is an infinite number of stripes converging from above upon the boundary.

Fig. 3.8(c) sums $p_f(|p_i|, \theta)$ for both particles which arrive at the barriers at the same time θ and $|p_i|$, but which arrive from opposite directions. Red represents cases in which both particles scatter to the right of the barriers ($p_f(|p_i|, \theta) > 0$ for both particles). Blue represents cases in which both particles scatter to the left of the barriers ($p_f(|p_i|, \theta) < 0$ for both particles). If the particles scatter to opposite sides of the barrier, e.g. if both are reflected or transmitted, no color is plotted. The intensity of the color corresponds to the magnitude of the sum of $p_f(|p_i|, \theta)$ for both particles.

Fig. 3.8(d) shows fractional particle transport $C_P(|p_i|)$ (see Eq. (4.3)). This function is considered over the entire range of θ for each $|p_i|$, i.e. $C_P(|p_i|)$ accounts for all particles at a given $|p_i|$. When $C_P(|p_i|)$ is averaged over all $|p_i|$, the symmetry theorem tells us that there is no net particle transport. However, there is transport (in either direction) within finite ranges of $|p_i|$. Fractional particle transport at a given $|p_i|$ can be understood by comparing Figs. 3.8(c) and (d). $C_P(|p_i|) < 0$ in the range $2.2 \lesssim |p_i| \lesssim 2.5$, indicating net particle flow to the left of the barriers. Examining Fig. 3.8(c), we see that only one colored lobe extends into this $|p_i|$ range. Its color (blue) indicates $(|p_i|, \theta)$ values for which both particles have $p_f(|p_i|, \theta) < 0$, meaning that both particles scatter to the left of the barriers. Since no red lobes extend into this $|p_i|$ range, there are no $(|p_i|, \theta)$ values for which both particles scatter to the right. Therefore, for any $(|p_i|, \theta)$ in this range, both particles can either scatter to the left of the barriers, or scatter to opposite sides, causing

net particle transport to the left.

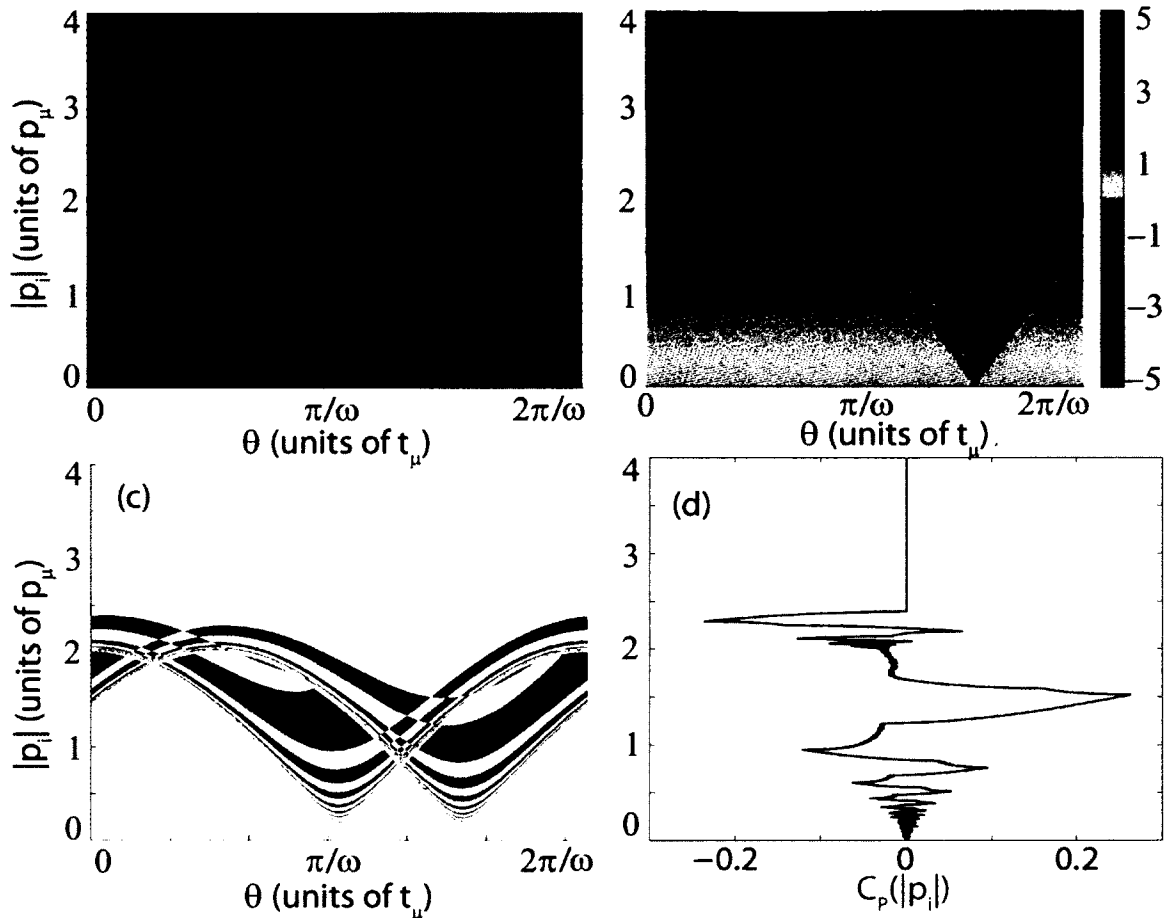


FIG. 3.9: Dynamics for wider touching, rectangular barriers. Same as Fig. 3.8, but with barriers four times as wide as those in Fig. 3.8 (σ and \hat{x} have been increased from 1.25 to 5). Increasing barrier width causes thinner ribbons of transmission and reflection for particles incident on the barriers from both sides.

Figure 3.9 illustrates the effects of increasing the barrier widths. In this calculation, all parameters are the same as those in Fig. 3.8 ($\hat{U} = 1$, $\alpha = 1$, $\omega = 1$, and $\phi = 3\pi/2$), except for σ and \hat{x} , which have been increased from 1.25 to 5. One can see that the ribbons of transmission and reflection span a more narrow $\Delta|p_i|$ range at a given θ , and that the widths ($\Delta|p_i|$) of the ribbons at a given θ do not decay as rapidly as in the previous case

as $p_i \rightarrow 0$. Comparing Figs. 3.9(c) and (d) to Figs. 3.8(c) and (d), we see that in this case the net particle transport fluctuates more rapidly with $|p_i|$. However, the magnitude of $C_P(|p_i|)$ within these smaller $\Delta|p_i|$ regions can be just as large (or larger) as in the case of narrow barriers.

The change in transmission and reflection ribbons for wide barriers can be understood by examining the condition for particles to transmit. Let us examine particles which approach from the left with $p_i > 0$ and arrive at the left barrier $\theta = \pi/\omega$, when the height of that barrier is zero. All particles arriving at $\theta = \pi/\omega$ hop onto the left barrier and traverse it with momentum $p_{b_1} = p_i$. The condition for them to transmit over the right barrier is

$$f(p_i, t_0) = p_i^2/2 + U_L(t_0) - U_R(t_0) > 0. \quad (3.34)$$

When $f(p_i) > 0$, particles transmit over the right barrier, and when $f(p_i) < 0$, particles reflect from the right barrier. The zeroes of $f(p_i)$ thus mark the boundaries between transmission and reflection ribbons.

We illustrate this for the barrier parameters from the preceding two examples ($\hat{U} = \alpha = \omega = 1$, $\phi = 3\pi/2$). For these barrier parameters, Eq. (3.34) reduces to

$$f(p_i) = \frac{p_i^2}{2} - 2 \cos\left(\frac{\pi}{4} + \frac{2\sigma}{p_i}\right) \sin\left(\frac{3\pi}{4}\right). \quad (3.35)$$

Eq. (3.35) shows that $f(p_i)$ oscillates about $p_i^2/2$, and the ratio $2\sigma/p_i$ governs its oscillation frequency. As $p_i \rightarrow 0$, $f(p_i)$ passes through zero an infinite number of times, resulting in an infinite number of transmission and reflection ribbons for any σ . Higher σ values (wider barriers) cause $f(p_i)$ to oscillate more rapidly as $p_i \rightarrow 0$. The maximum amplitude of oscillation is $2 \sin(3\pi/4) = \sqrt{2}$; thus, for $p_i^2/2 > \sqrt{2}$, i.e. $p_i > 2^{3/4} \approx 1.68$, all particles

will transmit, no matter the width of the barriers.

Eq. (3.35) is plotted for the selected barrier parameters in the left column of Fig. 3.10 while varying σ , the barrier width. The oscillatory curve is $f(p_i)$, and the two quadratic curves are $p_i^2/2 \pm \sqrt{2}$, which bound $f(p_i)$. The threshold $p_i = 2^{3/4}$ is the intersection between the left-most quadratic curve and the vertical line. The right column contains a zoom of $p_f(|p_i|, \theta)$ about $\theta = \pi/\omega$ for particles incident from the left for the respective σ . The top row represents $\hat{x} = \sigma = 1.25$ (see Fig. 3.8), the middle row is $\hat{x} = \sigma = 5$ (see Fig. 3.9), and the bottom row has $\hat{x} = \sigma = 20$. The infinite number of bands, and the reduction in their widths as the barriers get wider, are evident in these pictures.

3.4.2 Separated barriers

Inserting space between the barriers leaves many of the features of the preceding section intact, but introduces a critical difference in particle trajectories. Previously, a particle could reflect from a barrier no more than once. However, particles may now become trapped between the barriers for a long time, reflecting back and forth between them before finally arriving at the edge of a barrier with enough energy to transmit over it. These particle trajectories are thus very sensitive to initial conditions and the system is a model of chaotic scattering.

Numerical calculation of final momentum is performed in similar fashion as before. If a particle beginning on the left of the pump with positive momentum has enough energy to hop onto the left-hand barrier, we calculate its momentum p_{b_1} and the time t_0 at which it reaches the end of this barrier using Eqs. (3.28) and (3.29), respectively. However, instead of either reflecting from the right barrier or transmitting over it, the particle instead falls off the first barrier into the region between barriers with momentum

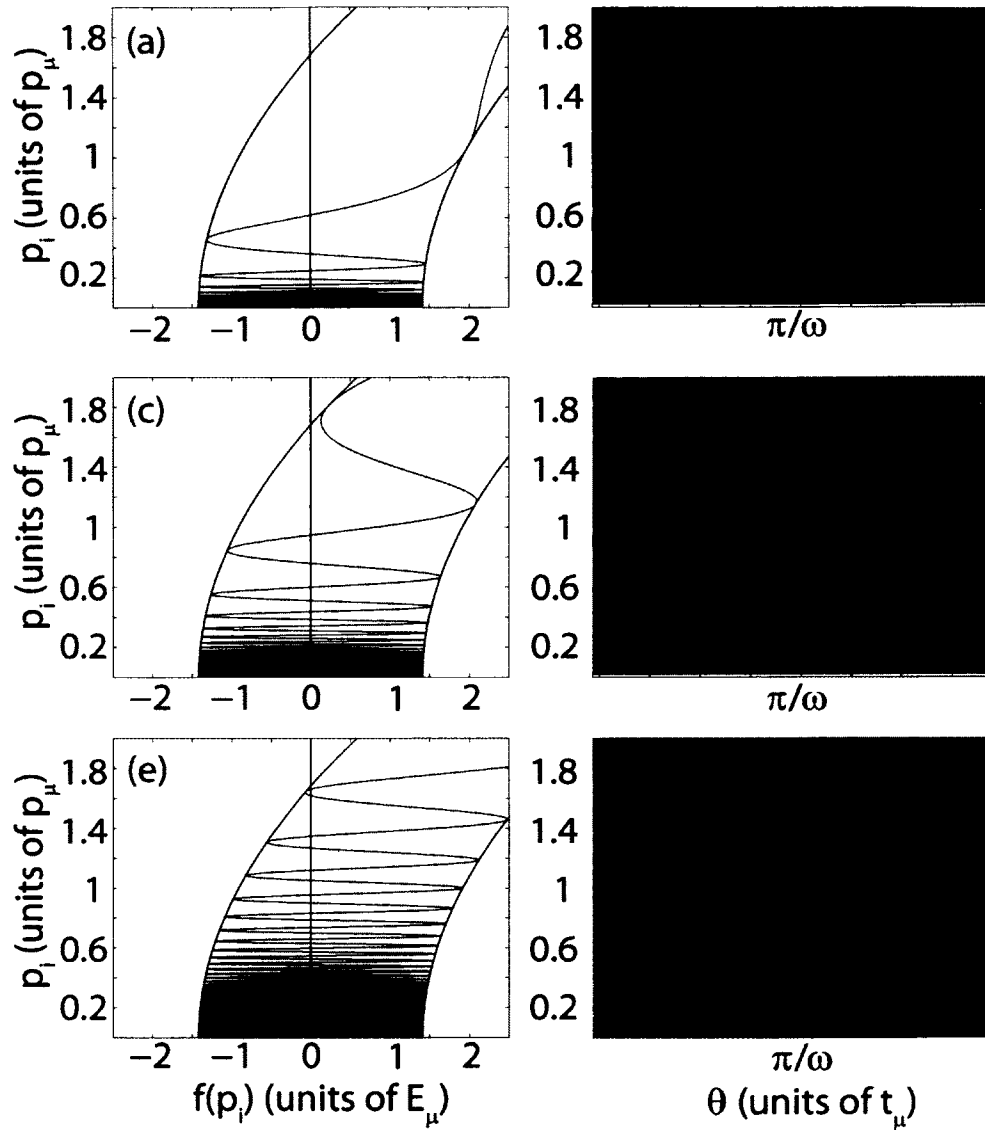


FIG. 3.10: Effect of barrier width on classical particle scattering from rectangular barriers that touch. Increasing barrier width decreases the widths of transmission and reflection ribbons. The zeroes of the functions in the left column mark the boundaries of transmission and reflection at the chosen θ . The right column shows zooms of $p_f(|p_i|, \theta)$ for the curves to the left. The top row has $\hat{x} = \sigma = 1.25$, the middle row has $\hat{x} = \sigma = 5$, and the bottom row has $\hat{x} = \sigma = 20$ with all other barrier parameters equal.

$$p_N = (-1)^{(N-1)} \sqrt{2 \left(U_L(t_0) + \frac{p_{b_1}^2}{2} \right)}, \quad (3.36)$$

with $N = 1$. The particle reaches the second barrier at time

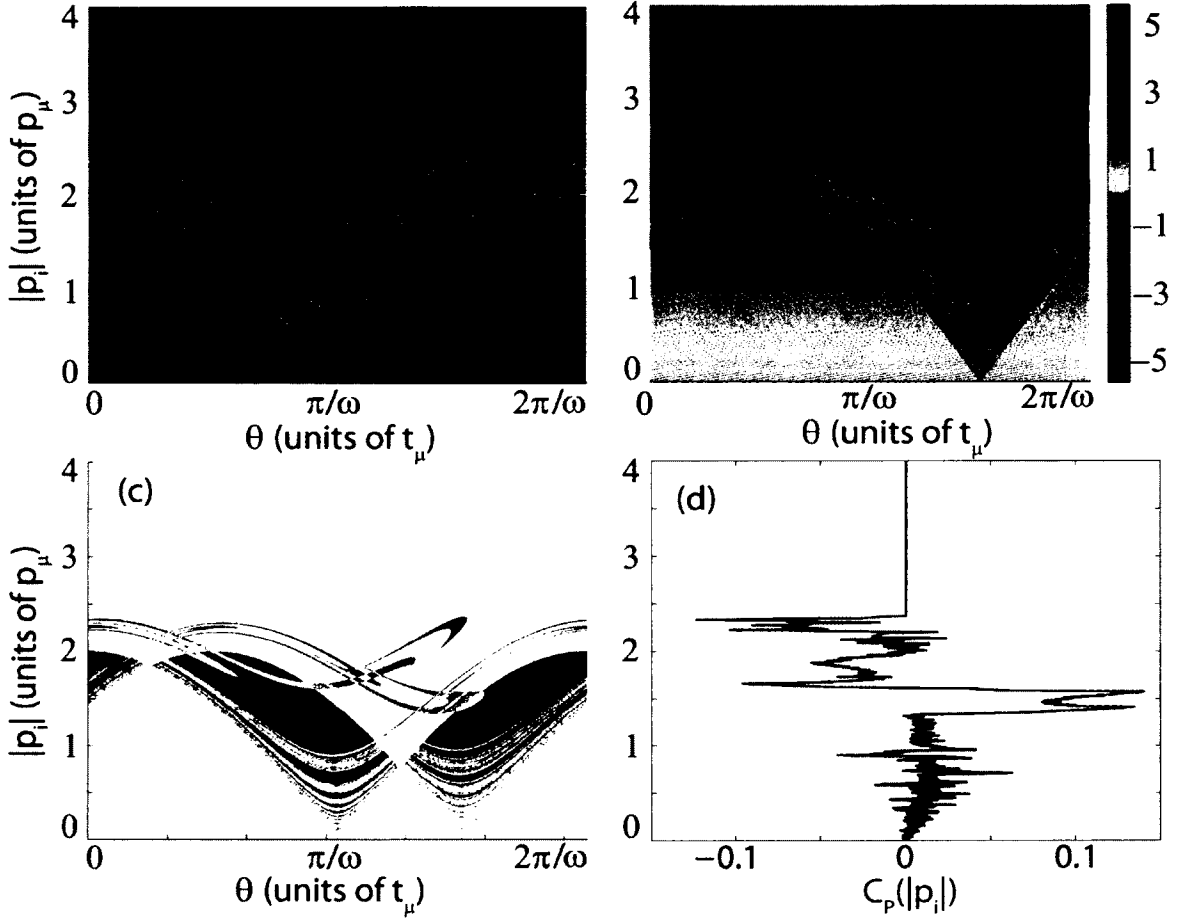


FIG. 3.11: Dynamics for separated, rectangular barriers. Same as Fig. 3.9, but with space between the barriers. The barriers are now centered at $\pm \hat{x} = \pm 15$, and have a distance of $d = 20$ between their inner edges.

$$t_N = N \frac{d}{p_N} + t_0, \quad (3.37)$$

where

$$d = 2\hat{x} - 2\sigma \quad (3.38)$$

is the distance between the inner edges of the barriers.

If the height of the second barrier is greater than the particle's energy, i.e., $U_R(t_N) > p_N^2/2$, the particle reflects from the second barrier, and we increment N by 1. The index N thus counts the number of trips between the barriers for each trajectory. Each time a particle arrives at the edge of a barrier, we compare its kinetic energy $p_N^2/2$ with the height of that barrier (for odd N we compare to $U_R(t_N)$, and for even N we compare to $U_L(t_N)$) until it has enough energy to hop onto a barrier. Once on top of a barrier, the particle's momentum is given by

$$p_{b_2} = \pm \sqrt{2 \left(\frac{p_N^2}{2} - U_{R,L}(t_N) \right)}, \quad (3.39)$$

where p_{b_2} is positive for odd N , and negative for even N . The particle then falls off the second barrier at time

$$t_b = \frac{2\sigma}{p_{b_2}} + t_N, \quad (3.40)$$

with final momentum

$$p_f = \pm \sqrt{2 \left(\frac{1}{2} p_{b_2}^2 + U_{R,L}(t_b) \right)}, \quad (3.41)$$

where $p_f > 0$ if $p_{b_2} > 0$, and $p_f < 0$ if $p_{b_2} < 0$. The calculation is similar for particles approaching the barriers from the right.

Figure 3.11 shows results for a pump with potentials given by Eqs. (3.3a) and (3.3b) with $\hat{x} = 15$, $\sigma = 5$, $\hat{U} = 1$, $\alpha = 1$, $\omega = 1$, and $\phi = 3\pi/2$. This pump is the same as the one from Fig. 3.9, except the inner edges of the barriers are now separated by a distance $d = 20$. Similar to the effect of making the barriers wider, inserting space between the barriers affects the ribbons of transmission and reflection for particles approaching the barriers from both sides. The width ($\Delta|p_i|$) of the ribbons decays more quickly as $|p_i| \rightarrow 0$ for a given θ . Consequently, the width $\Delta|p_i|$ for regions of large net particle transport is smaller. The magnitude of $C_P(|p_i|)$ has decreased in this example (although increasing the space between the barriers can also cause it to increase). Predicting the effect of increasing barrier separation on the magnitude of fractional particle transport is not possible without detailed calculations.

Fig. 3.12 shows $x_i(p_f)$ for two particle packets which approach the barriers from opposite sides with the same initial energy ($p_i = \pm 3.8$). The initial packets are described by Eq. (3.6) with $-x_c = \mp 450$ and $\beta = 100$. Their initial energy is large enough such that all particles transmit over both barriers. Particles approaching from the left are scattered to a larger range of p_f than those approaching from the right. This results in more peaks for $p_f > 0$ in the semiclassical probability density $P_f^{SC}(p_f)$ shown in Fig. 3.12(b). Figs. 3.12(c) and (d) show expansions of Fig. 3.12(b) (note the different scales). This calculation has not been extended into the classically-forbidden regions. In Fig. 3.12(c), the classical probability density $P^C(p_f)$ (dashed curve) and single-cycle semiclassical probability density

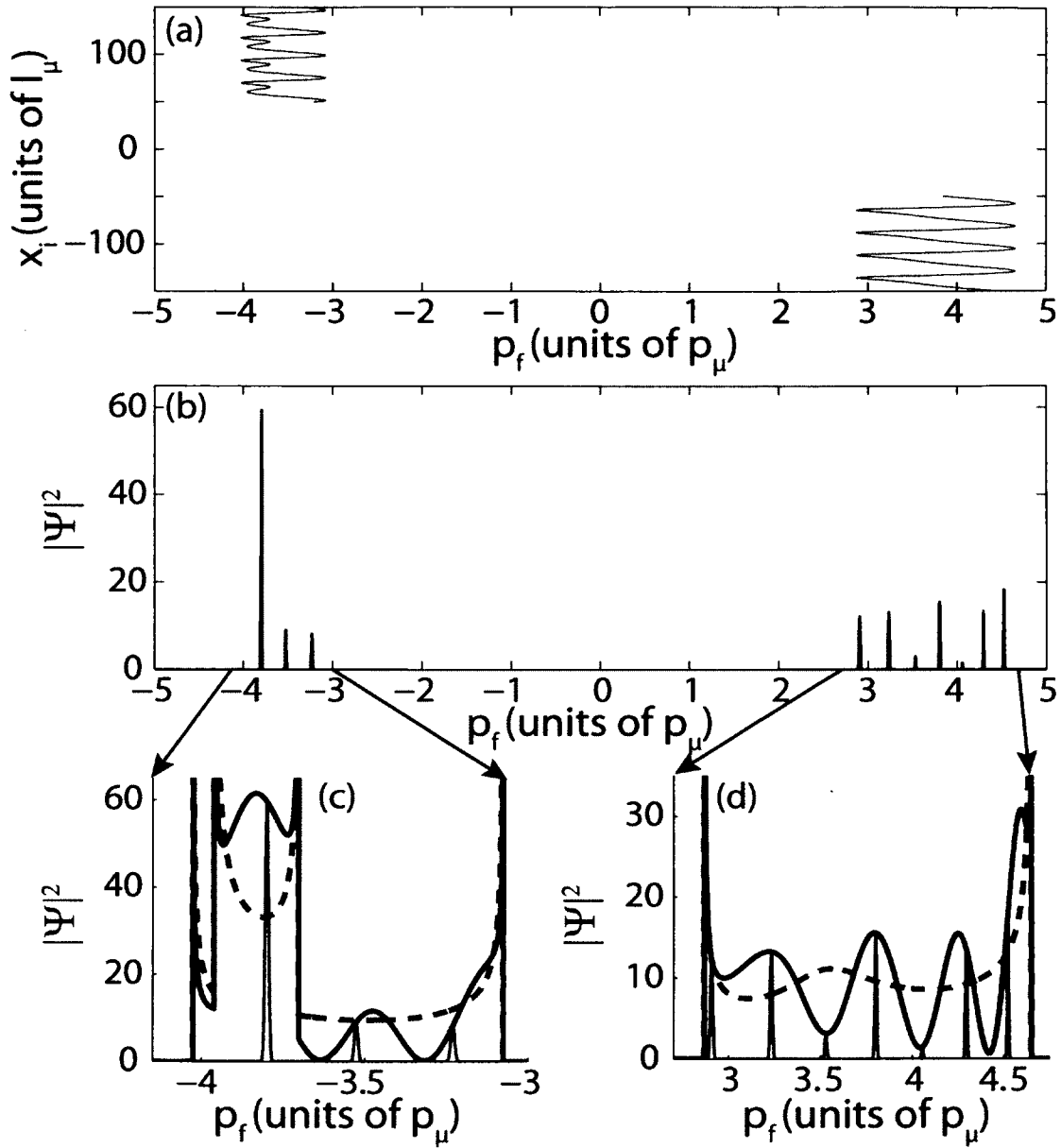


FIG. 3.12: Semiclassical analysis of scattering from separated rectangular barriers. Classical and primitive semiclassical final momentum probabilities for the separated barriers in Fig. 3.11. All curves are as described in Fig. 3.4

(oscillatory curve) $P_s^{SC}(p_f)$ diverge at each of the four turning points of $x_i(p_f)$. Interference among the four branches of $x_i(p_f)$ within one cycle causes $P_s^{SC}(p_f)$ to be larger than $P^C(p_f)$ at the location of the largest peak, $p_f \approx -3.53$. $P_s^{SC}(p_f)$ and $P^C(p_f)$ are scaled (multiplied by the same constant) in order to be plotted with $P_f^{SC}(p_f)$ (sharply-peaked curve), and the relative heights in the Floquet peaks can be seen to align closely with the discrete values of $P_s^{SC}(p_f)$ at momenta corresponding the Floquet energies.

Analysis of transmission and reflection ribbons is more difficult in the present case because of the possibility of multiple reflections between the barriers. However, we can gain insight by analyzing criteria for particles which directly transmit past both barriers with no reflection. For particles approaching from the left with $p_i > 0$ and arriving at the left-hand barrier at $\theta = \pi/\omega$ (i.e. when the height of the left barrier is zero), the condition for direct transmission past both barriers is

$$f_d(p_i, t_0) = p_i^2/2 + U_L(t_0) - U_R(t_N) > 0 \quad (3.42)$$

with $N = 1$, where the subscript d is the distance between the inner edges of the barriers (see Eq. (3.38)). Eq. (3.42) reduces to

$$f_d(p_i) = \frac{p_i^2}{2} - 2 \sin\left(\frac{\hat{x} - \sigma}{p_N} + \frac{3\pi}{4}\right) \cos\left(\frac{\hat{x} - \sigma}{p_N} + \frac{\pi}{4} + \frac{2\sigma}{p_i}\right) \quad (3.43)$$

for our selected barrier parameters.

The left and right columns of Fig. 3.13 show zooms of Figs. 3.9(a) ($\hat{x} = \sigma = 5$) and 3.11(a) ($\hat{x} = 15$ and $\sigma = 5$), respectively, about $\theta = \pi/\omega$. The color scheme has been changed to enhance visibility; black ribbons represent reflection and the lighter (yellow) ribbons represent transmission. The middle column of Fig. 3.13 shows $f_d(p_i)$ for these two

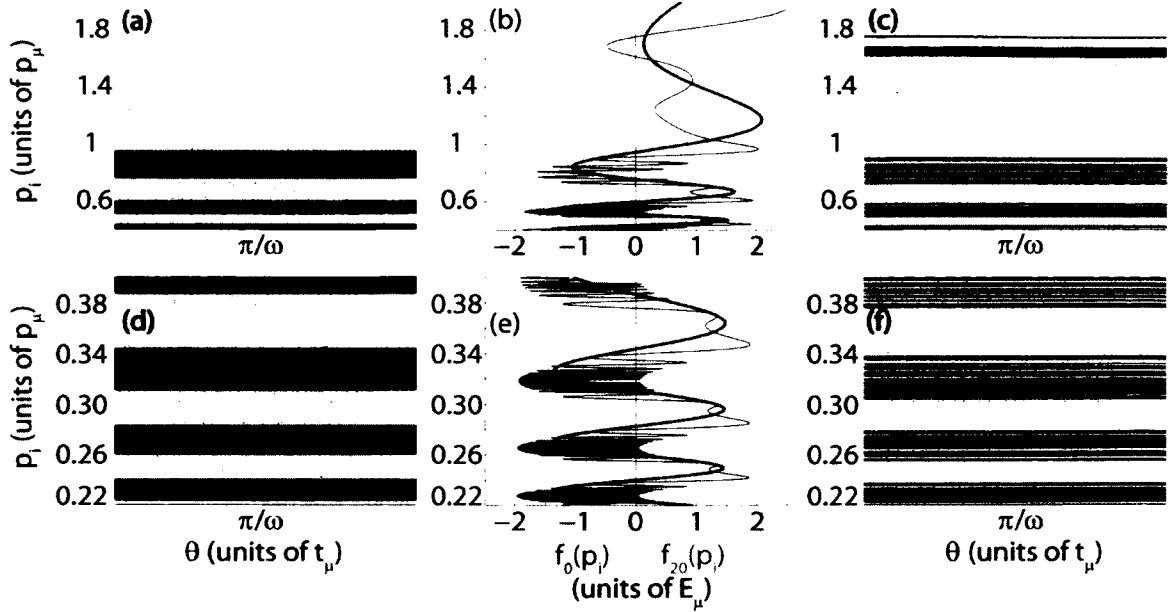


FIG. 3.13: Effect that separating the rectangular barriers has on classical particle scattering. Left column: Zooms of Fig. 3.9(a) about $\theta = \pi/\omega$ with color schemed changed. Black represents reflection; yellow represents transmission. Right column: Zooms of Fig. 3.11(a) about $\theta = \pi/\omega$. The zeroes of the thick (blue) oscillatory curve in the middle column mark the boundaries of transmission and reflection seen in the left column. When the thin (red) oscillatory curve is positive, particles in the right column transmit, but this function does not reveal all transmission ribbons in the right column.

pumps. The thick (blue) curve is $f_0(p_i)$ ($d = 0$), and is the same curve seen in Fig. 3.10. Its zeroes mark the boundaries of transmission and reflection in the left column. The thin curve (red) is $f_{20}(p_i)$ ($d = 20$), and corresponds to the right column.

When $f_{20}(p_i) > 0$, particles arriving at the pump in the right column transmit, and the ribbon in the right column is the light color (yellow). When $f_{20}(p_i) < 0$, the particle reflects from the right-hand barrier, and its ultimate fate is unspecified. It is evident that $f_{20}(p_i)$ oscillates more rapidly than $f_0(p_i)$. Consequently, regions which reflect when the barriers touch are split into multiple transmission and reflection ribbons as the barriers are moved apart. This is illustrated in the present case in regions where $f_0(p_i) < 0$ and

$f_{20}(p_i) > 0$. For each region in which $f_0(p_i)$ is negative, there is a reflection ribbon in the left column. However, in each such region, $f_{20}(p_i)$ oscillates through zero many times, and each positive segment of $f_{20}(p_i)$ represents a transmission ribbon in the right column. Increasing the barrier separation distance thus creates many transmission and reflection ribbons in regions where there is only pure reflection when the barriers touch. The minimum p_i above which all particles arriving at $\theta = \pi/\omega$ transmit has also been greatly increased by moving the barriers apart. With no barrier separation, this $p_i \approx 0.95$, but increasing \hat{x} to 15 increases this minimum to $p_i \approx 1.76$. In each case, there are an infinite number of ribbons as $p_i \rightarrow 0$.

This level of analysis predicts only the outcome of each particle's first arrival at the right-hand barrier. What happens after that is "left as an exercise for the reader."

The effects of increasing barrier width and separation can be summarized as follows. Increasing the width causes more transmission and reflection ribbons below arbitrary $|p_i|$, up to a maximum $|p_i|$ above which all particles will transmit for a given θ . The width of the ribbons (in terms of $\Delta|p_i|$) decays more slowly as $|p_i| \rightarrow 0$ for wider barriers. Ribbons produced by particles incident upon barriers with no separation are split into multiple ribbons by moving the barriers apart. Increasing barrier separation can also allow particles of much higher $|p_i|$ to reflect for a given θ . Increasing either of these parameters causes the widths ($\Delta|p_i|$) of regions in which there is significant fractional particle transport to decrease, although its magnitude is not systematically changed. Predictions on fractional transport are highly sensitive to the choice of initial conditions and parameters, and do not display any obvious pattern. Therefore, general predictions beyond what we have mentioned cannot be made without detailed calculations specific to a configuration and choice of parameters.

3.5 Symmetric Gaussian Barriers

While rectangular barriers provide a simplified model that addresses the essential pumping physics, Gaussian barriers are more likely to be used in experimental implementations using laser-based optical dipole barriers for ultracold atoms. In this section, we examine a turnstile pump (such as those in Section 3.4) with Gaussian potentials described by Eqs. (4.2) and (3.4b) with $\hat{U}_L = \hat{U}_R = 1$, $\alpha = 1$, $\omega = 1$, $\phi = 3\pi/2$, $\sigma = 2.5/(2\sqrt{2\ln 2})$, and $\hat{x} = 3.75$. Both barriers oscillate at the same frequency, but not in phase with one another. As in the previous section, particle trajectories for this type of pump are classically chaotic.

Fig. 3.14(a) and (b) show $p_f(|p_i|, \theta)$ for particles incident upon the barriers from the left and right, respectively. Unlike the previous cases with rectangular barriers, there is a minimum $|p_i|$ below which there is no particle transmission. As particles approach Gaussian-shaped repulsive barriers, they lose momentum, resulting in a minimum initial energy required to transmit past the first barrier encountered. In this case, all particles with $|p_i| \lesssim 0.90$ reflect from the first barrier. Different types of structure can be seen in $p_f(|p_i|, \theta)$ than for rectangular barriers, but qualitative features remain. The regions in which striping can be seen indicate particle trajectories which are temporarily trapped between the barriers before finally transmitting or reflecting. The lobe with significant striping seen in Fig. 3.14(a) is much wider than the narrow one seen in Fig. 3.14(b) in the range $1.75 \lesssim |p_i| \lesssim 2.25$, indicating that particles approaching from the left in this energy range are much more likely to become temporarily trapped between the barriers than those approaching from the right with equal energy. However, above this range, all particles approaching from the left transmit, while some approaching from the right are trapped between the barriers until $|p_i| \gtrsim 2.5$. A complete description of particle transport through the barrier region is difficult. We present a topological analysis in Ref.[121] and

Chapters 5 and 6.

Fig. 3.14(c) shows $(|p_i|, \theta)$ for which both particles scatter to the left (blue) or right (red). Whereas the previous cases with rectangular barriers have structure as $|p_i| \rightarrow 0$, no structure is present in this region for Gaussian barriers because of the nonzero minimum $|p_i|$ required to transmit past the first barrier. Fig. 3.14(d) shows $C_P(|p_i|)$. The vertical region in this curve below $|p_i| \lesssim 0.90$ corresponds to the region in which all particles directly reflect. Above this range, fractional particle transport occurs in both directions until $|p_i|$ is large enough for all particles to transmit past both barriers.

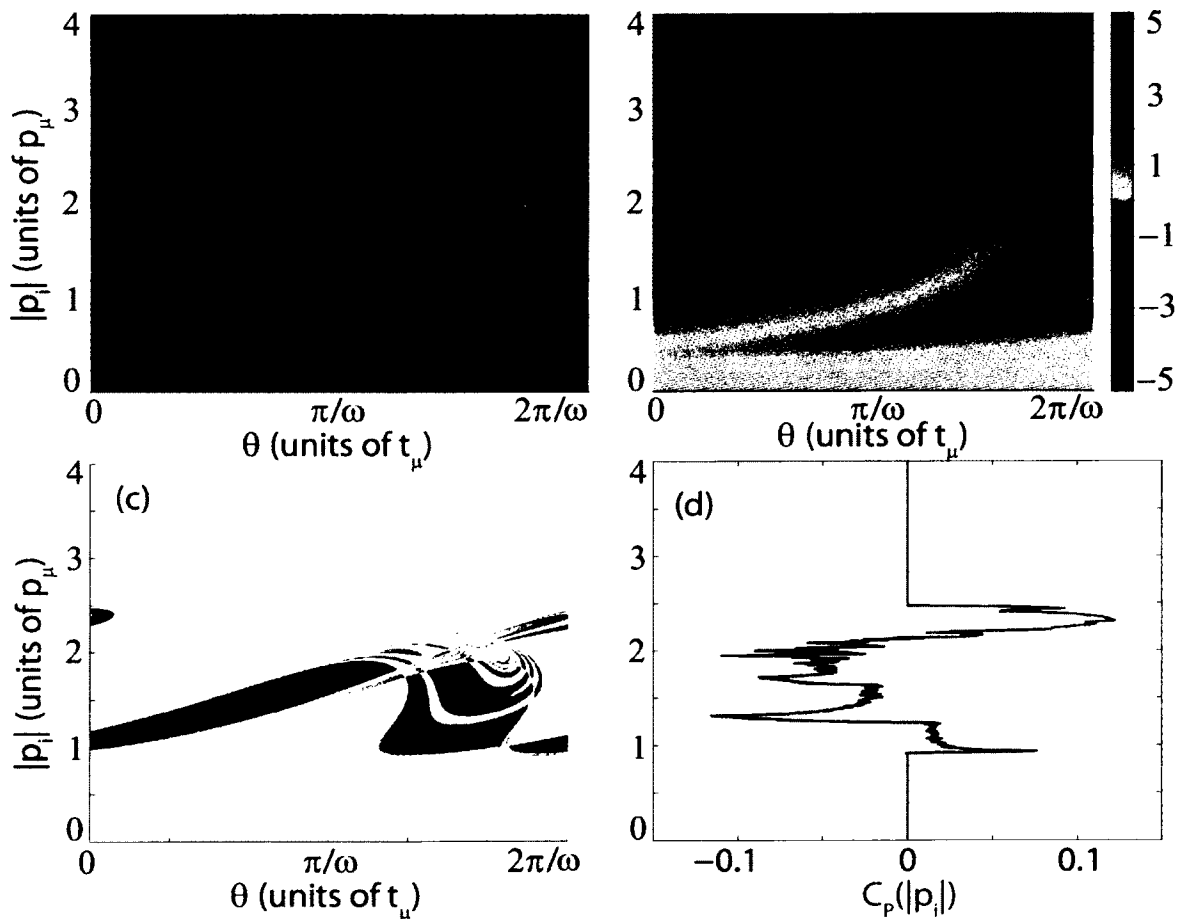


FIG. 3.14: Dynamics for symmetric Gaussian barriers. Same as Fig. 3.11, but for Gaussian barriers.

Figure 3.15 shows classical, semiclassical, and quantum-mechanical comparisons for two packets of particles approaching the barriers from opposite directions with $p_i = \pm 2.65$. The initial packets are described by Eq. (3.6) with $-x_c = \mp 450$ and $\beta = 100$.

Figure 3.15(a) shows classical initial position as a function of final momentum for particles approaching the barriers from both sides. All particles have enough energy to transmit over both barriers. Particles incident upon the barriers from the right scatter to a larger range of Δp_f than those approaching from the left.

Figure 3.15(b) shows $P_f^{SC}(p_f)$, the uniform semiclassical final momentum probability density (plotted upward), and $P_f^Q(p_f)$, the quantum mechanical final momentum probability (plotted downward). The uniform semiclassical calculation has been repaired near turning points of $p_f(x_i)$, where the primitive form is divergent, and has been extended into classically-forbidden regions. $P_f^Q(p_f)$ has been mirrored about the amplitude axis for ease in comparing the two calculations. The horizontal lines (red) in the upper half-plane are the heights of the peaks in $P_f^Q(p_f)$, and are plotted to allow one to compare the calculations more easily. Very good agreement between the two methods is evident.

Figures 3.15(c) and (d) show the classical probability density $P^C(p_f)$ (dashed curve), and the primitive semiclassical single-cycle probability density $P_s^{SC}(p_f)$ (thick oscillatory curve, red). The two sharply-peaked functions are the primitive semiclassical probability density $P_p^{SC}(p_f)$, given by summing Eq. (3.15) for all branches (lighter peaked curve, green), and the uniform semiclassical probability density $P_f^{SC}(p_f)$ (darker peaked curve, blue). The functions $P^C(p_f)$ and $P_s^{SC}(p_f)$ are scaled (multiplied by the same constant). The function $P_p^{SC}(p_f)$ (green) takes on discrete values of the curve $P_s^{SC}(p_f)$ (red) at momenta satisfying $E_n = E_i + n\hbar\omega$, showing that the single-cycle probability governs the relative heights of the Floquet peaks (the single-cycle probability shown is the primitive form).

The classical dynamics underlying the quantum treatment are therefore necessary to

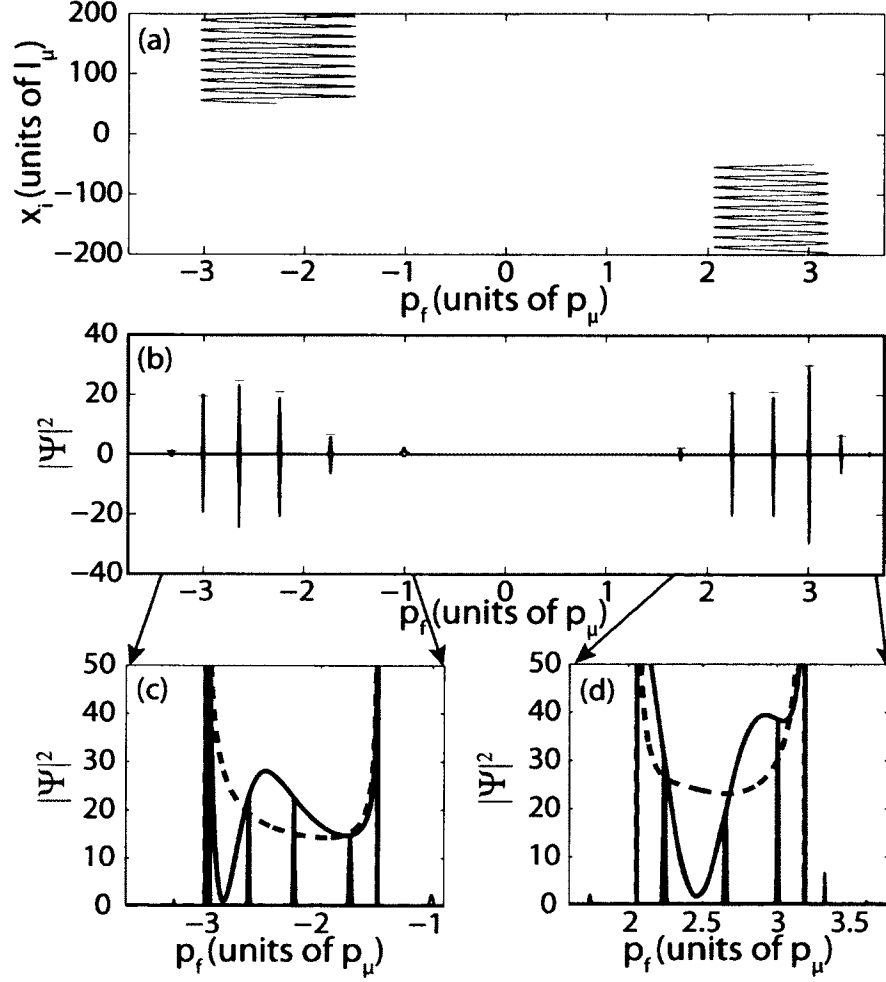


FIG. 3.15: Quantum and semiclassical analysis of scattering from symmetric Gaussian barriers. (a) $p_f(x_i)$ for particles approaching a pump with two oscillating Gaussian barriers from both sides. (b) Final uniform semiclassical momentum probability $P_f^{SC}(p_f)$ (plotted upward, blue), and quantum mechanical final momentum probability $P_f^Q(p_f)$ (plotted downward, red), for the particles in (a). (c) and (d) $P^C(p_f)$ (dashed curve), $P_s^{SC}(p_f)$ (oscillatory curve, red), $P_P^{SC}(p_f)$ (green) and $P_f^{SC}(p_f)$ (blue) for the particles in (a). See the text for a discussion of these functions.

fully understand the quantum mechanical result. While quantum theory tells us that the density will be peaked at momenta satisfying $E_n = E_i + n\hbar\omega$, it does not tell us the range of n for which the peaks will be of appreciable height. The final momentum region in which particles are classically scattered governs the range of n for which the quantum result yields large peaks. Quantum theory also does not indicate why some momentum states are more highly populated than others, but semiclassical tools give an intuitive explanation for that.

The double barrier turnstile pump might be viewed (with some caution) as a momentum-space interferometer. In this picture, each oscillating barrier acts as a multichannel beam-splitter which takes an incoming planewave and transforms it into a superposition of outgoing planewaves with different momenta (with energies $E_n = E_i + n\hbar\omega$). In a pure transmission case (such as Fig. 3.15), the first barrier produces multiple planewave states, and then the second barrier mixes these and produces additional planewave states. In this way a turnstile pump may be viewed as a discrete multipath momentum space interferometer. However, this description cannot be accurate if the barriers are not well-separated. The barriers must be sufficiently far apart that the configuration-space wave function in the region between them is approximately a superposition of plane waves, but not so far apart that packets associated with different Floquet states have separated.

3.6 Remarks

In summary, we have defined and described ballistic atom pumps, showing that for finite ranges of initial particle energies, such systems can create net particle transport in either direction. The direction of particle pumping is highly sensitive to barrier parameters and to the initial energy of the particles. It is not possible to predict the direction or magnitude of particle pumping without detailed calculations.

If tunneling can be neglected, diode pumps—which only allow net transport in one direction for particles below a certain initial energy—can be constructed. At sufficiently high incident particle energies, these diodes only allow net particle transport in the opposite direction.

We have studied these pumps classically, semiclassically, and quantum mechanically. While classical theory gives a slowly-varying final momentum probability for scattered particles, quantum theory yields final momentum probabilities sharply-peaked at momenta satisfying $E_n = E_i + n\hbar\omega$. The range of n for which there are appreciable peaks is governed by the underlying classically-allowed momentum range of scattered particles. Semiclassical theory gives an intuitive explanation for the relative heights of the peaks, and agrees well with the quantum description.

CHAPTER 4

Energy and Heat Transfer in Ballistic Atom Pumps

In this chapter we examine the effect that classical particle scattering from a ballistic atom pump has on net energy flow and heat transfer to the reservoirs. We consider pumps of the same type as studied in the last chapter, with a Hamiltonian given by

$$H(p, x, t) = p^2/2m + V(x, t). \quad (4.1)$$

We choose $V(x, t)$ to consist of two repulsive barriers, one or both of which oscillates. When both barriers oscillate they have the same frequency ω , but not the same phase. We examine the classical scattering of equal numbers of particles which approach such pumps from each reservoir with equal and fixed incident energy.

It has been shown that flows may be zero or negligible in pumps with idealized limits such as delta-function barriers or uniform phase-space density (see Chapter 3, Section 3.3) [18, 122]. Here we show that under more realistic conditions, such pumps can generate significant net transfer of both matter and energy. Understanding heat flow is also essential

for any transport mechanism, and is of fundamental importance for thermoelectric devices [123]. Studies that have been done in the context of mesoscopic pumps [124, 125] used a strictly quantum picture involving exchange of quasi-particles, and heat flow was shown to be outwards from the pump towards the reservoirs. The classical model discussed here is more appropriate for higher temperatures, and we show that the pump can heat or cool one or both reservoirs.

4.1 Summary of Results

In this chapter (and Ref. [126]) we show that for monoenergetic incident particles: (A) Such pumps can transfer energy from one reservoir to the other, and energy can be transferred from pump to particles or vice versa. (B) A net change of energy in each reservoir can occur even if there is no net particle transport. The direction of energy change is distinct from the direction of particle transport. (C) Such pumps can heat or cool one or both reservoirs, and the heating or cooling is distinct from the existence or direction of net particle transport and distinct from energy flow. (D) At some incident energies, such pumps can generate net particle transport while at the same time particles give energy to the pump.

4.2 System

We will establish properties (A)-(D) by examining one specific pump: a particle diode consisting of two Gaussian-shaped potential barriers, only one of which oscillates. We choose this pump as our example because the dynamics of the system become much more complicated when both barriers oscillate [122]. A diode is useful for studying heat and energy flow because the direction of net particle transport is predictable within certain

incident energy regimes, though the threshold energies are not predictable without calculation. We therefore discuss heat and energy transfer in this example system within the context of the direction of net particle transport.

In the chosen diode, the distance between the barriers is substantially larger than their widths, so their overlap is negligible. The right-hand barrier has a fixed height, while the left-hand barrier oscillates between zero and the height of the right-hand barrier. The pump is described by

$$V(x, t) = \hat{U}_L (1 + \alpha_L \cos(\omega t)) \exp\left(\frac{-(x + \hat{x})^2}{2\sigma^2}\right) + \hat{U}_R \exp\left(\frac{-(x - \hat{x})^2}{2\sigma^2}\right), \quad (4.2)$$

where $\hat{U}_{L,R}$ is the average height of each barrier, α_L is the amplitude of oscillation of the left barrier, $\omega = 2\pi/T$ is the frequency and T is the period, and σ is the standard deviation of each Gaussian. The left and right barriers are centered at $x = -\hat{x}$ and $x = \hat{x} = 4.5$, respectively. In our calculations, we set $\hat{U}_L = 1$, $\hat{U}_R = 2\hat{U}_L = 2$, $\alpha_L = 1$, $\omega = 1$, $\sigma = 1.5$, and $m = 1$. These are scaled units, as in previous chapters. These parameters are also within the experimentally-accessible regime discussed in Chapter 2.

The effects of the pump can be understood qualitatively as follows. For incident energies less than the height of the static barrier, all particles from the right reflect from the static barrier, but particles incident from the left may gain enough energy from the oscillating barrier to scatter past both barriers. Consequently, the only possible direction of net particle transport is from left-to-right. For incident energies greater than the height of the static barrier, computations show that, in this case, all particles incident from the right transmit past both barriers, but particles incident from the left may lose energy to the oscillating barrier, reflect from the static barrier, and ultimately scatter to the left reservoir. Thus the only possible direction of net particle transport reverses to right-to-left.

4.3 Method

Our computational algorithm can be summarized as follows: 1) For each initial energy, launch particles toward the barriers from the left and right. Particles begin with a range of positions $\Delta x = |p_i|2\pi/\omega$ where p_i is the initial momentum, which ensures that all barrier phases are encountered. 2) Record the reservoir to which each particle is scattered, and sum the results to obtain the net fractional transport (defined below) of particles scattered to the right (which may be negative if more particles are scattered to the left). 3) Compute the total energy gain of the two reservoirs after scattering, which may be negative if the system loses energy to the pump. 4) Compute the net gain (or loss) in the total energy of each reservoir. Energy being an extensive quantity, a reservoir gains total energy by gain in the number of particles as well as by gain of energy of individual particles passing through the pump. 5) Compute the change of energy of each particle scattered into each reservoir, and compute the average of these changes for all particles scattered into each reservoir. The average change of energy per scattered particle may be regarded as corresponding to a change of temperature of the reservoir. Temperature being an intensive property, the direction of temperature change need not be the same as the direction of energy change in each reservoir. Formulas for computation of these quantities are given below.

The fractional transport of particles through the pump is defined as

$$C_P(|p_i|) = \frac{R(|p_i|) - L(|p_i|)}{R(|p_i|) + L(|p_i|)}, \quad (4.3)$$

where $R(|p_i|)$ is the number of particles scattered to the right for each $|p_i|$, and $L(|p_i|)$ is the number of particles scattered to the left. The sum $R(|p_i|) + L(|p_i|)$ represents all particles incident on the pump for a given $|p_i|$. $C_P(|p_i|)$ is positive when more particles are scattered to the right (net particle transport to the right reservoir), negative when more

particles are scattered to the left (net particle transport to the left reservoir) and zero when equal numbers of particles scatter to the right and left reservoirs.

For each initial particle energy, the total energy change of the system and each reservoir are defined as

$$\Delta E^\alpha(|p_i|) = E_f^\alpha(|p_i|) - E_i^\alpha(|p_i|), \quad (4.4)$$

where $\alpha = \{T, L, R\}$. When $\alpha = T$, $E_f^T(|p_i|)$ and $E_i^T(|p_i|)$ represent the total final and initial energies, respectively, of all particles incident upon one cycle of the pump. When $\Delta E^T > 0$, the pump has added energy to the reservoirs; when $\Delta E^T < 0$, the reservoirs have lost energy to the pump. When $\alpha = L$ or R , $E_f^\alpha(|p_i|)$ represents the total final energy of all particles which scatter to the left or right reservoirs, and $E_i^\alpha(|p_i|)$ represents the corresponding total initial energy of all particles beginning in the left or right reservoir.

The last quantities examined in this chapter are the changes in *average* energy per particle scattered into each reservoir. These quantities are defined as

$$\overline{\Delta E^\beta(|p_i|)} = \frac{E_f^\beta(|p_i|)}{M^\beta} - \frac{E_i^\beta(|p_i|)}{N^\beta} = \frac{k_B}{2} \Delta T^\beta(|p_i|), \quad (4.5)$$

where $\beta = \{L, R\}$ and corresponds to the left and right reservoirs, respectively. N^β is the number of particles incident on the pump from the β reservoir in one cycle, and M^β is the number of particles scattered to the β reservoir. A total of $2N^\beta$ particles approach the pump for each incident energy (N^β from each reservoir); consequently $M^\beta > N^\beta$ corresponds to an increase in particle number for the β reservoir. This change of average energy per particle can be regarded as a change of temperature of those scattered particles. Then a positive (negative) $\Delta T^{L,R}$ produces an increase (decrease) in the temperature of the corresponding reservoir after thermalization.

4.4 Results

In Fig. 4.1 we show the results of calculations for net particle transport, energy changes in the total system, and temperature and energy changes in each reservoir for the selected pump. We discuss all properties in relation to the net particle transport, which is the thick curve in Fig. 4.1(a). While the direction of net particle direction is predictable for certain incident energy ranges (see Chapter 3), the boundaries of these regions are not predictable. There are four distinct regions of particle transport direction, and we discuss them in order of increasing complexity. This complexity arises for two reasons. (1) Depending on the initial energy and the frequency of the barrier, a particle can ride repeatedly up and down the oscillating barrier. (2) A particle can undergo multiple reflections between the two barriers; this is the source of chaos in the system.

4.4.1 Region I: No particle transport; left reservoir heated

($0 < |p_i| \lesssim 1.176$) At these low energies, no particle gets past the static barrier, so there is no net particle transport, and $C_P(|p_i|) = 0$ [thickest curve in Fig. 4.1(a)]. Particles incident from the right reflect from the static barrier into the right reservoir without a change in energy. Therefore the number of particles, their average energy, and the total energy in the right reservoir do not change, i.e. $\Delta T^R(|p_i|) = 0$ [medium curve (purple) in Fig. 4.1(a)] and $\Delta E^R(|p_i|) = 0$ [medium (purple) curve in Fig. 4.1(b)].

All particles incident from the left are scattered into the left reservoir, but the oscillating barrier changes their energy. They may gain or lose energy to the pump, depending on their time of arrival. On average, they gain energy. Accordingly, the temperature (average energy per particle) and total energy both rise in the left reservoir, i.e., $\Delta T^L(|p_i|) > 0$ and $\Delta E^L(|p_i|) > 0$ [thin (green) curves in Fig. 4.1(a) and 4.1(b)]. Considering both reservoirs together, there has been net addition of energy from the pump to the reservoirs

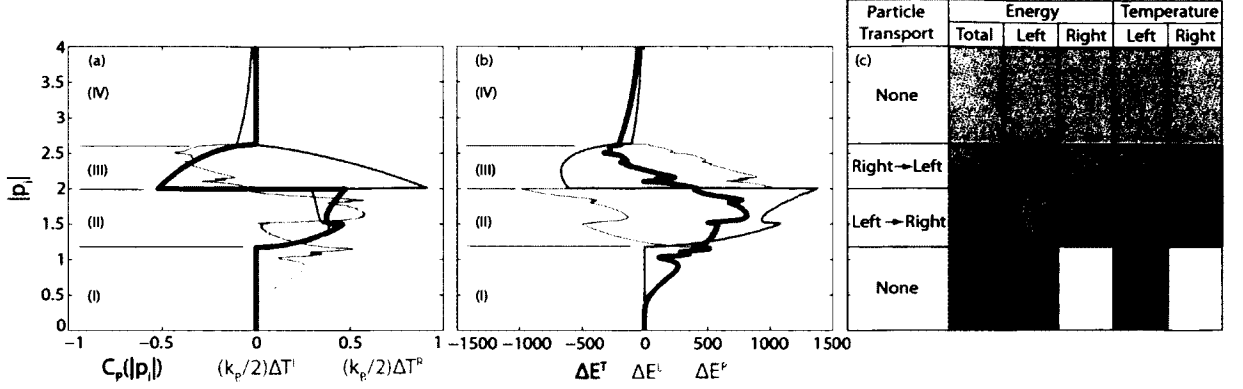


FIG. 4.1: Energy and heat transfer in an example ballistic atom pump. (a) Net particle transport, $C_P(|p_i|)$ [thickest curve], and the change in average energy per particle in the left reservoir, $(k_B/2)\Delta T^L(|p_i|)$ [thin (green) curve] and right reservoir, $(k_B/2)\Delta T^R(|p_i|)$ [medium (purple) curve]. When $C_P(|p_i|)$ is positive (negative) there is net particle transport from left-to-right (right-to-left). When $(k_B/2)\Delta T^{L,R}(|p_i|)$ is positive (negative), the pump increases (decreases) the average energy of particles scattered into the respective reservoir, and the temperature in that reservoir increases (decreases). (b) Total energy change in both reservoirs, $\Delta E^T(|p_i|)$ [thickest curve], in the left reservoir, $\Delta E^L(|p_i|)$ [thin (green) curve], and in the right reservoir, $\Delta E^R(|p_i|)$ [medium (purple) curve]. When $\Delta E^T(|p_i|)$ is positive, the pumps adds net energy to the reservoirs; when negative, the reservoirs lose net energy to the pump. When $\Delta E^{L,R}(|p_i|)$ is positive (negative), the pump increases (decreases) the total energy in the respective reservoir. (c) Summary of (a) and (b). Red indicates an increase, and blue represents a decrease. No color is plotted if the quantity does not change.

($\Delta E^T(|p_i|) > 0$) [thickest curve in Fig. 4.1(b)], and this energy is entirely added to the left reservoir.

These results are summarized in Fig 4.1(c), in which the blue represents a loss, red represents an increase, and white represents no change.

4.4.2 Region IV: No particle transport; both reservoirs cooled

($|p_i| \gtrsim 2.63$) At high incident momentum, all particles incident from both sides transmit past both barriers, and there is no net particle transport ($C_P(|p_i|) = 0$). Particles incident from both sides lose energy (on average) to the pump, which causes a decrease

in the total energy of each reservoir ($\Delta E^{L,R}(|p_i|) < 0$) and total energy of the system ($\Delta E^T(|p_i|) < 0$). The average energy changes of particles scattered into each reservoir are equal ($\Delta T^L(|p_i|) = \Delta T^R(|p_i|) < 0$) and each reservoir is cooled. Fig. 4.1(c) summarizes these results. Calculations show that the loss of energy to the pump decreases exponentially with $|p_i|$, a result that calls for a general proof.

4.4.3 Region II: Net left-to-right particle transport

($1.176 \lesssim |p_i| \leq 2$) This region is defined by the fact that all particles from the right are reflected by the static barrier, but some particles incident from the left gain enough energy from the pump to scatter into the right reservoir. Accordingly, the right-hand reservoir gains particles ($C_P(|p_i|) > 0$) and average energy per particle ($\Delta T^R(|p_i|) > 0$), and the reservoir is heated. The total energy of the reservoir increases ($\Delta E^R(|p_i|) > 0$).

Some particles which begin on the left scatter to the left, and the pump can change their energy. Over most of region II ($1.176 \lesssim |p_i| \lesssim 1.95$), the left-to-left scatterers gain energy from the pump (on average) ($\Delta T^L(|p_i|) > 0$), and temperature of the left reservoir increases. However at the high end of this region ($1.95 \lesssim |p_i| < 2$), the left-to-left scatterers lose energy (on average) to the pump ($\Delta T^L(|p_i|) < 0$), and the left reservoir is cooled.

The total energy change of this reservoir depends on the average energy change of left-scattered particles, and on the loss of particles to the right-hand reservoir. Over most of region II ($1.243 \lesssim |p_i| < 2$), there is a net loss of energy in the left-hand reservoir ($\Delta E^L(|p_i|) < 0$). However at the lower end of this region ($1.176 \lesssim |p_i| \lesssim 1.243$), the gain of energy of left-to-left scatterers exceeds the loss of energy associated with particle transport to the right, and the total energy in the left-hand reservoir rises ($\Delta E^L(|p_i|) > 0$).

Combining the energy changes of both reservoirs, the pump has added energy to the reservoirs for the entirety of region II ($\Delta E^T(|p_i|) > 0$). These results are summarized in

Fig 4.1(c).

4.4.4 Region III: Net right-to-left particle transport

($2 < |p_i| \lesssim 2.63$) This region is the most complex. For $|p_i| > 2$, for this pump, all particles incident from the right have enough energy to transmit past both barriers. Particles incident from the left initially have enough energy to get over the static barrier, but they may lose energy to the oscillating barrier, be reflected from the static barrier, and scatter into the left reservoir. Therefore the only possible direction of net particle transport is from right-to-left. Fig. 4.1(a) shows right-to-left particle transport ($C_P(|p_i|) < 0$) in the range $2 < |p_i| \lesssim 2.63$.

Particles which scatter to the right reservoir begin in the left reservoir. In the majority of this region ($2 < |p_i| \lesssim 2.616$) they (on average) gain energy from the pump ($\Delta T^R(|p_i|) > 0$), and the temperature in the right reservoir rises. Combining the gain of energy per particle with the loss of particles, the result is a loss of total energy in the right reservoir ($\Delta E^R(|p_i|) < 0$). In the remainder of region III, ($2.616 < |p_i| \lesssim 2.63$), the left-to-right scatterers lose energy to the pump (on average) ($\Delta T^R(|p_i|) < 0$), the right reservoir is cooled, and its total energy decreases ($\Delta E^R(|p_i|) < 0$) because of loss of particles and loss of average particle energy.

Particles which scatter to the left reservoir can begin in either reservoir. These particles on average lose energy to the pump ($\Delta T^L(|p_i|) < 0$), so the left reservoir is cooled. However its total energy rises ($\Delta E^L(|p_i|) > 0$) because scattering increases particle number in the reservoir. Examining both reservoirs together, over most of the lower portion of region III ($2 < |p_i| \lesssim 2.267$), the pump adds energy to the reservoirs, while over the remainder of the region ($2.267 \lesssim |p_i| \lesssim 2.63$), it removes energy from the reservoirs. Fig. 4.1(c) summarizes these results.

4.4.5 Averaging over energies

Thermodynamics (and physical intuition) tell us that if a pump is connected to a single reservoir (or two reservoirs with the same temperature, pressure, and chemical potential) then the net energy transfer can only go from the pump to the reservoirs if all incident energies are considered. Accordingly if we average the energy input $\Delta E^T(|p_i|)$ over a Maxwellian distribution at any temperature, that result must be nonnegative ($\int \Delta E^T(|p_i|) e^{-p_i^2/2mk_B T} dp \geq 0$). Scrutiny of $\Delta E^T(|p_i|)$ in Fig. 4.1(b) shows that this is satisfied in the example pump. This result is consistent with previous quantum studies showing that energy must go from pump to reservoirs (i.e., one cannot use such a pump to cool reservoirs). However if only finite bands of incident particle energies are considered, particles can (on average) give energy to the pump. Also the observation that at low incident particle energies (Region I), the net energy flow is from pump to particles must hold for any pump with multiple repulsive barriers, when at least one of them oscillates. This is another point that calls for a dynamical proof.

4.5 Remarks

We have by example established the following properties for our arbitrarily-selected pump:

- Such pumps can transfer energy from one reservoir to the other, and energy can be transferred from pump to particles or vice versa.
- A net change of energy in each reservoir can occur even if there is no net particle transport. The direction of energy change is distinct from the direction of particle transport.

- Such pumps can heat or cool one or both reservoirs, and the heating or cooling is distinct from the existence or direction of net particle transport and distinct from energy flow.
- At some incident energies, such pumps can generate net particle transport while at the same time particles give energy to the pump.

We can extend the conclusions drawn from this pump to all ballistic atom pumps that have multiple repulsive barriers, when at least one of them oscillates, because they all share the two mechanisms responsible for these conclusions: i.) such pumps can scatter monoenergetic particles incident from both reservoirs nonuniformly (i.e., such a pump can scatter a different number of particles into each reservoir), and ii.) such pumps modulate the energies of particles (i.e., energy is not conserved). We note that any change of barrier parameters for a diode can quantitatively affect properties such as the magnitude and direction of net particle transport and energy and heat flow, but no choice of diode parameters eliminates mechanisms i.) and ii.) above. Furthermore allowing a second barrier to oscillate also does not inhibit these mechanisms; therefore, conclusions (A)-(D) apply to all ballistic atom pumps that have multiple repulsive barriers, when one or more of them oscillate.

CHAPTER 5

Homotopic Lobe Dynamics (HLD)

Here we switch our attention to classical particle transport through the barrier region in ballistic atom pumps. As previously stated, the presence of two or more barriers that are separated leads to classically-chaotic trajectories. We have seen that even very slight differences in initial position can lead to dramatically different scattering properties; for example, slightly perturbing the initial position of a particle that reflects can cause transmission, or vice versa.

Fig. 5.1 shows what we call “continuous escape times” as a function of initial position. The plots show initial positions whose classical trajectories spend time temporarily trapped between two oscillating Gaussian barriers. The blue and red curves show the amount of time necessary for trajectories which began at each initial position to escape the barrier region, i.e. the time to finally scatter over one of the two barriers after becoming temporarily trapped between them. Each “icicle” corresponds to a pulse of atoms escaping the barrier region; red icicles represent trajectories that finally scatter over the left barrier, and blue icicles correspond to trajectories that ultimately scatter over the right barrier.

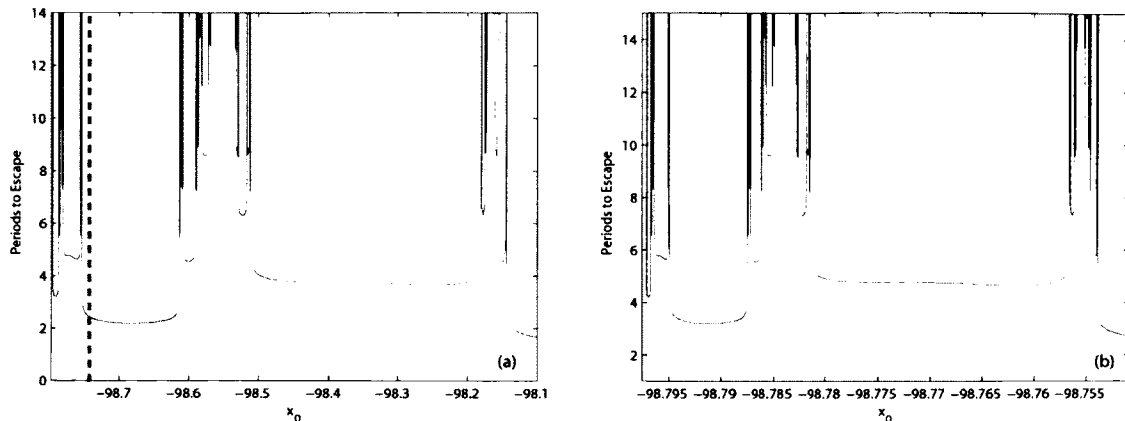


FIG. 5.1: Continuous escape times for particles temporarily trapped between two oscillating, Gaussian-shaped barriers. Blue icicles correspond to initial positions that ultimately scatter over the right barrier, and red icicles correspond to initial positions that ultimately scatter over the left barrier.

Fig. 5.1(b) shows a zoom of Fig. 5.1(a) between the left-most edge and the dashed line. Comparing the two plots, we see that a very similar structure occurs, but they begin at different times, and occur on a different length scale. If we continued by zooming into the left portion of Fig. 5.1(b), we would once again find a similar structure that occurs on a different length scale, and that begins at a different time. While this behavior suggests that escape-time plots will exhibit regular fractal structure, this repeated magnification process shows that not all escape segments fit into this regular, self-similar structure. These escape segments tend to disrupt the self-similar nature of these plots (see Fig. 5.8). For this reason, we say that escape-time plots show a type of fractal structure.

We seek to understand the patterns seen in these escape-time plots, as well as why they do not display full fractal structure. We gain insight into these properties by analyzing the system from a topological perspective. The next two chapters are devoted to this analysis. In this chapter a brief, informal introduction to the topological concepts that

we use is given. This chapter gives an overview of an existing theory that reveals details about escape-time plots; the next chapter generalizes and implements this theory on the double-barrier ballistic atom pump. This type of analysis is general and makes use of structures seen in a surface of section (defined below) for the given system of interest. This theory allows one to make predictions about the escape of trajectories from defined regions of the phase plane. In this chapter, we define a surface of section, discuss the geometry of the phase plane for an example system, and discuss each step necessary to construct a type of symbolic dynamics that gives information about orbits in the phase plane. Finally, we discuss an important theorem which describes some of the structure seen in plots illustrating the amount of time it takes for trajectories to escape a defined region of the phase plane.

The general procedure (discussed below) for this type of analysis is to compute stable and unstable manifolds of an unstable fixed point in the phase plane, record important information from the structure they create, assign labels to certain segments of the unstable manifold, characterize a line of initial conditions in terms of these labels, and perform a symbolic dynamics on these labels. It will be shown that the symbolic dynamics allows one to predict how certain segments of the line of initial conditions escape from a defined region of the phase plane, and that these escape segments are forced to display a type of self-similar behavior.

5.1 Phase Space

We begin the analysis by examining phase space for a potential energy consisting of two static Gaussian barriers of the same amplitude and width, as shown in Fig. 5.2. The barriers are centered at $x = \pm 5$. Because the barriers are static, they do not modulate the energy of particle trajectories. At high energies (corresponding to larger magnitudes of p in

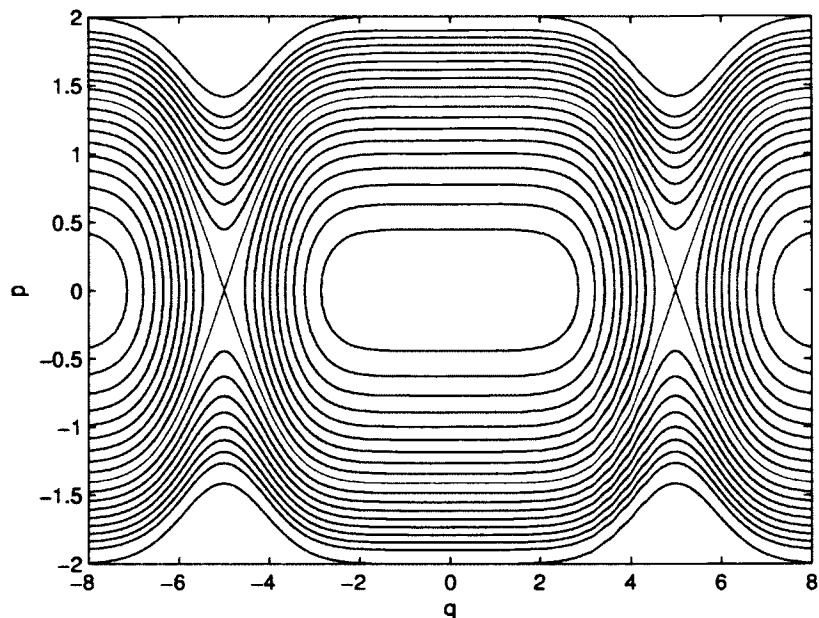


FIG. 5.2: Phase space for two static Gaussian potentials.

the figure), particles transmit over each barrier. When passing over a barrier, each trajectories' energy remains constant, but its momentum decreases due to energy conservation. At low energies between the barriers, bound orbits exist; these orbits represent particles that do not have enough energy to transmit over either barrier, and remain trapped between them. A stable fixed point exists at $(q, p) = (0, 0)$. This stable fixed point represents an orbit that remains stationary, and a slight perturbation will cause it to stay close to the fixed point. At low energies on both sides of the barriers, particles approach the barriers and reflect. There are two unstable fixed points at $(q, p) = (\pm 5, 0)$. These unstable fixed points correspond to orbits that sit on top of each barrier. A slight perturbation of these orbits causes them to fall away from the top of the barrier. These isolines are shown in red in the figure, and they separate the regions of bound and unbound trajectories. If an orbit is perturbed from one of the unstable fixed points and falls into the region between

the barriers, it asymptotically approaches the other unstable fixed point; it cannot leave the region between the barriers, and has just enough energy to make it to the top of the other barrier.

We next examine phase space for a single static barrier which has a steep repulsive “wall” to one side, and a well in between. An example potential of this type is $V(x) = x - x^3 + 2e^{-(x-1)^2/2}$, and it is plotted in Fig. 5.3(a). This potential has a stable fixed point which corresponds to a stationary particle in the bottom of the well in the potential. There is another fixed point at $(q, p) \approx (0.72, 0)$. This fixed point is unstable, and it corresponds to a particle sitting on top of the barrier. A slight perturbation of this orbit results in different behavior than in the previous case of two static barriers. Previously, we saw that a trajectory falling between the two barriers would asymptotically approach the other unstable fixed point (top of the other barrier), but in this case, the trajectory asymptotically approaches the same unstable fixed point. This orbit is the closed “loop” of the red curve in Fig. 5.3(b), and a trajectory traverses it in clockwise fashion. As in the previous example, this orbit separates the regions of bound and unbound motion.

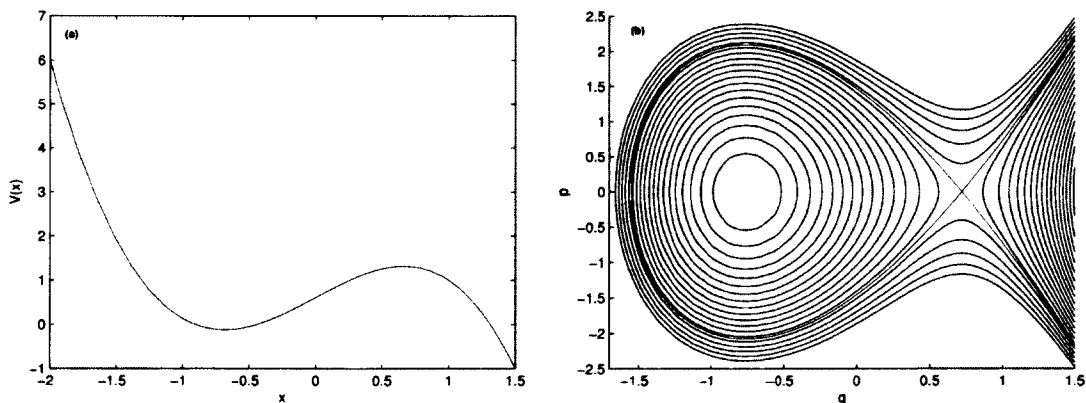


FIG. 5.3: The potential $V(x) = x - x^3 + 2e^{-(x-1)^2/2}$ and its corresponding phase space.

If we now add time-dependence to this potential, e.g.

$$V(x, t) = x - x^3 + 2(1 + A \cos(\omega t)) e^{-(x-1)^2/2}, \quad (5.1)$$

the phase space of the system changes. In order to study the phase-space of this time-dependent system, we introduce a surface of section. A surface of section is a tool for studying trajectories in reduced dimension. Typically, the method of constructing them is to choose a surface in the phase space, and “strobe” (record) trajectories each time they pass through this surface in the same direction. For the potential in Eq. 5.1, we may strobe trajectories one time per oscillation cycle of the barrier, and we strobe at the same barrier phase each cycle. In the double-barrier ballistic atom pump (discussed in the next chapter), we again strobe trajectories once each period of the barrier frequency, and at the same time within each period.

By using a surface of section to study the system, we have reduced the continuous system to a discrete map in the phase plane. For example, a trajectory at (x_0, p_0) at the first strobe time is mapped forward to (x_1, p_1) at the next strobe time, which is then mapped to (x_2, p_2) , etc. The maps we discuss in this thesis are two-dimensional, and conserve area and orientation in the phase plane.

A surface of section for the potential $V(x, t) = x - x^3 + 2(1 + A \cos(\omega t)) e^{-(x-1)^2/2}$ results in a complicated structure in the phase plane that is geometrically and topologically similar to the one pictured in Fig. 5.4. The reader is encouraged to compare Figs. 5.3(b) and Fig. 5.4. Each has one stable and one unstable fixed point (the unstable fixed point in Fig. 5.4 is labeled \mathbf{z}_x). The closed “loop” of the red curve in Fig. 5.3(b) should be compared to the thick curve in Fig. 5.4 (labeled \mathcal{O}). In both plots, the curves leave the unstable fixed point leftward and downward, turn in clockwise fashion, and asymptotically approach the same unstable fixed point. However in Fig. 5.4, the curve can be seen to

oscillate rapidly as it approaches the unstable fixed point, in contrast to the red curve in Fig. 5.3(b). Fig. 5.4 also has a curve (labeled \mathcal{I}) that approaches the unstable fixed point from the upper left, and if it is traced backwards, it can be seen to approach the unstable fixed point from the lower left while rapidly oscillating. These features are hallmarks of a “homoclinic tangle,” which we turn our attention in the next section.

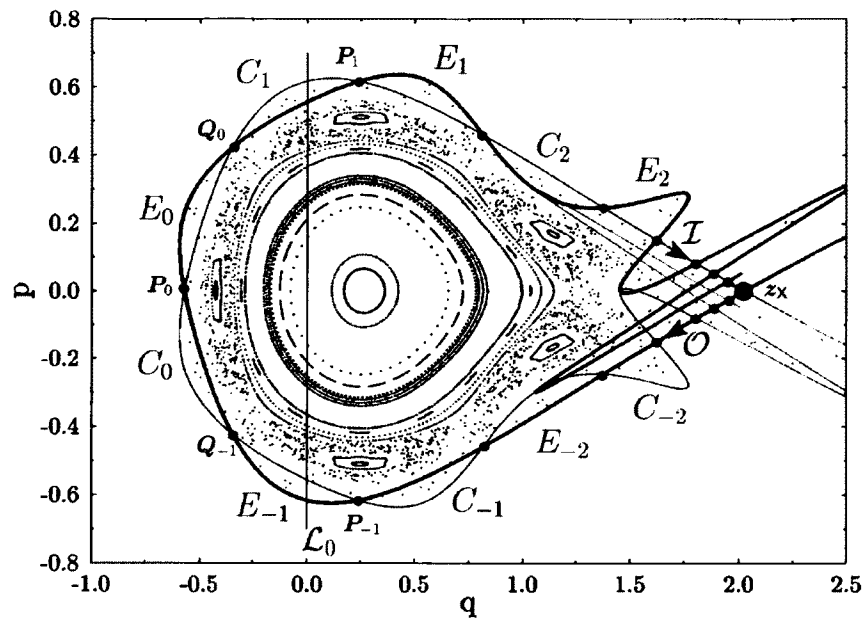


FIG. 5.4: An example homoclinic tangle. This figure originally appeared in [55].

5.2 Homoclinic Tangles

The remainder of this chapter develops the topological concepts using a map that is discrete, two-dimensional, and area- and orientation-conserving, but which has a simpler geometry than the double-barrier system. A surface of section of the system we use to develop the techniques is shown in Fig. 5.4. The map discussed in the remainder of this chapter corresponds to the classical description of chaotic ionization of a hydrogen atom

in electric and magnetic fields. When a hydrogen atom is ionized by a short pulse of light, electrons have an approximately fixed energy, but uncontrolled direction. The topological concepts introduced in this chapter allow one to make predictions about the time required for an electron to reach a detector as a function of its initial direction. The escape-time plots for this map are similar in structure to those seen for the double-barrier ballistic atom pump (Fig. 5.1). The steps we follow are to: i.) identify a region of the phase space representing the atom, and ii.) develop a theory that predicts how long different points inside this region take to escape. The mathematical concepts are the primary focus of this chapter, however, because escape from a tangle in phase space governs transport in many systems. The reader may choose to relate the following discussion to the potential $V(x, t) = x - x^3 + 2(1 + A \cos(\omega t)) e^{-(x-1)^2/2}$, as the geometry of its phase space is similar to the one discussed here.

Consider a hyperbolic (unstable) fixed point, \mathbf{z}_x , in the phase plane. This unstable fixed point has a stable manifold, S . A stable manifold is defined by its asymptotic behavior; it is an invariant curve containing all orbits that map to the unstable fixed point as $t \rightarrow +\infty$. More formally, $\forall x \in S, \lim_{n \rightarrow \infty} M^{+n}(x) = \mathbf{z}_x$, where M is the map and \mathbf{z}_x is the unstable fixed point. The unstable fixed point also has an unstable manifold U , which is an invariant curve containing all orbits that map to the fixed point \mathbf{z}_x as $t \rightarrow -\infty$, *i.e.*, for all $\forall x \in U, \lim_{n \rightarrow \infty} M^{-n}(x) = \mathbf{z}_x$. (If the reader is still thinking of the potential $V(x, t) = x - x^3 + 2(1 + A \cos(\omega t)) e^{-(x-1)^2/2}$, a stable manifold physically represents particle trajectories that asymptotically approach the unstable fixed point on top of the barrier as $t \rightarrow +\infty$, and unstable manifolds represent particle trajectories that asymptotically approach the top of the barrier as $t \rightarrow -\infty$). The curves \mathcal{O} and \mathcal{I} are unstable and stable manifolds, respectively, of the hyperbolic fixed point \mathbf{z}_x in Fig. 5.4.

An unstable manifold cannot intersect itself (or any other unstable manifold), and a stable manifold cannot intersect itself (or any other stable manifold), but stable and

unstable manifolds can intersect each other. Due to their asymptotic behavior, if a stable and an unstable manifold do intersect once, they must intersect each other an infinite number of times because each intersection point maps to another intersection point. These intersections are called a homoclinic orbit if the manifolds map asymptotically to the same hyperbolic fixed point.

We will limit the discussion in this section to stable and unstable manifolds which map asymptotically to the same fixed point \mathbf{z}_x . Furthermore our discussion is limited to a case in which one branch of the stable manifold, and one branch of the unstable manifold, go to infinity without intersecting any other manifold. When the remaining branches of these manifolds intersect, a homoclinic orbit is present, and the manifolds collectively create a very complex structure in the phase plane called a homoclinic tangle. Figure 5.5 shows a homoclinic tangle with increasing lengths of the stable and unstable manifolds shown, and the figure should be read in clockwise fashion. The purpose of this figure is to introduce the reader to a typical homoclinic tangle, and how they govern trajectories in the phase plane. A homoclinic tangle in two dimensions, like the one shown in Fig. 5.5, can be computationally constructed by placing initial conditions on the appropriate eigenvectors passing through the hyperbolic fixed point. The stable manifold is generated by mapping the appropriate points backward under the map, and the unstable manifold is computed by mapping the appropriate points forward.

Fig. 5.5(a) shows early iterates of the two manifolds; the upper (red) curve is the stable manifold, and the lower (blue) blue curve is the unstable manifold. (By “early iterates” we mean “early backward iterates” for the stable manifold, and “early forward iterates” for the unstable manifold). They intersect transversely at a point labeled P_0 . Together, these segments of the manifolds enclose a region which we call the “complex” or “resonance zone.” More formally, the segments $\mathbb{S} = S[P_0, \mathbf{z}_x]$ and $\mathbb{U} = U[\mathbf{z}_x, P_0]$, where S and U are the stable and unstable manifolds, bound the complex. The physical meaning

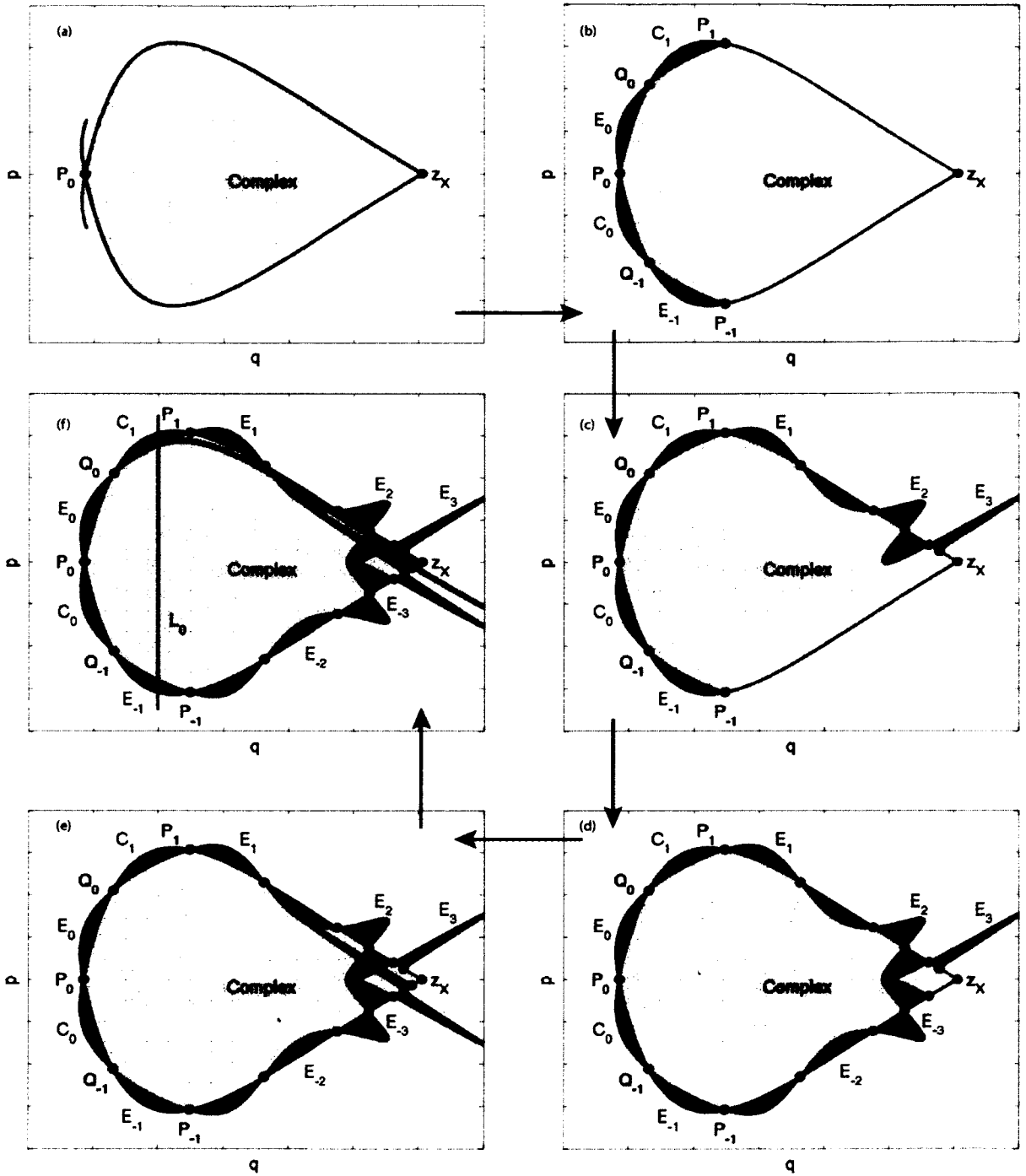


FIG. 5.5: Development of a homoclinic tangle. Plots courtesy of Kevin A. Mitchell.

Symbol	Meaning
S	Stable manifold $\rightarrow \mathbf{z}_x$ from the right as $t \rightarrow \infty$
U	Unstable manifold $\rightarrow \mathbf{z}_x$ from the right as $t \rightarrow -\infty$
\mathbb{S}	S from P_0 to \mathbf{z}_x ; part of complex boundary
\mathbb{U}	U from \mathbf{z}_x to P_0 ; part of complex boundary
S_0	$S[P_0, P_1]$; fundamental segment of S
U_0	$U[P_{-1}, P_0]$; fundamental segment of U
S_n	$S[P_n, P_{n+1}]$; n^{th} iterate of S_0
C_n and E_n ($-\infty < n < \infty$)	Capture and escape lobes
P_n and Q_n ($-\infty < n < \infty$)	Homoclinic intersections

TABLE 5.1: Notation used to describe manifold segments.

of the complex is problem-specific; for this map, the complex represents an atom, while in the double-barrier system, the complex represents the region between the potential-energy barriers. If the reader is still thinking of the time-dependent potential given by Eq. 5.1, the complex represents the region between the oscillating barrier and the steep “wall” of the potential. The complex is shaded and labeled in Fig. 5.5. Generally, we are interested in the amount of time (iterates of the map) it takes trajectories to escape the complex after entering it, and we will see that properties of the manifolds can be used to make predictions about sequences of escaping orbits. If we iterate the manifolds once more, as shown in Fig. 5.5(b), we see that additional homoclinic intersections occur. These new intersections are labeled P_{-1} , Q_{-1} , Q_0 , and P_1 . Points Q_{-1} and Q_0 , and also P_{-1} , P_0 , P_1 , are points along two homoclinic orbits. The point Q_{-1} maps forward to the point Q_0 , and $M(P_{-1}) = P_0$, $M(P_0) = P_1$, etc. We define the segment of the stable manifold $S[P_0, P_1]$ as the *fundamental segment of the stable manifold*, S_0 , and the segment of the unstable manifold $U[P_{-1}, P_0]$ as the *fundamental segment of the unstable manifold*, U_0 . Table 5.1 lists the notation used in this chapter.

The segments of stable and unstable manifolds between two successive points of the homoclinic orbit along \mathbb{S} and \mathbb{U} bound areas which we call “lobes.” For example, the stable and unstable manifold segments connecting points Q_{-1} and P_0 bound a lobe we call C_0 ,

which is shaded in green. By comparing Figs. 5.5(a) and (b), one can see that C_0 lies outside of the shaded complex. However, its forward iterate, the green lobe labeled C_1 , lies inside the complex. This is a very important feature of a homoclinic tangle: any orbit inside the lobe C_0 at a given iterate n will be inside the lobe C_1 at iterate $n + 1$, *i.e.*, a trajectory enters the complex by being mapped from lobe to C_0 to C_1 . In the present case, this is the only way for any orbit to enter the complex. We again stress that this map is area-preserving, so the lobes C_0 and C_1 have equal areas. We use C_n to label these lobes because they represent the “capture” of orbits into the complex.

Another important series of lobes are labeled E_n . In Fig. 5.5(b), the stable and unstable manifold segments connecting points P_{-1} and Q_{-1} bound a lobe denoted E_{-1} . By comparing Figs. 5.5(a) and (b), one can see that the lobe E_{-1} is inside the complex. However its forward iterate, the lobe labeled E_0 , is outside of the complex. This mapping represents how trajectories are mapped from inside to outside of the complex (“escape”); any trajectory in E_{-1} at iterate n will be inside the complex, but will be mapped out of the complex (and into E_0) at iterate $n + 1$. In the present case, this mapping from E_{-1} to E_0 is the only way an orbit can escape the complex.

Fig. 5.5(c) shows two more forward iterates of the unstable manifold. The lobe E_0 maps to E_1 , which maps to E_2 , which maps to E_3 . Generally, $M(E_n) = E_{n+1}$. The important feature of this plot is that once an orbit is inside E_0 , all of its forward iterates remain outside of the complex. For that reason, we say that any orbit has escaped the complex permanently once it is in E_0 . (Some types of tangles do permit “recapture,” but neither this example nor the one discussed in the next chapter that governs transport in the double-barrier ballistic atom pump permit any type of recapture method).

Fig. 5.5(d) shows two more backward iterates of the stable manifold. E_n lobes are shaded in purple, and C_n lobes are shaded in green. The important feature of this plot is that E_{-3} maps forward to E_{-2} which maps forward to E_{-1} . Since the mapping from

E_{-1} to E_0 maps orbits from inside the complex to outside of it, any trajectory in lobe E_{-n} will escape the complex n iterates later. Fig. 5.5(e) shows another backward iterate of the stable manifold, and the lobe E_{-4} can be seen (not labeled). Of note here is the effect of the map on the lobes: since the homoclinic orbit points approaching the hyperbolic fixed point \mathbf{z}_x are squeezed closer together with each iterate of the map, and since the map is area-preserving, the map stretches the lobes in order to preserve area. Fig. 5.5(f) shows another iterate of the stable manifold, and the lobe E_{-5} (not labeled). There are two intersections between the stable manifold segment bounding lobe E_{-5} and the arbitrarily-drawn line of initial conditions, L_0 , *i.e.*, a segment of L_0 is inside the lobe E_{-5} . Since any trajectory in E_{-5} will escape the complex five iterates later, the segment of L_0 in E_{-5} will escape the complex five iterates later. We can now see that if we can identify intersections between arbitrary lines of initial conditions L_0 and E_{-n} lobes, we can identify when segments of L_0 will escape. While this may seem like a laborious method of identifying escape segments, we will see that, from a topological perspective, the existence of escape segments at some iterate of the map forces later escape segments to occur, and that these forced escape segments have a predictable pattern.

Figure 5.6 (adapted from [55]) shows escape segments typical of an arbitrary line of initial conditions that is inside the complex of a homoclinic tangle. The horizontal axis, from left-to-right, represents increasing iterates of the map, and the vertical axis represents position along the line of initial conditions. Each escape segment corresponds to a portion of L_0 that escapes from the complex on the n^{th} iterate.

5.3 Homotopic Lobe Dynamics

Homotopic Lobe Dynamics is a topological theory based on properties of the homoclinic tangle that allows one to understand and predict some of the structure of escape

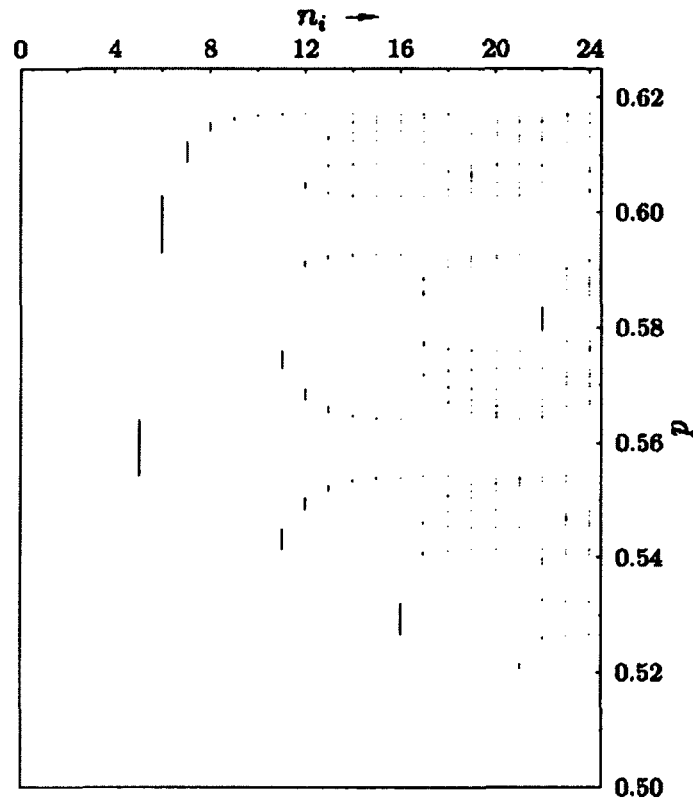


FIG. 5.6: Escape segments of an arbitrary L_0 inside a typical homoclinic tangle. This figure is adapted from a plot that originally appeared in [55].

segments like those seen in Fig. 5.6. Here we give an overview of the theory.

5.3.1 Fundamental Segments

To begin the theory, we use the fundamental segment of the stable manifold S_0 , and select an arbitrary number of times, J , to iterate the fundamental unstable segment, U_0 , forward. The choice of J is up to the researcher, but higher J values can lead to an increase in the amount of initial topological information used, which can in turn yield more predicted escape segments at higher iterates.

5.3.2 Neighbors

We define two homoclinic intersections, x and x' , to be “neighbors” if both of the open stable and unstable manifold segments connecting them, $S(x, x')$ and $U(x, x')$, contain no other homoclinic intersections. This simple definition implies that the open segments $S(x, x')$ and $U(x, x')$ bound a region that no stable manifold or unstable manifold enters (if a manifold of either type entered this region, x and x' would not satisfy the definition of neighbors because the manifold segments connecting them would contain homoclinic intersections). This type of manifold-excluding region is a key component of HLD, as we will later characterize manifold segments relative to how they wind around these manifold-excluding regions.

In reality, it is often impossible to ascertain whether or not two homoclinic intersections, x and x' , meet the definition of being neighbors to arbitrarily high iterates of the map. Therefore, we use the concept of “ J -neighbors”.

Starting with the segment $\mathbb{U} = U[\mathbf{z}_x, P_0]$ of the unstable manifold, we then iterate the fundamental segment U_0 forward a selected number of times, J . We will use information gleaned from this curve to predict aspects of future iterates. Two homoclinic intersections x and x' are said to be J -neighbors if they satisfy two conditions:

- Up to iterate J , both open segments $U(x, x')$ and $S(x, x')$ connecting them contain no homoclinic intersections, and
- Both have transition number $N \leq J$, where the transition number is the number of iterates N such that $M^{N+m}(z)$ lies on S_0 , when $M^m(z)$ lies on U_0 .

It should be noted that two homoclinic intersections may meet the definition of being J -neighbors for $J \leq j$, but are no longer J -neighbors for $j > J$. For example, a pair of homoclinic intersections may be 1-neighbors, 2-neighbors, 3-neighbors, but not 4-neighbors,

5-neighbors, etc. In Fig. 5.7(a), the points P_0 and Q_1 are 1-neighbors, 2-neighbors, and 3-neighbors, but are not 4-neighbors because when $J = 4$, the points α_4 and β_4 intersect the segment $S(P_0, Q_1)$ connecting P_0 and Q_1 . However, the points α_4 and β_4 are themselves 4-neighbors.

5.3.3 Holes

As mentioned previously, all pair of neighbors are connected by open segments of the manifolds $U(x, x')$ and $S(x, x')$ that bound a domain into which no manifold can enter. Similarly, each pair of J -neighbors are associated with a domain into which *it appears* no manifold can enter. A critical concept of HLD is to punch “holes” in the plane inside of these manifold-excluding domains. The map M then acts as a map of these holes, just as it does on directed curves in the phase plane.

In the first work on this subject [56], the entire manifold-excluding domains were defined as holes. In later papers [67, 106, 127], the hole was represented by a point. Here we take the latter approach; each hole is represented by a point that is both (i) inside the domain bounded by $U(x, x')$ and $S(x, x')$, and (ii) arbitrarily close to either x or x' . For each hole punched next to a point x along S_0 , holes are also punched at $M^n(x)$ for $-\infty < n < \infty$, leading to a sequence of holes $H_n = M^n(H_0)$ in the phase plane. This sequence of holes approaches the hyperbolic fixed point \mathbf{z}_x in the forward direction along \mathbb{S} , and approaches \mathbf{z}_x in the backward direction along \mathbb{U} . In between, there is only a finite number of holes within the complex that are a finite distance away from \mathbb{S} and \mathbb{U} . We characterize segments of the unstable manifold using homotopy theory, according to how they wind around these holes.

Fig. 5.7 shows a sequence of holes for a selected qualitative rendering of a homoclinic tangle using $J = 4$. The hyperbolic fixed point is labeled \mathbf{z}_x . The blue curve is the

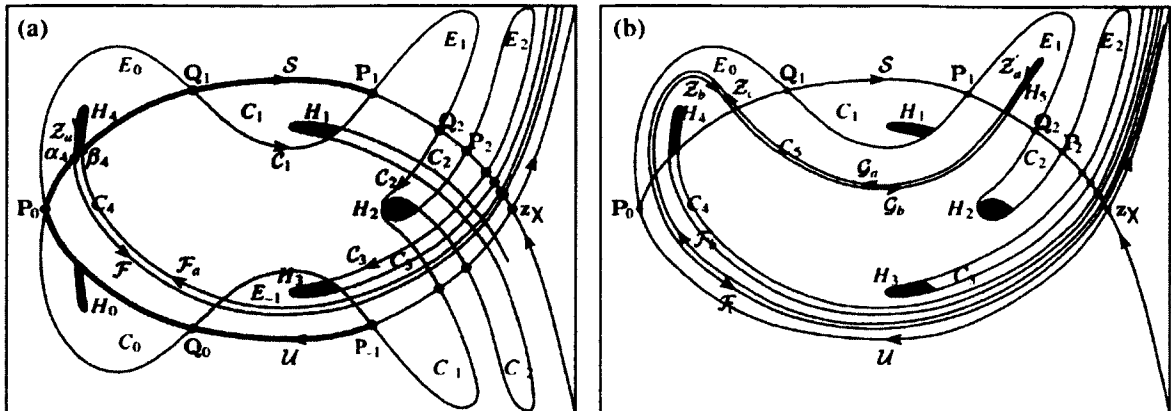


FIG. 5.7: Holes punctured in the phase plane for use in HLD in the context of a homoclinic tangle. See the text for additional details. This plot originally appeared in [107].

unstable manifold, and the red curve is the stable manifold. The fundamental segments U_0 and S_0 are the thick segments of these manifolds. The complex is shaded light blue in (a). Homoclinic intersections along \mathbb{S} and \mathbb{U} are represented by black dots. In Fig. 5.7(a), the homoclinic intersections α_4 and β_4 are 4-neighbors. The open segments $U(\alpha_4, \beta_4)$ and $S(\alpha_4, \beta_4)$ connecting them bound a domain into which it appears that no manifold can enter; this domain is shaded in purple, and is labeled H_4 . Its backward iterates $M^n(H_4)$ for $n = -1, -2, -3, -4$, *i.e.*, H_3, H_2, H_1 , and H_0 are also labeled and shaded in purple. Fig. 5.7(b) shows the same information with most of the stable manifold omitted, and also shows $M(H_4) = H_5$, which is shaded in purple.

5.3.4 Bridges

Here we consider directed curves in the punctured plane that begin and end on $\mathbb{S} = S[P_0, z_x]$, but do not otherwise intersect \mathbb{S} . We say that two such directed curves are homotopic if they can be continuously distorted into each other without (i) their endpoints leaving \mathbb{S} and (ii) passing through a hole. We define a homotopy-class as a set of all paths

homotopic to one another. The set of all homotopy-classes defines a group called the fundamental group. The product $[A] = [B][C]$ of path classes $[B]$ and $[C]$ is constructed by following $[B]$ from its beginning point to end point, following \mathbb{S} to the beginning of $[C]$, and then following $[C]$. The inverse of a homotopy class, $[C]^{-1}$, is defined by reversing the direction of $[C]$. The identity homotopy class consists of all paths that can be shrunk to a point.

With these definitions, any segment of the unstable manifold beginning and ending on \mathbb{S} , but not otherwise intersecting \mathbb{S} , has a well-defined homotopy class. We call such segments bridges. The reader may think of each bridge within the context of a homoclinic tangle as one of the two boundaries of a lobe. It should be noted that segments of S can intersect bridges (see Fig. 5.7(a)); the restriction on intersections between bridges and S only applies to the segment \mathbb{S} . After iterating U_0 forward J times, identifying J -neighbors, and puncturing and mapping holes in the phase plane, the next step is to characterize how each bridge of the unstable manifold winds around these holes. Each bridge inherits the direction of U . We say a bridge “surrounds” a hole if the hole lies within the area bounded by the bridge and the segment of \mathbb{S} connecting the bridge’s endpoints. If a bridge surrounds a hole, its forward iterate must surround the forward iterate of that hole, and the bridge’s endpoints must map closer to the hyperbolic fixed point along \mathbb{S} .

Each bridge class of the unstable manifold is given a symbol, e.g., c_1 . Fig. 5.7 shows the symbols given to specific bridges (in script italics). Since the bridge class c_1 surrounds hole H_1 and $M(H_1) = H_2$, the forward mapping of c_1 surrounds H_2 , and its endpoints lie closer to \mathbf{z}_x along \mathbb{S} than the endpoints of c_1 . In the figure, the $M(c_1) = c_2$ and $M(c_2) = c_3$. Since c_3 surrounds the hole H_3 , the forward mapping of c_3 must surround the forward mapping of H_3 .

Something new happens in the forward mapping of c_3 . Since a portion of the bridge class c_3 is inside the lobe E_{-1} , a segment of the forward mapping of c_3 lies inside lobe E_0 ,

which is outside of the complex. Therefore $M(c_3)$ must intersect \mathbb{S} in two places in addition to its endpoints. When this occurs, the forward mapping of c_3 forms three distinct bridges. In the diagram, these bridges are labeled F_a , Z_a , and F , and we say that $M(c_3) = F_a Z_a F$ (we follow the direction of the curve by reading left-to-right). Fig. 5.7(b) shows the forward mapping of $F_a Z_a F$, which is $M(F_a Z_a F) = F_b Z_b G_b Z'_a G_a Z_c F_c$. This curve's endpoints lie closer to the hyperbolic fixed point \mathbf{z}_x along \mathbb{S} than its previous iterate, but must enter the lobe E_1 without intersecting any portion of the unstable manifold. As can be seen in the plot, the only way for it to do that is to go "around" its previous iterate ($F_a Z_a F$) by first remaining below it inside the complex, entering the lobe E_0 , re-entering the complex, and entering lobe E_1 . It must traverse a similar path (in opposite direction) in order for its final endpoint to lie closer to \mathbf{z}_x . This stretching and folding of the unstable manifold is an important aspect of any homoclinic tangle, and is characteristic of chaotic systems.

Let us now simplify the notation from the preceding paragraph. Fig. 5.7 shows that the bridges F and F_c can be continuously distorted into one another without their endpoints leaving \mathbb{S} or passing through a hole, and they are homotopic to one another. We use the symbol $f = F$ for this homotopy class. The bridges F_a and F_b can be distorted into F or F_c if their orientation is reversed, so they are represented as f^{-1} . (Note that the direction of f goes from left-to-right in the plot). We also see that G_b is homotopic to c_1 , and we use the symbol c_1 for this homotopy class. G_a is thus represented c_1^{-1} because it has the opposite direction than c_1 . Finally, the bridges Z_a and Z_c are homotopic to one another, and the bridge Z_b is their homotopic inverse. Let us denote this homotopy class as $u_0 = Z_b$, so Z_a and Z_c are thus represented by u_0^{-1} . The advantage of using homotopy classes instead of individual bridges should be obvious: one has to keep track of fewer symbols, and all segments homotopic to one another evolve in a topologically-equivalent manner under the map.

5.3.5 Symbolic Dynamics

Since all bridge classes are represented by a symbol, the development of the homoclinic tangle can be represented by a dynamics on the symbols. The resulting symbolic dynamics reveals the structure of the homoclinic tangle that is *forced* to occur by the initial topological information used, i.e., the number of holes punched in the plane. The dynamics discussed in the previous chapter can be represented in compact form via

- $M(c_1) = c_2,$
- $M(c_2) = c_3,$
- $M(c_3) = f^{-1}u_0^{-1}f,$
- $M(f) = c_1^{-1}u_0^{-1}f,$
- $M(u_n) = u_{n+1}.$

The most important of this symbolic dynamics is that the symbol u_0 (and its inverse u_0^{-1}) represents a segment of the unstable manifold that escapes at the given iterate. If we take a section of the unstable manifold and use it as a line of initial conditions, we can use this symbolic dynamics to determine how many escape segments are forced to occur at each iterate of the map. To see how, let us use the segment $U_1 = M(U_0)$ as a line of initial conditions. The curve $L_0 = U_1$ is $L_0 = M(U[P_{-1}, P_0]) = U[P_0, P_1]$. By examining Fig. 5.7, we see that $L_0 = U_1$ can be expressed in terms of bridge classes as $L_0 = U_1 = u_0c_1$. We can iterate this curve symbolically an arbitrary number of times by iterating each symbol according to the dynamics above; the first few iterates are

- $L_0 = u_0c_1$
- $L_1 = u_1c_2$

- $L_2 = u_2 c_3$
- $L_3 = u_3 f^{-1} u_0^{-1} f$
- $L_4 = u_4 f^{-1} u_0 c_1 u_1^{-1} c_1^{-1} u_0^{-1} f$

and so on. The u_0 in L_0 means that a portion of the initial condition line is already outside the complex. The forward iterate of this portion outside of the complex appears as u_1 in L_1 . Generally, the symbols u_k and u_k^{-1} in L_n represent segments that escape at the $n - k$ iterate. The appearance of u_0^{-1} in L_3 means that a new escape segment is forced to occur at the third iterate. L_4 has a u_0 symbol that appears between the u_4 and u_1^{-1} symbols (i.e., between the segments that escaped at the zero and third iterates). In this fashion, we see that the symbolic dynamics predicts the relative order of escape segments along L_0 as well as the number forced to occur at each iterate. We also see that L_4 has a u_0^{-1} after u_1^{-1} , so there are two new escape segments at the fourth iterate.

For arbitrary lines of initial conditions that begin and end on \mathbb{S} , and which do not pass through a hole, a minimal set of topologically-forced escape segments can be predicted via the symbolic dynamics above. The steps for doing so are: (i) compute the forward mapping of U_0 J times, (ii) identify all pairs of J -neighbors, (iii) punch holes in the phase plane where appropriate, and map the holes accordingly, (iv) identify all bridge classes of the unstable manifold and assign each class a symbol, (v) determine the symbolic dynamics of the map on the bridge classes (vi) decompose the line of initial conditions L_0 and express it as a product of bridge classes, and (vii) symbolically iterate L_0 an arbitrary number of times.

5.3.6 Epistrophes

We state here without proof part of an important theorem which arises due to the stretching of manifolds by the map in the phase plane. For a detailed proof of this theorem, see [55]. This theorem assumes that the map M has all of the following properties:

- The map M is an analytic area- and orientation-preserving diffeomorphism of an open subset of the phase plane,
- The map M has an unstable fixed point z_x ,
- One branch of each of the stable and unstable manifolds goes to infinity without intersecting any other stable or unstable manifold, and one branch of the stable and unstable manifolds intersect each other transversely,
- In the initial development of the tangle, the stable and unstable manifolds intersect only once between P_0 and P_1 ,
- All trajectories, once inside the lobe E_0 , are mapped forward away from the complex (i.e., are not “recaptured”).

The map M discussed in this section meets all of these criteria, and the following theorem is therefore applicable. When these criteria are met, the following theorem is true.

Epistrophe Theorem

Let z_s be any transverse intersection between S and a differentiable curve of initial conditions L_0 . For each $k > 0$ choose the escape segment $\epsilon_k \cap L_0 \cap E_{-k}$ closest to z_s , as measured along L_0 . Then there is some k_0 such that for all $k \geq k_0$, an escape segment ϵ_k exists and these segments ϵ_k converge monotonically upon z_s , (i.e., the distance between z_s and ϵ_k decreases monotonically).

This theorem tells us that an infinite sequence of escape segments converges to each endpoint of every escape segment; we call these sequences epistrophes. Furthermore [55] also proves that these infinite sequences decrease geometrically in the asymptotic limit, and that different epistrophes differ from one another by an overall scale factor. Epistrophes are a direct consequence of the manner in which this type of map M stretches the manifolds; it tells us how the E_{-k} lobes are stretched. Since intersections between E_{-k} lobes and L_0 escape the complex k iterates later, this information thus yields the structure of escape segments.

Epistrophes have several important properties: (i) beginning at a certain iterate, each epistrophe has one escape segment at all later iterates, (ii) each epistrophe converges to a point on L_0 , (iii) within any epistrophe, the lengths of escape segments at higher iterates decrease geometrically, and the ratio of successive lengths converges to the largest eigenvalue of the unstable fixed point \mathbf{z}_x (the Liapunov factor).

Figure 5.8 shows the same escape-time plot seen in Fig. 5.6, and several prominent epistrophes are denoted by red arrows. The “tail” of each epistrophe (moving toward the right part of the plot) can be seen to converge upon the endpoint of an escape segment that escaped at an earlier iterate. Thus, the Epistrophe Theorem implies a type of self-similarity in escape-time plots.

On the other hand, the beginning of each epistrophe is not described by the Epistrophe Theorem. HLD predicts a minimal set of escape segments forced by the amount of initial topological information, and the Epistrophe Theorem thus tells us how epistrophes converge upon the ends of these predicted escape segments. In computations, however, escape segments which are not forced to occur by the initial topological information used in HLD always appear. We call these unpredicted escape segments “strophes.” Several strophes are labeled with green asterisks in Fig. 5.8. While the Epistrophe Theorem predicts a type of self-similar structure in escape time plots, the emergence of strophes tends to

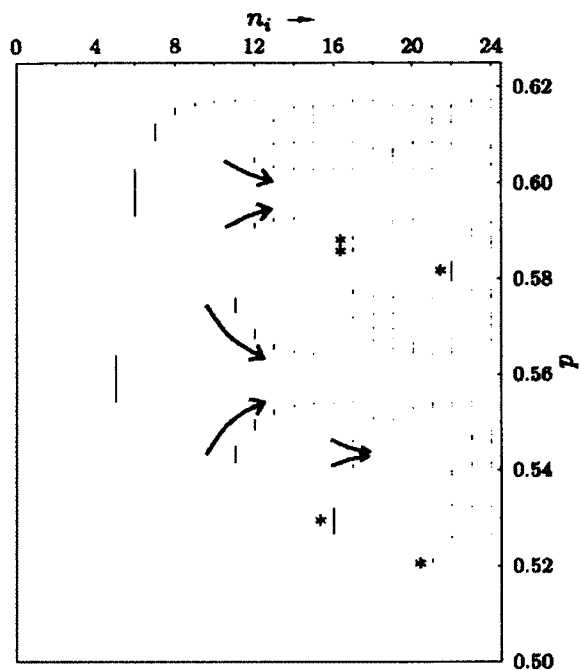


FIG. 5.8: Escape segments of an arbitrary L_0 inside a typical homoclinic tangle, with epistrophes and strophes labeled. Epistrophes are denoted by arrows, and strophes are denoted by asterisks. This figure is adapted from a plot that originally appeared in [55].

disrupt this self-similarity. Furthermore, at high iterates of the map, computations show that strophes dominate escape-time plots. In this sense, HLD gives information about “intermediate-time” behavior of chaotic trajectories, rather than their long-time behavior.

In the next chapter, we turn our attention to using these mathematical techniques on the phase plane of the double-barrier ballistic atom pump.

CHAPTER 6

HLD for a Full Scattering Problem with a Heteroclinic Tangle

The previous chapter gave an overview of a previously-developed topological method (homotopic lobe dynamics) for describing the structure of escape-time graphs. From computations of early iterates of the map, we extract essential topological information, express that information as a set of symbols, and construct an algebraic map on those symbols that describes the topological structure of forward iterates of the line of initial conditions. That symbolic dynamics predicts a minimal topologically-required set of escape segments that must occur in all future iterates.

The purpose of this chapter is to move this topological theory forward with a different type of example. A significant difference in previous studies and this work is that most previous work involved homoclinic tangles, while the present work involves a heteroclinic tangle. (A different heteroclinic tangle, and nested tangles, were also studied in [106, 128]). As a result, the algebra is more complex. The most important difference is that we are here considering a full scattering problem, in which particles come in from infinite distance

and eventually recede to infinite distance. (Our earlier studies of escape could be regarded as “half-scattering” problems.) The full scattering problem brings in several new elements to the theory that were not present in the previous papers.

Generalizing and extending homotopic lobe dynamics (HLD) for use with full scattering systems has many purposes. In a ballistic atom pump, the primary goal is to calculate the net flow of particles that approach the barriers from both sides, and HLD allows one to use stable manifolds to place lower bounds on the number of particles which are transmitted or reflected by the barriers for all incoming energies (this is much faster than computing all trajectories). In this chapter, HLD is primarily used to explain the fractal structure seen in escape-time graphs. In other contexts, HLD can also be used to find a minimal set of closed or periodic orbits [63, 128] in order to carry out semiclassical sums, to calculate topological entropy [67, 66, 106] (a measure of the complexity of the dynamics), and to partition mixed phase spaces [127].

The system we study here is the double-barrier ballistic atom pump, which has the Hamiltonian

$$H(x, p) = \frac{p^2}{2} + V(x, t), \quad (6.1)$$

where

$$\begin{aligned} V(x, t) = & U_0 (1 + \alpha \cos(\omega t)) e^{-(x+\hat{x})^2/2\sigma^2} \\ & + U_0 (1 + \alpha \cos(\omega t + \phi)) e^{-(x-\hat{x})^2/2\sigma^2}. \end{aligned} \quad (6.2)$$

This potential energy $V(x, t)$ has two repulsive Gaussian barriers centered at $\pm\hat{x}$; they have the same average height U_0 , they oscillate with the same amplitude α and frequency ω , but they are $\phi = \pi/2$ out of phase with each other. The choice of phase difference ϕ is arbitrary.

The structure of this chapter is as follows. In Section 6.1 we select particular pa-

rameters for our pump, and we define and compute the escape time graph, and display its fractal structure. In Section 6.2 we sketch the topological theory, with emphasis on the new elements that have to be examined. Then in Section 6.3 we show the results, and compare them with the computations. The rest of the chapter fills in the details of homotopic lobe dynamics for this full scattering problem.

6.1 Computation of Escape Times

We consider sets of particles approaching the barriers from far away. In the regions far from the barriers, $V(x, t) \approx 0$, so particles effectively travel through them as free particles. As particles approach the oscillating barriers, some of them may not have enough energy to transmit past the first barrier, and are directly reflected. Some particles may have enough energy to transmit past both barriers, which we call direct transmission. Other particles may transmit past the first barrier, but not have enough energy to transmit past the second barrier. In this case, particles may spend a considerable amount of time in between the barriers, reflecting back and forth from one barrier to the other, before finally reaching the left or right barriers with an appropriate energy and phase to get over the barrier and be transmitted to the right or reflected to the left.

We choose system parameters $U_0 = 1$, $\alpha = 0.5$, $\omega = 2\pi/3$, $\hat{x} = 3$, $\sigma = 1$, and $\phi = \pi/2$. The separation from the center of one repulsive barrier to the other is $2\hat{x} = 6\sigma$, so the effect of overlap between the two is negligible. We examine initial conditions such that all particles begin to the left of the barriers with the same initial momentum, $p_0 \approx 1.50$, but with variable initial position, $-20.9 \lesssim x_0 \lesssim -16.4$. It is sufficient to analyze a line segment of length $\Delta x_0 = p_0 2\pi/m\omega$, which is the distance each particle travels during the first cycle of the oscillating barriers. The methods we use naturally extend to any other set of barrier parameters, initial positions, and initial momenta.

We numerically integrate the classical equations of motion for the particles to obtain $x(t)$ and $p(t)$. We monitor $x(t)$, and define a particle's escape time as the amount of time required for the particle to escape the barrier region. Specifically, we say that a particle has escaped to the left if it passes through a line located at $x(t) = -\hat{x} - \gamma$ with negative momentum, and that a particle has escaped to the right if it passes through $x(t) = \hat{x} + \gamma$ with positive momentum, where $\gamma = 2 \times 10^{-7}$.

Figs. 6.1(a) and (b) show continuous escape times (smooth curves) as a function of initial position for particles temporarily trapped between the barriers. In this example, only a portion of the initial-condition line becomes temporarily trapped in this region; another portion directly reflects from the left barrier, and another portion directly transmits past both barriers. Dotted curves (red) represent particles that escaped to the left, and solid curves (blue) represent particles that escaped to the right. Also shown are discrete escape times (horizontal lines), which will be discussed later in the chapter. The continuous and discrete escape times are plotted relative to a specific time, which is discussed later in the chapter.

Fractal behavior is evident in these plots. Fig. 6.1(b) is a zoom of a small region of Fig. 6.1(a). We see the same structure of icicles, but with escape times shifted upward by a time equal to one period of the potential. We see that the same pattern of escape segments occurs on different scales, and that it begins at different times in different regions. This type of structure is repeatedly observed when examining even smaller sections of initial position. We also see an additional type of self-similar structure, called an "epistrophe." An epistrophe is an infinite sequence of escape segments that converges on the edge of an escape segment [55, 56]. Every edge of every escape segment has an epistrophe converging upon it.

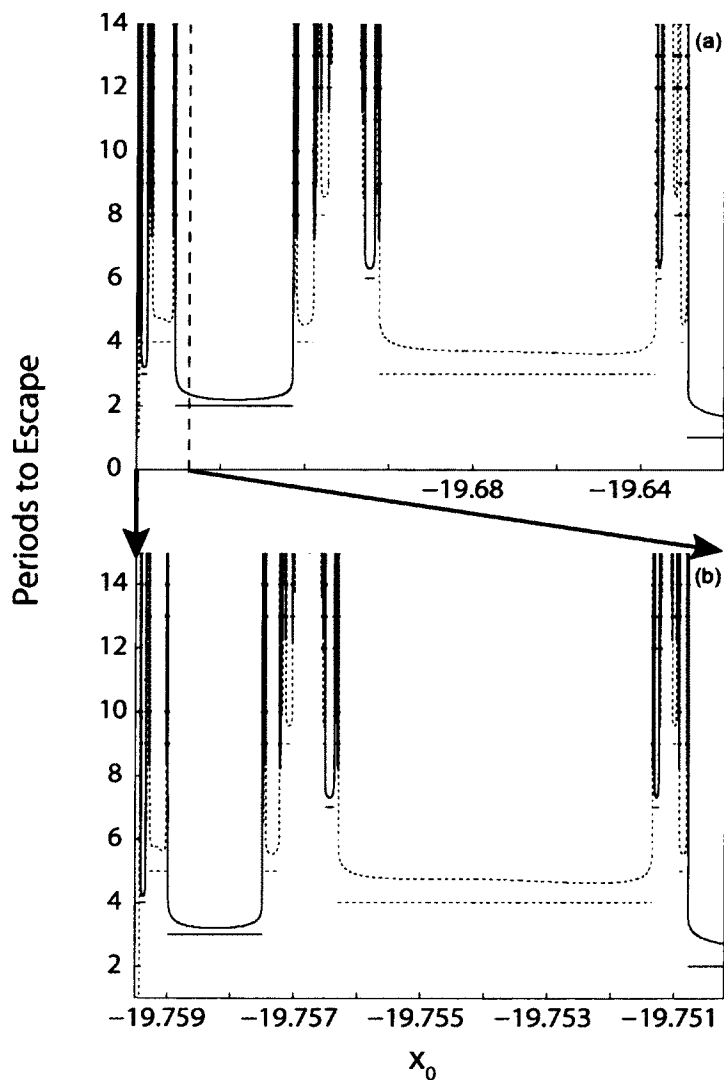


FIG. 6.1: Escape-time plot for trajectories escaping the heteroclinic tangle in the double-barrier system. Continuous (smooth curves) and discrete (horizontal lines) escape times as a function of initial position for particles temporarily trapped between the barriers. The dotted curves (red) represent particles that escaped to the left, and solid curves (blue) represent particles that escaped to the right. (b) is a zoom of the section of (a) between the left edge and the dashed black line, as denoted by the arrows.

6.2 Topological Analysis – Sketch of the Theory

The purpose of the topological analysis is to provide an interpretation of the structures seen in the escape-time plots. The methods are similar to those used in earlier work and the example discussed in the previous chapter. In this section we give only a brief sketch of the theory, pointing out the important differences from the systems studied previously and the previous example, and we show the result in Section 6.3. In later sections we fill in all the details.

First, a surface of section (SOS) must be defined. We strobe the continuous motion once per cycle of the pump, and record (x, p) . The SOS has two unstable fixed points, corresponding to particles riding up and down on top of the barriers. The stable and unstable manifolds of these fixed points create a heteroclinic tangle. In much of the earlier work and the previous example, there was only one fixed point, giving a homoclinic tangle. Figure 6.2 shows a homoclinic tangle (left) and a heteroclinic tangle (right). The homoclinic tangle has only one hyperbolic fixed point, while the heteroclinic tangle has two. While the homoclinic tangle consists of one stable and one unstable manifold, the heteroclinic tangle consists of two stable manifolds and two unstable manifolds. Both structures have an inner stable region consisting of many stable orbits of arbitrary period. In addition, both structures enclose many unstable periodic orbits of arbitrary period. The present chapter is the first application of homotopic lobe dynamics to a heteroclinic tangle for a full scattering system, in which particles come in from an infinite distance. These types of initial conditions, along with the additional fixed point, make this problem somewhat more complex than previous ones.

In previous work, we were studying escape from a complex, sometimes called a half-scattering process. Here we have a full scattering process, in which particles come in from infinite distances. We have to specify an appropriate line of initial conditions, l_0 , which

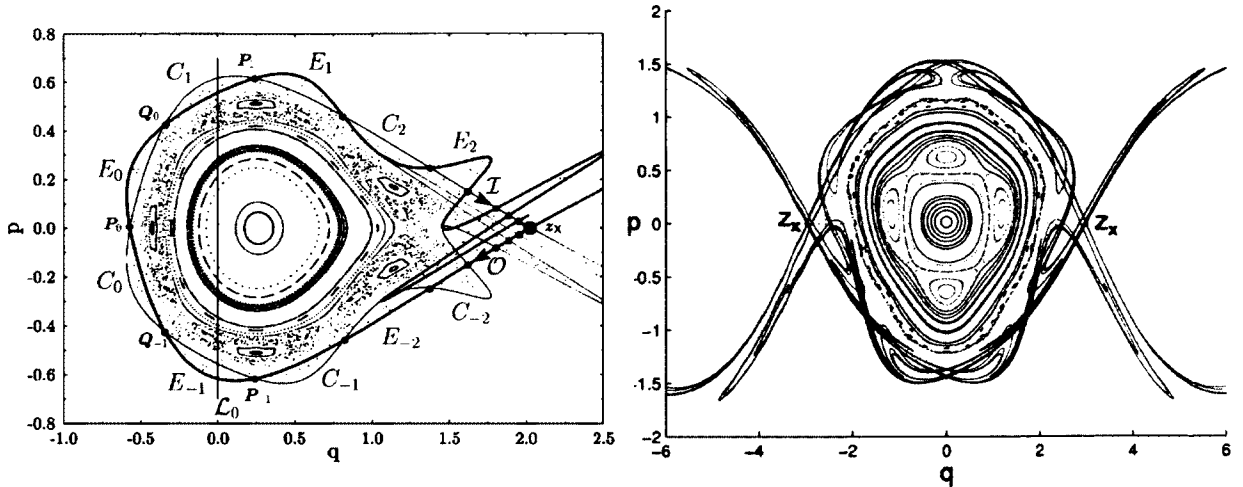


FIG. 6.2: A homoclinic tangle (left) and a heteroclinic tangle (right). The homoclinic tangle originally appeared in [55]. A heteroclinic tangle governs transport in the double-barrier ballistic atom pump (this tangle was computed for a selected set of barrier parameters).

models distributions of particles approaching the barriers from infinite distances. This is a line segment of fixed momentum p_0 having length equal to $\Delta x_0 = p_0 T/m$, where $T = 2\pi/\omega$ is the cycle time of the potential. We need to choose the endpoints of this line segment in an appropriate manner. The most convenient choice depends upon the value of the initial momentum, p_0 .

We have to map that line segment forward a sufficient number of times such that particles have first arrived in the pump. We need to define precisely the meaning of that statement. The resulting curve on the SOS is called L_0 .

We also need to compute the structure of the heteroclinic tangle, which is made up of two stable manifolds and two unstable manifolds of the two unstable fixed points. We need to define certain “fundamental segments” of these manifolds, and we need to map the fundamental segments of the unstable manifolds forward some selected number of times, J .

The next step is to define certain holes in the plane, which correspond to regions into which stable and unstable manifolds do not enter. The definition of holes given in earlier

work is not the optimal choice for the present work, and we give a modified definition of the holes.

Then we define bridges, which are usually segments of unstable manifolds. Here we find that to give a topological description of L_0 , we need to create additional bridges; these are curve segments in the SOS that are not segments of any unstable manifold.

Next, the homotopy class of each bridge is defined and named. The homotopy class of a bridge is the family of all curve segments that is made by smoothly distorting the bridge, with the restrictions that the endpoints do not change, and the distortion does not cause the bridge to pass through a hole. Homotopy classes are defined by how the bridges wind around the holes.

The names or symbols of the homotopy classes are used to create a symbolic dynamics. Evolution of each trajectory induces a mapping of each point in the plane, which therefore induces a mapping of curve segments, which induces a mapping of the homotopy classes of those curve segments, and this is expressed as a mapping or algebra of the symbols.

This whole process is carried out in Section 6.4. Here we present the result. For our chosen set of system parameters and l_0 , we find ten homotopy classes. Their symbols and

the mapping of those symbols are given by

$$\begin{aligned}
M(u_n^t) &= u_{n+1}^t \\
M(u_n^b) &= u_{n+1}^b \\
M(c_1^t) &= c_2^t \\
M(c_1^b) &= c_2^b \\
M(c_2^t) &= f^{tb}(u_0^b)^{-1}(f^{tb})^{-1} \\
M(c_2^b) &= f^{bt}(u_0^t)^{-1}(f^{bt})^{-1} \\
M(f^{tb}) &= f^{tb}u_0^b c_1^b \\
M(f^{bt}) &= f^{bt}u_0^t c_2^t \\
M(S_{LL}) &= S_{LL} \\
M(S_{LT}) &= S_{LT}c_1^t u_0^t.
\end{aligned} \tag{6.3}$$

The next step (also given in Section 6.4) is to ascertain the topological structure of L_0 relative to the holes in the plane, and express it as a product of those symbols. In our case we find

$$L_0 = S_{LL}S_{LT}(c_1^t)^{-1}(S_{LT})^{-1}. \tag{6.4}$$

Now the symbolic dynamics is complete. We construct an algebraic representation for each iterate of L_0 , denoted L_n , by mapping each symbol in Eq. (6.4) using the symbolic

representation given by Eq. (6.3). The first few iterates are:

$$L_0 = S_{LL}S_{LT}(c_1^t)^{-1}(S_{LT})^{-1} \quad (6.5)$$

$$L_1 = S_{LL}S_{LT}c_1^t \mathbf{u}_0^t (c_2^t)^{-1} (\mathbf{u}_0^t)^{-1} (c_1^t)^{-1} (S_{LT})^{-1} \quad (6.6)$$

$$L_2 = S_{LL}S_{LT}c_1^t \mathbf{u}_0^t c_2^t u_1^t f^{tb} \mathbf{u}_0^b (f^{tb})^{-1} (u_1^t)^{-1} \\ \times (c_2^t)^{-1} (\mathbf{u}_0^t)^{-1} (c_1^t)^{-1} (S_{LT})^{-1} \quad (6.7)$$

$$L_3 = S_{LL}S_{LT}c_1^t \mathbf{u}_0^t c_2^t u_1^t f^{tb} (\mathbf{u}_0^b)^{-1} (f^{tb})^{-1} \\ \times u_2^t f^{tb} \mathbf{u}_0^b c_1^b u_1^b (c_1^b)^{-1} (\mathbf{u}_0^b)^{-1} (f^{tb})^{-1} \\ \times (u_2^t)^{-1} f^{tb} \mathbf{u}_0^b (f^{tb})^{-1} (u_1^t)^{-1} \\ \times (c_2^t)^{-1} (\mathbf{u}_0^t)^{-1} (c_1^t)^{-1} (S_{LT})^{-1} \quad (6.8)$$

The formula for L_n tells us the topologically-forced structure of the escape-time plot. At the n^{th} iterate, every instance of u_0^b or u_0^t (and their inverses) describes a segment of L_n that escapes the complex at the n^{th} iterate toward the left or right, respectively, and which will not return to the barrier region. (Symbols representing new transmitted escape segments are highlighted in blue in Eqs. (6.6)-(6.8), and symbols representing new reflected escape segments are highlighted in red). These escape segments are forced to occur as a consequence of the topological structure of L_0 in relation to the holes punctured in the plane.

6.3 Comparison of Topologically-Predicted and Computed Escape Segments

We now compare topologically-predicted escape segments with those seen computationally, and take note of those that are not predicted by the topology. Fig. 6.3 shows

the number of iterates to escape for a directly-computed L_0 . To construct this graph, we numerically iterate a high density of points making up L_0 , and calculate the number of iterates at which each point escapes the complex. Dotted (red) horizontal segments represent reflection (i.e., escape to the left of the barriers), and solid (blue) horizontal segments represent transmission (i.e., escape to the right of the barriers). In Fig. 6.3(a), the dotted (red) segment toward the left of the graph at the first iterate is a segment of L_0 that is reflected from the left barrier and does not enter the complex. The solid (blue) segment in the middle at this iterate is a segment that is directly transmitted past both barriers with no reflection from the right-hand barrier, so it also does not enter the complex. Their escape at the “first” iterate (rather than at the zeroth iterate) is a convention chosen to agree with our algebraic method.

Subsequent escape segments of L_0 have a very complicated structure. Fig. 6.3(b) shows the section of the initial-condition line lying between the two segments that escape at the first iterate in Fig. 6.3(a). In Fig. 6.3(b), the dotted (red) escape segment barely visible at the left-most edge is the long reflected segment that escapes at the first iterate in Fig. 6.3(a); the solid (blue) segment at the right-most edge is the long transmitted segment that escapes at the first iterate in Fig. 6.3(a). The section of L_0 shown in Fig. 6.3(b) is one of two sections that enters the complex. We see that new escape segments occur at every iterate, and that there are many reflected and transmitted segments in this region.

Figs. 6.3(b), 6.3(c), and 6.3(d) show self-similar structure at different levels of resolution. Fig. 6.3(c) shows a small segment of L_0 seen in Fig. 6.3(b), and Fig. 6.3(d) shows a small segment of L_0 seen in Fig. 6.3(c). Figs. 6.3(c) and (d) show that similar structures seen in Fig. 6.3(b) repeatedly occur in smaller sections of L_0 , and begin at different iterates. Epistrophes are also present for every edge of every escape segment. The self-similar grouping of escape segments, and their associated epistrophes, are predicted by the algebra.

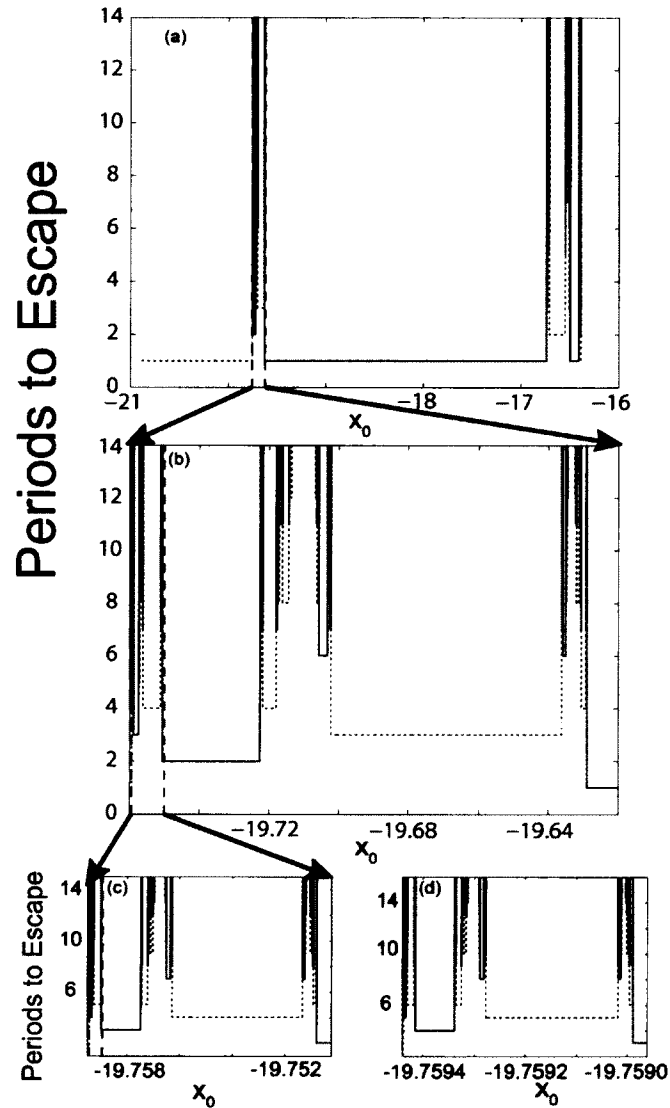


FIG. 6.3: Computed escape segments as a function of position along the initial-condition line. Solid (blue) segments represent transmission, and dotted (red) segments represent reflection. (b) Enlarged region of (a). This segment of L_0 enters the complex, and some segments are eventually reflected, while others are eventually transmitted. (c) Enlarged region of (b). (d) Enlarged region of (c), from far-left edge of (c) to the dashed vertical black line.

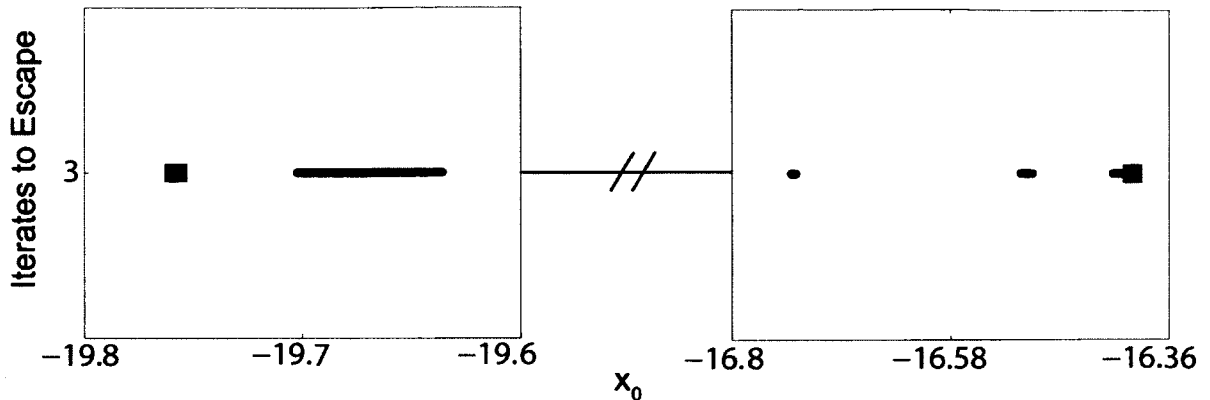


FIG. 6.4: Escape segments seen at the third iterate for directly-computed trajectories. Reflected segments are shown by thin red, and transmitted segments are shown in blue. There are a total of six new escape segments at this iterate, and both the number and the relative order of transmitted/reflected segments is predicted by the algebraic method.

Let us compare predicted escape segments with numerically-computed trajectories. We will look at the specific case of the third iterate. Our algebraic representation for L_3 is given by Eq. (6.8). Recall that each instance of u_0^b (or its inverse) represents a reflected segment (R), and each instance of u_0^t (or its inverse) represents a transmitted segment (T). Going from left to right in Eq. 6.8, and counting instances of u_0^b and u_0^t (or their inverses), we see that the symbolic representation predicts a total of six escape segments at this iterate, and that their sequence should be TRRRRT. Figure 6.4 shows the escape segments at the third iterate for directly-computed trajectories. Reflected segments are shown by thin curves (red), and transmitted segments are shown by thick curves (blue). In Fig. 6.4, we see a total of six escape segments at the third iterate, and we see the same sequence of transmitted/reflected segments that were predicted by the algebraic method.

This agreement holds for all iterates in the following sense: a topologically-predicted segment *must* appear in the computation. Sometimes these predicted segments are tiny, and they may be difficult to find in the computation, but they are always present. On the

Iterate	Predicted	Computed
1	2	2
2	3	3
3	6	6
4	10	10
5	16	16
6	28	28
7	52	56

TABLE 6.1: Escape segments predicted by the level of initial topological information used in the example, and the number of escape segments seen in directly-computed trajectories.

other hand, computation might show additional escape segments that are not predicted topologically for the chosen value of J . In particular, at high iterates, escape segments that are not forced by the initial topological structure start to emerge. Table 6.1 shows the number of escape segments predicted by using $J = 3$, and the number of escape segments seen in direct computation of trajectories. For the first six iterates, all computed escape segments are predicted by the algebraic method. At the seventh iterate, however, there are four escape segments seen in computation of trajectories that are not predicted by the algebraic method. This discrepancy is caused by our choice of using only a small amount of initial topological information (three iterates of the fundamental segments of the unstable manifolds). Agreement between the two methods can be extended to higher iterates by using more initial topological information as the basis for the symbolic representation [65, 66].

6.4 Homotopic Lobe Dynamics for a Full Scattering Problem with a Heteroclinic Tangle

In Sec. 6.2, we sketched the topological theory, mentioning the elements that are different from past work. In this section, we give all necessary details for carrying out the

topological analysis on this type of system.

6.4.1 Heteroclinic Tangle

We perform our topological analysis on a surface of section for this system. This surface of section is obtained by strobing trajectories at the same phase during each cycle of the potential. We choose our strobe time as $t = 3\pi/4\omega$ in each cycle. The surface of section is a continuous map of the (x, p) plane. There are two unstable fixed points, $\mathbf{z}_x^L = (-\hat{x}, 0)$ and $\mathbf{z}_x^R = (\hat{x}, 0)$, on the surface of section, each of which corresponds to a particle riding up and down on the top of a barrier. The stable and unstable manifolds of these fixed points are the most important elements of the theory; as in the previous chapter, they define a “complex” or “resonance zone” into which approaching particles can be temporarily captured, and from which they later escape. In addition, depending on the parameters of the system, there could be stable periodic orbits of any period which always remain inside the complex.

The reader is encouraged to consult Table 6.2 while studying the remainder of this section; this table provides a handy reference of notation used in the remainder of the chapter. Figure 6.5 shows segments of the eight stable and unstable manifolds for this system for a selected set of parameters. Together, these manifolds form a heteroclinic tangle. Different choices of parameters change the details of these manifolds, but leave essential topological properties unchanged. This type of tangle is sometimes referred to as a ternary horseshoe [129]. The stable manifold S^L comes from the upper-left quadrant of the surface of section and approaches the left-hand fixed point \mathbf{z}_x^L , and the unstable manifold U^L goes from that point into the lower-left quadrant. Likewise, the stable manifold S^R comes from the lower-right quadrant and approaches the fixed point \mathbf{z}_x^R , and the unstable manifold U^R goes from that point into the upper-right quadrant.

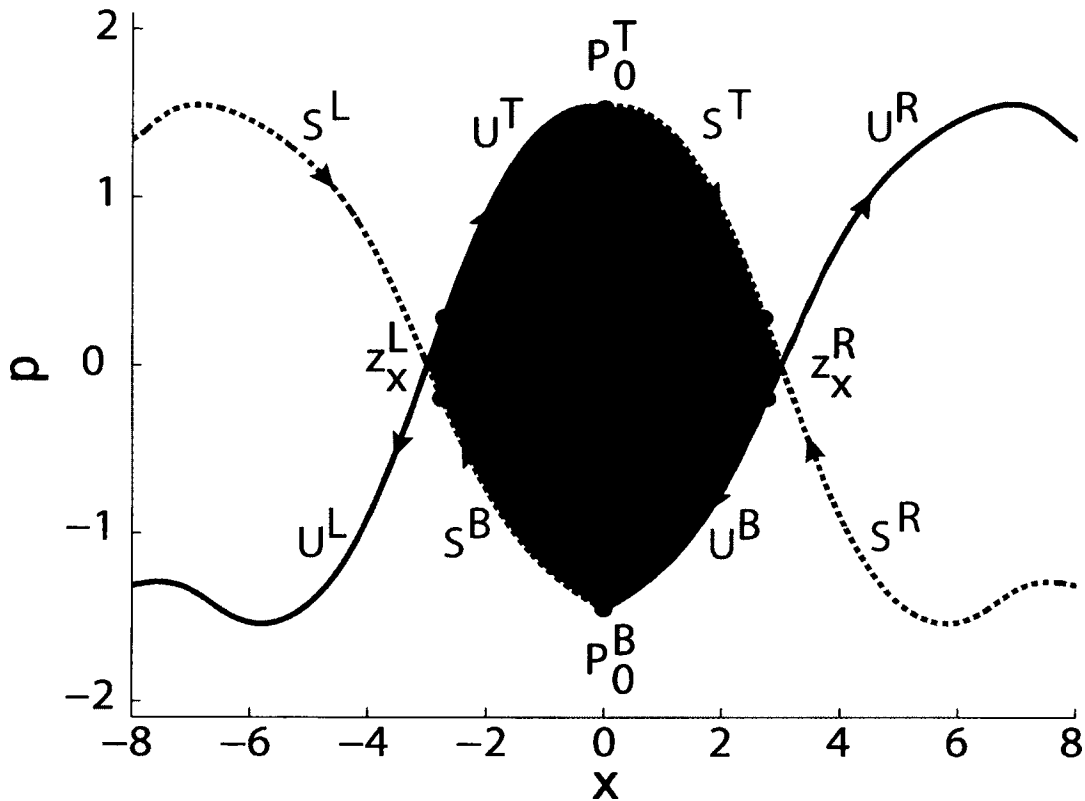


FIG. 6.5: Surface of section showing portions of the four stable (dotted red curves) and four unstable (solid blue curves) manifolds for two unstable points of the system, z_x^L and z_x^R , for a chosen set of parameters. z_x^L is the unstable point at the top of the left barrier, and z_x^R is the unstable point at the top of the right barrier. Unstable manifolds asymptotically approach an unstable point as $t \rightarrow -\infty$, and stable manifolds asymptotically approach an unstable point as $t \rightarrow +\infty$. The shaded area (greenish blue) is called the “complex” or “resonance zone,” and is discussed in the text.

Another unstable manifold leaves \mathbf{z}_x^L going toward the upper right. We call this manifold U^T , and a segment of it, called \mathbb{U}^T , corresponds to the left half of the top boundary of the complex. Similarly, a stable manifold S^B approaches \mathbf{z}_x^L from the lower right, and a segment of it, called \mathbb{S}^B , makes the left half of the lower boundary of the complex. Likewise, U^B (and its segment \mathbb{U}^B) and S^T (and its segment \mathbb{S}^T) connect with the right-hand fixed point \mathbf{z}_x^R , and also define the right halves of the lower and upper boundaries of the complex.

U^T and S^T are reflections of each other about the line $x = 0$, and they intersect at a heteroclinic point P_0^T having $(x = 0, p > 0)$, which we call the top primary intersection point. The segments \mathbb{U}^T and \mathbb{S}^T go from their respective fixed points to P_0^T . Similarly, U^B and S^B are reflections of each other through $x = 0$, and they intersect at a heteroclinic point which we call the bottom primary intersection point, P_0^B , having $(x = 0, p < 0)$. \mathbb{U}^B and \mathbb{S}^B are segments of these manifolds going from their respective fixed points to P_0^B .

The segments \mathbb{U}^T , \mathbb{S}^T , \mathbb{U}^B , and \mathbb{S}^B define the outer boundaries of the shaded region (blue) that we call the complex in Fig. 6.5. No stable manifold can intersect itself or any other stable manifold, and no unstable manifold can intersect itself or any other unstable manifold.

In Fig. 6.5, when the top primary intersection point, P_0^T is mapped forward one time, it maps to the point on \mathbb{S}^T called P_1^T . The segment $S^T[P_0^T, P_1^T]$ is called the fundamental segment, S_0^T , of S^T . Note that it is not the entire segment \mathbb{S}^T , which extends from P_0^T to \mathbf{z}_x^R . When P_0^T is mapped backward one time, it maps to the point P_{-1}^T on \mathbb{U}^T , and the fundamental segment of U^T , U_0^T , is the segment $U^T[P_{-1}^T, P_0^T]$. Similarly, the bottom primary intersection point P_0^B maps forward to P_1^B on \mathbb{S}^B , and backward to P_{-1}^B on \mathbb{U}^B . The fundamental segment, S_0^B , of S^B is the segment $S^B[P_0^B, P_1^B]$, and the fundamental segment of U^B , U_0^B , is the segment $U^B[P_{-1}^B, P_0^B]$.

The forward mapping of U_0^T can be expressed as $M(U_0^T = U^T[P_{-1}^T, P_0^T]) = U_1^T =$

Symbol	Meaning
S^L	Stable manifold from $x = -\infty$ to \mathbf{z}_x^L
S^R	Stable manifold from $x = +\infty$ to \mathbf{z}_x^R
S^B	Stable manifold $\rightarrow \mathbf{z}_x^L$ from the right as $t \rightarrow \infty$
S^T	Stable manifold $\rightarrow \mathbf{z}_x^R$ from the left as $t \rightarrow \infty$
U^L	Unstable manifold from \mathbf{z}_x^L to $x = -\infty$
U^R	Unstable manifold from \mathbf{z}_x^R to $x = +\infty$
U^B	Unstable manifold $\rightarrow \mathbf{z}_x^R$ from the left as $t \rightarrow -\infty$
U^T	Unstable manifold $\rightarrow \mathbf{z}_x^L$ from the right as $t \rightarrow -\infty$
\mathbb{S}^B	S^B from P_0^B to \mathbf{z}_x^L ; part of complex boundary
\mathbb{S}^T	S^T from P_0^T to \mathbf{z}_x^R ; part of complex boundary
\mathbb{U}^B	U^B from \mathbf{z}_x^R to P_0^B ; part of complex boundary
\mathbb{U}^T	U^T from \mathbf{z}_x^L to P_0^T ; part of complex boundary
S_0^B	$S^B[P_0^B, P_1^B]$; fundamental segment of S^B
S_0^T	$S^T[P_0^T, P_1^T]$; fundamental segment of S^T
U_0^B	$U^B[P_{-1}^B, P_0^B]$; fundamental segment of U^B
U_0^T	$U^T[P_{-1}^T, P_0^T]$; fundamental segment of U^T
S_n^B	$S^B[P_n^B, P_{n+1}^B]$; n^{th} iterate of S_0^B
S_n^T	$S^T[P_n^T, P_{n+1}^T]$; n^{th} iterate of S_0^T
U_n^B	$U^B[P_{n-1}^B, P_n^B]$; n^{th} iterate of U_0^B
U_n^T	$U^T[P_{n-1}^T, P_n^T]$; n^{th} iterate of U_0^T

TABLE 6.2: Notation used to describe manifold segments.

$U^T[P_0^T, P_1^T]$, where M is the symbol for the mapping. Generally, for all n , $M^n(U_0^T) = U_n^T$, and $M^n(U_0^B) = U_n^B$. Each U_n^T is the segment $U^T[P_{n-1}^T, P_n^T]$, and each U_n^B is the segment $U^B[P_{n-1}^B, P_n^B]$. Similarly, for all n , each S_n^B is the segment $S^B[P_n^B, P_{n+1}^B]$, and each S_n^T is the segment $S^T[P_n^T, P_{n+1}^T]$.

As U_0^T and U_0^B are mapped forward, and S_0^T and S_0^B are mapped backward, stable and unstable manifolds intersect each other an infinite number of times. Intersections occur at the collection of points $P^B = (P_{-\infty}^B, \dots, P_0^B, \dots, P_{\infty}^B)$ and at the collection of points $P^T = (P_{-\infty}^T, \dots, P_0^T, \dots, P_{\infty}^T)$, on the top and bottom boundaries of the complex, respectively. Both P^T and P^B are heteroclinic orbits, and these points are the endpoints for U_n^T , U_n^B , S_n^T , and S_n^B segments. In addition, for all $n > 0$, U_n^T intersects \mathbb{S}^T exactly once between $U^T[P_{n-1}^T, P_n^T]$, at a point we call Q_n^T . These points can be mapped forward and backward,

and are another heteroclinic orbit, which we call $Q^T = (Q_{-\infty}^T, \dots, Q_0^T, \dots, Q_{\infty}^T)$. For $n < 0$, the points Q_n^T lie on U^T . Similarly, for all $n > 0$, U_n^B intersects S^B exactly once between $U^B[P_{n-1}^B, P_n^B]$, at a point we call Q_n^B . These points can be mapped forward and backward, and are another heteroclinic orbit, which we call $Q^B = (Q_{-\infty}^B, \dots, Q_0^B, \dots, Q_{\infty}^B)$. For $n < 0$, the points Q_n^B lie on U^B .

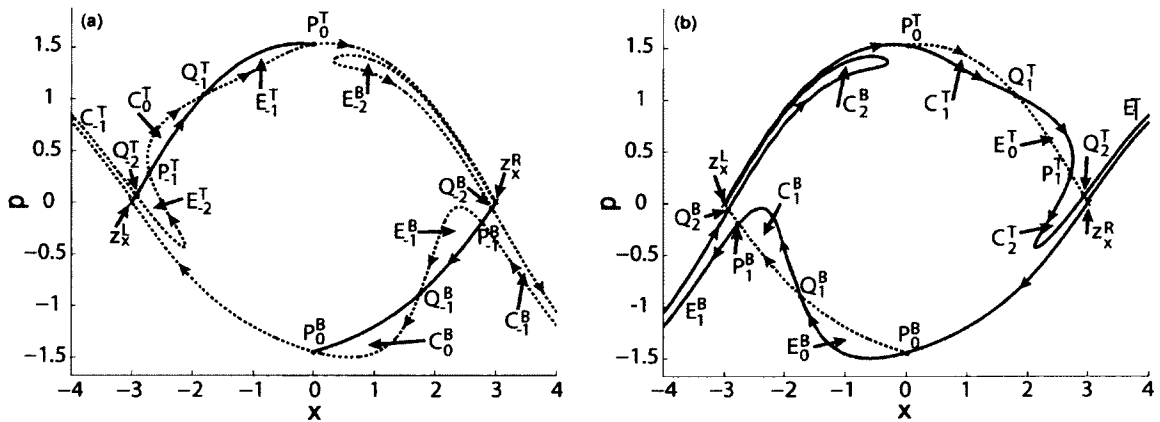


FIG. 6.6: Segments of stable and unstable manifolds. (a) S^T, S^B , and the first two back iterates of S_0^T and S_0^B (dotted red curves), along with U^T and U^B (solid blue curves). Each back iterate of the fundamental stable segments forms two lobes with either U^T or U^B . (b) U^T, U^B , and the first two forward iterates of U_0^T and U_0^B (solid blue curves), along with S^T and S^B (dotted red curves). Each forward iterate of the unstable fundamental segments forms two lobes with either S^T or S^B . The lobes C_0^T and C_0^B in (a) map from outside the complex to the lobes C_1^T and C_1^B , respectively, in (b), which are inside the complex. The lobes E_{-1}^T and E_{-1}^B in (a) map forward to the lobes E_0^T and E_0^B , respectively, in (b), which are outside the complex.

As can be seen in Fig. 6.6, segments U_n^T and S_{n-1}^T lie between P_{n-1}^T and P_n^T , and intersect at Q_n^T . Similarly, each U_n^B and S_{n-1}^B lie between P_{n-1}^B and P_n^B , and intersect at Q_n^B . These segments form the boundaries of lobes. For example, the segments of U_1^T and S_0^T between P_0^T and Q_1^T bound a lobe labeled C_1^T , and the segments of U_1^T and S_0^T between Q_1^T and P_1^T bound another lobe called E_0^T . The points P_0^T and Q_1^T map forward to points

P_1^T and Q_2^T , respectively, and the stable and unstable manifold segments connecting them bound the lobe C_2^T , which is the forward mapping of lobe C_1^T . Generally, the two lobes bounded by $U_n^{B,T}$ and $S_{n-1}^{B,T}$ map forward to two lobes bounded by $U_{n+1}^{B,T}$ and $S_n^{B,T}$, and map backward to two lobes bounded by $U_{n-1}^{B,T}$ and $S_n^{B,T}$.

The lobes are crucial for understanding the transport process. Since this system is Hamiltonian, the mapping is area-preserving, meaning that all forward and backward iterates of a given lobe have the same area. When the endpoints of manifold segments bounding a lobe are on \mathbb{S}^T (or \mathbb{S}^B), their forward iterates get closer together along \mathbb{S}^T (or \mathbb{S}^B) as $n \rightarrow \infty$. Consequently, the lobe's forward iterates must stretch in order to preserve the same area. Similarly, when the endpoints of manifold segments bounding a lobe are on \mathbb{U}^T (or \mathbb{U}^B), their backward iterates get closer together along \mathbb{U}^T (or \mathbb{U}^B) as $n \rightarrow -\infty$, and again the lobes must stretch in order to preserve the same area.

In Fig. 6.6, we can see that some lobes are inside the complex, and others are outside it. Two lobes, labeled C_0^B and C_0^T , lie outside the complex, but their forward mappings, labeled C_1^B and C_1^T , respectively, lie inside the complex. The areas inside C_0^B and C_1^B are equal (as are the areas inside C_0^T and C_1^T). This means that any particle in the phase plane that is inside the lobe C_0^T at any strobe time will be inside C_1^T one cycle later, i.e., the particle will be “captured”: transported from outside the complex to within it. At the next cycle, the particle will be in C_2^T , etc. The same process occurs for the lobes labeled C_0^B , C_1^B , and C_2^B .

Another pair of important lobes are labeled E_{-1}^T and E_{-1}^B . They are inside the complex but their forward iterates, labeled E_0^T and E_0^B , respectively, lie outside the complex. Any particle in the phase plane inside either E_{-1}^T or E_{-1}^B at any strobe time will be inside E_0^T or E_0^B , respectively, one cycle later, and will have “escaped,” i.e., been transported from within the complex to outside of it. More generally, a particle inside a lobe E_{-n}^T or E_{-n}^B will escape the complex n cycles later. Particles inside E_{-n}^T will eventually escape to the

right of both barriers, and particles inside E_{-n}^B will escape to the left of the barriers.

When Figs. 6.6 (a) and (b) are plotted together, one can see that capture and escape lobes within the complex intersect each other in very complicated fashion (see Fig. 6.8 (a)). However, they allow us to understand the transport process in the phase plane. We will use them later to develop a method for understanding the escape-time plots seen earlier.

6.4.2 Initial Conditions

In the past, because we were studying escape, lines of initial conditions were typically chosen to lie in the complex. However, since we now wish to study a scattering process, having particles approaching from $x = \pm\infty$ with a constant momentum p_0 , we take our line of initial conditions l_0 to be a horizontal line segment in phase space far away from the barriers, where the potential is effectively zero. We also define this line segment such that its length is $\Delta x_0 = p_0 T/m$, where $T = 2\pi/\omega$ is the cycle time of the barriers, and such that it has endpoints on a stable manifold. This allows us to describe the topological structure of the evolution of initial-condition lines in terms of the evolution of bridges, which are segments of the unstable manifolds.

Let \mathcal{L} represent l_0 and all its iterates. The curve \mathcal{L} cannot intersect itself. If it intersected itself on a particular iterate, it would intersect itself at every iterate. However, by construction, l_0 does not intersect itself. If one iterate in \mathcal{L} intersected another iterate in \mathcal{L} , then mapping that intersection backward many times, there would have to be a corresponding intersection on l_0 . However, at early times, the line of initial conditions represents particles of fixed momentum moving toward the barriers. No future iterate can intersect that line, because any particle reflected from the barriers (back toward the initial-condition line) will be traveling in the opposite direction of the initial-condition line, and will thus be in a different region of the phase plane.

While l_0 represents particles approaching the barriers from $x = \pm\infty$, we will base our topological analysis on a selected forward-iterate of l_0 , called L_0 , that has one of the following properties. If particles approach from the left,

- Type I: Its endpoints both lie on \mathbb{S}^T .
- Type II: Its endpoints both lie on S^L , and it intersects \mathbb{S}^T .

If particles approach from the right,

- Type III: Its endpoints both lie on \mathbb{S}^B .
- Type IV: Its endpoints both lie on S^R , and it intersects \mathbb{S}^B .

L_0 should be chosen at the earliest iterate of l_0 satisfying one of these conditions. In order for the endpoints of L_0 to lie on a stable manifold, the endpoints of its pre-iterate l_0 must also lie on the same stable manifold. Therefore, we must examine S^T , S^B , S^L , and S^R at many backward iterates, far from the barriers, when constructing l_0 .

In the rest of this chapter, we consider only particles approaching from the left, though the topological analysis is analogous for particles approaching from the right. Fig. 6.7 shows S^L (lowermost solid curve; black), S^T (uppermost solid curve; red) and S^B (dotted curve; purple) at many backward iterates in a region far to the left of both barriers. S^R cannot enter this region (see Fig. 6.5). The qualitative properties of the scattering depend upon the initial momentum; specifically, on whether l_0 lies in Region I, II, III or IV. These regions are determined according to maxima and minima of S^T and S^L .

If the initial momentum is large, so that l_0 is in Region I (above the max of S^T in this region), \mathcal{L} will never intersect a stable manifold. Since it begins above S^T , it will be directly transmitted past both barriers without entering the complex.

If the initial momentum is such that l_0 is in Region II (below the max of S^T and above the max of S^L in this region), a portion of \mathcal{L} will be directly transmitted past both

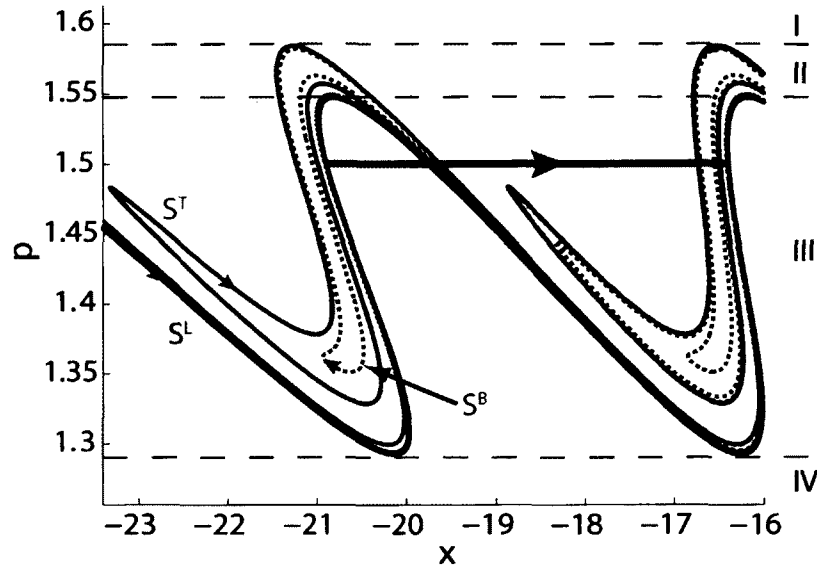


FIG. 6.7: An appropriate initial-condition line for the full scattering problem. Backward iterates of S^T (uppermost red curve), S^B (dotted purple curve), and S^L (lowermost curve; black) in a region far to the left of the barriers, where the potential is effectively zero, for a chosen set of parameters. Initial-condition lines in the Regions labeled I-IV scatter from the barriers with qualitatively different behavior, which is discussed in the text. Also shown is an example l_0 (horizontal green segment), constructed with the rules discussed in the text, which has an initial momentum corresponding to Region III.

barriers without entering the complex, and another portion of \mathcal{L} will enter the complex. The segments that lie above S^T in this region will be directly transmitted, and those that lie below S^T will enter the complex. Portions of segments entering the complex can be either reflected or transmitted. The endpoints of l_0 should be placed on the uppermost segments of S^T in this region, so that it will evolve into a Type I L_0 .

For initial momentum such that l_0 lies in Region III (between the min and max of S^L in this region), portions of \mathcal{L} can be directly transmitted or directly reflected without entering the complex, and portions can enter the complex. The endpoints of l_0 should be placed on S^L , so that it will evolve into a Type II L_0 . An example l_0 (horizontal curve;

green) is shown for $p_0 \approx 1.50$ in Fig. 6.7, with its endpoints on S^L .

If the initial momentum is small, so that l_0 lies in Region IV, \mathcal{L} will never intersect a stable manifold, cannot enter the complex, and will be directly reflected.

For initial momenta in Regions II and III, intersections between l_0 and any stable manifold will map to an unstable point. Our use of initial-condition lines with width $\Delta x_0 = p_0 2\pi / m\omega$ ensures that both endpoints of l_0 lie on the same stable manifold. Similar analysis for l_0 lines representing particles approaching from the right would allow us to construct L_0 of Types III and IV.

6.4.3 Homotopic Lobe Dynamics: Overview

Stable and unstable manifolds forming a heteroclinic tangle intersect each other an infinite number of times. Since stable manifolds cannot intersect themselves or any other stable manifold, and unstable manifolds cannot intersect themselves or any other unstable manifold, segments of stable and unstable manifolds connecting a pair of intersection points can create domains which no stable or unstable manifold can enter. These domains are part of the structure of the heteroclinic tangle, and are a main component of the topological analysis.

Another important aspect is that, as initial-condition lines evolve, they follow and approach unstable manifolds in the chaotic regions of the phase plane. For this reason, we topologically analyze the evolution of unstable manifolds, which we then relate to the evolution of initial-condition lines. Rather than analyze the entirety of each unstable manifold at once, we instead analyze how segments of unstable manifolds evolve. These segments are classified according to how they wind around the domains that manifolds cannot enter.

We then develop a symbolic algebra describing how the unstable manifold segments

evolve. The initial topological structure of the unstable manifold segments in relation to the manifold-excluding domains forces a minimal topological structure at later times. The algebra predicts this structure, and tells us both the minimum number and relative order (along L_0) of new escape segments at each forward iterate. One chooses the amount of topological information (i.e., the length of the stable and unstable manifolds) to use for the basis of analysis. Using more initial information may allow additional structure to be predicted at later times.

6.4.4 Fundamental Segments

To set up the topological theory, we map the fundamental segments U_0^B and U_0^T forward J times. As stated earlier, choosing a higher J may provide additional topological information, which in turn may allow additional escape segments to be predicted at later times. The solid blue curves in Fig. 6.8(a) show U_0^T and U_0^B mapped forward $J = 3$ times, and U^T and U^B . The dotted curves (red) show S_0^T and S_0^B mapped backward $J = 3$ times, along with S^T and S^B , for our selected set of parameters. The back-iterates of S_0^T and S_0^B shown in Fig. 6.8(a) are not needed for the topological method, but are shown to help the reader visualize the heteroclinic tangle.

6.4.5 J-neighbors

We must find domains that manifolds cannot enter. Each domain of this type is bounded by a stable manifold segment and an unstable manifold segment that intersect at two points. A pair of intersection points are called neighbors if both the stable and unstable manifold segments connecting them contain no other intersections with any stable or unstable manifolds. In practice, it is difficult to determine whether a pair of intersection points are neighbors; they may appear to be neighbors at some iterate J , but at some other

iterate $J' > J$, previously-unseen intersections may be revealed.

For this reason, we work with J -neighbors, which depend on the number of iterates, J , used for the topological analysis. To define them, we must define the transition number N of an intersection \mathbf{z} , which is the number of iterates N such that $M^{N+m}(\mathbf{z})$ lies on either S_0^T or S_0^B , when $M^m(\mathbf{z})$ lies on either U_0^T or U_0^B .

Two intersection points are J -neighbors if i.) they both have transition number $N \leq J$, and ii.) the stable and unstable manifold segments connecting them contain no other intersection points with transition number $N \leq J$.

An efficient method for finding J -neighbors for the chosen J is to iterate the fundamental unstable manifold segments U_0^T and U_0^B forward J times and examine heteroclinic intersections along S_0^T and S_0^B . Only adjacent pairs of heteroclinic points along S_0^T and S_0^B can possibly be J -neighbors. Furthermore, any intersection between $M^k(U_0^T)$ or $M^k(U_0^B)$ and S_0^T or S_0^B has transition number $N = k$. The J -neighbors found in this fashion can be mapped forward and backward to find all other pairs of J -neighbors for the chosen J .

Since the stable and unstable manifold segments connecting a pair of neighbors have no other intersection points, they bound a domain in the phase plane that no manifold can enter. The topological theory describes the evolution of unstable manifolds in relation to these manifold-excluding domains. One may think of J -neighbors as pairs of intersection points that appear to be neighbors through the chosen iterate J , i.e., the stable and unstable manifold segments connecting them bound a domain for which it appears that no manifold can enter. We use these manifold-excluding domains in the topological theory.

6.4.6 Holes

To describe the topological structure of curves, we need to punch holes in the plane and specify how the curves go around the holes. In the past, we used two different definitions

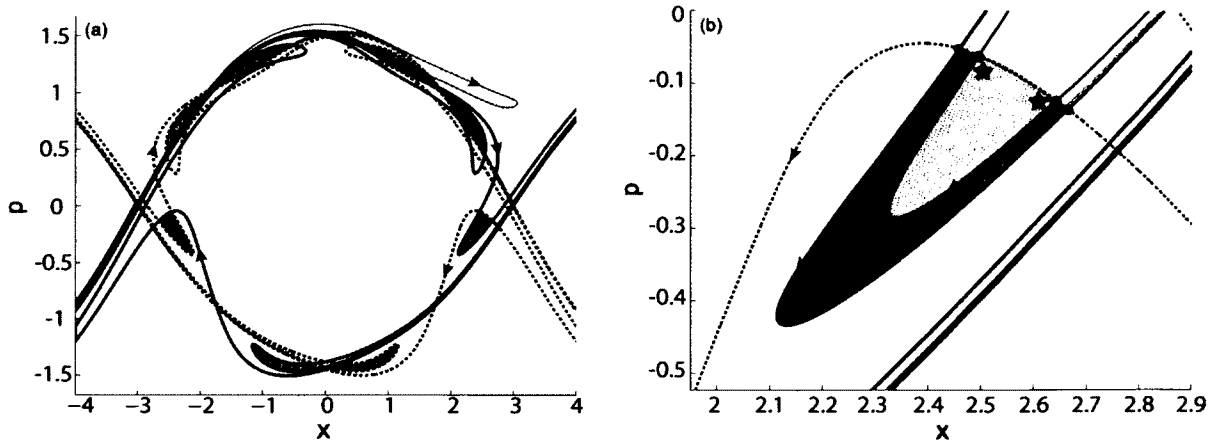


FIG. 6.8: Holes and subholes. (a) Unstable manifolds (blue) iterated forward $J = 3$ times, and stable manifolds (dotted red curves) iterated backwards $J = 3$ times. The uppermost solid curve (green) is L_0 . (b) Zoom of a domain-hole from (a). The shaded regions (yellow and pink) combined constitute the domain-hole, into which no S or U can enter. In [107], we shrunk such domain-holes to point-holes such that the point was inside the domain, but arbitrarily close to one of the two heteroclinic points on the boundary of the domain (large black dots). In this chapter, we use a different choice of point-hole: either of the points marked by a \star , which is inside the subhole (yellow), and arbitrarily close to one of the J -subneighbors (large green dots).

of holes. In the first paper [56], a hole was a domain of the plane into which iterates of stable and unstable manifolds could not enter. In a later paper [67], holes were represented as carefully-selected points within the previously-used domains. In this chapter we find it best to shrink the domain-holes to a different set of point-holes.

Fig. 6.8(a) shows L_0 , U^T , U^B , S^T , S^B , the first three forward iterates of U_0^T and U_0^B , and the first three back-iterates of S_0^T and S_0^B . Domain-holes are shaded, and no forward or backward iterate of S^T , S^B , U^B , or U^T enters these domain-holes for the chosen J . Fig. 6.8(b) shows a zoom of one domain-hole (shaded region; yellow and pink), and a portion of \mathcal{L} . It can and does enter the domain-hole. The uppermost solid curve (green) which enters the domain-hole is L_1 , and the two solid curves below it (orange) which

enter the domain-hole are portions of L_2 . Computations have shown that this commonly occurs for appropriately-constructed L_0 . In this system, each time a portion of \mathcal{L} enters a domain-hole, it will be closer to the unstable manifold bounding the domain-hole than the last time it entered, because points and curves are mapped forward toward and along unstable manifolds.

Each domain-hole is associated with a pair of J -neighbors. The boundary of the domain-hole is made up of a segment of an unstable manifold connecting the J -neighbors, and a segment of a stable manifold connecting them. In the past, each domain-hole was shrunk to a point and “moved” arbitrarily close to one of the J -neighbors associated with it, while remaining in the domain of the original domain-hole. Point-holes were then mapped forward and backward to represent domain-holes in the plane. Since we described the evolution of the manifolds (and lines of initial conditions) in terms of how they wound around domain-holes, using a point-hole to represent a domain-hole was sufficient, because a point-hole is within the domain of the domain-hole.

However, for this system, this method results in loss of important information; see Fig. 6.8(b). If we use a point-hole that is arbitrarily close to one of the J -neighbors (large black dots), we see that the segments of \mathcal{L} no longer wind around the point-hole in the same fashion as the unstable manifold segment which they approach. Since we want to describe the evolution of L_0 in terms of the way unstable manifold segments evolve in relation to point-holes, we must develop a method for selecting a point-hole such that both \mathcal{L} and the unstable manifold it approaches wind around the point-hole in the same fashion.

In the present case we see that \mathcal{L} enters the domain-hole. The uppermost solid curve (green) which enters the domain-hole in Fig. 6.8(b) is L_1 . All forward iterates of L_1 that enter this domain-hole lie in the pink region, between L_1 and the unstable manifold segment bounding the domain-hole, and not in the yellow region. This occurs because

\mathcal{L} approaches the unstable manifold; L_2 , which passes through the domain-hole twice, is the solid curve (orange) passing through the pink portion of the domain-hole. Therefore we may call the yellow region a subhole. In this chapter we define new point-holes by shrinking the yellow subdomain to either one of the points marked \star inside the subdomain, but arbitrarily close to one of the intersections of L_1 with S^B (large green dots). L_1 then goes around that hole, subsequent iterates of L_1 also go around it, and they must also go around iterates of that hole.

When a subhole is formed, there are two intersections between L_n and the stable manifold. Let us call these intersections J -subneighbors. The J -subneighbors are connected by two curves: a segment of L_n , and a segment of the stable manifold.

With these ideas, we can use the following framework to determine placement of point-holes. We first compute the L_0 we wish to examine. We next determine all iterates of U_0^T and U_0^B up to some iterate J . We then determine all pairs of J -neighbors that lie on S_0^T and S_0^B . We map each pair of J -neighbors forward $J - k$ times, and backward k times, where k is the transition number of the J -neighbors. We then see if J -subneighbors (intersections between L_0 and stable manifold segments connecting J -neighbors) are present. If no J -subneighbors are present, we puncture a point-hole in the plane inside the domain-hole along S_0^T and S_0^B and arbitrarily close to one of the J -neighbors. We then map this point-hole forward $J - k$ times, and backward k times.

If J -subneighbors exist between any pair of J -neighbors (or their iterates), a subhole is formed. If there is only one pair of J -subneighbors between a pair of J -neighbors, we puncture a point-hole in the plane within the subhole, and arbitrarily close to either J -subneighbor. We then map this point-hole forward and backward the appropriate number of times.

Puncturing point-holes in the phase plane that are developed in this fashion allows us to describe the topological evolution of initial-condition lines to the same level of accuracy

as previous methods.

6.4.7 Bridges

Bridges are curves that have endpoints on \mathbb{S}^T or \mathbb{S}^B , but do not otherwise intersect either of them. In past cases, each of these curves was a segment of an unstable manifold that was part of the boundary of a lobe. S^L and S^T may intersect bridges, but only if the segment intersecting the bridge is not part of \mathbb{S}^T or \mathbb{S}^B . Bridges can begin and end on \mathbb{S}^T , begin and end on \mathbb{S}^B , or have one endpoint on \mathbb{S}^T and the other on \mathbb{S}^B . Bridges are directed curves, and have the direction of the local unstable manifold. If a curve is not a segment of an unstable manifold, we choose its direction arbitrarily.

Homotopic Lobe Dynamics describes the topological evolution of bridges, i.e. the way they wind around the punctured point-holes in the plane. After puncturing all point-holes in the plane, we classify each bridge formed from iterating U_0^T and U_0^B forward J times according to its topological properties: i.) which stable manifold(s) its endpoints lie on, and ii.) which point-hole(s) it surrounds (if any).

Figure 6.9 shows U_0^T and U_0^B and their first $J = 3$ forward iterates (solid curves; blue), along with \mathbb{S}^T , \mathbb{S}^B , and S^L (dotted curves; red), and the punctured point-holes for a given set of parameters. Two bridges are said to be homotopic to one another if one can be continuously distorted into the other without passing through a point-hole, or having its endpoints leave the stable manifold(s). A family of bridges that are homotopic to each other is a “homotopy class.” In Fig. 6.9, there are three bridges below the label f^{tb} that i.) have one endpoint on \mathbb{S}^T and one on \mathbb{S}^B , ii.) pass under the point-hole H_{-1}^B , and iii.) pass above the point-hole H_{-3}^T . Each of these bridges can be continuously distorted into the others, are therefore homotopic to each other, and are elements of the same homotopy class.

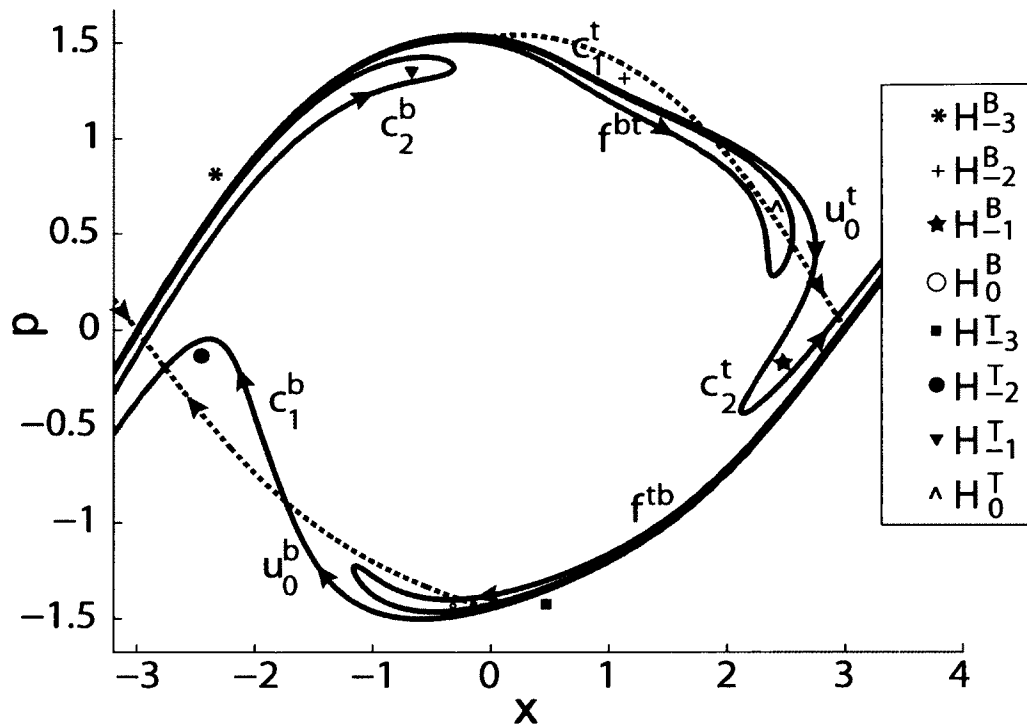


FIG. 6.9: U^T and U^B , U_0^T and U_0^B and their first $J = 3$ forward iterates (solid blue curves), and S^T , S^L , and S^B (dotted red curves) for a given set of parameters. The markers represent point-holes punched in the appropriate places in the phase plane. Bridge classes are constructed according to how these unstable manifold segments wind around the punctured point-holes.

We give each homotopy class of bridges a symbol, e.g. f^{tb} or c_2^t . If bridges in a homotopy class have opposite direction, they are said to be inverses of the other. We say a bridge surrounds a point-hole if the point-hole is inside the region bounded by the bridge and the stable manifold segment connecting the bridge's endpoints [67]. If a bridge in a homotopy class surrounds a point-hole, its forward iterate must surround the forward iterate of that point-hole, and its endpoints must move closer to the unstable fixed point(s) they are approaching. For example, the bridge c_1^t in Fig. 6.9 surrounds the hole H_{-2}^B , so its forward mapping must surround the hole H_{-1}^B . We then say that the bridge class c_1^t maps forward as $M(c_1^t) = c_2^t$, which gives us a symbolic representation for the evolution of c_1^t under one mapping. Similarly, the symbolic representation for the mapping of a bridge homotopic to c_1^t , but with opposite direction, is $M([c_1^t]^{-1}) = [c_2^t]^{-1}$.

If we repeat this on c_2^t , which surrounds H_{-1}^B , we can see that its forward iterate must surround H_0^B . We also know that its endpoints will be on \mathbb{S}^T between the right-most endpoint of c_2^t and \mathbf{z}_x^R . However, H_0^B lies outside the complex; consequently, the forward mapping of c_2^t intersects \mathbb{S}^B two times. Since a bridge can only intersect \mathbb{S}^T or \mathbb{S}^B at its endpoints, the forward mapping of c_2^t must be divided into three bridges: i.) the first bridge has its first endpoint on \mathbb{S}^T and second on \mathbb{S}^B , ii.) the second bridge has both endpoints on \mathbb{S}^B and surrounds H_0^B , and iii.) the third bridge has its first endpoint on \mathbb{S}^B , and final endpoint on \mathbb{S}^T . We say that the bridge class c_2^t maps forward to a product of three bridge classes: $M(c_2^t) = f^{tb}[u_0^b]^{-1}[f^{tb}]^{-1}$. Furthermore, we have also uncovered the critical information generated by the theory: the bridge class $[u_0^b]^{-1}$ (and its inverse) lies outside the complex, so any bridge homotopic to c_2^t (regardless of direction) will have a portion that escapes at the next iterate. In addition, we can also see that this portion will escape to the left of the barriers.

Similarly, bridge c_2^b surrounds point-hole H_{-1}^T , and its forward mapping must surround H_0^T , which lies outside the complex. When mapped forward, the bridge class c_2^b intersects

\mathbb{S}^T two times, and it must be divided into three bridge classes; we say that $M(c_2^b) = f^{bt}[u_0^t]^{-1}[f^{bt}]^{-1}$. The bridge class $[u_0^t]^{-1}$ (and its inverse) lies outside the complex, so any bridge homotopic to c_2^b will have a portion escape at the next iterate, and this portion will escape to the right of the barriers.

6.4.8 Additional Bridges

As mentioned earlier, an important difference between this problem and earlier ones [67, 55, 56, 57, 58, 59, 60, 61, 62, 63, 64, 65, 66, 106] is that we are now examining a full scattering system, with particles approaching from and receding to infinite distance. (In previous work, we examined only “half-scattering,” i.e. escape from a confined region). A consequence is that the sets of bridges previously defined using only the unstable manifolds are no longer sufficient for describing our initial-condition lines.

To see why, we must study L_0 in detail. Fig. 6.10 shows a qualitative L_0 of Type II (green), \mathbb{S}^T , \mathbb{S}^B , S^L , and S^R (dotted curves; red), and \mathbb{U}^T , \mathbb{U}^B , U^L , and U^R (solid blur curves). The starting point of L_0 is labeled A , and its endpoint is labeled E . One may follow L_0 from points A to B to C to D to E .

In the past [67], we defined bridges as homotopy classes of unstable manifold segments with endpoints on the stable manifolds bounding the complex, \mathbb{S}^T or \mathbb{S}^B . However, one can see that segments AB , BC , and DE of L_0 do not have both endpoints on \mathbb{S}^T or \mathbb{S}^B . Each of these segments has at least one endpoint on S^L . Furthermore, no unstable manifold can intersect S^L (if it did, the intersection would map to both an unstable fixed point and $x = -\infty$ as $t \rightarrow -\infty$). It follows that segments AB , BC , and DE cannot be homotopic to any bridges formed by segments of unstable manifolds. Hence, previous methods are not capable of fully describing the topological structure of all segments of L_0 for the present system. Similar problems occur for L_0 of Type IV.

We must develop a more general definition of bridges. From Fig. 6.10 it is plain that we need an additional bridge or bridges that go from S^L to S^T , which are homotopic to segments BC and DE . We also need an additional bridge that begins and ends on S^L , and which lies “below” it, so that it is homotopic to segment AB . The endpoints of segment AB march toward the fixed point z_x^L as L_0 is mapped forward, and the segment stretches to the left and down as they do so. Since the desired bridge is the entire homotopy class for segment AB , the bridge class will always map to itself, and it represents a segment of L_0 that is directly reflected, without entering the complex.

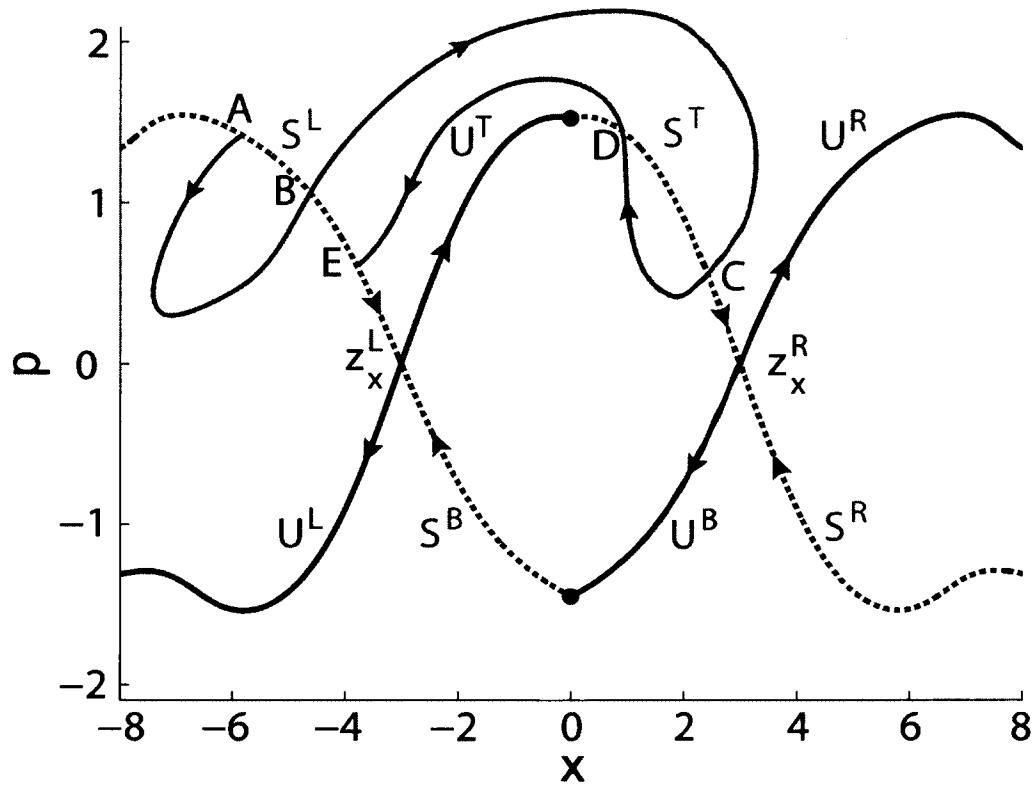


FIG. 6.10: Qualitative graph showing an initial-condition line and manifold segments. L_0 (green) is of Type II, S^T , and S^B , S^L , and S^R are plotted in red, while U^T , U^B , U^L , and U^R are plotted in blue. Since no unstable manifold can intersect S^L , the L_0 segments AB , BC , and DE cannot be homotopic to any bridge formed by an unstable manifold.

The same general arguments apply for L_0 representing particles approaching the barriers from the right. We need to include new bridges with endpoints on S^R . The types of new bridges that may be needed to accommodate L_0 can be summarized by the following. If particles approach from the left,

- Type S_{LL} : Both endpoints on S^L , lies “below” it.
- Type S_{LT} : One endpoint on S^L ; one endpoint on S^T .

If particles approach from the right,

- Type S_{RR} : Both endpoints on S^R , lies “above” it.
- Type S_{RB} : One endpoint on S^R ; one endpoint on S^B .

6.4.9 Topological Predictions

We now have all the tools necessary to begin the topological analysis of initial-condition lines through the barrier region. We start by computing the stable manifolds, and constructing the appropriate L_0 . We then iterate U_0^B and U_0^T forward J times, and identify all J -neighbors along S_0^T and S_0^B . These J -neighbor pairs are then mapped forward $J - k$ times and backward k times, where k is the transition number of the J -neighbors, which yields all J -neighbors for the chosen J . We check for the existence of J -subneighbors along the stable manifold segment connecting every pair of J -neighbors. We then punch a point-hole in the phase plane in the appropriate place for each pair. We next determine all homotopy classes of bridges, including “additional” bridges which are not segments of unstable manifolds, give each a symbol, and develop an algebraic representation for how each symbol evolves.

Since the forward iterates of L_0 approach and stretch along unstable manifolds, L_0 evolves topologically in the same manner as the unstable manifolds. We develop a symbolic

representation for L_0 by decomposing it into segments, each of which has endpoints on \mathbb{S}^B , \mathbb{S}^T , S^L , or S^R , and does not otherwise intersect those stable manifolds (as in Fig. 6.10). Each of these segments is homotopic to a bridge class, which allows us to symbolically express L_0 as a product of symbols. The mapping of curves induces a mapping of symbols. Each symbol can be mapped algebraically an arbitrary number of times, allowing us to express the n^{th} forward iterate of L_0 , L_n , by iterating each symbol in L_0 n times. Certain symbols in L_n represent escape to the left of the barrier region (u_0^b and its inverse), and other symbols represent escape to the right of the barrier region (u_0^t and its inverse). The relative order of escape segments along L_0 is also predicted by this method.

The symbolic representation thus tells us: i.) the number of reflected escape segments that are forced to occur at each iterate, ii.) the number of transmitted escape segments that are forced to occur at each iterate, iii.) their relative order along L_0 . It should be noted that all three of these depend on the amount of initial topological information used, and that starting with more initial topological information may yield additional predicted escape segments.

The initial topological structure of the heteroclinic tangle and L_0 forces certain topological properties to be present at later times. Homotopic lobe dynamics predicts all escape segments, and their relative order, that are forced to occur as a result of the initial topological information. Every predicted escape segment must be seen in computations, but there may be other escape segments that occur, which are not forced by the initial topological structure. In this sense, one may think of homotopic lobe dynamics as a method for finding the minimal number, and relative order, of escape segments forced to occur at each iterate by the initial topological structure. As previously mentioned, choosing to begin the analysis with more initial topological information, i.e. choosing a higher J , may allow additional escape segments to be predicted at later times.

In the next section, we implement the method discussed here on a specific case, the

results of which were given in Sec. 6.3.

6.5 Case Study

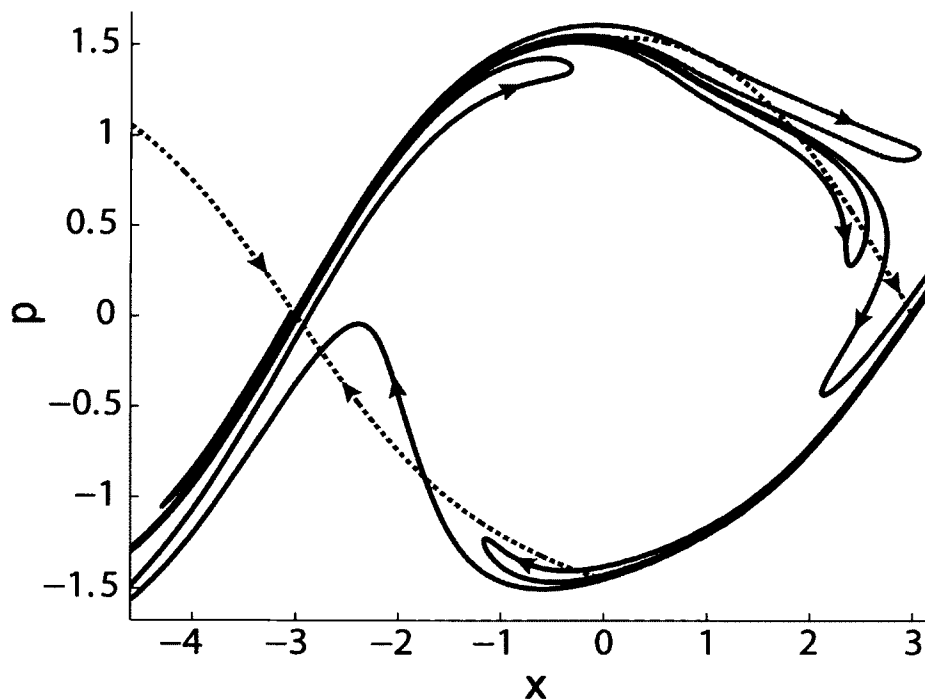


FIG. 6.11: Computed manifold segments and initial-condition line. \mathbb{S}^T , \mathbb{S}^B , and S^L (dotted red curves), \mathbb{U}^T , \mathbb{U}^B , and the first $J = 3$ forward iterates of U_0^T and U_0^B (blue curves), and L_0 (green), which is a forward iterate of l_0 . L_0 is chosen at the earliest iterate to have an intersection with \mathbb{S}^T , and is of Type II. The endpoints of L_0 are on S^L , at far left. The segment below S^L forms a loop.

Recall that our system parameters are $\hat{x} = 3$, $U_0 = 1$, $\alpha = 0.5$, $\omega = 2\pi/3$, $\phi = \pi/2$, $\sigma = 1$, and $m = 1$. We examine an initial-condition line of particles approaching the barriers from the left with initial momentum $p_0 \approx 1.50$ (more precisely $p_0 \approx 1.49959$).

Manifolds are constructed by iterating initial-condition lines that begin very close to,

and lying on eigenvectors passing through, the unstable fixed points. Stable manifolds are calculated by iterating the appropriate initial-condition lines backward, and unstable manifolds are computed by iterating forward. We must choose a number of iterates, J , to iterate the fundamental unstable manifold segments to use as the basis for our analysis; for this example, we have chosen three iterates, i.e., $J = 3$.

Examining S^B , S^T , and S^L , we see that our initial momentum $p_0 \approx 1.50$ lies in Region III in Fig. 6.7. By the rules discussed earlier, we place one endpoint of l_0 on S^L , and give it a width of $\Delta x_0 = p_0 2\pi / m\omega$. This l_0 is the solid green horizontal curve. Due to its construction, at a certain forward iterate, this l_0 will evolve into a Type II L_0 . We choose L_0 to be the earliest iterate at which l_0 intersects S^T . This L_0 is shown in Fig. 6.11, and its qualitative topological structure can be seen in Fig. 6.10.

Figure 6.12 shows all J -neighbors along S_0^T (a) and S_0^B (b). In Fig. 6.12(a), the J -neighbors along S_0^T , which we call (α, β) , are marked by large black dots. In Fig. 6.12(b), the J -neighbors along S_0^B , which we call (γ, δ) , are marked by large yellow dots. Since both (α, β) and (γ, δ) have transition number $k = J = 3$, all other pairs of J -neighbors can be found by mapping (α, β) and (γ, δ) backwards $k = 3$ times. Fig. 6.12(a) also shows the pair of J -neighbors $(\gamma^{-2}, \delta^{-2})$, which are the pair (γ, δ) mapped backwards twice. The J -neighbors $(\alpha^{-2}, \beta^{-2})$ shown in Fig. 6.12(b) are (α, β) mapped backwards twice.

We need to determine if each pair of J -neighbors (eight total) has any J -subneighbors in between them. To do this, we must determine if L_0 enters the domain-hole associated with each pair of J -neighbors. In this example, L_0 only enters domain-holes associated with the J -neighbor pair (γ, δ) and their mappings. Fig. 6.13 shows a zoom of the $(\gamma^{-2}, \delta^{-2})$ domain-hole, along with L_0 . The J -neighbors $(\gamma^{-2}, \delta^{-2})$ are represented by large black dots. Since L_0 intersects the stable manifold segment connecting the J -neighbors, we must identify and use J -subneighbors when puncturing point-holes in the plane for the series of holes associated with (γ, δ) and their mappings. The J -subneighbors are represented

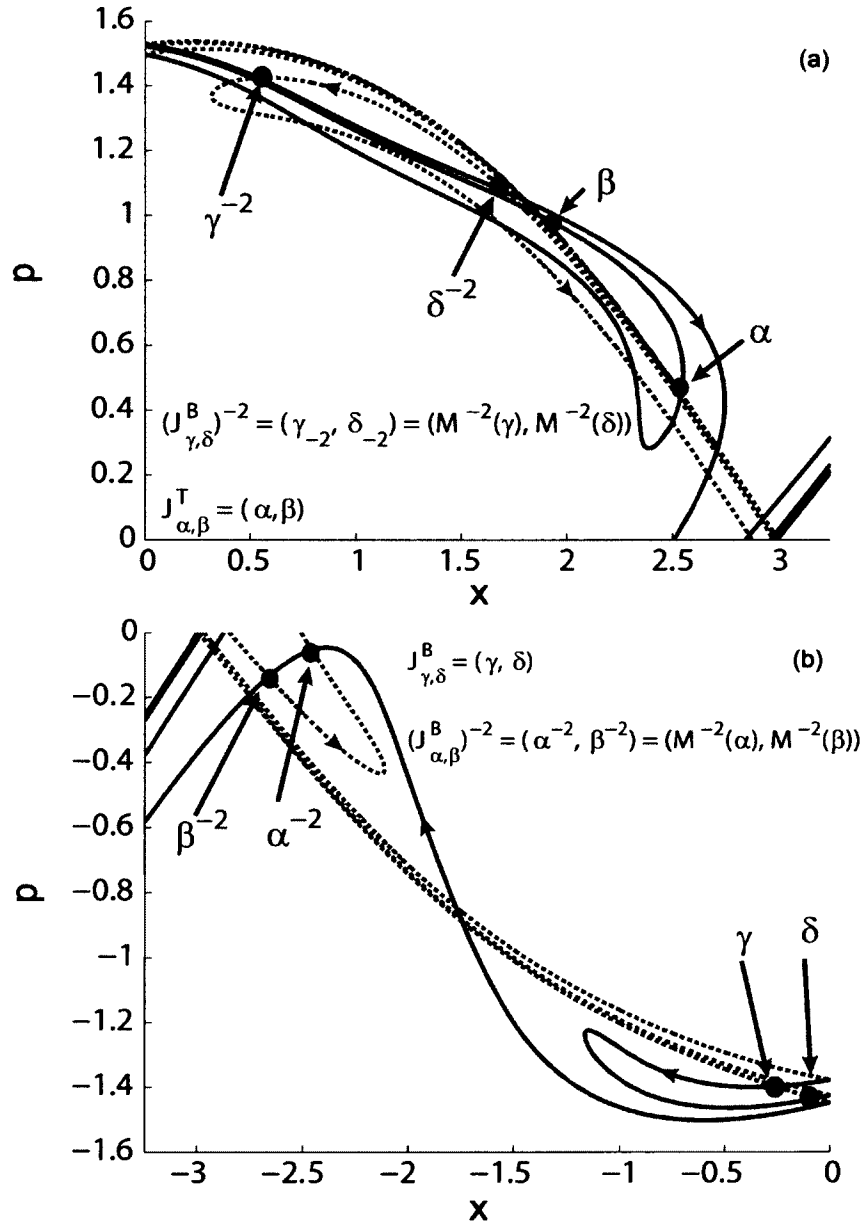


FIG. 6.12: J -neighbors. (a) Upper-right section of heteroclinic tangle. The black dots are J -neighbors along S_0^T , denoted (α, β) . (b) Lower-left section of heteroclinic tangle. The yellow dots are J -neighbors along S_0^B , denoted (γ, δ) . In (a), the yellow dots are the J -neighbors $(\gamma^{-2}, \delta^{-2})$, which are (γ, δ) from (b) mapped backwards twice. In (b), the black dots are the J -neighbors $(\alpha^{-2}, \beta^{-2})$, which are (α, β) from (a) mapped backwards twice.

by large green dots in Fig. 6.13. The entire shaded region is the domain hole (yellow and pink), and the subhole is the yellow portion.

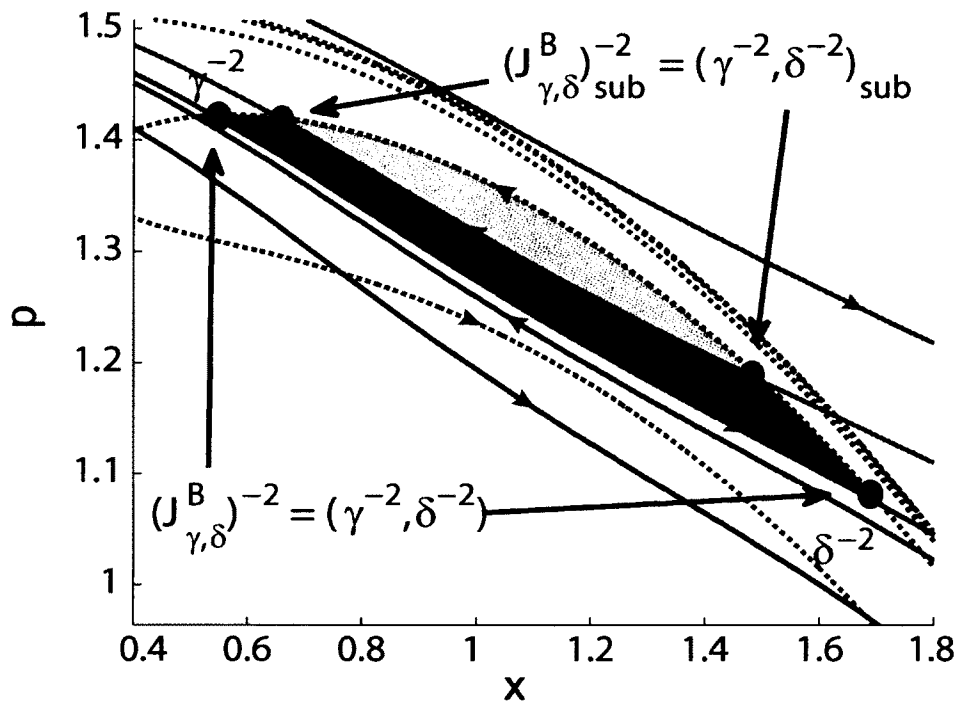


FIG. 6.13: J -neighbors and J -subneighbors. Zoom of the J -neighbors $(J_{\gamma,\delta}^B)^{-2} = (\gamma^{-2}, \delta^{-2}) = (M^{-2}(\gamma), M^{-2}(\delta))$. The J -neighbors are marked by the large black dots at the intersections between stable (red curves) and unstable (blue curves) manifolds. This pair of J -neighbors has a set of J -subneighbors associated with it, which are represented by the large green dots. The domain-hole for the J -neighbor pair is colored in yellow and pink, and the subhole associated with the J -subneighbor pair is the yellow portion.

We must place a point-hole within the subhole associated with the J -neighbor pair $(\gamma^{-2}, \delta^{-2})$, and arbitrarily close to either of the J -subneighbors. The location of the point-hole should be within the yellow region of Fig. 6.13, and arbitrarily close to either of the green dots. We then map this point-hole forward and backward the appropriate number of times, again puncturing a hole in the plane for each one.

No J -subneighbors exist between any of the $(M^n(\alpha), M^n(\beta))$ J -neighbors for this L_0 , so we choose a point-hole inside the domain-hole associated with (α, β) , and place it arbitrarily close to either α or β . We then map it backward $k = 3$ times, puncturing a hole in the phase plane each time.

One must note that we are not necessarily free to place a point-hole arbitrarily close to every J -neighbor pair that does not have a pair of J -subneighbors along L_0 associated with it. If L_0 creates a pair of J -subneighbors between a pair of J -neighbors (f, g) , then L_1 will create a pair of J -subneighbors between the J -neighbors $(M(f), M(g)) = (h, i)$. For this reason, one should not place a point-hole arbitrarily close to either (h, i) ; instead, one must place the point-hole arbitrarily close to a J -subneighbor associated with (f, g) , and then map it forward and backward. This method ensures that all point-holes associated with this series of holes are placed in the appropriate location.

Bridges of the manifolds are shown in Fig. 6.9, and their homotopy classes are summarized here. Homotopy classes are determined according to bridge's relations to the punctured holes.

- f^{bt} : Starts on \mathbb{S}^B , ends on \mathbb{S}^T , passes below H_{-3}^B and above H_{-1}^T , immediately surrounds no domain-holes.
- f^{tb} : Starts on \mathbb{S}^T , ends on \mathbb{S}^B , passes below H_{-1}^B and above H_{-3}^T , immediately surrounds no domain-holes.
- c_1^t : Starts and ends on \mathbb{S}^T ; surrounds H_{-2}^B .
- c_2^t : Starts and ends on \mathbb{S}^T ; surrounds H_{-1}^B .
- u_0^t : Starts and ends on \mathbb{S}^T ; surrounds H_0^T .
- u_0^b : Starts and ends on \mathbb{S}^T ; surrounds H_0^B .

- c_1^b : Starts and ends on \mathbb{S}^B ; surrounds H_{-2}^T .
- c_2^b : Starts and ends on \mathbb{S}^B ; surrounds H_{-1}^T .

Figures 6.10 and 6.11 show that some segments of L_0 cannot be described by existing bridges, i.e., by segments of unstable manifolds. We need to create two new bridges for our analysis, with homotopy classes:

- S_{LL} : Begins and ends on S^L , lies “below” it, and passes under H_B^{-3} .
- S_{LT} : Begins on S^L ; ends on \mathbb{S}^T .

We have to choose an appropriate endpoint of S_{LT} on \mathbb{S}^T so that segments of L_0 will be homotopic to it. We will choose S_{LT} to be arbitrarily close to one of the segments of L_0 that goes from S^L to \mathbb{S}^T .

Figure 6.14 shows a qualitative, but topologically correct, graph of L_0 (solid green curve) along with an example bridge from each homotopy class needed to carry out the topological analysis. The direction of L_0 is consistent with our chosen direction of l_0 (left-to-right). By construction, the endpoints lie on S^L . The starting point is labeled A. Segment AB is homotopic to S_{LL} . Segment BC is homotopic to bridge S_{LT} , which has a direction going from S^L to \mathbb{S}^T . We choose S_{LT} to lie arbitrarily close to segment BC , and any L_n segment with one endpoint on S^L , and the other endpoint between P_0^T and Q_0^T on \mathbb{S}^T , will be homotopic to S_{LT} (or its inverse). Segment CD is homotopic to $(c_1^t)^{-1}$. Segment DE is homotopic to the inverse of S_{LT} .

Now the theory is complete, and we return to Section 6.2. The symbols and mappings for these homotopy classes are given by Eq. (6.3). L_0 is expressed as a product of these symbols, given by Eq. (6.4). Each symbol in L_0 is algebraically mapped forward n times, which gives the symbolic representation for L_n . The first few symbolic representations are given by Eqs. (6.6)-(6.8). Each instance of u_0^b (or its inverse) or u_0^t (or its inverse) in L_n

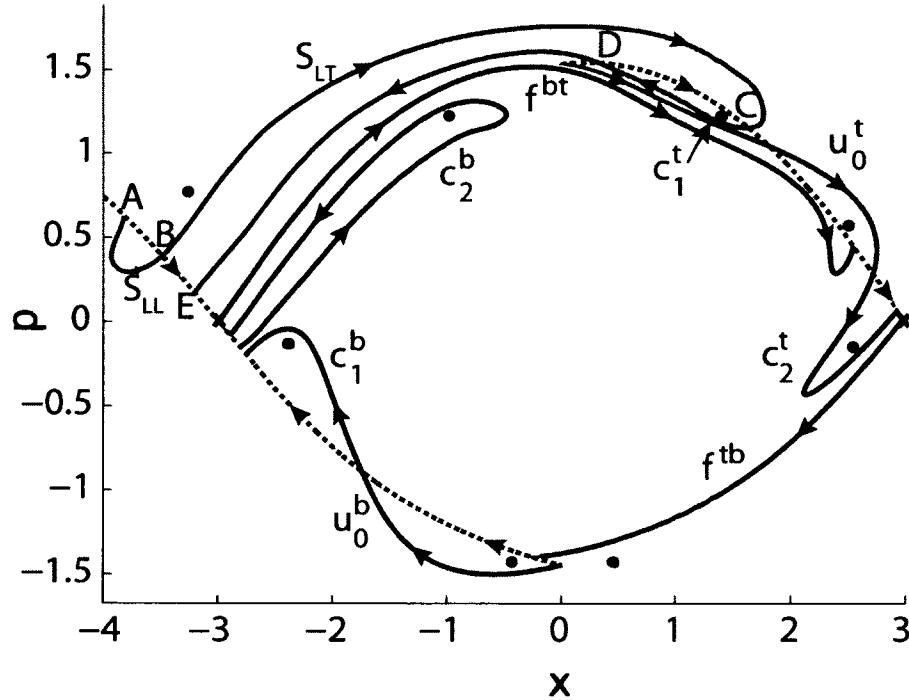


FIG. 6.14: Bridge classes. Qualitative rendering of S^T , S^B , and S^L (dotted red curves), L_0 (green), and all bridges necessary for the topological analysis for this example. The bridges S_{LL} and S_{LT} have at least one endpoint on S^L , and thus are not unstable manifold segments. All other bridges are unstable manifold segments (blue).

represents a segment that escapes to the left or right, respectively, of both barriers at the n^{th} iterate. Comparison and discussion of predicted and computed escape segments for this case were given in Sec. 6.3.

Generalizing and extending homotopic lobe dynamics (HLD) for use with full scattering systems has many purposes. In a ballistic atom pump, the primary goal is to calculate the net flow of particles that approach the barriers from both sides, and HLD allows one to use stable manifolds to place lower bounds on the number of particles which are transmitted or reflected by the barriers for all incoming energies (this is much faster

than computing all trajectories). In this chapter, HLD is primarily used to explain the fractal structure seen in escape-time graphs. In other contexts, HLD can also be used to find a minimal set of closed or periodic orbits [63, 128] in order to carry out semiclassical sums, to calculate topological entropy [67, 66, 106] (a measure of the complexity of the dynamics), and to partition mixed phase spaces [127].

6.6 Remarks

We have shown how to extend homotopic lobe dynamics so that it can be used to study a full scattering process with a heteroclinic tangle. We have shown how to select endpoints of the initial condition line, where to puncture point-holes in the phase plane, and we have shown that additional bridge types are necessary for the topological analysis. The methods outlined in this chapter are very general, and can thus be used for a large number of systems involving chaotic transport. Homotopic lobe dynamics can now be applied to full scattering systems in order to calculate topological entropy [67, 66, 106], partition mixed phase spaces [127], find a minimal set of closed or periodic orbits [63, 128], and sort interfering trajectories into groups for use in semiclassical theory.

This type of analysis allows one to make reliable predictions about some properties of a chaotic system at intermediate times, using topological properties of the system at early times. In this chapter, we have shown that homotopic lobe dynamics both explains and predicts the fractal structure seen in escape-time graphs for a ballistic atom pump, i.e., for particles incident on two Gaussian-shaped potential barriers oscillating out-of-phase with one another.

Eventually we hope that homotopic lobe dynamics can be automated, so that numerical computations of stable and unstable manifolds can extract the symbolic dynamics and its predictions without human intervention. That advance will require knowledge of

the application of homotopic lobe dynamics to many specific systems, such as the one considered here.

CHAPTER 7

Conclusion

We have shown that the quantum description of wavepacket scattering from amplitude-modulated Gaussian barriers yields final momentum probabilities that are populated at momenta satisfying $E_n = E_0 + n\hbar\omega$, where ω is the oscillation frequency of the barrier. Analyzing the underlying classical dynamics reveals that peaks seen in the quantum description are small outside the bounds of classically-scattered momenta. The semiclassical analysis reveals that many trajectories end at all momentum values within the classically-allowed range. Interference among these many trajectories can be broken down into two distinct types: (i) intracycle interference, which contains only trajectories from within one cycle of the periodic final momentum versus initial position graph; this type of interference determines the relative heights of the peaks seen in quantum calculations, and (ii) intercycle interference, which contains interference across all cycles. Intercycle interference leads to the emergence of the sharp peaks seen in the quantum calculation, and they occur at the same momenta in both the semiclassical and quantum descriptions.

When two barriers are present, we have shown that such pumps can preferentially pump particles from one reservoir to the other under certain conditions. If one barrier has

a fixed height and the other oscillates, it is possible to construct pumps that only allow net particle transport in one direction for certain initial particle energies, while in a different initial particle energy range, net transport is only possible in the opposite direction. It is not possible to predict the magnitude of net particle transport without detailed calculations, however. Symmetric pumps, which have identical barriers that oscillate between the same minimum and maximum amplitudes and oscillate at the same frequency but with a relative phase difference between oscillations, can also preferentially pump particles under certain conditions. Specifically, if a uniform distribution of initial conditions is used, no net pumping occurs; this classical result matches results obtained from quantum studies on similar systems. However, if only finite ranges of initial particle energies are considered, such pumps can create net particle transport in either direction. The magnitude and direction of this net transport is also not predictable without computations, and both of these properties are highly sensitive to barrier parameters.

We have also shown that classical scattering of monoenergetic particles from such pumps can create a net imbalance in the total energy in each reservoir after scattering. This imbalance can be caused by a transfer of energy between the pump and the particles (or vice versa), and by a flow of energy between reservoirs. Interestingly, the direction of energy change is distinct from the direction of net particle transport, and can occur even when there is no net particle transport. Ballistic atom pumps can also heat or cool one or both reservoirs, and the heating or cooling is also independent of energy flow and net particle transport. In addition, it is possible for particles of certain initial energies to give energy (on average) to the pump; this occurs for relatively high incident energies, when there is no net particle transport.

Finally, we have generalized and modified an existing topological theory, homotopic lobe dynamics (HLD), so that it can be used to study full-scattering problems. This is the first implementation of HLD on a full-scattering problem in which transport is governed

by a heteroclinic tangle. Modifications were necessary primarily due to the differences between previously-studied lines of initial conditions and ones necessary for this problem. We have shown that additional bridge classes may be necessary for this type of analysis, and have shown how to modify previous notions of where holes should be punched in the phase plane. The form of HLD implemented on the double-barrier ballistic atom pump predicts and explains the underlying mechanism responsible for the fractal-like patterns seen in computed escape times. However, as in previous studies, escape segments that are not predicted eventually emerge. It is possible to predict some of these escape segments by using more initial topological information as the basis for HLD, but HLD is not capable of predicting all escape segments. For this reason, we say that HLD predicts a minimal set of topologically-forced escape segments. All predicted segments are seen in computed escape segments, but the unpredicted escape segments dominate escape-time plots at high iterates of the map.

The results presented in this dissertation can be extended by future research. A ballistic atom pump of the type discussed here requires only a time-dependent potential energy in the channel connecting the reservoirs, and all results presented here concern potential energies with one or two repulsive barriers. Multiple oscillating potential energy wells can also allow net particle transport in either direction, and their preferential pumping of particles should be compared and contrasted with the repulsive barriers examined here. In the case of two oscillating rectangular barriers, we showed that chaotic trajectories only emerge when the barriers are separated. In the case of wells that oscillate between 0 and $-V_0$ ($V_0 > 0$), however, chaotic trajectories will be present even when the wells are not separated. The influence of these more-complex particle trajectories on net particle pumping should be studied. A potential energy consisting of two oscillating Gaussian-shaped wells will also likely prove to be an interesting study, as transport is expected to be governed by two homoclinic tangles emerging from the same fixed point.

The effect of introducing more than two barriers (or wells) can also be examined, as well as using combinations of barriers and wells. Using a time-dependent oscillation frequency, $\omega(t)$, may also dramatically affect net particle pumping. One could also examine the effect of allowing each barrier or well to oscillate at different frequencies. Future studies should also consider the effect of the trapping potential used to confine the BEC, which was neglected in this dissertation. In addition, considering inter-particle interactions in future research would greatly extend the results presented here.

APPENDIX A

Introduction to Semiclassical Theory

This appendix gives an overview of one-dimensional semiclassical approximations in configuration and momentum space. The derivations here are valid only in the classically-allowed regions, but they can be extended into classically-forbidden regions. The equations here are given for time-independent Hamiltonians, but the arguments outlined here can be applied to time-dependent systems. This appendix is intended to give a broad overview of the simplest aspects of semiclassical theory; for a detailed implementation of these approaches on the time-dependent ballistic atom pump in both classically-allowed and classically-forbidden regions, see the next appendix.

Table A.1 provides some of the basic equations for both configuration and momentum space, and the reader is encouraged to notice the similarities present in many of them, as well as to refer to the table while reading the appendix.

	Configuration Space	Momentum Space
Hamiltonian	$H(p, q)$	$H(p, q)$
Quantum Rule	$p \rightarrow -i\hbar\partial/\partial q$	$q \rightarrow +i\hbar\partial/\partial p$
Schrödinger Equation	$\left[H\left(-i\hbar\frac{\partial}{\partial q}, q\right) - E \right] \Psi(q) = 0$ $\left[\frac{1}{2m} \left(-i\hbar\frac{\partial}{\partial q}\right)^2 + V(q) - E \right] \Psi(q) = 0$	$\left[H\left(p, i\hbar\frac{\partial}{\partial p}\right) - E \right] \tilde{\Psi}(p) = 0$ $\left[\frac{p^2}{2m} + V\left(i\hbar\frac{\partial}{\partial p}\right) - E \right] \tilde{\Psi}(p) = 0$
Transform	$\Psi(q) = \frac{1}{\sqrt{-2\pi i\hbar}} \int e^{ipq/\hbar} \tilde{\Psi}(p) dp$	$\tilde{\Psi}(p) = \frac{1}{\sqrt{2\pi i\hbar}} \int e^{-ipq/\hbar} \Psi(q) dq$
WKB Approx.	$\Psi_{WKB}(q) = \frac{C \exp(\pm i \int \mathcal{P}(q') dq' / \hbar)}{[\mathcal{P}(q)]^{1/2}}$ $\Psi_{WKB}(q) = \frac{C \exp(iS(q)/\hbar)}{[\frac{\partial H(p, q)}{\partial p}]^{1/2}}$	$\tilde{\Psi}_{WKB}(p) = \frac{D \exp(-i \int \mathcal{Q}(p') dp' / \hbar)}{ F(q(p)) ^{1/2}}$ $\tilde{\Psi}_{WKB}(p) = \frac{D \exp(-i\tilde{S}(p)/\hbar)}{ \frac{\partial H(p, q)}{\partial q} ^{1/2}}$

TABLE A.1: Semiclassical Formulas.

A.1 WKB Approximation in Configuration Space

Starting with the classical Hamiltonian

$$\left[\frac{p^2}{2m} + V(q) - E \right] \tilde{\Psi}(q) = 0 \quad (\text{A.1})$$

we replace with p with the quantum operator

$$p \rightarrow -i\hbar\frac{\partial}{\partial q} \quad (\text{A.2})$$

to obtain

$$\left[-\frac{\hbar^2}{2m} \frac{\partial^2}{\partial q^2} + V(q) - E \right] \Psi(q) = 0. \quad (\text{A.3})$$

We seek a semiclassical approximation to a quantum wave function of the form,

$$\Psi(q) = A(q) \exp\left(\frac{iS(q)}{\hbar}\right). \quad (\text{A.4})$$

Inserting this form of $\Psi(q)$ into Eq. A.3, we obtain

$$0 = \left[-\frac{\hbar^2}{2m} \frac{\partial^2}{\partial q^2} + V(q) - E \right] A(q) \exp\left(\frac{iS(q)}{\hbar}\right) \quad (\text{A.5})$$

$$0 = e^{iS(q)/\hbar} \left[-\frac{\hbar^2 \partial^2}{2m \partial q^2} - \frac{i\hbar}{m} \frac{\partial S(q)}{\partial q} \frac{\partial}{\partial q} - \frac{i\hbar}{2m} \frac{\partial^2 S(q)}{\partial q^2} + \frac{1}{2m} \left(\frac{\partial S(q)}{\partial q} \right)^2 + V(q) - E \right] A(q) \quad (\text{A.6})$$

If we collect terms in powers of \hbar , we have

$$\mathcal{O}(\hbar^0) = e^{iS(q)/\hbar} \left[-\frac{1}{2m} \left(\frac{\partial S(q)}{\partial q} \right)^2 + V(q) - E \right] A(q) \quad (\text{A.7})$$

$$\mathcal{O}(\hbar^1) = e^{iS(q)/\hbar} \left[-\frac{i\hbar}{m} \frac{\partial S(q)}{\partial q} \frac{\partial A(q)}{\partial q} - A(q) \frac{i\hbar}{2m} \frac{\partial^2 S(q)}{\partial q^2} \right] \quad (\text{A.8})$$

$$\mathcal{O}(\hbar^2) = -e^{iS(q)/\hbar} \frac{\hbar^2}{2m} \frac{\partial^2 A(q)}{\partial q^2} \quad (\text{A.9})$$

For our approximation, we will assume \hbar is small, and thus that the term of $\mathcal{O}(\hbar^2)$ can be neglected. We then set Eqs. A.8 and A.9 equal to zero and solve for $S(q)$ and $A(q)$. We

first set Eq. A.8 equal to zero:

$$-\frac{1}{2m} \left(\frac{\partial S(q)}{\partial q} \right)^2 + V(q) - E = 0 \quad (\text{A.10})$$

$$\left(\frac{\partial S(q)}{\partial q} \right)^2 = 2m [E - V(q)] \quad (\text{A.11})$$

$$\frac{dS(q)}{dq} = (2m [E - V(q)])^{1/2} \quad (\text{A.12})$$

$$S(q) = \pm \int_{q_0}^q \mathcal{P}(q') dq' \quad (\text{A.13})$$

where we have used $\partial S(q)/\partial q = dS(q)/dq$. The function $\mathcal{P}(q)$ should not be regarded as the coordinate p ; it is a function describing a curve in phase space. (In the next appendix it will be shown that this curve is a constant-time slice of the Lagrangian manifold swept out by the trajectories we are using to construct a semiclassical approximation). Setting the terms of $\mathcal{O}(\hbar^1)$ equal to zero yields,

$$\frac{\partial S(q)}{\partial q} \frac{\partial A(q)}{\partial q} = -A(q) \frac{1}{2} \frac{\partial^2 S(q)}{\partial q^2} \quad (\text{A.14})$$

$$\frac{dA(q)/dq}{A(q)} = -\frac{1}{2} \frac{d^2 S(q)/dq^2}{dS(q)/dq} \quad (\text{A.15})$$

$$\ln A(q) = -\frac{1}{2} \ln dS(q)/dq C \quad (\text{A.16})$$

$$A(q) = C |dS(q)/dq|^{-1/2} = C |\mathcal{P}(q)|^{-1/2} \quad (\text{A.17})$$

where C is a constant. Substituting these expressions for $A(q)$ and $S(q)$ into $\Psi(q)$ gives

$$\Psi(q) = A(q) \exp \left(\frac{iS(q)}{\hbar} \right) \quad (\text{A.18})$$

$$\Psi(q) = C \left| \frac{1}{\mathcal{P}(q)} \right|^{1/2} \exp \left(\frac{\pm i \int_{q_0}^q \mathcal{P}(q') dq'}{\hbar} \right). \quad (\text{A.19})$$

This primitive approximation is valid in classically-allowed regions, away from turning points (regions where $E \approx V(q)$). The calculation can be extended into classically-forbidden regions, but for now we switch our attention to constructing a similar approximation in momentum space, which is what we are interested in for ballistic atom pumps.

A.2 WKB Approximation in Momentum Space

We again start with a time-independent Hamiltonian, and substitute in a quantum operator,

$$\left[\frac{p^2}{2m} + V(i\hbar \frac{\partial}{\partial q}) - E \right] \tilde{\Psi}(p) = 0. \quad (\text{A.20})$$

We define $\hat{q} = i\hbar \partial / \partial p$, so that $V(i\hbar \partial / \partial p) = V(\hat{q})$. As in the previous section, we assume a form for the semiclassical wave function, $\tilde{\Psi}(p) = \tilde{A}(p) \exp(i\tilde{S}(p)/\hbar)$. We wish to again evaluate all derivatives in the Hamiltonian, collect the resulting terms in powers of \hbar , and set them equal to zero to obtain solutions for $\tilde{A}(p)$ and $\tilde{S}(q)$. To achieve this, we assume without proof that $V(\hat{q})$ can be expressed as a convergent power series,

$$V(\hat{q}) = V \left(i\hbar \frac{\partial}{\partial p} \right) = \sum_n \frac{V^n}{n!} \left(i\hbar \frac{\partial}{\partial p} \right)^n. \quad (\text{A.21})$$

Since the derivatives we need to evaluate are contained in the operator $V(\hat{q})$, we begin by expressing $V(\hat{q})$ as a power series, and applying the operator $V(\hat{q})$ to $\tilde{\Psi}(p)$.

$$V \left(i\hbar \frac{\partial}{\partial p} \right) \tilde{\Psi}(p) = V \left(i\hbar \frac{\partial}{\partial p} \right) \left[\tilde{A}(p) \exp \left(i\tilde{S}(p)/\hbar \right) \right] \quad (\text{A.22})$$

$$= \sum_n \frac{V^n}{n!} \left(i\hbar \frac{\partial}{\partial p} \right)^n \left[\tilde{A}(p) \exp \left(i\tilde{S}(p)/\hbar \right) \right] \quad (\text{A.23})$$

We first examine the lowest-order, $n = 1$ term: $(i\hbar\partial/\partial p) [\tilde{A}(p) \exp(i\tilde{S}(p)/\hbar)]$:

$$i\hbar\frac{\partial}{\partial p} [\tilde{A}(p) \exp(i\tilde{S}(p)/\hbar)] = \exp\left(i\frac{\tilde{S}(p)}{\hbar}\right) \left[i\hbar\frac{\partial\tilde{A}(p)}{\partial p} - \hbar\tilde{A}(p) \left(\frac{\partial\tilde{S}(p)}{\hbar\partial p}\right) \right] \quad (\text{A.24})$$

$$= \exp\left(i\frac{\tilde{S}(p)}{\hbar}\right) \left[i\hbar\frac{\partial}{\partial p} - \left(\frac{\partial\tilde{S}(p)}{\partial p}\right) \right] \tilde{A}(p) \quad (\text{A.25})$$

$$= \exp\left(i\frac{\tilde{S}(p)}{\hbar}\right) [Q(p) + \hat{q}] \tilde{A}(p). \quad (\text{A.26})$$

using the definition $Q(p) = -\partial\tilde{S}(p)/\partial p$. For the next-order ($n = 2$) term, we square the operator \hat{q} , and see that $\hat{q}^2\tilde{\Psi}(p)$ is

$$\left(i\hbar\frac{\partial}{\partial p}\right)^2 \tilde{\Psi}(p) = \left(i\hbar\frac{\partial}{\partial p}\right)^2 [\tilde{A}(p) \exp(i\tilde{S}(p)/\hbar)] \quad (\text{A.27})$$

$$= \left(i\hbar\frac{\partial}{\partial p}\right) \left[\exp\left(i\frac{\tilde{S}(p)}{\hbar}\right) [Q(p) + \hat{q}] \tilde{A}(p) \right] \quad (\text{A.28})$$

$$= \exp\left(i\frac{\tilde{S}(p)}{\hbar}\right) \left[i\hbar\left(\frac{i}{\hbar}\frac{\partial\tilde{S}(p)}{\partial p}\right) [Q(p)\tilde{A}(p) + \hat{q}\tilde{A}(p)] \right] \quad (\text{A.29})$$

$$+ \hat{q} \left(Q(p)\tilde{A}(p) + \hat{q}^2\tilde{A}(p) \right) \quad (\text{A.30})$$

$$= \exp\left(i\frac{\tilde{S}(p)}{\hbar}\right) \left[Q(p) [\hat{q}\tilde{A}(p) + Q(p)\tilde{A}(p)] \right. \\ \left. + i\hbar\frac{\partial Q(p)}{\partial p}\tilde{A}(p) + Q(p)i\hbar\frac{\partial\tilde{A}(p)}{\partial p} + \hat{q}^2\tilde{A}(p) \right]$$

$$= \exp\left(i\frac{\tilde{S}(p)}{\hbar}\right) \left[2Q(p)\hat{q} + Q^2(p) + \hat{q}^2 + i\hbar\frac{\partial Q(p)}{\partial p} \right] \tilde{A}(p) \quad (\text{A.31})$$

$$= \exp\left(i\frac{\tilde{S}(p)}{\hbar}\right) [Q(p) + \hat{q}]^2 \tilde{A}(p). \quad (\text{A.32})$$

Repeated application of higher-order powers of the operator \hat{q}^n shows that

$$\left(i\hbar\frac{\partial}{\partial p}\right)^n = \exp\left(i\frac{\tilde{S}(p)}{\hbar}\right) [Q(p) + \hat{q}]^n \tilde{A}(p). \quad (\text{A.33})$$

We wish to collect terms in powers of \hbar , and neglect terms of order \hbar^2 and higher. For the $n = 1$ terms (Eq. A.26),

$$[Q(p) + \hat{q}] \tilde{A}(p) = Q(p)\tilde{A}(p) + i\hbar\frac{\partial\tilde{A}(p)}{\partial p}, \quad (\text{A.34})$$

the term $Q(p)\tilde{A}(p)$ is of order \hbar^0 , and the term $i\hbar\partial\tilde{A}(p)/\partial p$ is of order \hbar^1 . The $n = 2$ terms (Eq. A.32)

$$[Q(p) + \hat{q}]^2 \tilde{A}(p) = \left[2Q(p)\hat{q} + Q^2(p) + \hat{q}^2 + i\hbar\frac{\partial Q(p)}{\partial p}\right] \tilde{A}(p) \quad (\text{A.35})$$

can be collected in powers of \hbar as

$$\mathcal{O}(\hbar^0) = Q^2(p)\tilde{A}(p) \quad (\text{A.36})$$

$$\mathcal{O}(\hbar^1) = 2Q(p)\hat{q}\tilde{A}(p), \quad i\hbar\frac{\partial Q(p)}{\partial p}\tilde{A}(p) \quad (\text{A.37})$$

$$\mathcal{O}(\hbar^2) = \hat{q}^2\tilde{A}(p). \quad (\text{A.38})$$

The $n = 3$ case includes terms

$$[Q(p) + \hat{q}]^3 \tilde{A}(p) = \left[Q^3(p) + 3Q^2(p)\hat{q} + 3Qi\hbar\frac{\partial Q(p)}{\partial p} + \mathcal{O}(\hbar^2)\right] \tilde{A}(p), \quad (\text{A.39})$$

and these can be collected in terms of powers of \hbar as

$$\mathcal{O}(\hbar^0) = Q^3(p)\tilde{A}(p) \quad (\text{A.40})$$

$$\mathcal{O}(\hbar^1) = 3Q^2(p)\hat{q}\tilde{A}(p) , 3Qi\hbar\frac{\partial Q(p)}{\partial p}\tilde{A}(p) \quad (\text{A.41})$$

It can be shown via mathematical induction that the terms of order \hbar^0 and \hbar^1 from $[Q(p) + \hat{q}]^n$ can be written as:

$$\mathcal{O}(\hbar^0) = Q^n(p), \quad (\text{A.42})$$

$$\mathcal{O}(\hbar^1) = nQ^{n-1}(p)\hat{q} , \frac{n(n-1)}{2}Q^{n-2}(p)i\hbar\frac{\partial Q(p)}{\partial p}. \quad (\text{A.43})$$

Substituting Eq. A.33 into Eq. A.23, we can see that

$$V\left(i\hbar\frac{\partial}{\partial p}\right)\tilde{\Psi}(p) = \sum_n \frac{V^n}{n!} \left(i\hbar\frac{\partial}{\partial p}\right)^n \left[\tilde{A}(p)\exp\left(i\tilde{S}(p)/\hbar\right)\right] \quad (\text{A.44})$$

$$= \sum_n \frac{V^n}{n!} \exp\left(i\frac{\tilde{S}(p)}{\hbar}\right) [Q(p) + \hat{q}]^n \tilde{A}(p) \quad (\text{A.45})$$

$$= \sum_n \frac{V^n}{n!} \exp\left(i\frac{\tilde{S}(p)}{\hbar}\right) \left[Q^n(p) + nQ^{n-1}(p)\hat{q} + \frac{n(n-1)}{2}Q^{n-2}(p)i\hbar\frac{\partial Q(p)}{\partial p} + \mathcal{O}(\hbar^2)\right] \tilde{A}(p) \quad (\text{A.46})$$

We may think of the potential V in Eq A.46 as a power series in $Q(p)$, i.e.

$$V(Q(p)) = \sum_n \frac{V^n}{n!} Q^n(p); \quad (\text{A.47})$$

then

$$\frac{dV(Q(p))}{dQ(p)} = \sum_n \frac{V^n}{n!} n Q^{n-1}(p), \text{ and} \quad (\text{A.48})$$

$$\frac{d^2V(Q(p))}{dQ^2(p)} = \sum_n \frac{V^n}{n!} n(n-1) Q^{n-2}(p). \quad (\text{A.49})$$

Therefore we may write Eq. A.46 (neglecting terms of $\mathcal{O}(\hbar^2)$) as

$$\begin{aligned} V\left(i\hbar\frac{\partial}{\partial p}\right)\tilde{\Psi}(p) &= \exp\left(i\frac{\tilde{S}(p)}{\hbar}\right) \\ &\times \left[V(Q(p)) + \frac{dV(Q(p))}{dQ(p)}\hat{q} + \frac{d^2V(Q(p))}{dQ^2(p)}\frac{i\hbar}{2}\frac{\partial Q(p)}{\partial p} \right] \tilde{A}(p). \end{aligned} \quad (\text{A.50})$$

Returning to Eq. A.20 and substituting, we have

$$0 = \left[\frac{p^2}{2m} + V\left(i\hbar\frac{\partial}{\partial q}\right) - E \right] \tilde{\Psi}(p) \quad (\text{A.51})$$

$$= \left[\frac{p^2}{2m} + V\left(i\hbar\frac{\partial}{\partial q}\right) - E \right] \exp\left(i\frac{\tilde{S}(p)}{\hbar}\right) \tilde{A}(p) \quad (\text{A.52})$$

$$= \exp\left(i\frac{\tilde{S}(p)}{\hbar}\right) \left[\frac{p^2}{2m} + V(Q(p)) + \frac{dV(Q(p))}{dQ(p)}\hat{q} + \frac{d^2V(Q(p))}{dQ^2(p)}\frac{i\hbar}{2}\frac{\partial Q(p)}{\partial p} - E \right] \tilde{A}(p). \quad (\text{A.53})$$

Collecting terms in powers of \hbar , we have

$$\mathcal{O}(\hbar^0) = \frac{p^2}{2m} + V(Q(p)) - E \quad (\text{A.54})$$

$$\mathcal{O}(\hbar^1) = \frac{dV(Q(p))}{dQ(p)}\hat{q}\tilde{A}(p) + \frac{d^2V(Q(p))}{dQ^2(p)}\frac{i\hbar}{2}\frac{\partial Q(p)}{\partial p}\tilde{A}(p). \quad (\text{A.55})$$

For our approximation, we set each of these individually equal to zero. Identifying $Q(p) = \mathcal{Q}(p)$, we have

$$\mathcal{Q}(p) = -\frac{\partial \tilde{S}(p)}{\partial p} \quad (\text{A.56})$$

$$\tilde{S}(p) = -\int_{p_0}^p \mathcal{Q}(p') dp'. \quad (\text{A.57})$$

$\mathcal{Q}(p)$ is not to be regarded as the coordinate q ; rather, it is a function describing the curve in phase space. Note that the term $\tilde{S}(p)$ in the above equation and the term $S(q)$ are functions of different variables. We define the relationship between these two functions to be

$$S(q) = \mathcal{P}(q)q + \tilde{S}(\mathcal{P}(q)) \quad (\text{A.58})$$

$$S(\mathcal{Q}(p)) = p\mathcal{Q}(p) + \tilde{S}(p) \quad (\text{A.59})$$

We also explicitly note that the two functions $S(q)$ and $\tilde{S}(p)$ are the two functions that satisfy

$$\mathcal{P}(q) = \frac{\partial S(q)}{\partial q} \quad (\text{A.60})$$

$$\mathcal{Q}(p) = -\frac{\partial \tilde{S}(p)}{\partial p}. \quad (\text{A.61})$$

To solve A.55, we define $F(Q(p)) = -dV(Q(p))/dQ(p)$, and we have

$$0 = -F(Q(p))i\hbar \frac{\partial \tilde{A}(p)}{\partial p} - \frac{dF(Q(p))}{dQ(p)} \frac{i\hbar}{2} \frac{\partial Q(p)}{\partial p} \tilde{A}(p). \quad (\text{A.62})$$

Identifying $\partial Q(p)/\partial p = dQ(p)/dp$ and $\partial \tilde{A}(p)/\partial p = d\tilde{A}(p)/dp$, we have

$$\frac{d\tilde{A}(p)/dp}{\tilde{A}(p)} = -\frac{1}{2} \frac{\frac{dF(Q(p))}{dQ(p)} \frac{dQ(p)}{dp}}{F(Q(p))} \quad (\text{A.63})$$

$$\frac{d\tilde{A}(p)dp}{\tilde{A}(p)} = -\frac{1}{2} \frac{dF(Q(p))/dp}{F(Q(p))} \quad (\text{A.64})$$

$$\ln \tilde{A}(p) = -\frac{1}{2} \ln |F(Q(p))| \quad (\text{A.65})$$

$$\tilde{A}(p) = D |F(Q(p))|^{-1/2}, \quad (\text{A.66})$$

where D is a constant. Substituting Eqs. A.57 and A.66 into the form of our assumed wave function, $\tilde{\Psi}(p)$, we obtain

$$\tilde{\Psi}(p) = \tilde{A}(p) \exp\left(\frac{i\tilde{S}(p)}{\hbar}\right) \quad (\text{A.67})$$

$$= D \left| \frac{1}{F(Q(p))} \right|^{1/2} \exp\left(\frac{-i \int_{p_0}^p \mathcal{Q}(p') dp'}{\hbar}\right). \quad (\text{A.68})$$

Since $F(Q(p)) = -dV(Q(p))/dQ(p) = -dV(q(p))/dq(p) = -dV(q)/dq = -\partial H/\partial q = dp/dt$, this can be rewritten as

$$\tilde{\Psi}(p) = D \left| \frac{1}{dp/dt} \right|^{1/2} \exp\left(\frac{-i \int_{p_0}^p \mathcal{Q}(p') dp'}{\hbar}\right). \quad (\text{A.69})$$

A.3 Changing Coordinates to Describe the Wave Function

In some regions, one description of the wave function may fail, while the other form is valid (For example, $\Psi(q)$ is divergent when $E \approx V(q)$). $\tilde{\Psi}(p)$ can be obtained via a

Fourier transformation on $\Psi(q)$, and vice versa. The transformations are given by

$$\Psi(q) = (-2\pi i\hbar)^{-1/2} \int_{-\infty}^{\infty} e^{ipq/\hbar} \tilde{\Psi}(p) dp, \text{ and} \quad (\text{A.70})$$

$$\tilde{\Psi}(p) = (2\pi i\hbar)^{-1/2} \int_{-\infty}^{\infty} e^{-ipq/\hbar} \Psi(q) dq. \quad (\text{A.71})$$

The factors $(\pm 2\pi\hbar)^{-1/2}$ are included to preserve normalization, and the terms $\pm i^{-1/2}$ are arbitrary phase conventions, which we use consistently, following Ref. [110]. In practice, these integrals can be difficult to solve, and we typically use the method of stationary phase to evaluate them.

A.3.1 Stationary Phase Method

This method of stationary phase is an approximation technique for integrals of the form

$$I = \int_{-\infty}^{\infty} F(x) e^{iv\phi(x)} dx, \quad (\text{A.72})$$

when the phase of the integrand oscillates rapidly, $\phi(x)$ is real, and $F(x)$ is slowly-varying relative to the phase oscillation. In the limit of $v \rightarrow \infty$, $I = 0$ if $\phi(x) = x$, for any smooth function $F(x)$. This occurs because as v increases, the oscillations of the phase become more rapid, and I tends to zero over the range of integration. For finite v , the integrand tends to approximately zero everywhere except where $d\phi(x)/dx = 0$, i.e. where the phase is approximately stationary, due to these oscillations. These regions of stationary phase therefore make up the dominant non-zero contribution to the integral. In the context of the integrals we solve in this semiclassical analysis, $v = 1/\hbar$, and since \hbar is small, the

exponential oscillates very rapidly. The wavelength of oscillation is given by

$$\frac{d\phi(x)/dx}{\hbar} \lambda = 2\pi \quad (\text{A.73})$$

$$\lambda = \frac{2\pi\hbar}{d\phi(x)/dx} \quad (\text{A.74})$$

From Eq. A.74 it is clear that the dominant non-zero contribution to the integral occurs as $d\phi/dx \rightarrow 0$, i.e. at the point of stationary phase. This type of integrand is shown in Fig. A.1; in the figure, $F(x) = 1$ and $\phi(x) = x^2$ (see Eq. A.72). The top and bottom rows show the function for $v = 1$ and $v = 10$, respectively. In each case, the function rapidly oscillates everywhere except near where $d\phi(x)/dx = 2x = 0$, i.e., at $x = 0$. This is especially true in the lower row, where $v = 10$ causes the function to oscillate much more rapidly. When integrating over the regions away from $x = 0$, the oscillations cause the integral to tend toward zero, and only the regions near $x = 0$ contribute significantly to the integral Eq. A.72.

To solve integrals of the form of Eq. A.72, one expands $\phi(x)$ about the stationary phase point, \hat{x} ,

$$\phi(x) \approx \phi(\hat{x}) + \left. \frac{d\phi(x)}{dx} \right|_{\hat{x}} (x - \hat{x}) + \frac{1}{2} \left. \frac{d^2\phi(x)}{dx^2} \right|_{\hat{x}} (x - \hat{x})^2 + \mathcal{O}(x^3). \quad (\text{A.75})$$

The term $d\phi(x)/dx$ evaluated at $x = \hat{x}$ equals zero, however, so the above equation reduces to

$$\phi(x) \approx \phi(\hat{x}) + \frac{1}{2} \left. \frac{d^2\phi(x)}{dx^2} \right|_{\hat{x}} (x - \hat{x})^2 + \mathcal{O}(x^3). \quad (\text{A.76})$$

If we neglect the terms of $\mathcal{O}(x^3)$ and above and insert the last equation into Eq. A.72, we

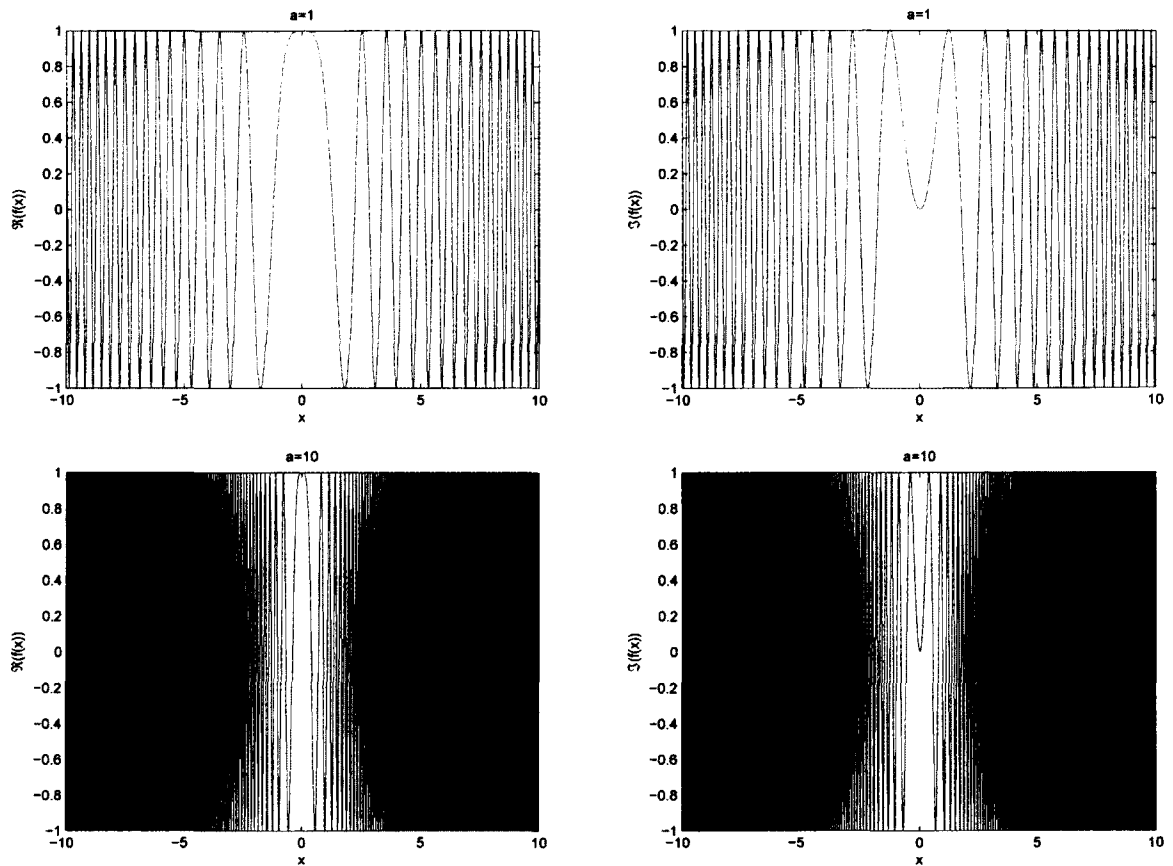


FIG. A.1: Highly oscillatory functions, for which the stationary phase method is an appropriate method for approximating the integral of. These functions are described by (see Eq. A.72) $F(x) = 1$ and $\phi(x) = x^2$. In the top row, $v = 1$, and the left and right plots show the real and imaginary parts of $F(x) \exp(iv\phi(x))$. The bottom row shows the same information for $v = 10$; notice the marked increase in oscillation frequency.

obtain

$$I \approx \int_{-\infty}^{\infty} F(x) \exp \left(\frac{i}{\hbar} \left[\phi(\hat{x}) + \frac{1}{2} \frac{d^2\phi(x)}{dx^2} \Big|_{\hat{x}} (x - \hat{x})^2 \right] \right) dx \quad (\text{A.77})$$

$$I \approx e^{i\phi(\hat{x})/\hbar} \int_{-\infty}^{\infty} F(x) \exp \left(\frac{i}{2\hbar} \frac{d^2\phi(x)}{dx^2} \Big|_{\hat{x}} (x - \hat{x})^2 \right) dx \quad (\text{A.78})$$

Since the term $F(x)$ is slowly-varying, $F(x) \approx F(\hat{x})$ in the range where rapid oscillations do not cause the integrand to tend to zero, and we may write

$$I \approx e^{i\phi(\hat{x})/\hbar} F(\hat{x}) \int_{-\infty}^{\infty} \exp \left(\frac{i}{2\hbar} \frac{d^2\phi(x)}{dx^2} \Big|_{\hat{x}} (x - \hat{x})^2 \right) dx, \quad (\text{A.79})$$

which may be evaluated as,

$$I \approx e^{i\phi(\hat{x})/\hbar} F(\hat{x}) \sqrt{\frac{2\pi\hbar}{-i\phi''(\hat{x})}}, \quad (\text{A.80})$$

where $\phi''(\hat{x}) = d^2\phi(x)/dx^2$ evaluated at $x = \hat{x}$. The above expression can be written as

$$I \approx e^{i\phi(\hat{x})/\hbar} F(\hat{x}) (2\pi\hbar)^{1/2} |\phi''(\hat{x})|^{-1/2} \exp \left(\frac{i\pi}{4} \text{sgn}(\phi''(\hat{x})) \right), \quad (\text{A.81})$$

where

$$\text{sgn}(x) = \begin{cases} 1, & \text{if } x > 0 \\ -1, & \text{if } x < 0. \end{cases} \quad (\text{A.82})$$

Eq. A.81 is the approximation we use when necessary to evaluate integrals in the form of Eq. A.72.

A.4 Time-Dependent Semiclassical Approximation

One can construct time-dependent semiclassical approximations by “expanding” the phase space of the system, meaning that E and t are regarded as a conjugate coordinate and momentum pair. The Hamiltonian must be adjusted so that Hamiltonian’s equations hold for these quantities. One is free to regard E as either a coordinate or momentum, but the Hamiltonian must be altered in different fashion depending on the choice. For the ballistic atom pump, we wish to obtain $\tilde{\Psi}(\mathbf{p})$, where $\mathbf{p} = (p_x, t)$, and we regard t as a momentum and E as its conjugate coordinate. The same steps discussed in this appendix are used for constructing $\tilde{\Psi}(\mathbf{p})$ (with the adjusted Hamiltonian), and this process yields $\tilde{\Psi}(\mathbf{p}) = \tilde{\Psi}(p_x, t)$. This time-dependence yields an additional term in $\tilde{S}(p)$, however. The full details of this time-dependent approach, which includes repairing the wavefunction near turning points and extending it into classically-forbidden regions, is given in the next appendix.

APPENDIX B

Implementation of Semiclassical Theory

This section provides additional details regarding the construction of a time-dependent semiclassical momentum-space approximation to a quantum wavefunction. The method is explained using the specific case of a classical distribution of particles incident on a single oscillating barrier, but the same method is used when multiple barriers are present. The method is quite general and can be implemented on a wide variety of problems.

B.1 Local Wavefunction

For this discussion we will examine a monoenergetic distribution of particles approaching a single oscillating Gaussian-shaped barrier from the left; an analogous method is used for particles incident from the right. The Hamiltonian for this system is given by

$$H = \frac{p^2}{2m} + U(x, t), \quad (\text{B.1})$$

where

$$U(x, t) = U_0 \exp\left(\frac{-x^2}{2\sigma^2}\right) (1 + \alpha \sin \omega t). \quad (\text{B.2})$$

At an initial time t_0 the (x, t) -space wavefunction for $x \ll 0$ (far to the left of the barrier) is given by

$$\Psi_0(x, t_0) = F(x) e^{i(p_0 x - E_0 t_0)/\hbar}, \quad (\text{B.3})$$

where $F(x)$ is a function describing the envelope of the initial packet in (x, t) space. While this is a one-dimensional scattering problem, we choose to include time and energy as canonical variables, expanding the phase space for the system. For reasons that will become clear, one regards t as a canonical momentum, and E as a canonical coordinate, *i.e.*, $q = (x, E)$ and $p = (p, t)$. Thus by constructing $\Psi(p) = \Psi(p, t)$ we will obtain the desired time-dependent momentum-space wave function. Then defining an effective Hamiltonian, \mathcal{H} , given by

$$\mathcal{H} = \frac{p^2}{2m} + U(x, t) - E, \quad (\text{B.4})$$

the equations of motion are

$$\frac{dx}{d\tau} = \frac{\partial \mathcal{H}}{\partial p} = \frac{\partial H}{\partial p} \quad (\text{B.5a})$$

$$\frac{dp}{d\tau} = -\frac{\partial \mathcal{H}}{\partial x} = -\frac{\partial H}{\partial x} \quad (\text{B.5b})$$

$$\frac{dE}{d\tau} = \frac{\partial \mathcal{H}}{\partial t} = \frac{\partial U}{\partial t} \quad (\text{B.5c})$$

$$\frac{dt}{d\tau} = -\frac{\partial \mathcal{H}}{\partial E} = 1 \quad (\text{B.5d})$$

$$\frac{dS}{d\tau} = p \frac{dx}{d\tau} - E \frac{dt}{d\tau} \quad (\text{B.5e})$$

$$\frac{d\tilde{S}}{d\tau} = -x \frac{dp}{d\tau} - E \frac{dt}{d\tau} \quad (\text{B.5f})$$

where τ is a “timelike” progress variable along the trajectories, and is related to t in the Schrödinger Equation via $\tau = t_0 + t$. We call S the classical action along the trajectory, and \tilde{S} can be thought of as a “momentum-space action” along the trajectory. The form of equations (B.5c) and (B.5d) justify the identification of E as a canonical coordinate and t as its conjugate momentum.

We want to compute the probability that the particles end with a given final momentum, using the momentum-space wavefunction $\tilde{\Psi}(p, t)$. Therefore, we want a semiclassical approximation in momentum space. However, since we have chosen an initial distribution with very small momentum spread, the initial wavefunction in momentum space is nearly a delta function, which cannot be described by a semiclassical approximation. Therefore, in order to calculate the desired momentum-space wavefunction, we start our calculation in (x, t) space, and later transform to (p, t) space.

The first step in constructing a semiclassical wavefunction is to propagate classical trajectories from a line of initial conditions. We choose the line of initial conditions to have a constant starting time $t_0 = 0$, variable starting position x covering the domain of the initial packet, and a fixed initial momentum p_0 . The resulting trajectories sweep out

a two-dimensional surface called a Lagrangian manifold in the four-dimensional (x, p, E, t) phase space. A typical Lagrangian manifold for this system is shown in Fig. B.1.

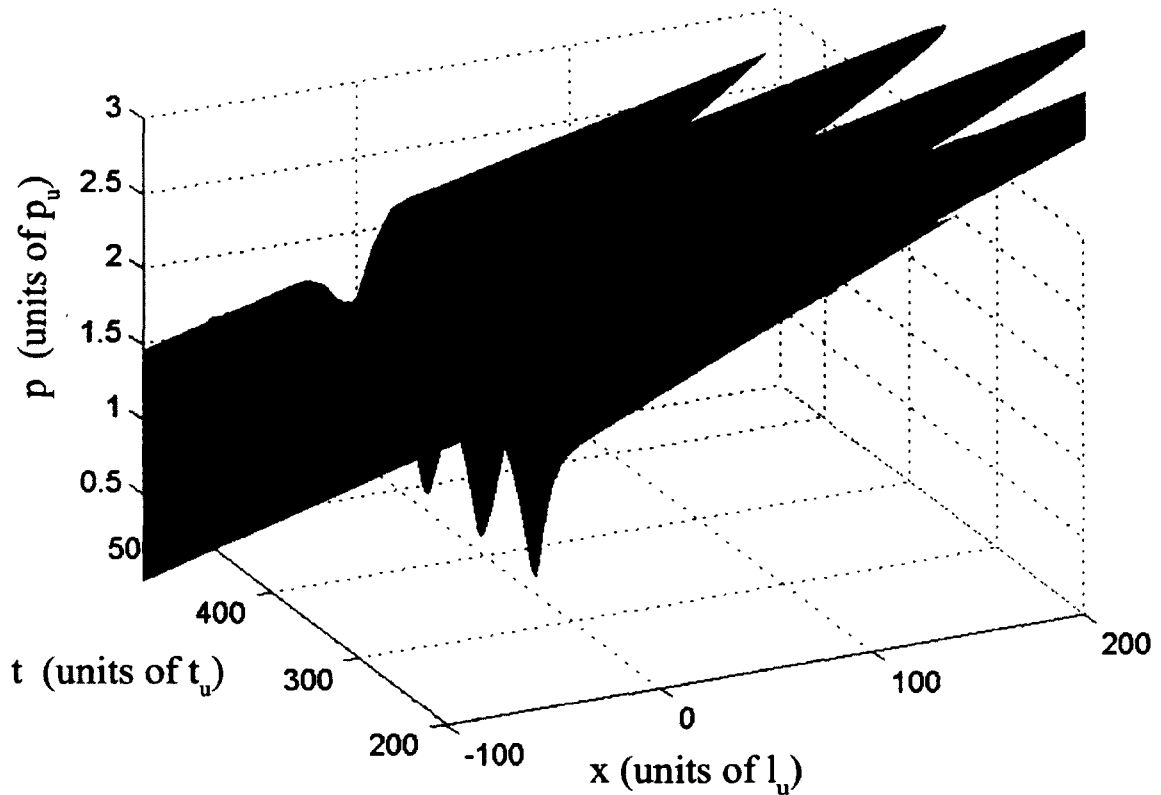


FIG. B.1: A typical Lagrangian manifold for the one-barrier system. The solid line (red online) shows a slice at a constant time.

Integration of trajectories with respect to τ gives a relationship between (x_0, τ) and (z, t) , where z is any dynamical variable x, p, E, S , or \tilde{S} . From our choice of $t_0 = 0$, t is simply equal to τ , and x is the point at which the trajectory arrives at time $t = \tau$. We may think of each of these quantities as a function of the initial variable x_0 and the progress variable τ , e.g., $x(x_0, \tau), p(x_0, \tau)$, etc.

We define a Jacobian,

$$J(x_0, \tau) = \det \left(\frac{\partial(x, t)}{\partial(x_0, \tau)} \right) = \frac{\partial x}{\partial x_0} \quad (\text{B.6})$$

with $J_0 = J(x_0, 0) = 1$. This Jacobian is a single-valued function of (x_0, τ) . For τ not too large (and x not too far from x_0) there is an invertible relationship between (x_0, τ) and (x, t) ; i.e., we may consider (x_0, τ) as a function of (x, t) . With this relationship, we may also consider the position-space action S and Jacobian J to be functions of (x, t) ,

$$\begin{aligned} S(x_0, \tau) &= S(x_0(x, t), \tau(x, t)) = \mathcal{S}(x, t) \\ J(x_0, \tau) &= J(x_0(x, t), \tau(x, t)) = \mathcal{J}(x, t) \end{aligned} \quad (\text{B.7})$$

We may use these functions in the primitive semiclassical approximation for the (x, t) space wavefunction

$$\Psi(x, t) = \Psi_0(x_0, \tau = 0) \left| \frac{\mathcal{J}_0}{\mathcal{J}(x, t)} \right|^{1/2} e^{i\mathcal{S}(x, t)/\hbar}, \quad (\text{B.8})$$

where (x_0, τ) are considered to be functions of (x, t) . The initial Maslov index has been set equal to zero, and

$$\Psi_0(x_0, \tau = 0) = F(x_0) e^{ip_0 x_0/\hbar}, \quad (\text{B.9})$$

where (x_0, τ) are again considered as functions of (x, t) .

As the trajectories are propagated forward in τ , they eventually arrive at the barrier region, where p is no longer constant, and we may use (p, t) locally as independent variables to describe the Lagrangian manifold, as shown in Figs. B.1, B.2(a) and B.2(c), and Fig. B.3.

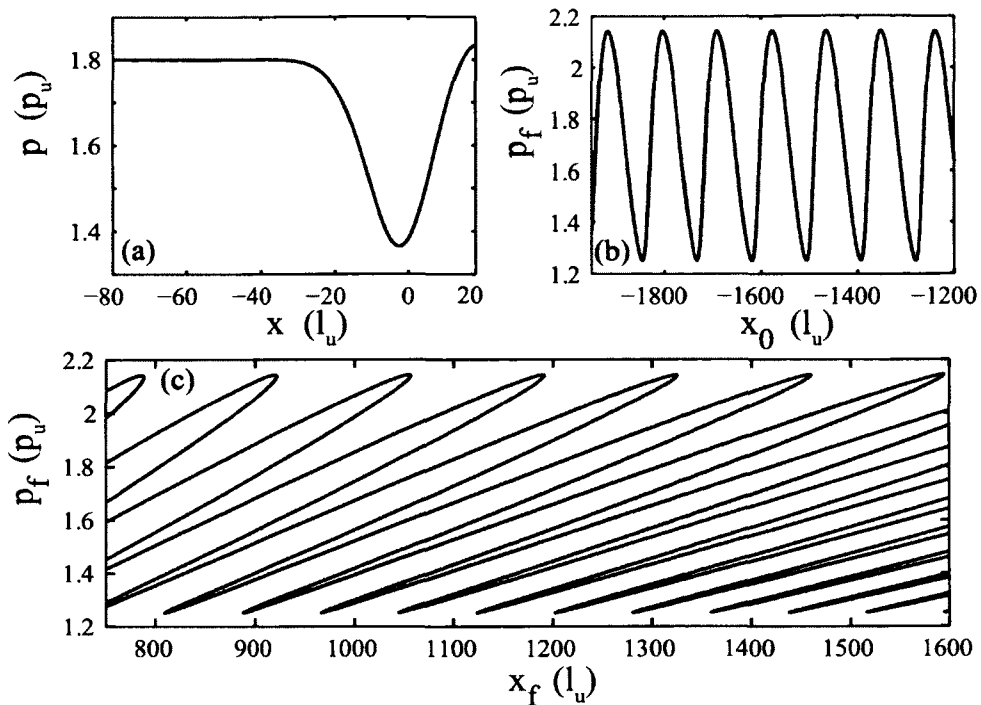


FIG. B.2: Different views of a typical Lagrangian manifold for one-barrier system. (a) Slice of Lagrangian manifold at small time. (b) Periodic final momentum as a function of initial position. (c) Final momentum, $p_f = p(x_0, \tau_f)$, as a function of final position, $x_f = x(x_0, \tau_f)$. This corresponds to the final-time slice of the Lagrangian manifold.

A “momentum chart” is a region of the Lagrangian manifold that has a diffeomorphic projection to momentum space, (p, t) . In Fig. B.3, a constant-time slice of the Lagrangian manifold is shown for an intermediate time. For each value of p , there are many corresponding values of x ; each lies on what can be regarded as a “branch” of a multivalued function $\mathcal{P}_x(x, t)$ describing the Lagrangian manifold. Each branch is separated by extrema of the function $\mathcal{P}_x(x, t)$, *i.e.*, regions where $\partial \mathcal{P}_x(x, t) / \partial x = 0$.

Since (p, t) are locally valid coordinates for describing the Lagrangian manifold, we

transform to the momentum-space representation of the wavefunction via

$$\tilde{\Psi}(p, t) = (2\pi i\hbar)^{-1/2} \int \Psi(x, t) e^{-ipx/\hbar} dx \quad (\text{B.10})$$

$$= (2\pi i\hbar)^{-1/2} \quad (\text{B.11})$$

$$\times \int F(x_0(x, t)) \left| \frac{1}{\partial x / \partial x_0} \right|^{1/2} \exp(i/\hbar [\mathcal{S}(x, t) - px + p_0 x_0(x, t) - E_0 t_0(x, t)]) dx.$$

We may evaluate that part of the wavefunction that corresponds to the first momentum-

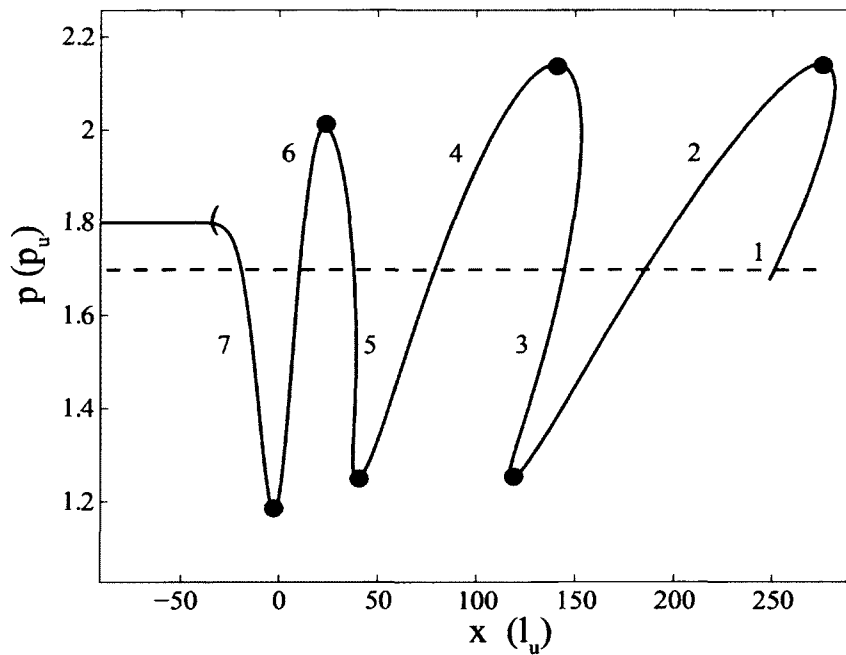


FIG. B.3: Slice of Lagrangian manifold at an intermediate time. The numbers correspond to intermediate-time slices of different momentum charts, which are separated by local extrema in the function $p = P(x, t)$ for fixed time, denoted by large circles. For every given momentum (e.g., the dashed line), there are many corresponding values of x .

chart of the Lagrangian Manifold by using the stationary phase approximation,

$$\int C(x; p, t) e^{i\Phi(x; p, t)/\hbar} dx \approx (2\pi\hbar)^{1/2} C(\hat{x}; p, t) \quad (\text{B.12})$$

$$\times \exp\left(\frac{i\pi}{4} \text{sgn}(\Phi''(\hat{x}; p, t))\right) \exp(i\Phi(\hat{x}; p, t)/\hbar) |\Phi''(\hat{x}; p, t)|^{-1/2}.$$

By inspection, one can see that

$$\Phi(x; p, t) = \mathcal{S}(x, t) - px + p_0 x_0(x, t) - E_0 t_0(x, t). \quad (\text{B.13})$$

We seek the stationary phase point, \hat{x} , where $\partial\Phi(x; p, t)/\partial x = 0$. Recalling that

$$\mathcal{S}(x, t) = S(x_0(x, t), \tau(x, t)), \quad (\text{B.14})$$

$$\frac{\partial\mathcal{S}(x, t)}{\partial x} = \frac{\partial S}{\partial x} + \frac{\partial S}{\partial x_0} \frac{\partial x_0}{\partial x}, \text{ and} \quad (\text{B.15})$$

$$\frac{\partial\Phi(x; p, t)}{\partial x} = -p + p_0 \frac{\partial x_0}{\partial x} + \frac{\partial S}{\partial x} + \frac{\partial S}{\partial x_0} \frac{\partial x_0}{\partial x}. \quad (\text{B.16})$$

Since

$$\frac{\partial S}{\partial x_0} = -p_0 \text{ and } \frac{\partial S}{\partial x} = \mathcal{P}_x(x, t), \quad (\text{B.17})$$

$$\frac{\partial\Phi(x; p, t)}{\partial x} = -p + p_0 \frac{\partial x_0}{\partial x} + \mathcal{P}_x(x, t) - p_0 \frac{\partial x_0}{\partial x} \quad (\text{B.18})$$

$$= -p + \mathcal{P}_x(x, t). \quad (\text{B.19})$$

Here p is used as the independent variable in $\tilde{\Psi}(p, t)$. Each value of p has a stationary phase point, \hat{x} , where $p = \mathcal{P}_x(\hat{x}, t)$, *i.e.*, where the line $p = \text{constant}$ intersects the Lagrangian

Manifold, as discussed in the caption of Fig. B.3. At the stationary phase point, \hat{x} ,

$$\frac{\partial \Phi(\hat{x}; p, t)}{\partial x} = 0 = -p + \mathcal{P}_x(\hat{x}, t) \quad (\text{B.20})$$

$$\Rightarrow p = \mathcal{P}_x(\hat{x}, t). \quad (\text{B.21})$$

In order to evaluate (B.12), we write out $\Phi(\hat{x}; p, t)$, and integrate by parts

$$\Phi(\hat{x}; p, t) = -p\hat{x} + p_0 x_0(\hat{x}, t) - E_0 t_0 + \int p(x_0(x, t), \tau(x, t)) \frac{dx}{d\tau} d\tau \quad (\text{B.22})$$

$$\begin{aligned} & - \int E(x_0(x, t), \tau(x, t)) \frac{dt}{d\tau} d\tau \\ & = - \int x(x_0, \tau) \frac{dp(x_0, \tau)}{d\tau} d\tau - \int E(x_0, \tau) \frac{dt(x_0, \tau)}{d\tau} d\tau \end{aligned} \quad (\text{B.23})$$

$$= - \int x dp - \int E dt \quad (\text{B.24})$$

$$\equiv \tilde{S}(x_0, \tau) \quad (\text{B.25})$$

$$= \tilde{S}(p_x, t) \quad (\text{B.26})$$

In (B.23), we have integrated by parts, cancelled the boundary terms, and used our choice of $t_0 = 0$ to eliminate terms. Eq. (B.24) is a terse abbreviation of Eq. (B.23). $\tilde{S}(x_0, \tau)$ is defined as the integral in (B.23), and the invertible relationship between (p, t) and (x_0, τ) allows us to consider it to be a function of (p, t) . We also use this relationship to define a Jacobian for the momentum space, *i.e.*,

$$\tilde{S}(x_0(p, t), \tau(p, t)) = \tilde{S}(p, t) \quad (\text{B.27})$$

$$\tilde{J}(x_0(p, t), \tau(p, t)) = \tilde{J}(p, t) \quad (\text{B.28})$$

We may think of $\tilde{S}(p_x, t)$ as a momentum-space action along the trajectory from the initial

surface to the final point on the Lagrangian Manifold. Now we can write (B.12) as

$$\begin{aligned} \tilde{\Psi}(p, t) &= (2\pi i\hbar)^{-1/2} (2\pi\hbar)^{1/2} F(x_0(\hat{x}; p, t)) \left| \frac{1}{\partial x / \partial x_0} \right|_{x=\hat{x}}^{1/2} \exp\left(i\tilde{\mathcal{S}}(p_x, t)/\hbar\right) \\ &\times \exp\left(\frac{i\pi}{4} \operatorname{sgn}(\Phi''(\hat{x}; p, t))\right) |\Phi''(\hat{x}; p, t)|^{-1/2} \end{aligned} \quad (\text{B.29})$$

$$\begin{aligned} &= e^{-i\pi/4} F(x_0(p, t)) \left| \frac{1}{\partial x / \partial x_0} \right|_{x=\hat{x}}^{1/2} \exp\left(i\tilde{\mathcal{S}}(p_x, t)/\hbar\right) \\ &\times \exp\left(\frac{i\pi}{4} \operatorname{sgn}(\Phi''(\hat{x}; p, t))\right) |\Phi''(\hat{x}; p, t)|^{-1/2} \end{aligned} \quad (\text{B.30})$$

To finish evaluating the integral, we need to determine $\Phi''(\hat{x}; p, t)$; from equation (B.19),

$$\Phi''(\hat{x}; p, t) = \frac{\partial \mathcal{P}_x(x, t)}{\partial x} \Big|_{x=\hat{x}(p, t)} \quad (\text{B.31})$$

Now we can write (B.31) as

$$\begin{aligned} \tilde{\Psi}(p, t) &= e^{-i\pi/4} F(x_0(p, t)) \left| \frac{1}{\frac{\partial x}{\partial x_0} \frac{\partial \mathcal{P}_x(x, t)}{\partial x}} \right|_{x=\hat{x}}^{1/2} \\ &\times \exp\left(i\tilde{\mathcal{S}}(p_x, t)/\hbar\right) \exp\left(\frac{i\pi}{4} \operatorname{sgn}\left(\frac{\partial \mathcal{P}_x(x, t)}{\partial x} \Big|_{x=\hat{x}}\right)\right) \\ &= e^{-i\pi/4} F(x_0(p, t)) \left| \frac{1}{\tilde{\mathcal{J}}(p_x, t)} \right|^{1/2} \exp\left(i\tilde{\mathcal{S}}(p_x, t)/\hbar\right) \exp\left(\frac{i\pi}{4} \operatorname{sgn}\left(\frac{\partial \mathcal{P}_x(x, t)}{\partial x} \Big|_{x=\hat{x}}\right)\right), \end{aligned} \quad (\text{B.32})$$

$$(\text{B.33})$$

where $\tilde{\mathcal{J}}(p_x, t) = \partial p / \partial x_0$. As particles approach the barrier, their momentum decreases, and we see from computed Lagrangian manifolds (Fig. B.2(a)) that

$$\frac{\partial \mathcal{P}_x(x, t)}{\partial x} \Big|_{x=\hat{x}(p, t)} < 0 \quad (\text{B.34})$$

at the point of transformation, so

$$\text{sgn} \left(\left. \frac{\partial \mathcal{P}_x(x, t)}{\partial x} \right|_{x=\hat{x}(p, t)} \right) = -1. \quad (\text{B.35})$$

Therefore the local momentum-space wavefunction for the first momentum-chart is

$$\tilde{\Psi}(p, t) = e^{-i\pi/2} F(x_0(p, t)) \left| \frac{1}{\tilde{\mathcal{J}}(p_x, t)} \right|^{1/2} \exp \left(i\tilde{\mathcal{S}}(p_x, t)/\hbar \right). \quad (\text{B.36})$$

Generally, for every momentum chart of the Lagrangian manifold, there is a comparable term contributing to the global momentum-space wavefunction. We write the local, primitive form of the momentum-space wavefunction for each momentum chart as

$$\tilde{\Psi}_j(p, t) = F(x_0^j(p, t)) \left| \frac{1}{\tilde{\mathcal{J}}_j(p, t)} \right|^{1/2} \exp \left(\frac{i\tilde{\mathcal{S}}_j(p, t)}{\hbar} - \frac{i\pi\tilde{\mu}_j}{2} \right), \quad (\text{B.37})$$

where $\tilde{\mu}_j$ is the Maslov index for the given momentum chart.

B.1.1 Maslov Index

As indicated in Figs. B.2(c) and B.3, momentum charts are separated by momentum turning points, which are extrema of locally-defined functions $p = \mathcal{P}(x, t)$ for fixed t , i.e., points where $\partial \mathcal{P}(x, t)/\partial x = 0$. Near these regions, (p, t) are not appropriate independent variables for describing the Lagrangian Manifold, and so we transform back to (x, t) as the independent variables to use. Away from these regions, we transform back again to (p, t) . These transformations introduce phase differences in the localized primitive momentum-space wavefunctions between successive branches. The Maslov index keeps track of these phase differences.

To see how these coordinate transformations introduce phase differences in the prim-

itive wavefunctions for successive branches, we isolate the terms responsible for the phase differences from each of the two types of transformations, and develop a rule for determining the Maslov Index for each branch relative to the previous one.

We saw that the transformation from using (x, t) as local coordinates to using (p, t) as local coordinates introduced an “extra” $e^{-i\pi/2}$ term in the primitive wavefunction (compare Eqs. (B.8) and (B.36)). We chose to set the initial Maslov Index in (x, t) space equal to zero, and the extra $e^{-i\pi/2}$ in (B.36) corresponds to $\tilde{\mu}_j = 1$, in terms of equation (B.37).

Consider again the equation describing a transformation from (x, t) coordinates to (p, t) to coordinates, given by equations (B.29) and (B.31). The two terms in (B.31) responsible for the “extra” $e^{-i\pi/2}$ in (B.36) are

$$e^{-i\pi/4}, \text{ and} \tag{B.38}$$

$$\exp\left(\frac{i\pi}{4}\text{sgn}(\Phi''(\hat{x}; p, t))\right) = \exp\left(\frac{i\pi}{4}\text{sgn}\left(\left.\frac{\partial\mathcal{P}_x(x, t)}{\partial x}\right|_{x=\hat{x}}\right)\right). \tag{B.39}$$

Furthermore, also consider a transformation from (p, t) coordinates to (x, t) coordinates, where we use the form of (B.37) for $\tilde{\Psi}(p, t)$,

$$\Psi(x, t) = (-2\pi i\hbar)^{-1/2} \int \tilde{\Psi}(p, t) e^{ipx/\hbar} dp \tag{B.40}$$

$$= (-2\pi i\hbar)^{-1/2} \int F(x_0(p, t)) \left| \frac{1}{\partial p/\partial x_0} \right| e^{-i\pi\tilde{\mu}/2} \exp\left(\frac{i}{\hbar}(\tilde{\mathcal{S}}(p_x, t) + px)\right) dp \tag{B.41}$$

$$= e^{i\pi/4} F(x_0(x, t)) \left| \frac{1}{\partial x/\partial x_0} \right|^{1/2} e^{-i\pi\tilde{\mu}/2} \exp\left(\frac{i}{\hbar}\mathcal{S}(x, t)\right) \tag{B.42}$$

$$\times \exp\left(\frac{-i\pi}{4}\text{sgn}\left(\left.\frac{\partial\chi(p, t)}{\partial p}\right|_{p=\hat{p}_x}\right)\right).$$

Analogous to equations (B.38) and (B.39), one can see that the two terms in (B.42) which may combine to yield an extra phase during a transformation from (p, t) coordinates to

(x, t) coordinates are

$$e^{i\pi/4}, \text{ and} \tag{B.43}$$

$$\exp\left(\frac{-i\pi}{4} \operatorname{sgn}\left(\left.\frac{\partial\chi(p, t)}{\partial p}\right|_{p=\hat{p}_x}\right)\right). \tag{B.44}$$

Successive branches of the function $\mathcal{P}_x(x, t)$ describing the Lagrangian manifold are separated by a region in which $\partial\mathcal{P}_x(x, t)/\partial x = 0$. Since (p, t) are not appropriate coordinates for describing the Lagrangian manifold near these regions, we must transform from (p, t) to (x, t) to describe the Lagrangian manifold in these regions, and transform back to (p, t) away from this region on the next branch. Therefore when expressing the primitive local wavefunction for successive branches in terms of (p, t) , our equations must include the additional phases introduced by the two transformations described by Eqs. (B.38)-(B.39) and Eqs.(B.43)-(B.44).

More explicitly, when constructing the local primitive wavefunction $\Psi(p, t)$ for the i^{th} momentum-chart of the Lagrangian Manifold, there will always be a region in which $\partial\mathcal{P}_x(x, t)/\partial x \rightarrow 0$ (*i.e.*, where $\partial p/\partial x_0 \rightarrow 0$), which separates the i^{th} momentum-chart from the j^{th} momentum-chart. Equation (B.37) is not valid in these regions, and we transform from the (p, t) space representation of the wavefunction to the (x, t) space representation, which is valid. Continuing past the caustic, we transform back to the (p, t) space representation, and denote this new momentum-chart the j^{th} one. Included in these transformations are four terms, given by (B.38), (B.39), (B.43), and (B.44), whose product yields a phase difference in the (p, t) representation of the wavefunction on the j^{th} momentum-chart relative to the i^{th} momentum-chart. We write the general form for $\tilde{\Psi}_j(p, t)$ as

$$\tilde{\Psi}_j(p, t) = F(x_0^j(p, t)) \left| \frac{1}{\tilde{\mathcal{J}}_j(p, t)} \right|^{1/2} \exp \left(\frac{i\tilde{\mathcal{S}}_j(p, t)}{\hbar} - \frac{i\pi\tilde{\mu}_j}{2} \right) \quad (\text{B.45})$$

but it can also be written using the Maslov index for the adjacent i^{th} chart and the terms that arise from transforming from $(p, t) \rightarrow (x, t) \rightarrow (p, t)$:

$$\begin{aligned} \tilde{\Psi}_j(p, t) = & F(x_0^j(p, t)) \left| \frac{1}{\tilde{\mathcal{J}}_j(p, t)} \right|^{1/2} \exp \left(\frac{i\tilde{\mathcal{S}}_j(p, t)}{\hbar} - \frac{i\pi\tilde{\mu}_i}{2} \right) \quad (\text{B.46}) \\ & \times \left[e^{i\pi/4} \exp \left(\frac{-i\pi}{4} \text{sgn} \left(\frac{\partial\chi(p, t)}{\partial p} \Big|_{p=\hat{p}_x} \right) \right) \right]_i \left[e^{-i\pi/4} \exp \left(\frac{i\pi}{4} \text{sgn} \left(\frac{\partial\mathcal{P}_x(x, t)}{\partial x} \Big|_{x=\hat{x}} \right) \right) \right]_j. \end{aligned}$$

We can combine terms in the above equation and write a more compact version:

$$\begin{aligned} \tilde{\Psi}_j(p, t) = & F(x_0^j(p, t)) \left| \frac{1}{\tilde{\mathcal{J}}_j(p, t)} \right|^{1/2} \exp \left(\frac{i\tilde{\mathcal{S}}_j(p, t)}{\hbar} - \frac{i\pi\tilde{\mu}_i}{2} \right) \\ & \times \exp \left[-\frac{i\pi}{4} \text{sgn} \left(\frac{\partial\chi(p, t)}{\partial p} \Big|_{p=\hat{p}_x} \right)_i + \frac{i\pi}{4} \text{sgn} \left(\frac{\partial\mathcal{P}_x(x, t)}{\partial x} \Big|_{x=\hat{x}} \right)_j \right] \quad (\text{B.47}) \end{aligned}$$

If $\partial\chi(p, t)/\partial p < 0$ at the point of transformation on the i^{th} momentum chart, then $\partial\mathcal{P}_x(x, t)/\partial x > 0$ at the point of transformation on the j^{th} momentum chart, and Eq. (B.47) reduces to

$$\tilde{\Psi}_j(p, t) = F(x_0^j(p, t)) \left| \frac{1}{\tilde{\mathcal{J}}_j(p, t)} \right|^{1/2} \exp \left(\frac{i\tilde{\mathcal{S}}_j(p, t)}{\hbar} - \frac{i\pi\tilde{\mu}_i}{2} \right) \exp \left[-\frac{i\pi}{4} (-1) + \frac{i\pi}{4} (1) \right] \quad (\text{B.48})$$

$$= F(x_0^j(p, t)) \left| \frac{1}{\tilde{\mathcal{J}}_j(p, t)} \right|^{1/2} \exp \left(\frac{i\tilde{\mathcal{S}}_j(p, t)}{\hbar} - \frac{i\pi\tilde{\mu}_i}{2} \right) \exp \left(\frac{i\pi}{2} \right) \quad (\text{B.49})$$

$$= F(x_0^j(p, t)) \left| \frac{1}{\tilde{\mathcal{J}}_j(p, t)} \right|^{1/2} \exp \left(\frac{i\tilde{\mathcal{S}}_j(p, t)}{\hbar} - \frac{i\pi}{2} (\tilde{\mu}_i - 1) \right) \quad (\text{B.50})$$

Comparing Eqs. (B.45) and (B.50), we see that $\tilde{\mu}_j = \tilde{\mu}_i - 1$. Similarly, if $\partial\chi(p, t)/\partial p > 0$ at the point of transformation on the i^{th} momentum chart then $\partial\mathcal{P}_x(x, t)/\partial x < 0$ at the point of transformation on the j^{th} momentum chart, and $\tilde{\mu}_j = \tilde{\mu}_i + 1$. Thus we see that the Maslov Index on the j^{th} momentum chart $\tilde{\mu}_j = \tilde{\mu}_i \pm 1$, and is determined by signature of the derivatives in Eq. (B.47) at the point of transformations. If we restrict ourselves to using a typical right-handed coordinate system, as shown in Fig. B.1, we can summarize the Maslov index for successive momentum-charts via the following theorem.

B.1.2 Theorem I

Each time any path on the Lagrangian Manifold passes through a caustic, *i.e.*, where $\partial\mathcal{P}_x(x, t)/\partial x = 0$, the Maslov Index will change by ± 1 from its value on the previous momentum-chart. We use the path shown in Fig. B.2(c), which is a constant-time slice of the Lagrangian manifold swept out by trajectories at a chosen final time which is large enough such that all particles have scattered far from the potential barrier. Each time the path passes through a caustic, the Maslov Index changes by ± 1 , and we use the following rule to determine the increment.

When the path passes through a caustic which separates the i^{th} region from the j^{th} region,

$$\tilde{\mu}_j = \tilde{\mu}_i + 1, \quad \text{if the path turned right (clockwise) through the caustic, and} \quad (\text{B.51})$$

$$\tilde{\mu}_j = \tilde{\mu}_i - 1, \quad \text{if the path turned left (counterclockwise) through the caustic.} \quad (\text{B.52})$$

The Maslov index for the first momentum-chart to encounter the barrier is $\tilde{\mu}_1 = 1$ and is determined by the initial transformation to (p, t) coordinates (Eqs. (B.10)-(B.37)), and Maslov indices for all other momentum-charts are calculated relative to it from the rule stated above.

B.1.3 Corrections Near Momentum Turning Points

The primitive semiclassical wavefunction (Eq. (B.37)) diverges at momentum turning points, where $\tilde{\mathcal{J}}_b(p, t)$ vanishes. To correct this divergence, we construct an alternative way of writing the semiclassical wavefunction, which will be valid near momentum turning points in classically-allowed regions. We then match this form of the wavefunction to a linear combination of the Airy function and its derivative, in order to extend the semiclassical approximation into classically-forbidden regions [130].

We start by adding the primitive forms of the wavefunction, (B.37), for two successive momentum charts, and we denote this wavefunction $\tilde{\Psi}_{m+n}(p, t)$. We introduce the following notation

$$A(p, t) = \left| \tilde{\mathcal{J}}(p, t) \right|^{-1/2} \quad (\text{B.53a})$$

$$\Delta \tilde{\mathcal{S}}(p, t) = \tilde{\mathcal{S}}_n(p, t) - \tilde{\mathcal{S}}_m(p, t) \quad (\text{B.53b})$$

$$\tilde{\mathcal{S}}(p, t) = \left[\tilde{\mathcal{S}}_n(p, t) + \tilde{\mathcal{S}}_m(p, t) \right] / 2 \quad (\text{B.53c})$$

$$\Delta A(p, t) = A_n(p, t) - A_m(p, t) \quad (\text{B.53d})$$

$$\mathbb{A}(p, t) = [A_n(p, t) + A_m(p, t)] / 2 \quad (\text{B.53e})$$

$$\Delta F(x_0(p, t)) = F_n(x_0(p, t)) - F_m(x_0(p, t)) \quad (\text{B.53f})$$

$$\mathbb{F}(x_0(p, t)) = [F_n(x_0(p, t)) + F_m(x_0(p, t))] / 2, \quad (\text{B.53g})$$

where the m and n subscripts denote the momentum chart with the lower and higher Maslov index, respectively (*i.e.*, $\tilde{\mu}_n = \tilde{\mu}_m + 1$). With these definitions, we may write $\tilde{\Psi}_{m+n}$

as

$$\begin{aligned} \tilde{\Psi}_{m+n}(p, t) = \exp\left(\frac{i\tilde{\mathcal{S}}(p, t)}{\hbar}\right) e^{-i\pi\tilde{\mu}_m/2} & \left\{ \mathbb{A} \left[F_m e^{-i\Delta\tilde{\mathcal{S}}(p, t)/2\hbar} + F_n e^{i(\Delta\tilde{\mathcal{S}}(p, t)/2\hbar - \pi/2)} \right] \right. \\ & \left. + (\Delta A/2) \left[-F_m e^{-i\Delta\tilde{\mathcal{S}}(p, t)/2\hbar} + F_n e^{i(\Delta\tilde{\mathcal{S}}(p, t)/2\hbar - \pi/2)} \right] \right\}. \end{aligned} \quad (\text{B.54})$$

Finally, we factor and make use of (B.53f) and (B.53g) in (B.54) to obtain

$$\begin{aligned} \tilde{\Psi}_{m+n}(p, t) = \exp\left(\frac{i\tilde{\mathcal{S}}(p, t)}{\hbar}\right) e^{-i\pi\tilde{\mu}_m/2} & \left\{ \mathbb{A}\mathbb{F} \left[e^{-i\Delta\tilde{\mathcal{S}}(p, t)/2\hbar} + e^{i(\Delta\tilde{\mathcal{S}}(p, t)/2\hbar - \pi/2)} \right] \right. \\ & + \frac{\mathbb{A}\Delta F}{2} \left[-e^{-i\Delta\tilde{\mathcal{S}}(p, t)/2\hbar} + e^{i(\Delta\tilde{\mathcal{S}}(p, t)/2\hbar - \pi/2)} \right] \\ & + \frac{\Delta A\mathbb{F}}{2} \left[-e^{-i\Delta\tilde{\mathcal{S}}(p, t)/2\hbar} + e^{i(\Delta\tilde{\mathcal{S}}(p, t)/2\hbar - \pi/2)} \right] \\ & \left. + \frac{\Delta A\Delta F}{4} \left[e^{-i\Delta\tilde{\mathcal{S}}(p, t)/2\hbar} + e^{i(\Delta\tilde{\mathcal{S}}(p, t)/2\hbar - \pi/2)} \right] \right\} \end{aligned} \quad (\text{B.55})$$

Combining terms, (B.55) may be written in the simplified form,

$$\begin{aligned} \tilde{\Psi}_{m+n}(p, t) = \exp\left(\frac{i\tilde{\mathcal{S}}(p, t)}{\hbar} - \frac{i\tilde{\mu}_m\pi}{2}\right) & \\ \times \left\{ \left[\mathbb{A}\mathbb{F} + \frac{\Delta A\Delta F}{4} \right] \left[e^{-i\Delta\tilde{\mathcal{S}}(p, t)/2\hbar} + e^{i(\Delta\tilde{\mathcal{S}}(p, t)/2\hbar - \pi/2)} \right] \right. & \\ \left. + \left[\frac{\mathbb{A}\Delta F}{2} + \frac{\Delta A\mathbb{F}}{2} \right] \left[-e^{-i\Delta\tilde{\mathcal{S}}(p, t)/2\hbar} + e^{i(\Delta\tilde{\mathcal{S}}(p, t)/2\hbar - \pi/2)} \right] \right\}. & \end{aligned} \quad (\text{B.56})$$

We may further simplify (B.56) by combining the exponential terms into trigonometric

functions. If we focus on the exponential terms in line two of (B.56), we see that

$$e^{-i\Delta\tilde{\mathcal{S}}(p,t)/2\hbar} + e^{i(\Delta\tilde{\mathcal{S}}(p,t)/2\hbar - \pi/2)} = e^{-i\pi/4} \left[e^{-i\Delta\tilde{\mathcal{S}}(p,t)/2\hbar} e^{i\pi/4} + e^{i\Delta\tilde{\mathcal{S}}(p,t)/2\hbar} e^{-i\pi/4} \right] \quad (\text{B.57})$$

$$= e^{-i\pi/4} \left[e^{-i(\Delta\tilde{\mathcal{S}}(p,t)/2\hbar - \pi/4)} + e^{i(\Delta\tilde{\mathcal{S}}(p,t)/2\hbar - \pi/4)} \right] \quad (\text{B.58})$$

$$= 2e^{-i\pi/4} \cos \left(\frac{\Delta\tilde{\mathcal{S}}(p,t)}{2\hbar} - \frac{\pi}{4} \right). \quad (\text{B.59})$$

Similarly, if we focus on the bracketed term involving the exponents in the last line of (B.56), we see that

$$-e^{-i\Delta\tilde{\mathcal{S}}(p,t)/2\hbar} + e^{i(\Delta\tilde{\mathcal{S}}(p,t)/2\hbar - \pi/2)} = e^{-i3\pi/4} \left[-e^{-i\Delta\tilde{\mathcal{S}}(p,t)/2\hbar} e^{i3\pi/4} + e^{i\Delta\tilde{\mathcal{S}}(p,t)/2\hbar} e^{i\pi/4} \right] \quad (\text{B.60})$$

$$= e^{-i3\pi/4} \left[e^{-i\pi} e^{-i\Delta\tilde{\mathcal{S}}(p,t)/2\hbar} e^{i3\pi/4} + e^{i\Delta\tilde{\mathcal{S}}(p,t)/2\hbar} e^{i\pi/4} \right] \quad (\text{B.61})$$

$$= e^{-i3\pi/4} \left[e^{-i(\Delta\tilde{\mathcal{S}}(p,t)/2\hbar + \pi/4)} + e^{i(\Delta\tilde{\mathcal{S}}(p,t)/2\hbar + \pi/4)} \right] \quad (\text{B.62})$$

$$= 2e^{-i3\pi/4} \cos \left(\frac{\Delta\tilde{\mathcal{S}}(p,t)}{2\hbar} + \frac{\pi}{4} \right). \quad (\text{B.63})$$

We may now substitute (B.59) and (B.63) into (B.56) to write

$$\begin{aligned} \tilde{\Psi}_{m+n}(p,t) &= 2 \exp \left(\frac{i\tilde{\mathcal{S}}(p,t)}{\hbar} - \frac{i\tilde{\mu}_m\pi}{2} \right) \\ &\times \left\{ \left[\mathbb{A}\mathbb{F} + \frac{\Delta A \Delta F}{4} \right] e^{-i\pi/4} \cos \left(\frac{\Delta\tilde{\mathcal{S}}(p,t)}{2\hbar} - \frac{\pi}{4} \right) \right. \\ &\left. + \left[\frac{\mathbb{A}\Delta F}{2} + \frac{\Delta A\mathbb{F}}{2} \right] e^{-i3\pi/4} \cos \left(\frac{\Delta\tilde{\mathcal{S}}(p,t)}{2\hbar} + \frac{\pi}{4} \right) \right\} \quad (\text{B.64}) \end{aligned}$$

Noting that $\cos(x - \pi/4) = \sin(x + \pi/4)$, we may write (B.64) as

$$\begin{aligned} \tilde{\Psi}_{m+n}(p, t) = & 2 \exp\left(\frac{i\tilde{\mathcal{S}}(p, t)}{\hbar} - \frac{i\tilde{\mu}_m\pi}{2}\right) \\ & \times \left\{ \left[\mathbb{A}\mathbb{F} + \frac{\Delta A \Delta F}{4} \right] e^{-i\pi/4} \sin\left(\frac{\Delta\tilde{\mathcal{S}}(p, t)}{2\hbar} + \frac{\pi}{4}\right) \right. \\ & \left. + \left[\frac{\mathbb{A}\Delta F}{2} + \frac{\Delta A\mathbb{F}}{2} \right] e^{-i3\pi/4} \cos\left(\frac{\Delta\tilde{\mathcal{S}}(p, t)}{2\hbar} + \frac{\pi}{4}\right) \right\} \end{aligned} \quad (\text{B.65})$$

Eq. (B.65) is an alternative way of writing the primitive wavefunction (Eq. (B.37)) near momentum turning points, but unlike Eq. (B.37), this form of the wavefunction does not diverge in these regions.

B.1.4 Relation to Airy Function

We wish to extend the semiclassical wavefunction into classically-forbidden regions. We achieve this by matching Eq. (B.65) to a linear combination of the first-order asymptotic form of the Airy function and its derivative. These first-order terms are given by

$$Ai(-z) \approx \pi^{-1/2} z^{-1/4} \sin\left(\zeta + \frac{\pi}{4}\right) \quad (\text{B.66})$$

$$Ai'(-z) \approx -\pi^{-1/2} z^{1/4} \cos\left(\zeta + \frac{\pi}{4}\right), \quad (\text{B.67})$$

where ($|\arg z| < \frac{2\pi}{3}$) and $\zeta = (2/3)z^{3/2}$, as given by Abramowitz 10.4.60 and 10.4.62.

We wish to match the terms of Eq. (B.65) with an equation in the form of

$$\tilde{\Psi}_{m+n}(p, t) = C_1(p, t)Ai(-z(p, t)) + C_2(p, t)Ai'(-z(p, t)). \quad (\text{B.68})$$

By inspecting Eqs. (B.65)-(B.67), we immediately see that

$$\zeta = \left| \frac{\Delta\tilde{\mathcal{S}}(p, t)}{2\hbar} \right| = (2/3) [z(p)]^{3/2} \quad (\text{B.69})$$

$$z(p) = \left(\frac{3\zeta}{2} \right)^{2/3} = \left(\frac{3\Delta\tilde{\mathcal{S}}(p, t)}{4\hbar} \right)^{2/3} \quad (\text{B.70})$$

We must now match terms in Eqs. (B.65) with terms in Eq. (B.68) in order to determine the coefficients $C_1(p, t)$ and $C_2(p, t)$. By inspection, we see that

$$\begin{aligned} \pi^{-1/2} [z(p)]^{-1/4} C_1(p, t) \sin\left(\zeta + \frac{\pi}{4}\right) &= 2 \exp\left(\frac{i\tilde{\mathcal{S}}(p, t)}{\hbar} - \frac{i\tilde{\mu}_m\pi}{2}\right) \left[\mathbb{A}\mathbb{F} + \frac{\Delta A \Delta F}{4} \right] \quad (\text{B.71}) \\ &\times e^{-i\pi/4} \sin\left(\frac{\Delta\tilde{\mathcal{S}}(p, t)}{2\hbar} + \frac{\pi}{4}\right) \end{aligned}$$

$$\begin{aligned} \pi^{-1/2} [z(p)]^{-1/4} C_1(p, t) &= 2 \exp\left(\frac{i\tilde{\mathcal{S}}(p, t)}{\hbar} - \frac{i\tilde{\mu}_m\pi}{2}\right) \left[\mathbb{A}\mathbb{F} + \frac{\Delta A \Delta F}{4} \right] \quad (\text{B.72}) \\ &\times e^{-i\pi/4} \end{aligned}$$

$$C_1(p, t) = \frac{2 \exp\left(\frac{i\tilde{\mathcal{S}}(p, t)}{\hbar} - \frac{i\tilde{\mu}_m\pi}{2}\right) \left[\mathbb{A}\mathbb{F} + \frac{\Delta A \Delta F}{4} \right] e^{-i\pi/4}}{\pi^{-1/2} [z(p)]^{-1/4}} \quad (\text{B.73})$$

Similarly,

$$-\pi^{-1/2}[z(p)]^{1/4}C_2(p, t) \cos\left(\zeta + \frac{\pi}{4}\right) = 2 \exp\left(\frac{i\tilde{S}(p, t)}{\hbar} - \frac{i\tilde{\mu}_m\pi}{2}\right) \left[\frac{\mathbb{A}\Delta F}{2} + \frac{\Delta A\mathbb{F}}{2}\right] \quad (\text{B.74})$$

$$\times e^{-i3\pi/4} \cos\left(\frac{\Delta\tilde{S}(p, t)}{2\hbar} + \frac{\pi}{4}\right)$$

$$-\pi^{-1/2}[z(p)]^{1/4}C_2(p, t) = 2 \exp\left(\frac{i\tilde{S}(p, t)}{\hbar} - \frac{i\tilde{\mu}_m\pi}{2}\right) \left[\frac{\mathbb{A}\Delta F}{2} + \frac{\Delta A\mathbb{F}}{2}\right] \quad (\text{B.75})$$

$$\times e^{-i3\pi/4}$$

$$C_2(p, t) = \frac{-2 \exp\left(\frac{i\tilde{S}(p, t)}{\hbar} - \frac{i\tilde{\mu}_m\pi}{2}\right) \left[\frac{\mathbb{A}\Delta F}{2} + \frac{\Delta A\mathbb{F}}{2}\right] e^{-i3\pi/4}}{\pi^{-1/2}[z(p)]^{1/4}} \quad (\text{B.76})$$

We may now insert these coefficients into Eq. (B.68) to obtain

$$\tilde{\Psi}_{m+n}(p, t) = \frac{2 \exp\left(\frac{i\tilde{S}(p, t)}{\hbar} - \frac{i\tilde{\mu}_m\pi}{2}\right) \left[\mathbb{A}\mathbb{F} + \frac{\Delta A\Delta F}{4}\right] e^{-i\pi/4}}{\pi^{-1/2}[z(p)]^{-1/4}} \text{Ai}(-z(p, t)) \quad (\text{B.77})$$

$$- \frac{2 \exp\left(\frac{i\tilde{S}(p, t)}{\hbar} - \frac{i\tilde{\mu}_m\pi}{2}\right) \left[\frac{\mathbb{A}\Delta F}{2} + \frac{\Delta A\mathbb{F}}{2}\right] e^{-i3\pi/4}}{\pi^{-1/2}[z(p)]^{1/4}} \text{Ai}'(-z(p, t))$$

We use this form of the wavefunction in the regions where the primitive expression diverges, *i.e.*, near caustics. Figure B.4(d) shows an example $|\tilde{\Psi}_{m+n}(p, t)|^2$ constructed via the primitive forms for $\tilde{\Psi}_m(p, t)$ and $\tilde{\Psi}_n(p, t)$ (Eq. (B.37); red curve) and the corrected form (Eq. (B.77); blue curve). The primitive form can be seen to diverge near the boundary of the classically-allowed region, while the corrected form does not. Away from the boundary of the classically-forbidden region, and inside the classically-allowed region, the two forms agree. The corrected form in the plot can be seen to extend into the classically-forbidden region; the details of this extrapolation are discussed next.

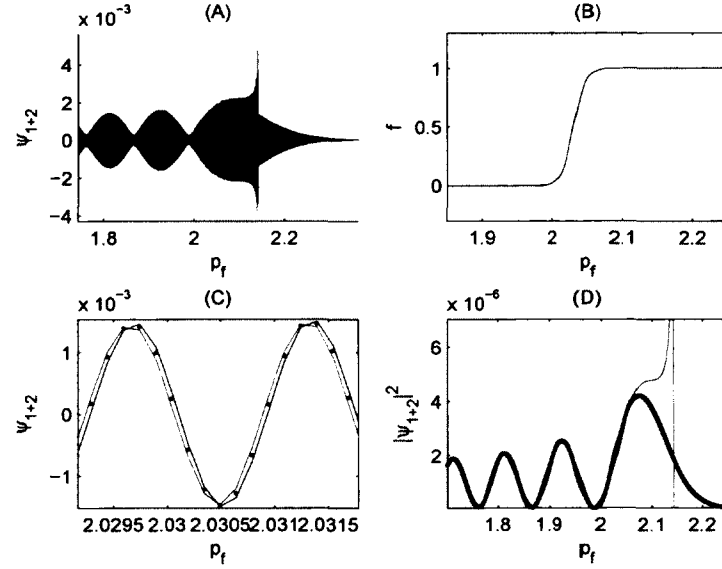


FIG. B.4: Primitive and corrected forms of local wavefunctions. (a) An example $\tilde{\Psi}_{m+n}(p, t)$. The red curve is the primitive semiclassical form, represented by the summation of equation (B.37) for the two consecutive branches, while the blue curve is the form given by equation (B.77). The primitive form can be seen to diverge, while the blue curve matches the primitive semiclassical form within the classically-allowed region, passes through the caustic smoothly, and decays in the forbidden region. (b) An example switching function used to smoothly go from the primitive semi-classical form of the wavefunction to (B.77). (c) Zoom of (a), in the region of transition between use of the primitive and Airy forms of the wavefunction. The black points show the values actually used for the local wavefunction. The black points lie between the primitive and Airy forms of the wavefunction, and are determined via the switching function. (d) Example of $|\tilde{\Psi}_{m+n}(p, t)|^2$. The red curve is the primitive form, the blue curve is the Airy form, and the black points are the values which are actually used.

B.1.5 Classically-Forbidden Regions

Equation (B.77) can also be used to describe the wavefunction in classically-forbidden regions. In order to use it in the forbidden regions, however, we must first construct a method of extrapolating values of $\Delta\tilde{\mathcal{S}}(p, t)$, $\tilde{\mathcal{S}}(p, t)$, $\Delta A(p, t)$, $A(p, t)$, $\Delta F(x_0(p_x, t))$, and $F(x_0(p_x, t))$ into the forbidden regions. We start by examining the behavior of $\Delta\tilde{\mathcal{S}}(p, t)$; recall that

$$\Delta\tilde{\mathcal{S}}(p, t) = \tilde{\mathcal{S}}_n(p, t) - \tilde{\mathcal{S}}_m(p, t) \quad (\text{B.78})$$

$$\approx - \int_n x_n(x_0, \tau) \frac{dp(x_0, \tau)}{d\tau} d\tau + \int_m x_m(x_0, \tau) \frac{dp(x_0, \tau)}{d\tau} d\tau \quad (\text{B.79})$$

$$\approx - \int_{\hat{p}_x}^p x_n(p') dp' + \int_{\hat{p}_x}^p x_m(p') dp' \quad (\text{B.80})$$

As can be seen in Fig. B.5(A), near the caustic, the relationship between p and x may be approximated as

$$p - \hat{p}_x = \alpha (x - \hat{x})^2, \quad (\text{B.81})$$

where \hat{p}_x and \hat{x} are the (x, p) values at which $\partial\mathcal{P}_x(x, t)/\partial x = 0$. Solving for x , we obtain

$$x = \pm \left[\frac{(p - \hat{p}_x)}{\alpha} \right]^{1/2} + \hat{x}. \quad (\text{B.82})$$

We substitute (B.82) into (B.80) to obtain

$$\Delta\tilde{\mathcal{S}}(p, t) \approx - \int_{\hat{p}_x}^p \left(\pm \left[\frac{(p' - \hat{p}_x)}{\alpha} \right]^{1/2} + \hat{x} \right) dp' + \int_{\hat{p}_x}^p \left(\pm \left[\frac{(p' - \hat{p}_x)}{\alpha} \right]^{1/2} + \hat{x} \right) dp' \quad (\text{B.83})$$

As can be seen in Fig. B.5(A), x_n and x_m are the positive and negative roots of (B.82).

We are examining the action values for trajectories ending on two successive momentum charts near a caustic; our use of (B.81) tells us that $(x_n - \hat{x}) = -(x_m - \hat{x})$. If we take x_n to be the negative root of (B.82), x_m is the positive root, and we may write the last equation as

$$\Delta\tilde{S}(p, t) \approx \int_{\hat{p}_x}^p \left(\left[\frac{(p' - \hat{p}_x)}{\alpha} \right]^{1/2} - \hat{x} \right) dp' + \int_{\hat{p}_x}^p \left(\left[\frac{(p' - \hat{p}_x)}{\alpha} \right]^{1/2} + \hat{x} \right) dp' \quad (\text{B.84})$$

$$\approx 2 \int_{\hat{p}_x}^p \left(\left[\frac{(p' - \hat{p}_x)}{\alpha} \right]^{1/2} \right) dp' \quad (\text{B.85})$$

$$\approx \frac{4}{3\sqrt{\alpha}} [(p - \hat{p}_x)]^{3/2} \quad (\text{B.86})$$

In this manner, we see that the following linear relationship has been established

$$\left[\Delta\tilde{S}(p, t) \right]^{2/3} \propto (p - \hat{p}_x). \quad (\text{B.87})$$

This relationship is shown in Fig. B.5(d). We will use (B.87) for extrapolating $\Delta\tilde{S}(p, t)$ into the forbidden regions. We also wish to develop an approximation for the relationship between $\tilde{S}(p, t)$ and $(p - \hat{p}_x)$ to use for extrapolation into the forbidden regions. Recall that

$$\tilde{S}(p, t) = \frac{\tilde{S}_n(p, t) + \tilde{S}_m(p, t)}{2} \quad (\text{B.88})$$

$$\approx - \int_n x_n(x_0, \tau) \frac{dp(x_0, \tau)}{d\tau} d\tau - \int_m x_m(x_0, \tau) \frac{dp(x_0, \tau)}{d\tau} d\tau \quad (\text{B.89})$$

$$\approx - \int_{\hat{p}_x}^p x_n(p') dp' - \int_{\hat{p}_x}^p x_m(p') dp' \quad (\text{B.90})$$

$$\approx - \int_{\hat{p}_x}^p \left(\pm \left[\frac{(p' - \hat{p}_x)}{\alpha} \right]^{1/2} + \hat{x} \right) dp' - \int_{\hat{p}_x}^p \left(\pm \left[\frac{(p' - \hat{p}_x)}{\alpha} \right]^{1/2} + \hat{x} \right) dp' \quad (\text{B.91})$$

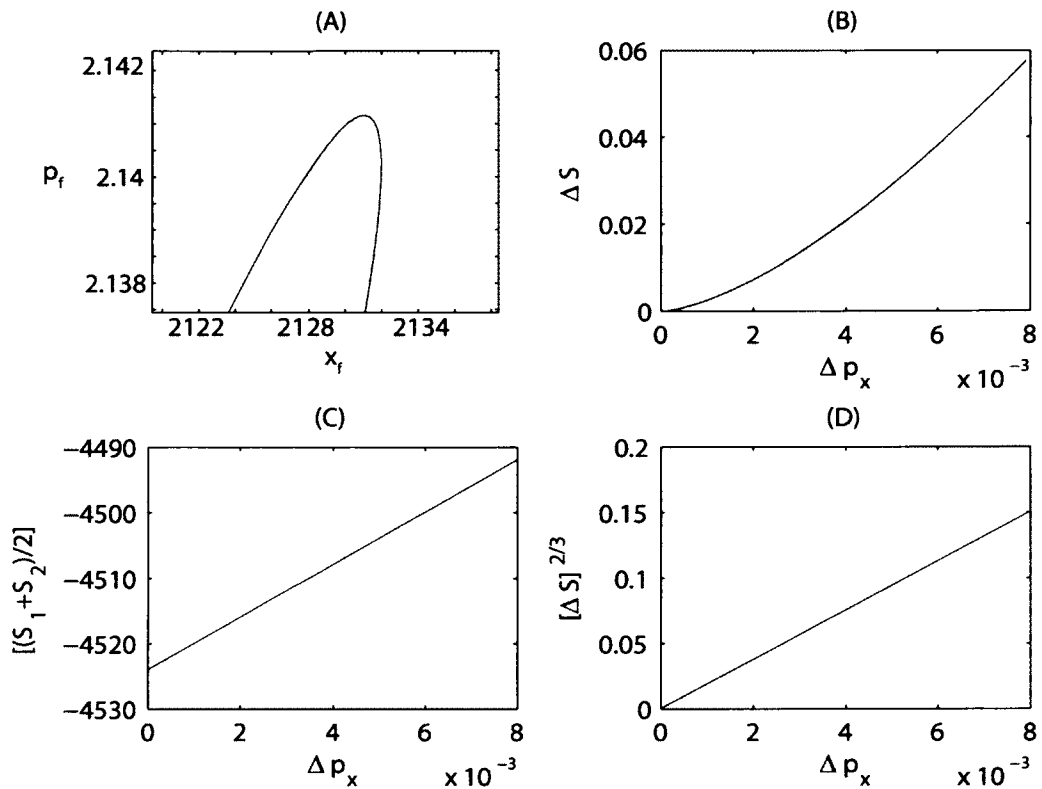


FIG. B.5: Functions used for extrapolating momentum-space actions into classically-forbidden regions. (A) Final momentum as a function of initial position near a caustic. The caustic is the point where $\partial p/\partial x_f = 0$. In the immediate vicinity of the caustic, the curve can be approximated as quadratic. (B) $\Delta \tilde{S}(p, t)$ as a function of $\Delta p = (p - \hat{p}_x)$. (C) $\tilde{S}(p, t)$ as a function of $\Delta p = (p - \hat{p}_x)$, illustrating equation (B.94). The blue curve is computed data, and the red curve is fitted from a polynomial fit. The red curve is used for extrapolating $\tilde{S}(p, t)$ into the forbidden region. (D) $\Delta \tilde{S}(p, t)$ as a function of $\Delta p = (p - \hat{p}_x)$, illustrating equation (B.87). The blue curve is computed data, and the red curve is fitted from a polynomial fit. The red curve is used for extrapolating $\Delta \tilde{S}(p, t)$ into the forbidden region.

Again taking x_n as the negative root and x_m as the positive root of (B.82), (B.91) becomes

$$\tilde{\mathbb{S}}(p, t) \approx - \int_{\hat{p}_x}^p \left(- \left[\frac{(p' - \hat{p}_x)}{\alpha} \right]^{1/2} + \hat{x} \right)_2 dp' - \int_{\hat{p}_x}^p \left(\left[\frac{(p' - \hat{p}_x)}{\alpha} \right]^{1/2} + \hat{x} \right)_1 dp' \quad (\text{B.92})$$

$$\approx -2 \int_{\hat{p}_x}^p \hat{x} dp'. \quad (\text{B.93})$$

Solving equation (B.93) establishes a linear relationship between $\tilde{\mathbb{S}}(p, t)$ and $(p - \hat{p}_x)$, which will be used for extrapolating $\tilde{\mathbb{S}}(p, t)$ into the forbidden regions, *i.e.*,

$$\tilde{\mathbb{S}}(p, t) \propto (p - \hat{p}_x). \quad (\text{B.94})$$

This relationship is shown in Fig. B.5(c).

Computations show that in the classically-allowed regions near caustics, the following linear relationships hold:

$$[\mathbb{A}(p, t)]^{-4} \propto (p - \hat{p}_x) \quad (\text{B.95})$$

$$[\Delta A(p, t)]^4 \propto (p - \hat{p}_x), \quad (\text{B.96})$$

as shown in Fig. B.6.

In order to construct values for $\mathbb{F}(x_0(p_x, t))$ and $\Delta F(x_0(p_x, t))$ in the classically-forbidden regions, we extrapolate x_0 into the forbidden regions, and use these x_0 values to evaluate the two functions. This is achieved by constructing polynomial fits for $\mathcal{P}_x(x_0)$ in the vicinity of the caustic, and inverting the relationship between $\mathcal{P}_x(x_0)$ and x_0 to obtain $x_0(p)$ values for classically-forbidden momenta. Since $\mathcal{P}_x(x_0)$ is a locally-quadratic function near the caustic, this technique yields two complex $x_0(p)$ values (one for each momentum-chart). These complex $x_0(p)$ values are then used to numerically determine $\mathbb{F}(x_0(p_x, t))$ and $\Delta F(x_0(p_x, t))$ in classically-forbidden regions.

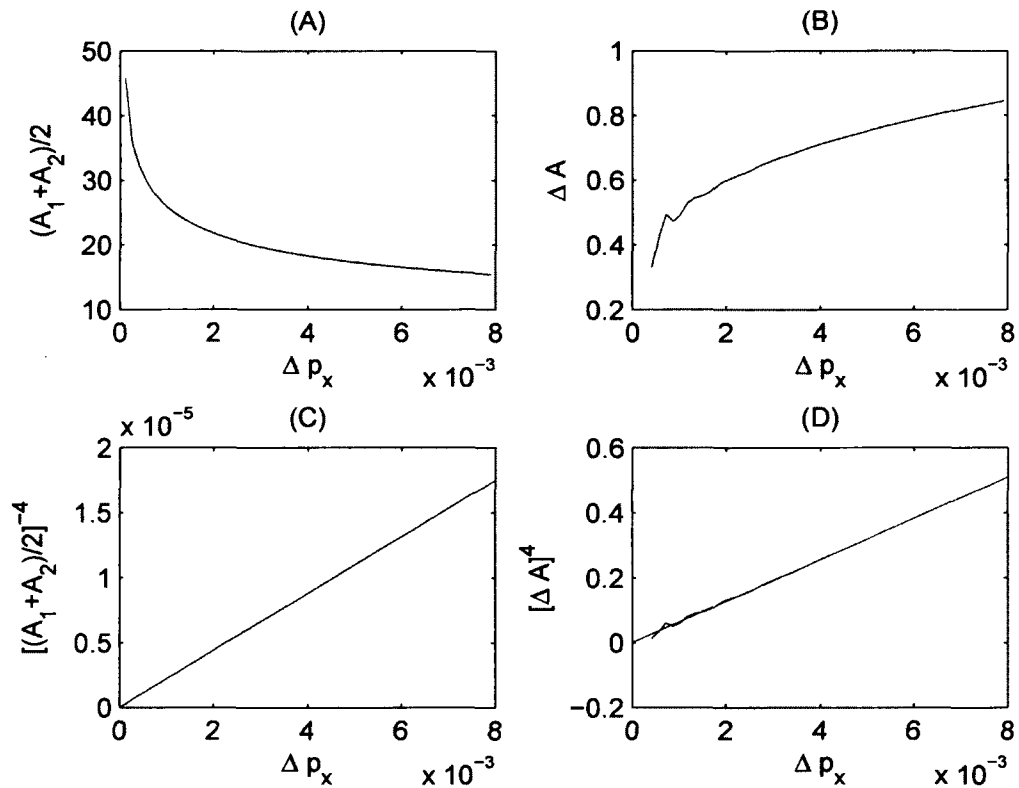


FIG. B.6: Functions used for extrapolating amplitudes into classically-forbidden regions. (A) $\mathbb{A}(p, t)$ as a function of $\Delta p = (p - \hat{p}_x)$. (B) $\Delta A(p, t)$ as a function of $\Delta p = (p - \hat{p}_x)$. (C) $[\mathbb{A}(p, t)]^{-4}$ as a function of $\Delta p = (p - \hat{p}_x)$, illustrating equation (B.95). (D) $[\Delta A(p, t)]^4$ as a function of $\Delta p = (p - \hat{p}_x)$, illustrating equation (B.96). In (C) and (D), the blue curve is computed data, and the red curve is fitted from a polynomial fit. The red curve is used for extrapolating $\Delta A(p, t)$ into the forbidden region.

We now have everything we need to construct a non-divergent form for local wavefunctions near caustics and in classically-forbidden regions. We use Eq. (B.77) for the wavefunction, and use the relationships given by Eqs. (B.87), (B.94), (B.95), and (B.96) to obtain values for $\Delta\tilde{\mathcal{S}}(p, t)$, $\tilde{\mathcal{S}}(p, t)$, $\mathbb{A}(p, t)$, and $\Delta A(p, t)$ in classically-forbidden regions. These values, along with values for $\mathbb{F}(x_0(p_x, t))$ and $\Delta F(x_0(p_x, t))$ for complex x_0 , are then used in Eq. (B.77) in classically-forbidden regions.

B.2 Global Wavefunction

We have seen that each momentum-chart of the constant-time slice of the Lagrangian manifold contributes a term to the global wavefunction. The global wavefunction is then given by a linear combination of these local wavefunctions,

$$\tilde{\Psi}(p, t) = \sum_b \tilde{\Psi}_b(p, t). \quad (\text{B.97})$$

We will illustrate the steps necessary to construct the final wavefunction for the simplest case, like that shown in Fig. 2.3(a), which contains two branches per cycle. Here we denote as “branches” the regions separated by momentum turning points in $p(x_0, \tau_f)$, i.e., regions separated by points where $\partial p(x_0, \tau_f)/\partial x_0 = 0$. We define a “cycle” as one barrier oscillation, i.e., one period of $p(x_0, \tau_f)$. We must determine the regions of validity of the two forms of the wavefunction, Eqs. (B.37) and (B.77), for all branches. Due to the periodicity of final momentum and initial position, we can do this for a single cycle only, as Eqs. (B.37) and (B.77) are valid in the same regions for the i^{th} branch within every cycle.

We choose the cycle spanning branches (a, b, c) in Fig. 2.3(a). We start with branches a and b , and construct the primitive form of the wavefunction by adding Eq. (B.37) for

the two branches. We then construct $\tilde{\Psi}_{a+b}(p, t)$ via Eq. (B.77). These two forms of the wavefunction are valid in different but overlapping regions, and we compare the two to determine the region of validity for each. This comparison shows that the Airy form is valid in regions D and E in Fig. 2.3(a) ($p \lesssim 1.66$). In region D ($1.36 \lesssim p \lesssim 1.66$), where both forms of the wavefunction are valid, we use a switching function that varies between 0 and 1 to weight each form, and use a linear combination of the two (an example of a switching function is shown in Fig. B.4(b)). We then use

$$\tilde{\Psi}_{a+b}(p, t) = f_1(p) [\text{Airy form}] + (1 - f_1(p)) [\text{Prim. form}], \quad (\text{B.98})$$

as the local wavefunction for branches a and b in regions C , D , and E , where

$$f_1(p) = \frac{1}{2} [\tanh(K[p - \bar{p}]) + 1] \quad (\text{B.99})$$

is the switching function; $f_1 \rightarrow 0$ at the boundary between regions C and D . “Airy form” and “Prim. form” in Eq. (B.98) refer to $\tilde{\Psi}_{a+b}(p, t)$ calculated via Eqs. (B.77) and (B.37), respectively.

We repeat this process for branches b and c , and find that the Airy form of this wavefunction, $\tilde{\Psi}_{b+c}(p, t)$, is valid in regions A and B ($p \gtrsim 1.77$). Both forms of the wavefunction are valid in region B ($1.77 \lesssim p \lesssim 2.01$). We use a switching function in region B to weight each form of the wavefunction, and use a linear combination of the two. We use primitive semiclassical wavefunctions for all branches in region C ($1.66 \lesssim p \lesssim 1.77$).

With knowledge of where each branch’s primitive and Airy forms of the local wavefunction may be used, one may construct a final wavefunction, which is a linear combination of all local wavefunctions. For cases with more than two branches per cycle, a more elaborate version of the same process is used. However, the steps for constructing the global

wavefunction remain the same: (i) all local wavefunctions must be summed to obtain the global wavefunction, (ii.) care must be taken to determine the regions for each branch in which one should use the primitive form for the wavefunction (Eq. (B.37)) or corrected form (Eq. (B.77)), or a linear combination of the two.

B.3 Semiclassical Implications of Periodicity

Since the classical initial distributions we use are wide in configuration space, the entire distribution needs many barrier oscillations to pass through the barrier region. Consequently, the summation of $\tilde{\Psi}_j(p, t)$ (Eq.(B.37)) over all j momentum-charts corresponds to summing over many trajectories that end at each classically-allowed momentum, and these trajectories begin with x_0 values from many different oscillation cycles, as seen in Fig. B.2(b). Therefore, the semiclassical calculation includes interference from trajectories from many different oscillation cycles. It was shown earlier that interference of trajectories from different oscillation cycles yields peaks in final momentum distributions at momenta satisfying $E_n = E_0 + n\hbar\omega$, consistent with Floquet theory. This section serves to quantitatively show how this arises from a semiclassical perspective. This discussion is limited to classically-forbidden regions, but its validity could be extended to include regions near caustics and in classically-forbidden regions by using the corrected form of local wavefunctions, Eq. (B.77).

Here we let L denote the range of initial x_0 values for which the initial distribution is defined, and we consider trajectories ending at a given p_f . These trajectories can begin with any x_0 in L . We also only consider trajectories which have these properties at a large enough $\tau_f = t_f$ such that they have been scattered far from the barriers, and the potential is effectively zero. We examine an interval of L , denoted by I , which has length $|p_0|T/m$, which corresponds to one oscillation period within L . We label all trajectories

which begin in I and which end at a given p_f using the label b . (For example, an initial x -value from inside I is denoted as x_0^b). We may then think of groups of initial positions $x_0^{(b,c)} = x_0^b - c|p_0|T/m$ which, when c is an integer, scatter to the same final momentum p_f . The meaning of these labels is that b (branch) labels a trajectory from within one oscillation cycle, and c (cycle) denotes different oscillation cycles.

We may now use these labels to express the equation for the global primitive wavefunction in a different manner than before,

$$\begin{aligned} \tilde{\Psi}(p, t) = \sum_b \sum_{c=-\infty}^{\infty} F(x_0^{(b,c)}(p, t)) \left| \frac{1}{\tilde{\mathcal{J}}_{(b,c)}(p, t)} \right|^{1/2} \\ \times \exp\left(\frac{i\tilde{\mathcal{S}}_{(b,c)}(p, t)}{\hbar} - \frac{i\pi\tilde{\mu}_{(b,c)}}{2}\right). \end{aligned} \quad (\text{B.100})$$

Here, we are explicitly summing over all branches within a cycle, and then summing over all cycles. The label c is allowed to extend over all integers, because the initial envelope $F(x_0) \rightarrow 0$ outside of L . Since all trajectories which have the same b index and differ only by a different c index, such as $x_0^{(b,c)}$ and $x_0^{(b,c')}$, scatter from the barriers in identical fashion, they have the same Jacobian and Maslov index,

$$\begin{aligned} \tilde{\mathcal{J}}_{(b,c)}(p, t) = \tilde{\mathcal{J}}_{(b,0)}(p, t) \equiv \tilde{\mathcal{J}}_b(p, t), \\ \tilde{\mu}_{(b,c)} = \tilde{\mu}_{(b,0)} \equiv \tilde{\mu}_b. \end{aligned} \quad (\text{B.101})$$

Furthermore, the relationship of these trajectories' actions can be expressed algebraically. If we consider $\tilde{\mathcal{S}}_{(b,0)}$ and $\tilde{\mathcal{S}}_{(b,1)}$, the $(b, 0)$ and $(b, 1)$ trajectories follow the same path; however, the $(b, 1)$ trajectory spends one more oscillation cycle on the left side of the barrier(s), but the $(b, 0)$ cycle spends one more oscillation cycle to the right of the barrier(s). Therefore by Eq. (B.24),

$$\tilde{\mathcal{S}}_{(b,1)}(p, t) - \tilde{\mathcal{S}}_{(b,0)}(p, t) = \Delta ET, \quad (\text{B.102})$$

where $\Delta E = p^2/2 - p_0^2/2$ is the difference in the trajectories' final and initial energies. By noting that this quantity is independent of both b and c , we see that

$$\tilde{\mathcal{S}}_{(b,c)} = \tilde{\mathcal{S}}_{(b,0)} + c\Delta ET \equiv \tilde{\mathcal{S}}_b + c\Delta ET. \quad (\text{B.103})$$

Eqs. (B.101) and (B.103) provide an efficient method for constructing terms when computing the semiclassical wavefunction. Rather than directly integrating the entire line of initial conditions L , one only needs to integrate trajectories for initial conditions within one cycle, e.g. the interval I , and construct $\tilde{\mathcal{J}}_{(b,c)}(p, t)$, $\tilde{\mu}_{(b,c)}$, and $\tilde{\mathcal{S}}_{(b,c)}$ for other cycles via (B.101) and (B.103). The semiclassical sum can now be rewritten as

$$\tilde{\Psi}(p, t) = \sum_b D_b(p, t) \left| \frac{1}{\tilde{\mathcal{J}}_b(p, t)} \right|^{1/2} \exp\left(\frac{i\tilde{\mathcal{S}}_b(p, t)}{\hbar} - \frac{i\pi\tilde{\mu}_b}{2}\right), \quad (\text{B.104})$$

where

$$D_b(p, t) = \sum_{c=-\infty}^{\infty} F(x_0^b(p, t) - cp_0T/m) e^{ic\Delta ET/\hbar}. \quad (\text{B.105})$$

Generally, this sum is performed numerically. However, in some cases, the sum can be expressed in closed form. We examine one such case next. Consider an initial packet envelope which is ‘‘rectangular’’ or ‘‘square,’’ meaning that $F(x_0) = F_0$ is constant over a length $L = N|p_0|T$, and $F(x_0) = 0$ outside L . L corresponds to an initial distribution that is N oscillation cycles wide. This type of envelope allows us to write Eq. (B.105) as

$$D_b(p, t) = D(p) = F_0 \sum_{c=0}^{N-1} e^{2\pi ic\epsilon} = F_0 e^{2\pi i\epsilon(N-1)/2} \frac{\sin(\pi\epsilon N)}{\sin(\pi\epsilon)}, \quad (\text{B.106})$$

where $\epsilon = \Delta E/(\hbar\omega)$. Because $D(p)$ does not depend on b , Eq. (B.104) factors into the

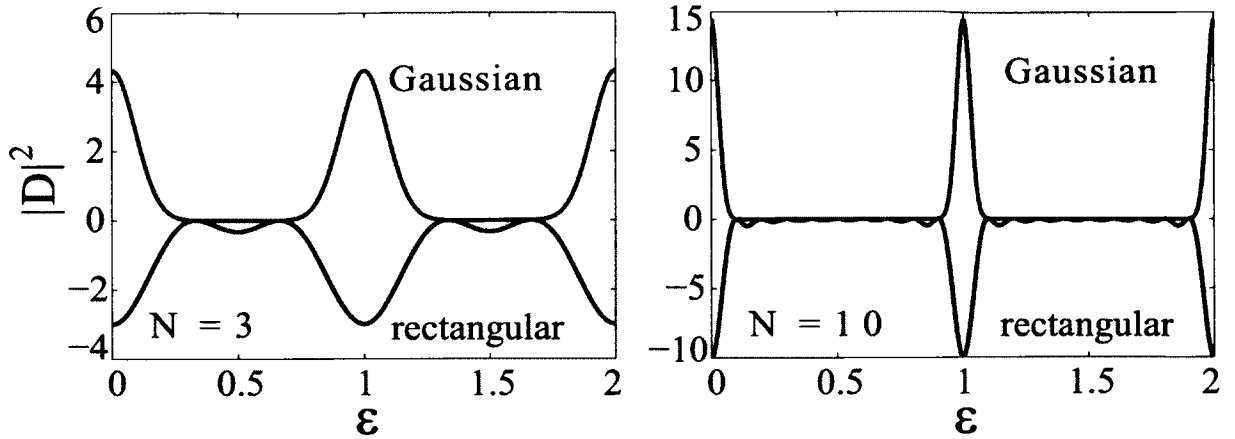


FIG. B.7: “Comb” functions which are responsible for sharply-peaked final momentum probabilities. Plot of $|D|^2$ for an initial rectangular [lower curve, Eq. (B.106)] and Gaussian [upper curve] initial packet profiles. For the rectangular case, $N = 3, 10$, showing convergence to delta functions at integer values of ϵ . The widths β of the Gaussian packets are chosen to match the standard deviations of the corresponding rectangular packets.

product of two quantities: (i) $D(p)$, which involves only a c sum, and (ii) a quantity involving only a sum over b :

$$\tilde{\Psi}(p, t) = D(p) \sum_b \left| \frac{1}{\tilde{\mathcal{J}}_b(p, t)} \right|^{1/2} \exp \left(\frac{i\tilde{\mathcal{S}}_b(p, t)}{\hbar} - \frac{i\pi\tilde{\mu}_b}{2} \right). \quad (\text{B.107})$$

If we allow the width of the initial distribution to tend to infinity, $D(p)$ approaches a “comb” of delta functions according to

$$\lim_{N \rightarrow \infty} \frac{\sin(\pi\epsilon N)}{\sin(\pi\epsilon)} = \sum_{k=-\infty}^{\infty} \delta(\epsilon - k). \quad (\text{B.108})$$

Therefore the final wavefunction is sharply-peaked at momenta satisfying $\Delta E = k\hbar\omega$ (*i.e.*, $E_k = E_0 + k\hbar\omega$) which is consistent with Floquet theory. This is shown in the lower curves of Fig. B.7 for different values of N . The sum over branches in Eq. (B.107), as discussed in

earlier chapters, thus “weights” this comb of delta-like functions, and is responsible for the relative heights of the peaks. It is not always possible to express this sum analytically in such compact form, but the same principles apply for other types of initial envelopes. The upper curves in Fig. B.7 show calculations of the “comb” function for a Gaussian-shaped initial envelope.

BIBLIOGRAPHY

- [1] M. Büttiker and R. Landauer, *Phys. Rev. Lett.* **49**, 1739 (1982).
- [2] P. K. Tien and J. P. Gordon, *Phys. Rev.* **129**, 647 (1963).
- [3] A. Pimpale, S. Holloway, and R. J. Smith, *J. Phys. A* **24**, 3533 (1991).
- [4] V. A. Fedirko and V. V. Vyurkov, *Phys. Status Solidi B* **221**, 447 (2000).
- [5] A.-P. Jauho, *Phys. Rev. Lett.* **41**, 12327 (1990).
- [6] M. Garttner, F. Lenz, C. Petri, F. K. Diakonov and P. Schmelcher, *Phys. Rev. E* **81**, 051136 (2010).
- [7] A. Emmanouilidou and L. E. Reichl, *Phys. Rev. A* **65**, 033405 (2002).
- [8] M. Henseler, T. Dittrich, and K. Richter, *Phys. Rev. E* **64**, 046218 (2001).
- [9] W. A. Lin and L. E. Ballentine, *Phys. Rev. Lett.* **65**, 2927 (1990).
- [10] L. M. Pecora, H. Lee, D. H. Wu, T. Antonsen, M. J. Lee, E. Ott, *Phys. Rev. E* **83**, 065201 (2011).
- [11] D. A. Steck, W. H. Oskay, and M. G. Raizen, *Science* **293**, 274 (2001).
- [12] D. A. Steck, W. H. Oskay, and M. G. Raizen, *Phys. Rev. Lett.* **88**, 120406 (2002).
- [13] F. Grossmann, T. Dittrich, P. Jung, and P. Hänggi, *Phys. Rev. Lett.* **67**, 516 (1991).

- [14] S. Rahav and P. W. Brouwer, *Phys. Rev. B* **74**, 205327 (2006).
- [15] D. J. Thouless, *Phys. Rev. B* **27**, 6083 (1983).
- [16] P. W. Brouwer, *Phys. Rev. B* **58**, R10135 (1998).
- [17] M. Moskalets and M. Büttiker, *Phys. Rev. B* **66**, 205320 (2002).
- [18] K. K. Das and T. Opatrný, *Phys. Lett. A* **374**, 485 (2010).
- [19] E. R. Mucciolo, C. Chamon, and C. M. Marcus, *Phys. Rev. Lett.* **89**, 146802 (2002).
- [20] D. Ferry, S. M. Goodnick, and J. Bird, *Transport in Nanostructures* (Cambridge, USA, 2009), 2nd ed.
- [21] Y. Levinson, O. Entin-Wohlman, and P. Wölfle, *Physica A* **302**, 335 (2001).
- [22] J. E. Avron, A. Elgart, and L. Sadun, *J. Stat. Phys.* **116**, 425 (2004).
- [23] M. Moskalets and M. Büttiker, *Phys. Rev. B* **66**, 205320 (2002).
- [24] S. W. Kim, *Phys. Rev. B* **66**, 235304 (2002).
- [25] L. Arrachea, *Phys. Rev. B* **72**, 125349 (2005).
- [26] J. E. Avron, A. Elgart, G. M. Graf, and L. Sadun, *Phys. Rev. B* **62**, 10618(R) (2000).
- [27] M. Blaauboer and C. M. L. Fricot, *Phys. Rev. B* **71**, 041303 (2005).
- [28] P. Samuelsson and M. Büttiker, *Phys. Rev. B* **71**, 245317 (2005).
- [29] F. Romeo and R. Citro, e-print arXiv:0903.2362 (2009).
- [30] J. Splettstoesser, M. Governale, J. König, and R. Fazio, *Phys. Rev. Lett.* **95**, 246803 (2005).

- [31] F. Romeo and R. Citro, *Phys. Rev. B* **80**, 235328 (2009).
- [32] M. Switkes, C. M. Marcus, K. Campman, and A. C. Gossard, *Science* **283**, 1905 (1999).
- [33] P. W. Brouwer, *Phys. Rev. B* **63**, 121303 (2001).
- [34] F. Giazotto, P. Spathis, S. Roddaro, S. Biswas, F. Taddei, M. Governale, and L. Sorba, *Nature Phys.* **7**, 857 (2011).
- [35] K. K. Das, S. Kim, and A. Mizel, *Phys. Rev. Lett.* **97**, 096602 (2006).
- [36] K. K. Das and S. Aubin, *Phys. Rev. Lett.* **103**, 123007 (2009).
- [37] K. K. Das, *Phys. Rev. A* **84**, 031601 (2011).
- [38] K. K. Das, M. R. Meehan, and A. J. Pyle, *Phys. Rev. A* **89**, 063626 (2014).
- [39] B. Zhao, Y.-A. Chen, X.-H. Bao, T. Strassel, C.-S. Chuu, X.-M. Jin, J. Schmiedmayer, Z.-S. Yuan, S. Chen, and J.-W. Pan, *Nature Physics* **5**, 95 (2009).
- [40] J.-P. Brantut, J. Meineke, D. Stadler, S. Krinner, and T. Esslinger, e-print arXiv:1203.1927 (2012).
- [41] A. A. Zozulya and D. Z. Anderson, *Phys. Rev. A* **88**, 043641 (2013).
- [42] R. A. Pepino, J. Cooper, D. Z. Anderson, and M. J. Holland, *Phys. Rev. Lett.* **103**, 140405 (2009).
- [43] S. Eckel, J. G. Lee, F. Jendrzejewski, N. Murray, C. W. Clark, C. J. Lobb, W. D. Phillips, M. Edwards, and G. K. Campbell, *Nature* **506**, 200 (2014).
- [44] C. C. Rankin and W. H. Miller, *J. Chem. Phys.* **55**, 3150 (1971).

- [45] T. Uzer, C. Jaffé, J. Palacian, P. Yanguas, S. Wiggins, *Nonlinearity* **15**, 957 (2002).
- [46] P. Gaspard, *Chaos, scattering, and statistical mechanics* (Cambridge University Press, Cambridge, MA, 1998).
- [47] J. U. Nöckel and A. D. Stone, *Optical processes in microcavities* (World Scientific Publishers, Singapore, 1996).
- [48] S. Sridhar, W. Lu, W. Sinai, *J. Stat. Phys.* **180**, 755 (2002).
- [49] K. Burke and K. A. Mitchell, *Phys. Rev. A* **80**, 033416 (2009).
- [50] K. Mitchell, J. Handley, B. Tighe, A. Flower, and J. Delos, *Phys. Rev. Lett.* **92**, 73001 (2004).
- [51] K. A. Mitchell and D. A. Steck, *Phys. Rev. A* **76**, 031403 (2007).
- [52] J. M. Ottino, A. Souvaliotis, and G. Metcalfe, *Chaos, Solitons, and Fractals* **6**, 425 (1995).
- [53] R. Samelson, *Stochastic Modelling in Physical Oceanography* (Birkhauser, Boston, 1996).
- [54] C. Jaffé and T. Uzer, *Ann. N Y Acad. Sci.* **1017**, 39 (2004).
- [55] K. A. Mitchell, J. P. Handley, B. Tighe, J. B. Delos, S. K. Knudson, *Chaos* **13**, 880 (2003).
- [56] K. A. Mitchell, J. P. Handley, J. B. Delos, S. K. Knudson, *Chaos* **13**, 892 (2003).
- [57] K. A. Mitchell, J. P. Handley, B. Tighe, A. Flower, and J. B. Delos, *Phys. Rev. Lett.* **92**, 073001 (2004).

- [58] K. A. Mitchell, J. P. Handley, B. Tighe, A. Flower, and J. B. Delos , Phys. Rev. A **70**, 043407 (2004).
- [59] J. B. Delos and K. A. Mitchell, Few-Body Systems **38**, 181 (2006).
- [60] P. Hansen, K. A. Mitchell, and J. B. Delos, Phys. Rev. E **73**, 066226 (2006).
- [61] C. Bracher and J. B. Delos, Phys. Rev. Lett. **96**, 100404 (2006).
- [62] C. R. Schleif and J. B. Delos, Phys. Rev. A **76**, 013404 (2007).
- [63] K. A. Mitchell and J. B. Delos, Physica D **229**, 9 (2007).
- [64] C.T. Whelan and J.H. McGuire, eds., K. A. Mitchell, J. P. Handley, B. Tighe, A. A. Flower, S. K. Knudson, and J. B. Delos, *From the Atomic to the Nano-Scale* (Old Dominion University, 2003).
- [65] J. Novick, M. L. Keeler, J. Giefer, J. B. Delos, Phys. Rev. E **85**, 016205 (2012).
- [66] J. Novick and J. B. Delos, Phys. Rev. E **85**, 016206 (2012).
- [67] K. A. Mitchell and J. B. Delos, Physica D **221**, 170 (2006).
- [68] G. P. Agarwal, *Nonlinear Fiber Optics* (Academic press, San Diego, CA, 2001).
- [69] it is an integrable singularity.
- [70] R. P. Feynman, *Quantum Mechanics and Path Integrals* (McGraw-Hill, New York, 1965).
- [71] G. Roati, M. Zaccanti, C. D'Errico, J. Catani, M. Modugno, A. Simoni, M. Inguscio, and G. Modugno, Phys. Rev. Lett. **99**, 010403 (2007).

- [72] S. Richard, F. Gerbier, J. H. Thywissen, M. Hugbart, P. Bouyer, and A. Aspect, *Phys. Rev. Lett.* **91**, 010405 (2003).
- [73] M. Razavy, *Quantum Theory of Tunneling* (World Scientific Publishing Company, Singapore, 2003).
- [74] R. W. Easton, *Trans. Am. Math.* **294**, 719 (1986).
- [75] M. J. Davis and S. K. Gray, *J. Chem. Phys.* **84**, 5389 (1986).
- [76] M. J. Davis, *J. Chem. Phys.* **83**, 1016 (1985).
- [77] R. S. MacKay, J. D. Meiss, and I. C. Percival, *Physica D* **13**, 55 (1984).
- [78] A. Tiyapan and C. Jaffé, *J. Chem. Phys.* **99**, 2765 (1993).
- [79] A. Tiyapan and C. Jaffé, *J. Chem. Phys.* **101**, 10393 (1994).
- [80] A. Tiyapan and C. Jaffé, *J. Chem. Phys.* **103**, 5499 (1995).
- [81] C. Jaffé, S. D. Ross, M. W. Lo, J. Marsden, D. Farrelly, and T. Uzer, *Phys. Rev. Lett.* **89**, 011101 (2002).
- [82] C. Jaffé, D. Farrelly, and T. Uzer, *Phys. Rev. A* **60**, 3833 (1999).
- [83] C. Jaffé, D. Farrelly, and T. Uzer, *Phys. Rev. Lett.* **84**, 610 (2000).
- [84] C. Jaffé and T. Uzer, *Journal of Phys. Chem. A* **105**, 2783 (2001).
- [85] S. Wiggins, L. Wiesenfeld, C. Jaffé, and T. Uzer, *Phys. Rev. Lett.* **86**, 5478 (2001).
- [86] V. Rom-Kedar, *Physica D* **43**, 229 (1990).
- [87] V. Rom-Kedar, *Nonlinearity* **7**, 441 (1994).

- [88] B. Eckhardt and C. Jung, *J. Phys. A* **19**, L829 (1986).
- [89] B. Eckhardt, *J. Phys. A* **20**, 5971 (1987).
- [90] C. Jung and H. J. Scholz, *J. Phys. A* **20**, 3607 (1987).
- [91] B. Ruckerl and C. Jung, *J. Phys. A* **27**, 55 (1994).
- [92] B. Ruckerl and C. Jung, *J. Phys. A* **27**, 6741 (1994).
- [93] C. Lipp and C. Jung, *J. Phys. A* **28**, 6887 (1995).
- [94] C. Jung, C. Lipp, and T. H. Seligman, *Ann. Phys.* **275**, 151 (1999).
- [95] C. Jung and A. Emmanouilidou, *Chaos* **15**, 023101 (2005).
- [96] A. Emmanouilidou and L. E. Reichl, *Phys. Rev. A* **62**, 022709 (2000).
- [97] A. Emmanouilidou and C. Jung, *Phys. Rev. E* **73**, 016219 (2006).
- [98] P. Collins, *Internat. J. Bifur. Chaos Appl. Sci. Engrg.* **12**, 605 (2002).
- [99] P. Collins, *Dyn. Syst.* **19**, 1 (2004).
- [100] P. Collins, *Dyn. Syst.* **20**, 369 (2005).
- [101] P. Collins, *Experiment. Math.* **14**, 75 (2005).
- [102] P. Collins and B. Krauskopf, *Phys. Rev. E* **66**, 056201 (2002).
- [103] E. A. Jackson, *Perspectives of Nonlinear Dynamics* (Cambridge University Press, Cambridge, 1990).
- [104] S. Wiggins, *Chaotic Transport in Dynamical Systems* (Springer, New York, 1992).

- [105] F. R.N. Koch, F. Lenz, C. Petri, F. K. Diakonov, P. Schmelcher, *Phys. Rev. E* **78**, 056204 (2008).
- [106] K. A. Mitchell, *Physica D* **238**, 737 (2009).
- [107] K. A. Mitchell and J. B. Delos, *Physica D* **221**, 170 (2006).
- [108] J. B. Delos, S. K. Knudson, and D. W. Noid, *Phys. Rev. A* **30**, 1208 (1984).
- [109] T. A. Byrd, M. K. Ivory, A. J. Pyle, S. Aubin, K. A. Mitchell, J. B. Delos, and K. K. Das, *Phys. Rev. A* **86**, 013622 (2012).
- [110] V. Maslov and M. Fedoriuk, *Semi-classical Approximation in Quantum Mechanics* (Kluwer Academic Publishers, 2002).
- [111] J. B. Delos, *Advances in Chemical Physics* **65**, 161 (1986).
- [112] C. D. Schwieters, J. A. Alford, and J. B. Delos, *Phys. Rev. B* **54**, 10652 (1996).
- [113] N. Spellmeyer, D. Kleppner, M.R. Haggerty, V. Kondratovich, J.B. Delos, and J. Gao, *Phys. Rev. Lett.* **79**, 1650 (1997).
- [114] M. R. Haggerty, N. Spellmeyer, D. Kleppner, and J. B. Delos, *Phys. Rev. Lett.* **81**, 1592 (1998).
- [115] M. R. Haggerty and J. B. Delos, *Phys. Rev. A* **61**, 053406 (2000).
- [116] C .D. Schwieters and J. B. Delos, *Phys. Rev. A* **51**, 1023 (1995).
- [117] C .D. Schwieters and J. B. Delos, *Phys. Rev. A* **51**, 1030 (1995).
- [118] M.L. Du and J. B. Delos, *Phys. Rev. Lett.* **58**, 1731 (1987).
- [119] M. L. Du and J. B. Delos, *Phys. Rev. A* **38**, 1896 (1988).

- [120] M. L. Du and J. B. Delos, *Phys. Rev. A* **38**, 1913 (1988).
- [121] T. A. Byrd and J. B. Delos, *Phys. Rev. E* **89**, 022907 (2014).
- [122] M. K. Ivory, T. A. Byrd, A. J. Pyle, K. K. Das, K. A. Mitchell, S. Aubin, and J. B. Delos, *Phys. Rev. A* **90**, 023602 (2014).
- [123] G. Casati, C. Mejía-Monasterio, and T. Prosen, *Phys. Rev. Lett.* **101**, 016601 (2008).
- [124] M. Moskalets and M. Büttiker, *Phys. Rev. B* **66**, 035306 (2002).
- [125] B. Wang and J. Wang, *Phys. Rev. B* **66**, 125310 (2002).
- [126] T. A. Byrd, K. K. Das, K. A. Mitchell, S. Aubin, J. B. Delos, *Phys. Rev. E* **90**, 052107 (2014).
- [127] K. A. Mitchell, *Physica D* **241**, 1718 (2012).
- [128] K. A. Mitchell, *AIP Conference Proceedings* **1468**, 268 (2012).
- [129] C. Jung, C. Mejía-Monasterio, O. Merlo, and T. H. Seligman, *New Journal of Physics* **6**, 48 (2004).
- [130] M. S. Child, *Semiclassical Mechanics with Molecular Applications* (Oxford University Press, New York, 1991).

VITA

Tommy Byrd

Tommy Byrd was born and grew up in northeast Tennessee. After high school, he worked various jobs for a few years but eventually decided to go to college. He received a B.S. in physics from East Tennessee State University in 2008. Tommy began graduate school at Clemson University in 2008 studying astrophysics, but he didn't like it, and he transferred to The College of William and Mary in 2009. There, he worked with advisor John Delos and collaborated with Seth Aubin. His work focused on the theory of atom pumping, and chaotic transport. He earned an M.S. in physics in 2011.